Revista Română de Inginerie Civilă

Indexată în bazele de date internationale (BDI)

ProQuest, IET INSPEC, EBSCO, GOOGLE SCHOLAR, CROSSREF, TDNET, DIMENSIONS, DRJI, J-GATE, INDEX COPERNICUS, ULRICH'S, JOURNALSEEK, RESEARCH GATE, SEMANTIC SCHOLAR, ERIHPLUS, WORLDCAT

Volumul 17 (2026), Numărul 2

MATRIX ROM
3 Politehnicii Street, Bucharest, Romania
Tel. +4021.4113617, +40733882137
e-mail: office@matrixrom.ro
www.matrixrom.ro

EDITORIAL BOARD

Romanian Journal of Civil Engineering is founded, published and funded by publishing house MATRIX ROM
Executive Director: mat. Iancu ILIE

Online edition ISSN 2559-7485

Print edition ISSN 2068-3987; ISSN-L 2068-3987

Regulating the temperature of the heating agent in district heating systems with the aim of RES integration and the recovery of residual thermal energy

Reglarea temperaturii agentului termic în sistemele de termoficare cu scopul integrării SER și a recuperării energiei termice reziduale

Daniel Muntean[1], Dănuț Tokar[1], Adriana Tokar[1], Daniel Bisorca[1], Alexandru Dorca[1]

[1]Universitatea Politehnica Timișoara,
Victoriei Square, Nr. 2, Timișoara, Romania
E-mail: *daniel-beniamin.muntean@upt.ro, adriana.tokar@upt.ro, danut.tokar@upt.ro, daniel.bisorca@upt.ro, alexandru.dorca@upt.ro*

DOI: 10.37789/rjce.2026.17.2.1

Abstract. Given the energy crisis the entire planet is going through, the waste of any form of fuel or energy source is clear evidence of irresponsibility towards both humanity and the planet we manage. The study presents several proposals for making the district heating system more efficient by integrating renewable sources into the heat production process and recovering the residual thermal energy resulting from technological processes.

Key words: renewable energy sources, district heating, waste energy recovery

1. Introduction

District heating systems in Romania are still among the most polluting public services, contributing substantially to the increase in global temperature, through CO_2 emissions per Gcal, which have reached alarming levels [1-3]. Regarding current challenges, the development of urban heating systems is essential to face the energy transition phase.

For this reason, this scientific report presents possible solutions for energy efficiency of district heating systems, using the district heating system in Timișoara as an example. Although the district heating system in Timișoara has the capacity to cover a fairly high percentage of the city's thermal energy consumption, modernization measures by replacing existing pipes with preinsulated pipes have not solved the problem of energy efficiency of the system [4]. Over time, centralized thermal energy supply systems have evolved, moving from generation I and currently reaching, in Timișoara, generation III, and the proposals for the current period are those of moving to generation IV [5,6].

The article was received on 07.04.2025, accepted on 08.06.2026 and published on 12.06.2026

In the context of the requirements regarding the quality of constructions, regarding energy saving and thermal insulation, respectively the sustainable use of natural resources, the 4th generation of systems represents a natural evolution of the 3rd generation and highlights the efficiency-oriented characteristics. The temperatures of the thermal agent for transporting or distributing thermal energy continue to have a decreasing trend, the equipment used is increasingly modular, and the materials are increasingly flexible and with reduced energy losses, but the most important aspect is the fact that the system allows for easier integration of renewable energy sources (RES).

Currently, district heating systems allow for the long-distance distribution of thermal energy and the use of an increasing percentage of renewable energy, thus increasing the fight against global warming and the energy crisis. For this reason, sustainable district heating systems will have to ensure planning structures, low costs correlated with efficient operation and strategic investments, as illustrated in Fig. 1 [7].

Fig. 1. The concept of 4th Generation District Heating

The main efficiency solutions considered in the study relate to the integration of RES, the reduction of the temperature of the heat carrier in the primary network and the recovery of waste heat [4-6,8,20].

Traditional district heating systems are composed of thermal power plants that pump hot water or steam through pipes to provide heat to metropolitan areas. A district heating system incorporates a heat generating unit, a transport and distribution network, heat points and heat consumers (end users) (Fig. 2) [9].

The scheme of the district heating network is shown in Fig. 2. In the primary circuit, hot water is transported through a transport network to the district heating points and then returns to the heat source, and in the secondary circuit, this heat is transferred to the final consumers via heating elements.

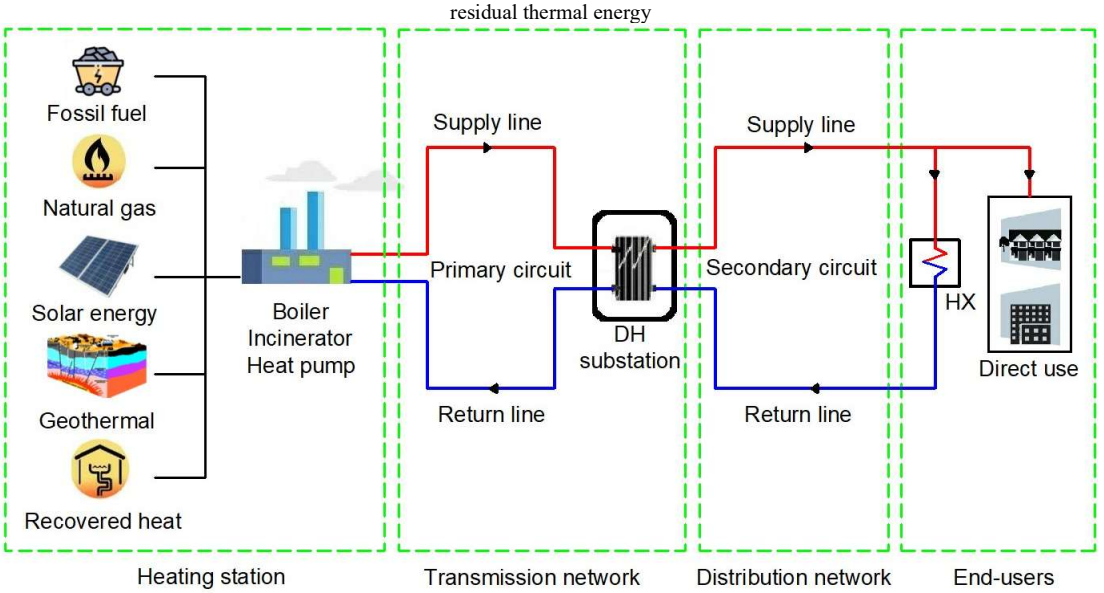

Fig. 2. Essential district heating system components

Surplus industrial heat can be recovered and used in a district heating system [10]. The incorporation of RES into district heating systems results in lower outlet temperatures than those of a conventional supply network. In this context, geothermal systems using heat pumps have attracted increasing interest in several countries in the last few years, as they allow for a sustainable replacement of fossil fuels and create zero CO_2 emissions [9]. In addition, nations such as Sweden, Denmark, Germany and Austria have increased their use of solar energy for the production of thermal energy used in district heating systems [9].

There are four distinct generations of district heating systems [11]. Generation I transported steam at temperatures above 200 °C using concrete pipes. As a result, it was not particularly efficient and was replaced due to the risk of pipe bursting. Generation II used concrete pipes to transport pressurized water at temperatures above 100 °C and is known as high-temperature district heating.

Generation III uses pre-insulated pipes buried directly in the ground and operates with water at supply temperatures between 65 and 95 °C. Generation IV district heating systems are now being developed and referred to as low-temperature district heating systems (50-60 °C). When end-user temperatures are increased with heat pumps, ultra-low supply temperatures (35-45 °C) are also used [12].

The fifth generation of district heating Is an extension of the fourth generation, a new concept based on a decentralized network that allows direct energy flows between and within buildings. Its key features are: low exergy network using low-temperature heat sources; closed thermal energy loops that ensure the exchange of heat and cold between groups of buildings; integration and synergy between thermal and electrical networks; 100% renewable energy target [13]. The evolution of district heating generations over time is presented in Fig. 3.

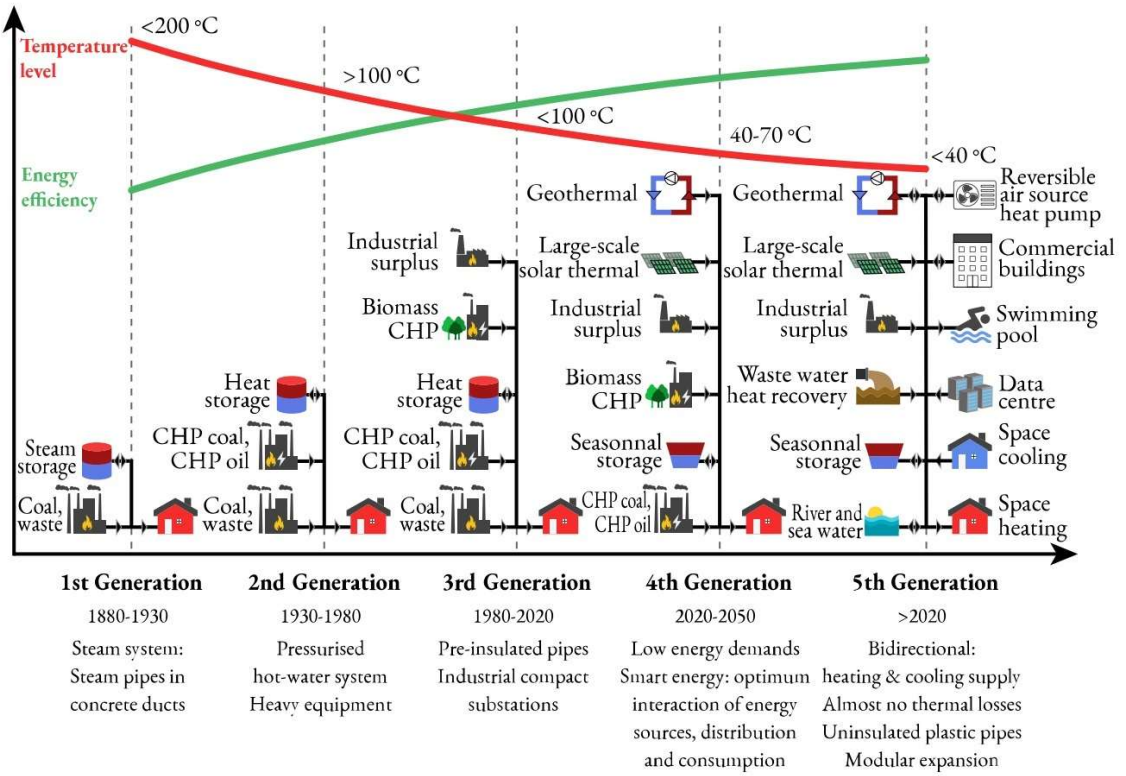

Fig. 3. The evolution of the district heating systems generations [9]

The temperature reduction in district heating networks is constrained by the heat requirements and the technical specifications of residential and commercial buildings (domestic hot water demand or space heating design).

Table 1 defines the different types of district heating systems according to the technical requirements of the buildings, the corresponding heating terminal units and the previous definitions. Recent investigations have suggested that low temperature systems have a significant potential for space heating in existing buildings [14].

Figure 4 illustrates the required supply temperatures for radiators in space heating systems for buildings with different heat requirements.

Table 1

The five types of district heating networks [9]

DH network generation	DH network type	Supply temperature (°C)	Limitation	Suitable terminal unit
1GDH	Very high temperature	160-210	The necessity of using condensate collection and transport equipment	High pressure tubular heater
2GDH	High temperature	100-125	The necessity of using pressurised tanks that may be linked directly to the system	Tubular heating radiator
3GDH	Medium temperature	65-95	Minimum temperature for DHW in the tank (65 °C)	Radiator
4GDH	Low	50-60	Minimum DHW comfort	Radiant system

DH network generation	DH network type	Supply temperature (°C)	Limitation	Suitable terminal unit
	temperature		temperature (50 °C)	(floor, wall, ceiling), radiator, fan coil
4GDH	Ultra-low temperature	35-45	Minimum floor heating temperature (35 °C)	Radiant floor
5GDH	Ambient temperature	0-30	Minimum supply temperature of WSHP (0 °C)	Radiant system

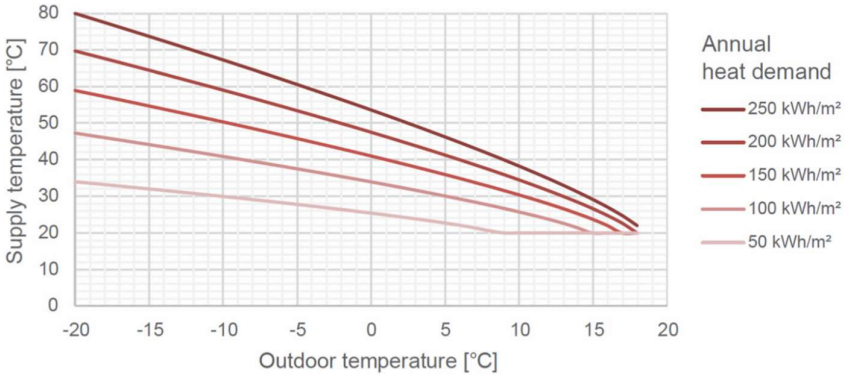

Fig. 4. The necessary supply temperatures in a radiator [15]

2. Proposals to improve the efficiency of the district heating system

As can be seen in Fig. 3, both the reduction of heat losses and the possibility of introducing/using RES and recovering residual heat energy require a decrease in the temperature regime used for transporting energy from the source(s) to the final consumers.

If the entire district heating system is taken into account, both the total heat loss and its saving potential are significant. The typical primary supply network for different areas of the city requires different supply temperatures, depending on the type of existing buildings, so for new residential areas, the required temperature is considerably lower than in residential areas with old buildings or industrial areas. Reducing heat losses on the transport network can be achieved by thermal insulation of the pipes using the most efficient and new solutions and materials or by reducing the temperature of the transported heat carrier [5].

2.1. Delivery temperature zoning in the primary district heating network

Zoning of the primary network is achieved by installing a mixing loop that injects water from the return pipe into the supply pipe (Fig. 5), resulting in a mixture that provides the necessary temperature for end users.

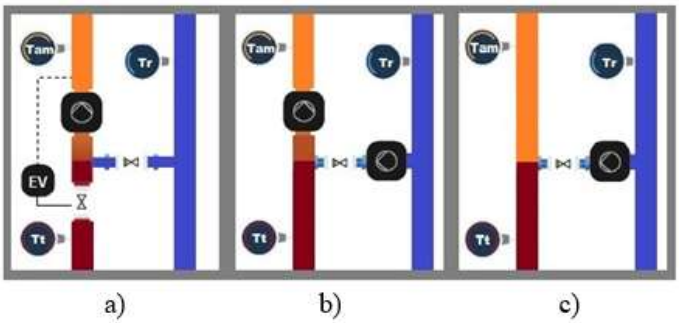

Fig. 5. Mixing loop control systems [5]
a) Classic loop; b) Free flow loop; c) By-pass pump loop
Tt – flow temperature, Tr – return temperature, Tam – mixing temperature, EV – solenoid valve

In Fig. 6a it is observed that each building zone is supplied by a branch of the primary network, and at the branching points a reduction of the flow/return temperature regime can be achieved depending on the specific needs of that zone. In Fig. 6b, the temperature zoning is observed on the branches supplying residential buildings that use a lower temperature heat carrier to ensure the thermal needs for heating and preparation of hot water for consumption.

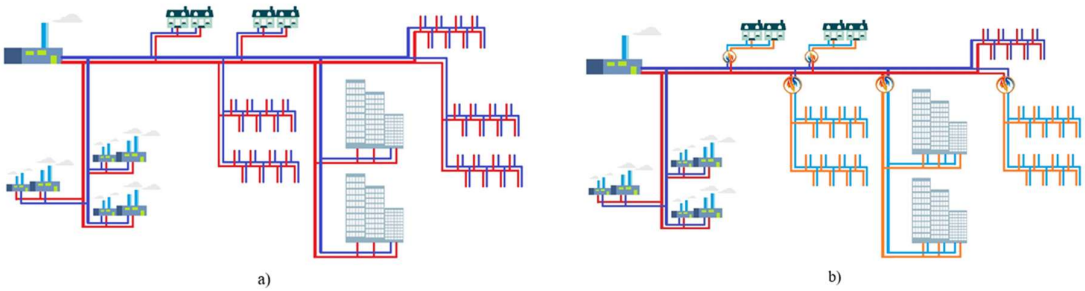

Fig. 6. Schema sistemului centralizat de termoficare [5]
a) înainte de zonare; b) după zonare

2.2. RES integration and expansion of the prosumer concept

The diversification of energy sources, but also the variation in consumption, generates on the one hand the need to store the energy obtained, especially that from renewable sources and to transform some networks from unidirectional to bidirectional. The selection of thermal energy sources that ensure a quality supply for consumers will have an important role in optimizing the operation of thermal networks and transforming classic networks into smart networks. In this context, this study addresses the advantages of smart thermal networks related to the local integration of RES (heat pumps and photovoltaic panels), transforming consumers into prosumers of thermal and electrical energy. The problem of RES variability and fluctuation can only be solved by storage. It is estimated that thermal energy storage in both the civil construction and industrial sectors can ensure annual energy savings of up to 7.8% and a 5.5% reduction in CO_2 emissions [16].

On the other hand, changes are also occurring in terms of the requirements that the sources must provide, emphasizing the ecological aspect at the expense of the economic aspect. For this reason, a mix of conventional and renewable sources is inevitable in the energy sector. The development of energy solutions that integrate renewable energy into thermal and electrical energy production systems has been of major interest to energy producers and distributors in recent years [17]. The proposal for the integration of RES is addressed to the buildings of the educational unit "Henri Coandă Technical College Timișoara" and the thermal point PT34 (Fig. 7).

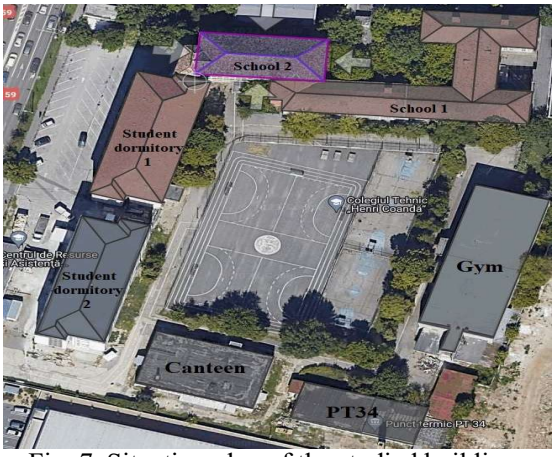

Fig. 7. Situation plan of the studied buildings

The placement of photovoltaic panels on the roofs of the buildings (Fig. 8) was carried out using the Polysun calculation program [18]. The electrical energy produced is used in the first phase to ensure its own electrical energy consumption. Table 2 presents the output data resulting from the simulation performed by installing 1956 EvoloCells 400 MIB 400 W photovoltaic panels, on a total roof area of 13,592 m².

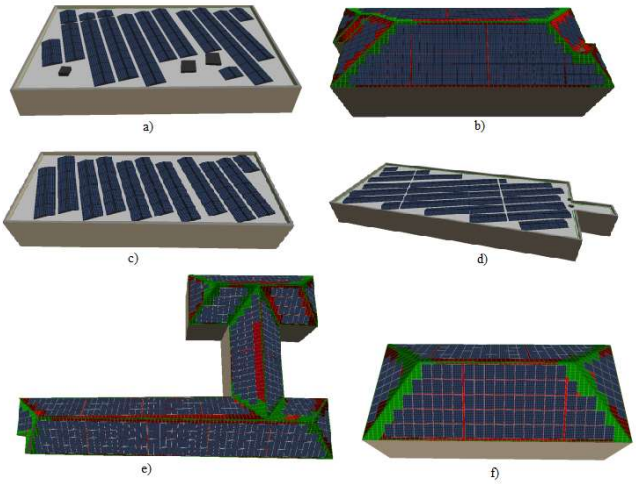

Fig. 8. The placement of photovoltaic panels on the studied buildings [19]
a) Canteen; b) Student dormitory 1 and 2; c) PT34; d) Gym; e) School 1; f) School 2

Table 2

The output data of the studied buildings [19]

Building	Nr. of panels	PV inst. [MW]	PV prod. [MWh/an]
Canteen	154	61.60	67.60
Student dormitory 1	333	133.20	142.60
Student dormitory 2	297	118.80	124.35
PT 34	122	48.80	53.96
Gym	294	117.60	130.04
School 1	552	220.80	218.43
School 2	204	81.60	82.54
Total	1,956	782.40	820.00

Given the considerable surplus of annual electricity produced after ensuring the own electricity consumption necessary for the operation of the educational buildings, 6 air-to-water heat pumps were installed, each with a heating capacity of 200 kW, which use the electricity from the photovoltaic system. The thermal energy produced by the heat pumps using the electricity from the photovoltaic system of the educational institution can be used first for the preparation of hot water consumed in the own buildings as well as for heat supply in their heating installations, resulting on the heating side a hybrid system that uses as primary thermal energy the one from the DH system with input of energy from RES. In table 3 you can see the production of the photovoltaic system (PV prod), the consumption of electricity for lighting (El. Enec), the preparation of hot water for consumption (Hw Enec) and the input of thermal energy for the heating system (Heat. Enec) and surpluses of solar electricity produced (S. Epv).

Table 3

Monthly production and consumption of electricity [19]

Month	Elec. Enec (MWh)	Heat Enec (MWh)	Hw Enec (MWh)	PV prod. (MWh)	S Epv (MWh)
Jan	20.00	90.64	21.74	24.07	-108.31
Feb	18.50	73.11	20.14	36.44	-75.31
March	18.00	57.95	22.25	64.84	-33.36
April	17.00	27.79	20.90	88.45	22.76
May	16.00	9.28	20.49	106.31	60.54
June	9.50	1.62	18.61	111.35	81.61
July	1.00	0.03	18.17	115.98	96.78
Aug.	1.00	0.00	17.58	101.20	82.62
Sept.	10.00	7.88	17.07	70.83	35.88
Oct.	17.00	30.90	18.31	50.99	-15.23
Nov.	18.00	56.08	18.80	30.87	-62.01
Dec.	20.00	81.72	20.68	18.73	-103.67
Sum	166.00	437.00	234.74	820.00	-17.69

Even after using the photovoltaic electricity produced to cover the various types of energy required for the operation of the buildings, there are several months during the summer period that remain with a considerable surplus of electricity produced.

The classic solution is for this surplus electricity to be delivered to the national energy system, but there is a possibility that this surplus cannot be taken over. It is proposed that the electricity not consumed in the summer months be used to produce

domestic hot water (DHW), which will be introduced into the DHW distribution network of the district heating system, also considering the fact that the PT34 thermal point is located in the immediate vicinity of the educational buildings.

Also, the surplus photovoltaic energy is used by the 6 heat pumps to prepare DHW and introduce it into the district heating system to supply the neighboring residential district "City of Mara". Table 4 summarizes the solar energy surplus (S Epv) for the summer months, the electrical energy required to produce domestic hot water that is delivered to the "City of Mara" residential district (Hw Enec "City of Mara") and the electrical energy delivered in NES (Elec. In NES).

Table 4

Electrical and thermal energy introduced into the system [19]

Month	S Epv (MWh)	Hw Enec "City of Mara" (MWh)	Elec. in NES (MWh)
April	22.76	52.24	-
May	60.54	51.22	9.32
June	81.61	46.54	35.08
July	96.78	45.43	51.35
Aug.	82.62	43.95	38.67
Sept.	35.88	42.66	-

Fig. 22 shows the functional diagram of the photovoltaic electricity and heating and ACC thermal energy production plant and its integration into the district heating system, so that the beneficiary of the buildings considered becomes a prosumer of thermal and electrical energy [22]. The thermal energy produced is stored in a storage tank (RS).

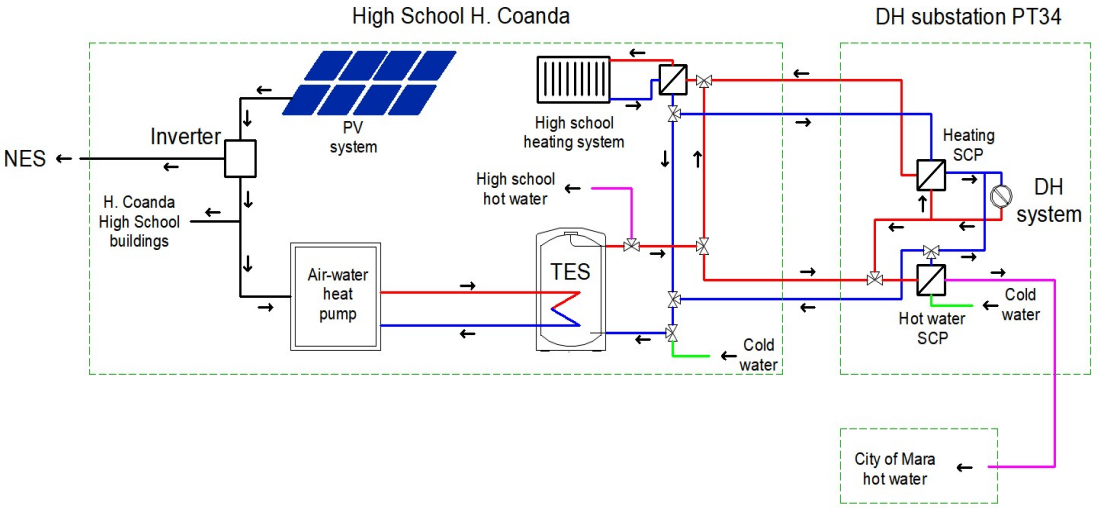

Fig. 22. Functional scheme of the thermal and electrical installation [19]

Beneficiaries of residential or public buildings must view the need to use RES as an opportunity to move from being consumers to being prosumers of thermal and electrical energy.

2.3. The recovery and utilization of residual heat from data centers

The rapid increase in the need for data storage and processing and digital telecommunications have recently generated a massive development of the data center (DC) industry. Although the digitization of various fields of human activity brings major benefits to the quality of his life, the secondary effects that appear because of this trend must also be assumed and solutions found to reduce the negative effects. Considering the exponential increase in human dependence on IT devices and services, an increase in energy consumption for manufacturing and powering these devices is also generated [20].

Considering that the potential of recoverable energy from DC residual heat varies depending on their size, the characteristics of the equipment used and the classification class of the DC, the applications for its subsequent use will be of two types, namely: local use, by integrating the energy under the form of hot water in the own heating installation and hot water supply for consumption and centralized use by providing thermal energy, as a prosumer, to the city's district heating system [20].

2.3.1. Local use of recovered energy

The local use of recovered energy is chosen as a technical solution for situations where the amount of thermal energy recovered is less than or equal to the total thermal energy required to cover the needs of the buildings in which the DC is located, for space heating in the winter and the production of domestic hot water in the summer.

For the recovery of residual heat from DC, an air-water heat exchanger connected to the primary circuit of a water-water heat pump can be used, which will raise the temperature of the heating agent so that it can still be used as needed in the thermal heating installation or for the production and accumulation in a hot water tank (HWT) of domestic hot water. The functional scheme of the waste heat recovery installation and the production of thermal energy in the form of hot water is presented in Fig. 2 [20].

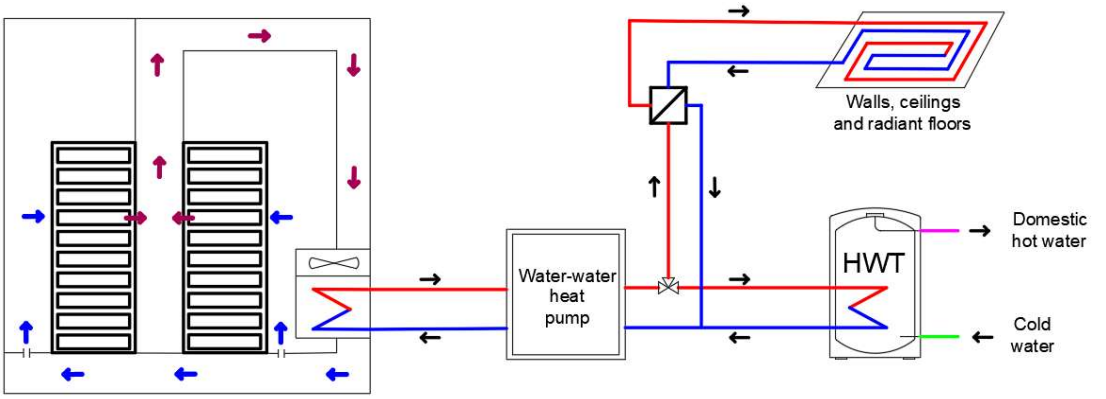

Fig. 2. Functional scheme of the recovery and local use installation

2.3.2. Introducing the recovered energy into the heating system

An important aspect that must be taken into account when we talk about RES integration is the fact that the temperature of the thermal agent produced by these sources is lower than in the case of the classic ones, so that the use of additional equipment is required to raise the temperature of the agent to the necessary value so it could finally be used by the consumers of the heating system, in most cases using water-to-water heat pumps (Fig. 5).

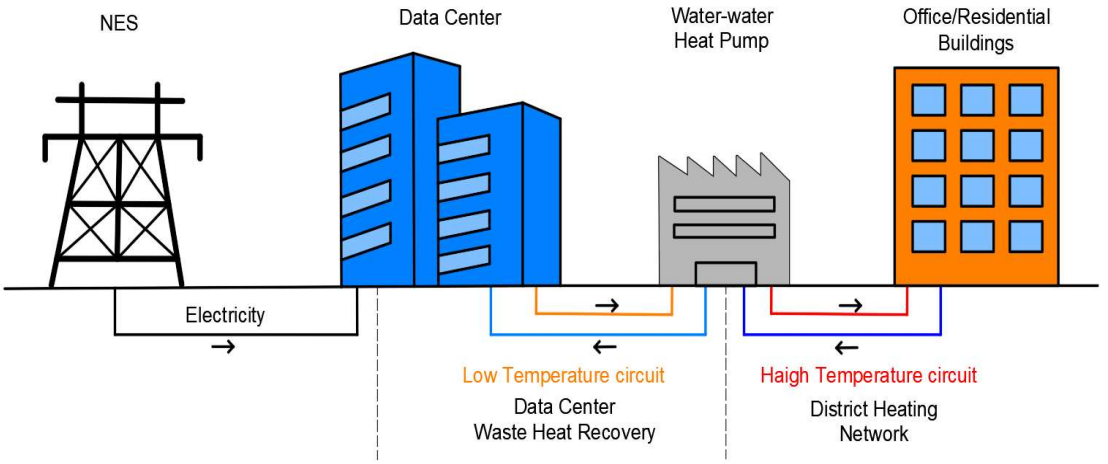

Fig. 5. Integration of thermal energy recovered from data centers in the district heating system

3. Conclusions

The proposed energy efficiency measures aim at the sustainable implementation and use of district heating networks, in accordance with the policy of reducing energy consumption and CO_2 emissions.

The integration of renewable energy sources into the production process of the thermal agent represents a pressing necessity for which the most efficient technical solutions must be found so that thermal energy losses through transport are reduced as much as possible.

The residual energy potential in the EU presented in specialized literature is estimated to be approximately 2860 TWh/year of which approximately 56 TWh/year comes from the DC sector [21,22]. So, the residual energy potential recoverable from DC is a source for the preparation of hot water in various applications like domestic hot water or thermal agent for heating installations.

References

[1] Tokar A, Tokar D, Adam M, Păcurar C, Muntean D, Dragotă C. Considerations for limiting the contribution of buildings to climate change through efficient energy use. Proceedings of the conference with international participation Building Services and Ambiental Comfort, Timișoara, 2023, pp. 98-105.

[2] Fouladvand J, Ghorbani A, Mouter N, Herber P. Analysing community-based initiatives for heating and cooling: A systematic and critical review. Energy Research & Social Science 2022;88:102507.
[3] van den Broek M, Veenendaal P, Koutstaal P, Wim T, Faaij A. Impact of international climate policies on CO_2 capture and storage deployment: Illustrated in the Dutch energy system. Energy Policy 2011;39(4):2000-2019.
[4] Muntean D, Tokar A. Reducing operating costs in district heating systems by optimizing functional parameters: Comparative studies. IOP Conf. Series: Earth and Environmental Science 2023;1136:012060.
[5] Muntean D, Mirza M, Tokar A. Soluții de reducere a pierderilor de căldură în sistemele de termoficare prin zonarea temperaturii de livrare. Revista Ingineria Instalațiilor 2021;1:26-31.
[6] Sârbu I, Mirza M, Crâșmăreanu E. A review of modeling and optimization techniques for district heating systems. International Journal of Energy Research 2019;43(13):6572-6598.
[7] Lund H, Werner S, Wiltshire R, Svendsen S, Thorsen JE, Hvelplund F, Mathiesen BV. 4th generation district heating (4GDH) integrating smart thermal grids into future sustainable energy systems. Energy 2014;68:1-11.
[8] Muntean D, Mirza M, Tokar A, Tokar D. Modernization of the heat supply system of the University of Agricultural Sciences and Veterinary Medicine of Banat, from Timișoara. 7th World Multidisciplinary Civil Engineering - Architecture - Urban Planning Symposium 2022, 5-9 September 2022, Prague, Czech Republic, AIP Conf. Proc. 2928, 2023.
[9] Sârbu I, Mirza M, Muntean D. Integration of renewable energy sources into low-temperature district heating systems: A review. Energies 2022;15(18):6523.
[10] ANRE. Ordin 105/2021 privind aprobarea prețului de referință al energiei electrice produse în cogenerare de înaltă eficiență care beneficiază de bonus. Autoritatea Națională de Reglementare în Domeniul Energiei, Monitorul Oficial nr. 983, București, 14 octombrie 2021.
[11] Lund R, Mohammadi S. Choice of insulation standard for pipe networks in 4th generation district heating systems. Applied Thermal Engineering 2016;98:256-264.
[12] Zvingilaite E, Ommen T, Elmegaard B, Franck ML. Low temperature DH consumer unit with micro heat pump for DHW preparation. In Proceedings of the 13th International Symposium on District Heating and Cooling, Copenhagen, Denmark, 3-4 September, 2012.
[13] https://5gdhc.eu/5gdhc-in-short/, accessed on 12.06.2024.
[14] Østergaard DS, Svendsen S. Experience from a practical test of low-temperature district heating for space heating in five Danish single-family houses from the 1930s. Energy 2018;159:569-578.
[15] Romanov D, Leiss B. Geothermal energy at different depths for district heating and cooling of existing and future building stock. Renewable and Sustainable Energy Reviews 2022;167:112727.
[16] Guelpa E, Verda V. Thermal energy storage in district heating and cooling systems: A review. Applied Energy 2019;252:113474.
[17] Brand L, Calvén A, Englund J, Landersjö H, Lauenburg P. Smart district heating networks - A simulation study of prosumers' impact on technical parameters in distribution networks. Applied Energy 2014;129:39-48.
[18] Polysun software. User manual. Vela Solaris, Bern, Switzerland; 2020.
[19] Muntean D, Tokar A, Dorca A, Tokar D, Adam M. Expanding the prosumer concept to enhance the efficiency of district heating systems. A case study. Revista Română de Inginerie Civilă 2024;15:311-318.
[20] Tokar A, Muntean D, Tokar D, Bisorca D, Cinca M. Considerations regarding the recovery and utilization of residual heat from data centers. Hidraulica. Magazine of Hydraulics, Pneumatics, Tribology, Ecology, Sensorics, Mechatronics 2024;1:29-33.
[21] Charlotte Elton, Euro.green, Published on 27/02/2023, accessed on 13.02.2024, https://www.euronews.com/green/2023/02/27/europe-could-be-powered-by-recycled-heat-from-data-centres-and-fridges-report-reveals.
[22] Eduard Oró, Paolo Taddeo, Jaume Salom. Waste heat recovery from urban air cooled data centres to increase energy efficiency of district heating networks. Sustainable Cities and Society, Volume 45, February 2019, Pages 522-542.

Valorization of textile waste through the production of new products

Valorificarea deșeurilor textile cu obținerea produselor noi

Irina Ceban [1*], Elena Bunduchi [2], Cristina Cujba [3]

[1]Institute of Chemistry of Moldova State University, 3 Academiei street, Chisinau, MD-2028, Republic of Moldova
[2]Moldova State University, 60 Alexei Mateevici Street, Chisinau, MD-2009, Republic of Moldova
[3]SRL COORDINATE, 1 Iurii Gagarin Street, Molești, Ialoveni, MD-6820, Republic of Moldova
e-mail: irina.ginsari@outlook.com

DOI: 10.37789/rjce.2026.17.2.2

Abstract. *The present study investigates the valorization of textile and cellulose-based waste through the production of sustainable composite materials. Post-consumer textile waste (cotton, polyester, and blends) was combined with paper and cardboard residues to produce decorative panels, bricks, composite boards, handmade paper, compost, and industrial absorbents. The manufacturing processes involved pressing, molding, extrusion, and maceration with eco-friendly binders and mineral additives to enhance mechanical, thermal, and fire-resistant properties. Characterization included thermal conductivity, compressive strength, morphological analysis, and aesthetic evaluation. Results indicate that the recycled products exhibit comparable performance to conventional materials, offering good thermal and acoustic insulation, fire resistance, and low emissions. The approach provides a viable circular economy solution, reducing landfill waste and conserving natural resources.*

Key words: *textile, waste, cellulose, recycled, product*

Rezumat. *Studiul de față investighează valorificarea deșeurilor textile și a celor pe bază de celuloză prin obținerea unor materiale compozite sustenabile. Deșeurile textile post-consum (bumbac, poliester și amestecuri) au fost combinate cu reziduuri de hârtie și carton pentru a produce panouri decorative, cărămizi, plăci compozite, hârtie manuală, compost, etc. Procesele de fabricare au inclus presarea, turnarea, extrudarea și macerarea, utilizând lianți ecologici și aditivi minerali pentru îmbunătățirea proprietăților mecanice, termice și de rezistență la foc. Caracterizarea materialelor a cuprins determinarea conductivității termice, a rezistenței la compresiune, analiza morfologică și evaluarea estetică. Rezultatele indică faptul că produsele reciclate prezintă performanțe comparabile cu cele ale materialelor convenționale, oferind o bună izolație termică și acustică, rezistență la foc și emisii reduse. Abordarea propusă reprezintă o soluție viabilă de economie circulară, contribuind la reducerea cantității de deșeuri depozitate și la conservarea resurselor naturale*

Cuvinte cheie: *textile, deșeuri, celuloză, reciclat, produs*

The article was received on 21.01.2026, accepted on 27.05.2026 and published on 12.06.2026

1. Introduction

The textile industry is one of the largest consumers of natural resources and a major source of solid waste globally. According to data from the literature [1], the equivalent of one garbage truck full of textiles is either incinerated or landfilled every second. At the same time, the paper and cardboard industry generates large amounts of waste, especially from packaging, used paper, and post-industrial residues. These two waste streams – textile and cellulose-based – can represent a valuable resource if intelligently combined and processed through innovative material recovery solutions.

Textile waste processing increasingly involves combining it with cardboard waste or other cellulose sources to obtain new products such as thermal insulation panels, composite materials, particle boards, or textile paper. This approach relies on the synergy between textile fibers (natural or synthetic) and the cellulose matrix, which helps improve the mechanical, thermal, or aesthetic properties of the final product [2,3].

From a technical perspective, textile fibers – especially cotton and cellulose blends – show high compatibility with paper and cardboard fibers, allowing the formation of composite structures with increased strength and reduced environmental impact. Recent studies indicate that mixing textiles with paper waste can result in products with good thermal insulation properties and potential applications in construction, eco-friendly packaging, or urban furniture [4,5].

This recovery method has multiple advantages: it reduces the volume of waste sent to landfills; it replaces virgin resources with secondary materials; it contributes to circular economy objectives and reduces the carbon footprint.

Moreover, this approach aligns with recent European directives regarding Extended Producer Responsibility (EPR) and the EU Strategy for Sustainable and Circular Textiles [6], which require the separate collection of textiles by 2025 and encourage innovation in the recycling of mixed textile materials.

Therefore, research and development of new products made from textile–cellulose blends represent not only an ecological necessity but also an industrial opportunity. This paper proposes an evaluation of the potential for valorizing textile waste by combining it with cardboard and paper waste to obtain composite materials with practical applications in various fields.

2. Materials and Methods

Pressed Agglomeration Process (Manufacturing of Thermal Insulation Panels). Textile waste is shredded and combined with rehydrated cardboard slurry (or recyclable paper). An eco-friendly binder (starch, natural latex, vegetable resin) is added. The mixture is placed into molds, pressed, and dried at temperatures of 80–120°C [7]. Thermal insulation panels for construction (interior walls, attics) and sound-absorbing boards are obtained (Composite panels made of 70% used cotton + 30% ground cardboard, bound with modified starch → thermal conductivity of 0.045 W/mK, comparable to expanded polystyrene).

For the manufacturing of decorative panels, recycled textile waste (cotton, polyester, blends) and cellulosic waste (paper, recycled cardboard) were used. These materials were selected due to their high availability and renewable nature, contributing to the reduction of environmental impact [8].

As a binder, eco-friendly gypsum-based compounds (universal PVA glue, wallpaper adhesive) were employed, ensuring the structural cohesion of the composite. In addition, mineral additives such as borax, liquid glass, kieselguhr, bio-adhesives, and modified starch were incorporated to enhance mechanical strength, improve fire resistance, and ensure dimensional stability. To achieve a uniform visual appearance, dyes were added, while tap/drinking water was used as a solvent and dispersion medium (Table 1).

Table 1

Raw materials and additives used for the manufacturing of panels, bricks, and other decorative objects from recycled materials

Component	*Exemple / Type*	*Main role*
Textile waste	Cotton, polyester, blends	Recyclable raw material, providing bulk and strength
Cellulosic waste	Paper, recycled cardboard	Filler and reinforcement, utilization of wastepaper
Eco-friendly binders	PVA glue, wallpaper adhesive, gypsum	Structural cohesion
Mineral additives	Borax, liquid glass, kieselguhr, bio-adhesives, modified starch	Mechanical strength, fire resistance, dimensional stability
Colorants	Eco-friendly pigments	Visual uniformity
Potable water	-	Solvent and dispersion medium

Molding Process (Manufacturing of Eco-friendly Bricks). Textile fibers, paper/cardboard pulp, and a binder such as cement or clay are combined. Water is added until a homogeneous mixture is formed. The mixture is poured into brick or block molds and left to harden [9,10]. Eco-friendly bricks for non-load-bearing construction, decorative masonry, or gardening can be obtained (Bricks made from a mix of used jeans + recycled newspaper + cement → reduced weight and improved insulation).

Extrusion Process (Manufacturing of Composite Boards). Textile fibers and cardboard waste are mixed with a thermoplastic matrix (e.g., PLA, polypropylene). The mixture is introduced into an extruder (160–200°C) and homogenized. It is formed by molding or laminating [11,12]. Rigid composite boards can be obtained, used for furniture, flooring, or partitions (Boards made from 40% textile fibers + 20% cardboard + 40% PLA → reduced density, good resistance to mechanical shocks).

Handmade Paper Manufacturing Process with Textile Inserts. Paper/cardboard waste is macerated in water to obtain pulp. Very finely cut textile fibers are added (e.g., white cotton). Sheets are formed by screening and pressing, then naturally dried [13,14]. Textured handmade paper can be obtained, used for invitations, luxury packaging, and artistic stationery (Handmade paper made from 60% recycled newspaper + 30% white linen scraps + 10% plant fibers → natural appearance, increased durability).

Co-composting Process (Biological Valorization). Natural textile waste (cotton,

flax, wool) and paper/cardboard scraps are shredded. They are introduced into compost along with organic waste (leaves, plant residues). Moisture and aeration are controlled for 30–60 days [15,16]. A natural fertilizing compost is obtained, used in agriculture or gardening (Compost made from a mix of paper napkins + cotton clothes + leaves → neutral pH, rich in nitrogen).

Manufacturing Process of Industrial Absorbent Materials. Textile waste (including synthetic fibers) and cardboard are shredded, then impregnated with hydrophilic agents. Absorbent materials are formed into rolls or mats [17,18]. Industrial absorbents for oils, toxic substances, or automotive maintenance are obtained (Mats made from polyester + shredded cardboard → oil absorption capacity >8x its own weight).

The technological process included the following stages (Table 2): *preparation of raw materials* – sorting, shredding, and homogenization of textile and cellulosic waste; *mixture preparation* – combining the recycled materials with the gypsum-based binder and mineral additives in optimal proportions; *molding* – producing panels and bricks with standard dimensions (200 × 100 × 60 mm), in both solid and hollow variants; *drying and curing* – carried out under controlled conditions to prevent cracking and to achieve the desired density (0.87 g/cm³); *finishing and packaging* – ensuring mechanical protection and resistance against moisture absorption during transport and storage.

Table 2

Technological process for the production of panels, bricks, and other decorative objects from textile and cellulosic waste

Stage	*Description*
Preparation of raw materials	Sorting, shredding, homogenization
Mixture preparation	Combining recycled materials with binders and additives in optimal proportions
Molding	Production of standard panels/bricks (200 × 100 × 60 mm)
Drying and curing	Controlled process to prevent cracking and achieve target density
Finishing and packaging	Mechanical protection and moisture resistance

The products were labeled in accordance with Government Decision no. 913/2016 and the harmonized standards *SM EN 14322:2022* [19]. The label provides information on composition, qualitative characteristics, intended use, shelf life, and environmental benefits (≥30% recycled materials), and is accompanied by the environmental declaration according to *SM EN ISO 14021:2016* (Table 3) [20].

Table 3

Labeling and applicable regulations for recycled construction products

Regulation / Standard	*Content / Relevance*
Government Decision no 913/2016	Minimum requirements for the marketing of construction products
SM EN 14322:2022	Technical requirements for wood-based panels with melamine-faced surfaces
ISO 14021:2016	Environmental declaration (≥30% recycled materials)
Product label	Includes: composition, characteristics, intended use, shelf life, marking

The products were intended exclusively for interior use (wall decoration, panels, non-load-bearing partitions), with structural applications, high-humidity areas, and horizontal surfaces subjected to traffic being excluded. Performance testing focused on mechanical strength, acoustic and thermal insulation, fire resistance, and the determination of volatile emissions and toxic element migration (Table 4).

Table 4

Instructions for use and recommended applications for recycled decorative panels

Application area	*Example / Limitations*
Recommended	Wall decoration, panels, lightweight partitions
Not recommended	Horizontal surfaces, high-humidity areas, structural applications
Tests performed	Mechanical strength, acoustic and thermal insulation, fire resistance, volatile emissions, and element migration

The obtained samples were characterized using thermal conductivity, mechanical resistance, morphological analysis, and aesthetic and practical evaluation.

Thermal Conductivity determined using a Hot Disk device. The Hot Disk method is a transient thermal conductivity measurement technique using a dual-purpose sensor: a heat source and a thermometer. The sensor is placed between two material samples, and the temperature variation is analyzed to determine the thermal conductivity. It is applied to insulating, porous, composite materials. The measurement is conducted according to the ISO 22007-2 standard [21,22].

Compression Test (Evaluation of Mechanical Strength). Conducted according to the ISO 844 standard. The compression test determines the resistance to forces applied perpendicular to the material's surface. It is essential for evaluating construction materials, insulating panels, or rigid composites. The test is performed according to the ISO 844:2014 standard – "Rigid cellular plastics — Determination of compression properties" [23]. Obtained parameters: elastic modulus, compressive strength at 10% strain [24].

Morphological Analysis. Optical microscopy for fiber distribution analysis. Optical microscopy is used to investigate the internal structure of composites and the distribution of textile and cellulose fibers. Agglomerations, fiber orientation, and material porosity can be observed [25]. Sample preparation involves cutting a cross-sectional slice and observing it with a binocular microscope or digital camera. It can be complemented with image analysis (ImageJ) [26].

Aesthetic and Practical Evaluation. Aesthetic and functional evaluation is carried out by applying a standardized questionnaire to a group of users (e.g., 20 people) [27]. This method is commonly used in product design studies, innovative materials, or eco-design. The questionnaire may include Likert scale items (1–5) regarding: visual appearance, touch sensation, perception of durability, and utility. The responses are analyzed statistically (mean, standard deviation, relative scores) [28,29].

3. Results and discussion

The experimental results highlight that decorative panels produced from textile

and cellulosic waste represent a viable alternative to conventional materials used in interior finishes. They combine the necessary technical performance with significant environmental benefits, positioning them as a competitive option in the sustainable construction materials market (Table 5) [30,31].

Table 5

Physico-mechanical properties of recycled panels

Tested parameter	*Obtained result*	*Advantage*
Acoustic insulation	Confirmed by laboratory tests	Acoustic comfort
Thermal insulation	Confirmed by laboratory tests	Energy efficiency
Fire resistance	Enhanced by mineral additives	Fire safety
Emissions / migration	Within acceptable limits	Sanitary safety for interior use

From a physico-mechanical perspective, the standardized dimensions (200 × 100 × 60 mm) and an average density of 0.87 g/cm³ indicate a lightweight structure, which facilitates transport and installation while simultaneously reducing the static load on structural elements. The absence of cracks and deformations during internal inspections confirms dimensional stability, an essential criterion for long-term use under varying interior microclimate conditions.

Laboratory tests confirmed the acoustic and thermal insulation capabilities, properties that enhance the comfort of interior spaces and reduce energy costs. These characteristics make the product particularly suitable for educational, cultural, and commercial spaces, where acoustic comfort and energy efficiency are priorities. Fire resistance, improved through the use of mineral additives such as borax and liquid glass, provides an additional safety advantage, increasing the material's acceptability in construction and renovation projects, especially in areas with stringent fire protection requirements (Table 6).

Regarding user health safety, analyses of volatile emissions and element migration demonstrated compliance with the permissible limits. This aspect is crucial, as it ensures that the panels can be used in residential, office, and public spaces without health risks, thereby confirming the product's conformity with current quality and safety requirements.

Table 6

Functional performance of recycled panels

Tested parameter	*Obtained result*	*Advantage*
Acoustic insulation	Confirmed by laboratory tests	Acoustic comfort
Thermal insulation	Confirmed by laboratory tests	Energy efficiency
Fire resistance	Enhanced by mineral additives	Fire safety
Emissions / migration	Within permissible limits	Sanitary safety for interior use

A major differentiating factor is the environmental and economic component. The use of at least 30% post-consumer textile and cellulosic waste contributes to reducing the volume of waste sent to landfills, supporting the principles of a circular economy (Table 7). Furthermore, the choice of recyclable and biodegradable

packaging reduces environmental impact and increases the product's appeal to consumers who are conscious of the importance of sustainability [32].

Table 7

Environmental and economic advantages of decorative panels made from recycled materials

Characteristic	Obtained result	Ecological / Economic benefit
Recycled material	≥30% post-consumer textile and cellulosic waste	Reduction of waste volume
Packaging	Recyclable cardboard, biodegradable film	Reduced environmental impact
Environmental declaration	In accordance with ISO 14021:2016	Official recognition of sustainability

Practical aspects also confirm the feasibility of the product: rapid installation (performed using polymer adhesives and simple tools such as a cutter or scissors) and easy maintenance (periodic cleaning and application of an eco-friendly protective lacquer) make the panels accessible even to non-specialist users. This characteristic renders them a material that is not only environmentally friendly but also user-friendly (Table 8).

Table 8

Practicality and maintenance of recycled panels

Aspect	*Obtained result*	*Practical advantage*
Installation	Easy (polymer adhesives, simple cutting)	Accessible and quick to install
Maintenance	Periodic cleaning, eco-friendly protective lacquer	Extended service life and preserved appearance

A comprehensive analysis of the results indicates that decorative panels based on textile and cellulosic waste meet the technical and environmental requirements of modern finishing materials, offering an optimal combination of performance, safety, and sustainability. They can be regarded as an innovative solution for green construction, with a high potential for integration into the interior design materials market**.**

6. Conclusions

The study demonstrates that combining textile and cellulose-based waste enables the production of functional and sustainable materials suitable for interior construction and decorative applications. The manufactured panels and bricks, composed of ≥30% post-consumer waste, achieve standardized dimensions, adequate density, and improved mechanical, thermal, and fire-resistance properties, making them suitable for wall cladding, partitions, and sound-absorbing applications. Aesthetic and practical evaluations confirmed user acceptability and ease of installation. Environmental assessment highlighted the significant ecological benefits, including reduced landfill deposition, lower resource consumption, and alignment with international

sustainability standards such as ISO 14021:2016. Overall, the proposed valorization strategy not only provides high-performance alternative materials but also contributes to the circular economy, promoting innovation in sustainable construction and interior design.

Acknowledgments

This research was funded by the subprogram "Valorization of Textile Waste for the Production of New Products" (code 24.80015.7007.05VI) of the SRL COORDINATE and Moldova State University.

References

[1] E. MacArthur, "A New Textiles Economy: Redesigning fashion's future". Foundation, 2017.
[2] C. Palacios-Mateo, Y. van der Meer, G. Seide, "Analysis of the polyester clothing value chain to identify key intervention points for sustainability" in Environmental Science Europe, 2021, 33(1), 25.
[3] L. Shen, E. Worrell, M. K. Patel, "Environmental impact assessment of man-made cellulose fibres" Resources, Conservation and Recycling, 2010, 55(2), pp. 260–274.
[4] X. Yang, W. Fan, H. Wang, I. Shi, S. Wang, R. K. Liew, S. Ge, "Recycling of bast textile waste into high value-added products: a review" Environmental Chemistry Letter, 2022, 20, pp. 3747–3763.
[5] G. Sandin, G. M. Peters, "Environmental impact of textile reuse and recycling – A review" Journal of Cleaner Production, 2018, 184, pp. 353–365.
[6] European Commission. EU Strategy for Sustainable and Circular Textiles. 2022.
[7] I. C. Valverde, L. H. Castila, D. F. Nunez, E. Rodriguez-Senin, R. de la Mano Ferreira, "Development of New Insulation Panels on Textile Recycled Fibres" Waste and Biomass Valorization, 2012, 4(1), pp. 139-146.
[8] A. Pappu, M. Saxena, S. R. Asolekar, "Solid wastes generation in India and their recycling potential in building materials" Building and Environment, 2007, 42(6), 2311–2320.
[9] A. K. Jha, S. P. Kewate, "Manufacturing of Eco Bricks: A Sustainable Solution for Construction" Engineering Proceedings, 2024, 66(1), 28 p.
[10] S. Tedesco, E. Montacchini, "From Textile Waste to Resource: A Methodological Approach of Research and Experimentation" Sustenability, 2020, 12(24), pp. 10667.
[11] S. H. Kamarudin, M. S. Mohd Basri, M. Rayung, F. Abu, S. Ahmad, M. N. Norizan, S. Osman, N. Sarifuddin, M. S. Z. M. Desa, U. H. Abdullah, et al. „A Review on Natural Fiber Reinforced Polymer Composites (NFRPC) for Sustainable Industrial Applications" Polymers, 2022, 14, pp. 3698.
[12] L. Lifang, Y. Jianyong, C. Longdi, Y. Xiaojie, "Biodegrability of poly(butylene succinate) (PSB) composite reinforced with jute fibre" Polymer Degradation and Stability, 2009, 94(1), pp. 90-94.
[13] J. Prerna, G. Charu, "A Sustainable Journey of Handmade Paper from Past to Present: A Review" Problemy Ekorozwoju, 2021, 16(2), pp. 233-244.
[14] R. Y. Siti, M. J. Jazmin, M. Liu, C Guo, "Recycling Textile Waste for Craft Industries: An Experimental Approach to eco-friendly Papermaking" Environment-Behaviour Proceedings Journal, 2024, 9, pp. 297-304.
[15] M. Sujauddin, S. M. S. Huda, A. T. M. R. Hoque, "Household solid waste characteristics and management in Chittagong, Bangladesh" Waste Management, 2008, 28(9), pp. 1688–1695.
[16] E. V. Ramon, et al. "Transforming textile wastes into biobased building blocks via enzymatic hydrolysis: A review of key challenges and opportunities" Cleaner and Circular Bioeconomy, 2002, 3, pp. 1000026.

[17] J. S. Chandra, et al. "Cotton from industrial waste modified for effective absorption of oil spills" Journal of Applied Polymer Science, 2025, 142(16), pp. 9.
[18] J. Lee, S. Park, H. Roh, S. Oh, S. Kim, M. Kim, D. Kim, J. Park, "Preparation and Characterization of Superabsorbent Polymers Based on Starch Aldehydes and Carboxymethyl Cellulose" Polymers, 2018, 10, pp. 605.
[19] EN 14322:2022. Wood-based panels – Melamine faced boards for interior uses – Requirements. European Committee for Standardization.
[20] ISO 14021:2016. Environmental labels and declarations — Self-declared environmental claims (Type II environmental labelling). International Organization for Standardization.
[21] M. Gustavsson, et al. "Thermal conductivity, thermal diffusivity, and specific heat of thin samples from transient measurements with Hot Disk" Review of Scientific Instruments, 1994, 65(12), pp. 3856–3859.
[22] ISO 22007-2:2015 – Plastics — Determination of thermal conductivity and thermal diffusivity — Part 2: Transient plane heat source (Hot Disk) method.
[23] ISO 844:2014 – Rigid cellular plastics — Determination of compression properties.
[24] L. J. Gibson, M. F. Ashby, "Cellular Solids: Structure and Properties" Cambridge University Press, Cambridge, 1999.
[25] D. Hull, T. W. Clyne, "An Introduction to Composite Materials" Cambridge University Press, 1996.
[26] M. S. Sreekala, S. Thomas, "Effect of fibre surface modification on water-sorption characteristics of oil palm fibres" Composites Science and Technology, 2003, 63(6), pp. 861–869.
[27] ISO 20282-2:2013 – Usability of consumer products and products for public use.
[28] D. A. Norman, "Emotional Design: Why We Love (or Hate) Everyday Things" Basic Books, 2004.
[29] V. Papanek, "Design for the Real World: Human Ecology and Social Change" Thames and Hudson, 1985.
[30] H. Binici, O. Aksogan, T. Shah, "Investigation of fibre reinforced mud brick as a building material" Construction and Building Materials, 2005, 19(4), pp. 313–318.
[31] A. Briga-Sá, D. Nascimento, N. Teixeira, J. Pinto, F. Caldeira, H. Varum, A. Paiva, "Textile waste as an alternative thermal insulation material solution" Construction and Building Materials, 2013, 38, 155–160.
[32] ISO 8302:1991. Thermal insulation — Determination of steady-state thermal resistance and related properties — Guarded hot plate apparatus. International Organization for Standardization.

Enhancing seismic resilience through insurance mechanisms: insights from the Romanian building stock

Îmbunătățirea rezilienței seismice prin mecanisme de asigurare: perspective asupra fondului rezidențial din România

Bogdan Gheorghe[1], Radu Văcăreanu[1]

[1] Technical University of Civil Engineering of Bucharest
121-126 Bvd Lacul Tei, Bucharest, Sector 2, Romania
E-mail: ionut-bogdan.gheorghe@phd.utcb.ro, radu.vacareanu@utcb.ro

DOI: 10.37789/rjce.2026.17.2.3

Abstract. *Seismic risk in Romania is mainly triggered by relatively rare but very severe earthquake events capable of generating significant structural damage and socio-economic losses. While traditional seismic risk mitigation has focused primarily on structural measures, increasing attention is being paid to the concept of seismic resilience, which also includes post-event recovery capacity. This paper discusses the role of insurance mechanisms as a financial component of seismic resilience, with emphasis on the Romanian context. By analysing seismic risk characteristics, expected losses and the current level of insurance coverage, the study highlights the existing protection gap and the limitations of current approaches. The paper argues for integrated strategies combining structural risk reduction and financial risk transfer to enhance seismic resilience.*

Key words: *seismic risk, seismic resilience, insurance, earthquake losses*

Rezumat. *Riscul seismic din România generat în principal de producera unor cutremure relativ rare, dar foarte severe, cu potențial ridicat de pierderi structurale și socio-economice. În mod tradițional, reducerea riscului seismic a fost abordată în principal prin măsuri structurale, însă conceptul de reziliență seismică implică și capacitatea de recuperare după producerea evenimentului. Lucrarea analizează rolul asigurărilor ca instrument financiar în creșterea rezilienței seismice, cu accent pe contextul românesc. Pe baza analizei riscului seismic, a pierderilor potențiale și a nivelului actual de asigurare, este evidențiat decalajul existent între pierderile așteptate și capacitatea de compensare. Sunt subliniate necesitatea unor strategii integrate care să coreleze reducerea vulnerabilității structurale cu mecanismele financiare de transfer al riscului.*

Cuvinte cheie: *risc seismic, reziliență seismică, asigurări, pierderi seismice*

The article was received on 04.02.2026, accepted on 27.05.2026 and published on 12.06.2026

Introduction

Seismic risk represents one of the major natural hazards affecting the built environment in Romania. The characteristics of the Vrancea seismic source, combined with the vulnerability of a large part of the existing building stock, lead to the potential for significant structural damage and severe socio-economic consequences during major earthquakes. Past events, most notably the 1977 Vrancea earthquake, have clearly demonstrated the extent of human, material and economic losses that may result from strong ground shaking [1].

Traditionally, seismic risk mitigation in civil engineering has focused primarily on structural measures, such as seismic design provisions for new buildings and strengthening or retrofitting interventions for existing structures. While these measures are essential for reducing physical damage and loss of life, they do not fully address the broader consequences of earthquakes. Even when structural performance is improved, significant economic losses may still occur, and the recovery process after a major seismic event can be long and costly.

In recent years, the concept of seismic resilience has gained increasing attention [2]. Seismic resilience extends beyond structural safety and refers to the ability of the built environment and society to absorb seismic shocks, limit disruptions, and recover within a reasonable time after a damaging earthquake. From this perspective, resilience depends not only on the physical performance of buildings, but also on the availability of financial mechanisms that support post-earthquake recovery.

Insurance systems represent an important financial tool in this context. By transferring part of the seismic risk from individual property owners to a collective pool, insurance mechanisms can help transform rare but potentially catastrophic losses into manageable annual costs [3] [4]. In this way, insurance can contribute to reducing the financial burden on both affected populations and public authorities following a major earthquake, supporting faster and more effective reconstruction [5] [6].

Despite the high seismic risk, the current level of seismic insurance coverage in Romania remains limited. The existing compulsory insurance system provides only partial protection and is characterized by relatively low penetration rates and modest coverage limits when compared to the potential scale of seismic losses. This situation highlights a significant gap between expected earthquake-induced losses and the financial capacity available for recovery.

The objective of this paper is to discuss the role of insurance mechanisms as a component of seismic resilience, with a particular focus on the Romanian context. The study presents a qualitative analysis of seismic risk, expected losses and current insurance coverage, emphasizing the limitations of existing approaches and the need for integrated strategies that combine structural risk reduction with appropriate financial instruments. By doing so, the paper aims to contribute to a broader understanding of seismic resilience in civil engineering practice and policy-making.

2. Seismic risk and the existing building stock in Romania

Romania is exposed to a significant seismic risk, primarily associated with the intermediate-depth seismic source in the Vrancea region [7] [8]. This source is characterized by the ability to generate strong earthquakes with large affected areas, producing significant ground motions amplitudes over extensive parts of the country. As a result, seismic events in Romania have the potential to cause widespread structural damage and economic losses.

The impact of seismic actions is strongly influenced by the characteristics of the existing building stock. A large proportion of residential and public buildings in Romania were constructed before the introduction of modern seismic design regulations or according to earlier codes that did not fully account for the current understanding of seismic demand and structural behavior [9] [10]. Consequently, many existing buildings exhibit varying degrees of seismic vulnerability, particularly in urban areas with dense and aging construction.

Historical earthquakes provide clear evidence of this vulnerability. The 1977 Vrancea earthquake remains a reference event, illustrating both the severity of structural damage and the scale of socio-economic consequences. Post-earthquake investigations revealed significant differences in damage levels among buildings with similar apparent characteristics, highlighting the complex interaction between seismic demand, structural systems, construction quality, and detailing practices. These observations underline the difficulty of predicting damage at the level of individual buildings and emphasize the importance of considering seismic risk at a portfolio or regional scale.

The typology of the Romanian building stock further contributes to this complexity. Residential buildings include a wide range of structural systems, such as unreinforced and confined masonry structures, reinforced concrete frames, shear wall systems, and large-panel prefabricated buildings. Each of these typologies exhibits distinct seismic performance characteristics, leading to non-uniform damage patterns during strong ground shaking. Moreover, the spatial distribution of these building types often results in concentrated losses in certain urban zones.

From a risk assessment perspective, seismic risk in Romania results from the interaction between seismic hazard, exposure, and vulnerability. While hazard levels are primarily controlled by the Vrancea source, exposure is determined by the number, type, and value of buildings, as well as by population density. Vulnerability reflects the expected structural response of buildings subjected to seismic loading. Together, these components lead to the possibility of large, infrequent loss events with severe consequences.

Importantly, even when the probability of occurrence of major earthquakes is relatively low on an annual basis, the associated potential losses are extremely high. This characteristic place seismic risk in the category of low-probability, high-consequence events. For such events, conventional approaches based solely on average or expected annual losses are insufficient to capture the full extent of potential damage and disruption. This aspect has direct implications for risk management strategies and for the financial capacity required to support post-earthquake recovery.

In this context, the seismic risk associated with the existing building stock in Romania represents not only a structural engineering challenge, but also a broader societal and economic issue. Understanding the characteristics of hazard, exposure, and vulnerability is therefore a fundamental step toward developing integrated approaches that address both damage reduction and recovery capacity after major seismic events.

3. Seismic losses and limitations of conventional loss indicators

Seismic losses associated with earthquakes differ significantly from losses caused by other types of natural hazards. Earthquake-induced losses are typically rare, but when they occur, they can be extremely large and highly concentrated in space and time [11]. This characteristic makes seismic risk particularly challenging to assess and manage using conventional indicators.

In engineering practice and risk assessment studies, seismic losses are often expressed using average-based indicators, such as the average annual loss. This metric represents the expected value of losses averaged over a long period of time, accounting for both frequent low-intensity events and rare high-intensity earthquakes. While average annual loss can be useful for comparative analyses or long-term planning, it does not adequately reflect the potential impact of extreme seismic events.

Major earthquakes generate losses that are far greater than the values suggested by average indicators, as shown in Figure 1 [12].

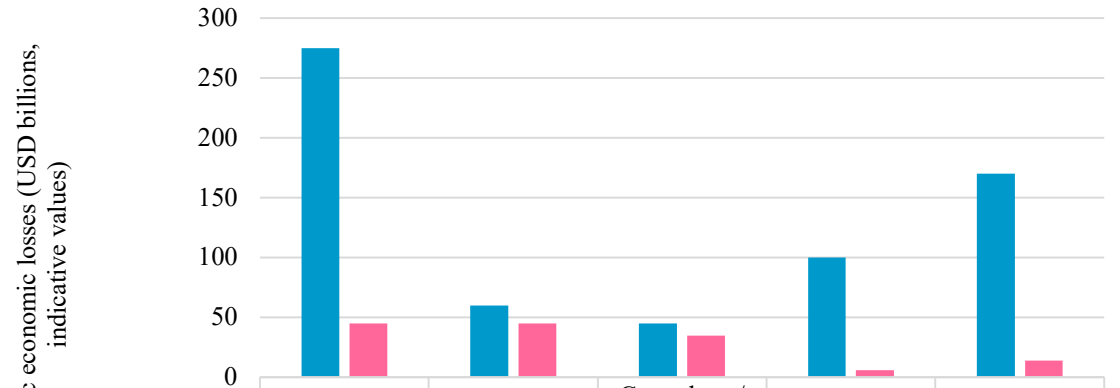

	Great East Japan Tohoku 2011	Northridge, USA 1994	Canterbury/ Christchurch New Zealand 2010-2011	Great Kanto, Japan 1923	San Francisco 1906
Total Economic Loss	275	60	45	100	170
Insured Loss	45	45	35	6	14

Fig. 1. Comparison between direct economic losses and insured losses for major earthquake events [13].

All values are expressed in USD at 2025 price levels. For historical events (1906 and 1923), insured loss data mainly reflect fire-related claims and are not fully comparable with modern earthquake insurance systems.

A single destructive event may cause economic losses that exceed the cumulative average losses expected over several decades. For decision-makers and stakeholders involved in post-earthquake recovery, it is precisely these extreme scenarios that dominate the real-world consequences, rather than the long-term average behavior of seismic losses.

Another important aspect of seismic losses is their strong dependency on the spatial distribution of damage. Due to the characteristics of seismic wave propagation and the clustering of vulnerable buildings, losses tend to be highly concentrated in specific urban areas. As a result, the financial burden imposed by a major earthquake is not uniformly distributed, but instead affects particular regions and communities disproportionately. This spatial concentration further amplifies the socio-economic impact of seismic events.

From a structural perspective, observed damage patterns also exhibit significant variability, even among buildings with similar structural systems and construction periods. This variability introduces additional uncertainty into loss estimation and complicates predictions at the level of individual buildings. Consequently, loss assessment methods are generally more reliable when applied at the level of building portfolios or regions, rather than single structures.

These characteristics place seismic risk in the category of low-probability, high-consequence events. For such risks, approaches based solely on expected or average losses provide an incomplete picture of the potential damage and disruption. Indicators capable of capturing extreme loss scenarios and tail behavior of loss distributions are therefore essential for effective risk management.

The limitations of conventional loss indicators have important implications for post-earthquake recovery planning. In the absence of sufficient financial preparedness, large seismic losses may overwhelm the capacity of public authorities, households, and private stakeholders to fund reconstruction efforts. This gap between potential losses and available financial resources represents a critical vulnerability in the overall seismic resilience of the built environment.

In this context, seismic loss assessment should not be viewed only as a technical exercise, but as a foundation for identifying appropriate risk transfer and risk financing mechanisms. Understanding the scale and nature of potential seismic losses is a key prerequisite for evaluating the role of insurance systems and other financial instruments in supporting post-earthquake recovery and enhancing seismic resilience.

4. The role of insurance in enhancing seismic resilience

As discussed in the previous sections, seismic risk in Romania is characterized by the potential for large and concentrated losses associated with rare but severe earthquakes. Although structural measures are essential for reducing physical damage and loss of life, they cannot fully mitigate the economic consequences of major events. Therefore, seismic resilience should be understood not only in terms of structural performance, but also in terms of the capacity to finance post-earthquake recovery.

Insurance systems represent an important financial mechanism for managing seismic

losses [14] [15]. From an engineering perspective, insurance enables the transfer of part of the economic consequences of structural damage from individual owners to a collective framework. By pooling risks across many insured assets and over time, insurance helps transform rare, high-impact losses into more predictable financial flows.

The primary contribution of insurance to seismic resilience lies in its role in supporting post-earthquake recovery. Following a damaging event, the availability of financial resources is critical for repair, reconstruction, and restoring functionality [16]. Insurance payouts can facilitate these processes by providing timely funds, reducing reconstruction delays and limiting prolonged social and economic disruption. In this sense, insurance complements structural risk reduction measures rather than replacing them.

Conceptually, the interaction between seismic hazard, building vulnerability, economic losses, and recovery capacity can be described as a sequential process, as illustrated in Figure 2.

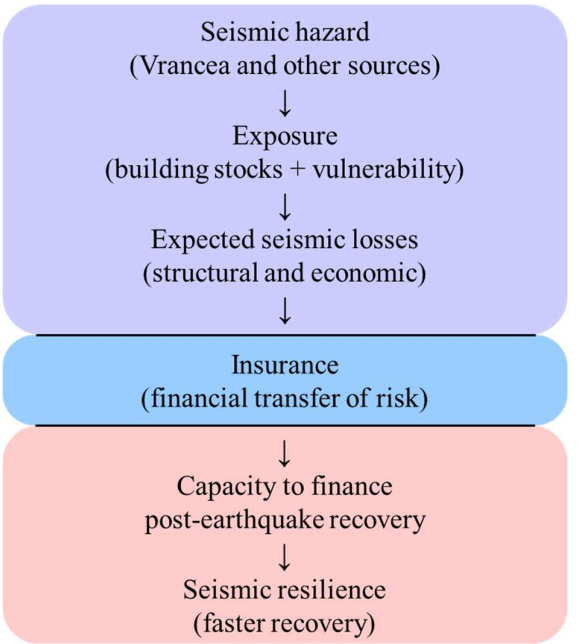

Fig. 2. Conceptual framework linking seismic hazard, losses and insurance within seismic resilience

Seismic hazard acts on the exposed and vulnerable building stock, generating structural and non-structural damage that leads to economic losses. Insurance mechanisms intervene at this stage by transferring part of these losses into financial compensation, which in turn supports post-earthquake recovery and contributes to enhanced seismic resilience. This perspective highlights the integrative role of insurance within the broader framework of seismic risk management.

It is important to note that insurance effectiveness depends on the characteristics of the insured portfolio and on the level of coverage. Low insurance penetration rates and limited coverage caps reduce the ability of insurance systems to significantly influence recovery at a regional or national scale. In such cases, large portions of seismic losses remain uninsured, and the responsibility for recovery falls primarily on affected

individuals and public authorities. This situation may lead to delayed reconstruction and increased long-term socio-economic impacts.

From a risk management standpoint, insurance mechanisms are particularly relevant for low-probability, high-consequence events, such as major earthquakes. Because these events can generate losses that exceed the financial capacity of individual households or local administrations, the absence of adequate risk transfer instruments amplifies overall vulnerability. Insurance, when appropriately designed and widely adopted, can therefore contribute to reducing the protection gap between potential seismic losses and available financial resources.

In summary, insurance represents a key component of seismic resilience by addressing the financial dimension of earthquake risk. When integrated with structural mitigation measures and informed by realistic loss assessments, insurance systems can enhance the capacity of societies to recover more rapidly from major seismic events. Understanding this role is essential for evaluating the current state of seismic risk management and insurance coverage, particularly in high-risk regions such as Romania.

5. Current state of seismic insurance in Romania

Despite the compulsory nature of the insurance scheme, the level of seismic insurance coverage in Romania remains limited, with a national penetration rate of approximately 24% in 2024 [17]. However, the coverage achieved through this system represents only a fraction of the potential losses that may be generated by a major seismic event.

One of the key characteristics of the current insurance framework is the relatively low penetration rate. A significant proportion of residential buildings are not insured against seismic risk, despite the compulsory nature of the scheme. This situation reduces the effectiveness of insurance as a collective risk transfer mechanism and limits its potential contribution to post-earthquake recovery at a national scale.

In addition to low penetration, the level of coverage provided by existing insurance policies is modest when compared to the expected scale of earthquake-induced losses. Coverage limits are fixed and generally insufficient to reflect the actual replacement or repair costs associated with severe structural damage. As a result, even insured buildings may remain partially exposed to significant uninsured losses following a major earthquake.

From a loss perspective, this mismatch leads to a pronounced protection gap between potential seismic losses and the financial resources available through insurance mechanisms [18]. Large-scale seismic events may generate losses that far exceed the capacity of the insurance system to provide compensation. In such scenarios, a substantial part of the financial burden associated with reconstruction is transferred to affected households and public authorities.

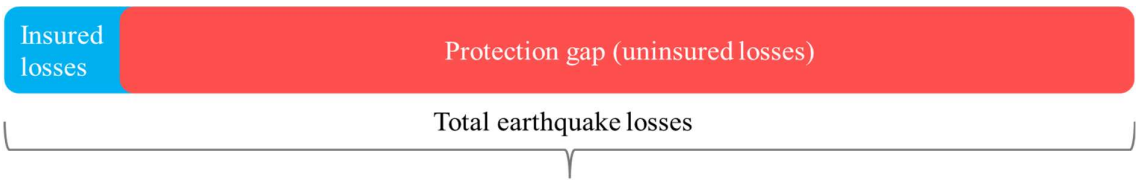

Fig. 3. Conceptual illustration of the seismic insurance protection gap in Romania

The figure highlights the limited share of losses currently covered by insurance and the resulting protection gap, which may have significant implications for post-earthquake recovery.

Another important aspect concerns the distribution of insured buildings across different structural typologies and urban areas. Insurance coverage is not systematically aligned with seismic vulnerability or exposure. Consequently, areas with high concentrations of vulnerable buildings may also exhibit low insurance coverage, further amplifying the potential socio-economic impact of a major earthquake.

The current structure of seismic insurance in Romania also limits its ability to influence risk reduction at the building level. In the absence of differentiated premiums that reflect seismic vulnerability or structural performance, there are limited financial incentives for building owners to invest in seismic strengthening measures. As a result, the interaction between structural risk mitigation and insurance remains weak.

Overall, the existing seismic insurance system provides an important but incomplete contribution to seismic risk management in Romania. While it offers a basic financial safety net, its current penetration, coverage limits, and limited integration with structural vulnerability considerations constrain its role in enhancing seismic resilience. Addressing these limitations is essential for reducing the gap between expected seismic losses and the financial capacity available for post-earthquake recovery.

6. Discussion

The analysis presented in the previous sections highlights the multifaceted nature of seismic risk and resilience in Romania. Structural vulnerability, seismic hazard, and exposure collectively define the potential for damage, but the consequences of a major earthquake extend well beyond structural performance alone. The ability to recover after a seismic event emerges as a critical component of overall resilience, requiring both technical and financial preparedness.

From an engineering perspective, structural mitigation measures such as seismic strengthening and improved design standards remain essential for reducing physical damage and loss of life. However, these measures are typically implemented gradually and often focus on a limited portion of the existing building stock. Even in scenarios where structural vulnerability is reduced, significant economic losses may still occur due to the large scale and concentration of exposed assets [19]. This observation reinforces the need for complementary mechanisms that address the financial dimension of seismic risk [20].

Insurance systems have the potential to play a significant role in bridging this gap. By providing a structured mechanism for risk transfer and loss compensation, insurance can support post-earthquake recovery and reduce the burden placed on public authorities and affected communities. However, the effectiveness of such systems depends strongly on their design, coverage levels, and degree of integration with structural risk reduction strategies.

In the Romanian context, the limited penetration of seismic insurance and the relatively low coverage limits constrain the impact of insurance on national-scale

recovery. These factors, combined with the absence of vulnerability-based premium differentiation, weaken the link between structural performance and financial protection. As a result, the current system does not fully capitalize on the potential synergies between engineering-based risk reduction and financial risk management.

A more integrated approach to seismic resilience would involve the coordinated development of structural and financial measures. From a conceptual standpoint, improvements in seismic performance achieved through retrofitting or strengthening interventions could be reflected in insurance conditions, thereby providing financial incentives for risk reduction. Such an approach would reinforce the role of engineering interventions not only in reducing damage, but also in enhancing financial preparedness.

Finally, it is important to recognize that seismic resilience is a systemic property that emerges from the interaction of technical, economic, and institutional factors. Insurance alone cannot ensure resilience, just as structural measures alone cannot guarantee rapid recovery. Effective seismic risk management requires coherent strategies that address both damage prevention and post-event recovery capacity. In this respect, insurance mechanisms should be viewed as integral components of a broader resilience framework, rather than as standalone solutions.

7. Conclusions

Seismic risk in Romania remains a major challenge due to the combined effects of a strong seismic hazard, a vulnerable existing building stock, and high levels of exposure in urban areas. While significant progress has been made in seismic design practice for new constructions, the potential consequences of future major earthquakes continue to raise serious concerns with respect to both structural damage and socio-economic impact.

This paper has emphasized that seismic resilience cannot be defined solely in terms of structural safety. Although engineering measures aimed at reducing vulnerability are essential, they are not sufficient to ensure rapid and effective recovery after a damaging seismic event. The financial capacity to support post-earthquake reconstruction represents a critical dimension of resilience that must be explicitly considered within seismic risk management frameworks.

Insurance mechanisms play an important role in addressing this financial dimension by facilitating the transfer and distribution of seismic losses. By providing access to post-event financial resources, insurance systems can support recovery processes and reduce the long-term disruption associated with major earthquakes. However, the current level of seismic insurance coverage in Romania, characterized by limited penetration and modest coverage limits, constrains the ability of insurance to significantly contribute to national-scale resilience.

The analysis highlights the existence of a clear protection gap between potential seismic losses and the financial resources available through existing insurance mechanisms. Reducing this gap requires not only improvements in insurance design and coverage, but also a closer integration between structural risk reduction measures and financial instruments. Such integration could enhance both damage prevention and

recovery capacity.

In conclusion, enhancing seismic resilience in Romania calls for a comprehensive and integrated approach that combines engineering-based mitigation measures with effective financial risk transfer mechanisms. Recognizing insurance as a complementary component of seismic risk management, alongside structural interventions, can contribute to more robust and sustainable recovery following future seismic events.

References

[1] *E.-S. Georgescu, A. Pomonis*, "The Romanian earthquake of March 4, 1977, revisited: new insights into its territorial, economic, and social impacts and their bearing on the preparedness for the future", in Proceedings of the 14th World Conference on Earthquake Engineering, Beijing, China, 2008.

[2] *M. Bruneau, S. E. Chang, R. T. Eguchi, G. C. Lee, T. D. O'Rourke, A. M. Reinhorn, M. Shinozuka, K. Tierney, W. A. Wallace, D. von Winterfeldt*, "A framework to quantitatively assess and enhance the seismic resilience of communities", in Proceedings of the 3rd World Conference on Earthquake Engineering, 2003.

[3] *A. Gkimprixis, J. Douglas, E. Tubaldi*, "Seismic risk management through insurance and its sensitivity to uncertainty in the hazard model", Natural Hazards, 108, nr. 2, 2021, pp. 1629–1657. https://doi.org/10.1007/s11069-021-04748-z

[4] *K. Goda, F. Wenzel, J. Daniell*, "Insurance and Reinsurance Models for Earthquake", în Encyclopedia of Earthquake Engineering, Springer, Berlin, 2014, pp. 1–24.

[5] *H. Yoshikawa, K. Goda*, "Financial seismic risk analysis of building portfolios", Natural Hazards Review, 15, nr. 2, 2014, pp. 112–120.

[6] *K. Goda*, "Seismic risk management of insurance portfolio using catastrophe bonds", Computer-Aided Civil and Infrastructure Engineering, 30, nr. 7, 2015, pp. 570–582.

[7] *F. Pavel, R. Văcăreanu, J. Douglas, M. Radulian, C. Cioflan, A. Barbat*, "An updated probabilistic seismic hazard assessment for Romania and comparison with the approach and outcomes of the SHARE Project", Pure and Applied Geophysics, 173, nr. 6, 2016, pp. 1881–1905.

[8] *C. Arion, F. Pavel, R. Văcăreanu, C. Neagu, M. Iancovici, V. Popa, I. Damian*, "Seismic risk assessment of Romania", in Seismic Risk Assessment and Mitigation, Springer, 2018, pp. 251–265.

[9] *CEN*, "EN 1998-1: Eurocode 8 – Design of structures for earthquake resistance", Brussels, 2004.

[10] *Ministerul Dezvoltării Regionale și Administrației Publice*, "Cod de proiectare seismică P100-1/2013", București, 2013.

[11] *L. Hofer, M. A. Zanini, F. Faleschini, C. Pellegrino*, "Expected losses vs. earthquake magnitude curves, for seismic risk mitigation and for insurance purposes", Procedia Structural Integrity, 44, 2023, pp. 1824–1831.

[12] *M. Kohrangi, A. N. Papadopoulos, S. R. Kotha, D. Vamvatsikos, P. Bazzurro*, "Earthquake catastrophe risk modeling: application to the insurance industry", în Springer Tracts in Civil Engineering, Springer, 2021, pp. 239–274.

[13] *J. E. Daniell, B. Khazai, F. Wenzel, A. Vervaeck*, "The CATDAT damaging earthquakes database", Natural Hazards and Earth System Sciences, 11, nr. 8, 2011, pp. 2235–2251.

[14] *D. Asprone, F. Jalayer, S. Simonelli, A. Acconcia, A. Prota, G. Manfredi*, "Seismic insurance model for the Italian residential building stock", Structural Safety, 44, 2013, pp. 70–79.

[15] *K. Goda*, "Earthquake insurance gaps for Canadian homeowners", in Proceedings of the 3rd European Conference on Earthquake Engineering & Seismology (3ECEES) Bucharest, Romania, 2022.

[16] *World Bank*, "Financial protection against natural disasters: an operational framework", World Bank Group, Washington DC, 2014.

[17] *PAID România*, "Raport privind solvabilitatea și situația financiară", București, 2024.
[18] *Swiss Re*, "Lessons from recent major earthquakes", Swiss Reinsurance Company, Zürich, 2012.
[19] *S. Perazzini, G. Gnecco, F. Pammolli*, "A public–private insurance model for disaster risk management: an application to Italy", Italian Economic Journal, 10, 225–267, 2024. https://doi.org/10.1007/s40797-022-00210-6.
[20] *P. Grossi, H. Kunreuther*, "Catastrophe modeling: a new approach to managing risk", Springer, New York, 2005.

Adaptation of the pressure-based algorithm used by EPANET 2.2 to the provisions in force for different situations

Adaptarea algoritmului bazat pe presiune utilizat de EPANET 2.2 la prevederile în vigoare pentru diferite situații

Hocine Lakhdari[1], Andrei-Mugur Georgescu[2]

[1] Faculty of Hydrotechnics, department of Hydraulics, Sanitary Environmental Protection, Technical University of Civil Engineering of Bucharest, Romania
E-mail: lakhdari_hocine@hotmail.fr

[2] Faculty of Hydrotechnics, department of Hydraulics, Sanitary Environmental Protection,Technical University of Civil Engineering of Bucharest, Romania
E-mail: andrei_georgescu2003@yahoo.com

DOI: 10.37789/rjce.2026.17.2.4

Abstract. *This paper adapts the pressure-based algorithm of EPANET 2.2 to comply with national plumbing standards under different operating contexts. The study focuses on calibrating the discharge coefficient (C) and pressure exponent (γ), which govern flow behavior in pressure-driven conditions. Case studies in Algeria and Romania demonstrate how regulatory provisions influence these parameters, with γ converging around 0.6 and C varying according to building typologies. Results highlight the advantages of Pressure Driven Analysis (PDA) over Demand Driven Analysis (DDA), offering more realistic simulations for water distribution networks.*

Key words: *water distribution system, calibration, simulation, demand driven analysis, pressure driven analysis, EPANET*

1. Introducere

Water distribution networks are vital infrastructure systems that ensure the efficient and reliable delivery of drinking water to users. To achieve optimal design, operation, and management, analyzing and simulating these networks is crucial. One of the most commonly used tools for this purpose is EPANET, open-source software created by the U.S. Environmental Protection Agency (EPA) [1]. EPANET enables extended period simulations to analyze the hydraulic and water quality performance of pressurized pipe networks. It provides valuable information on factors such as flow rates, head losses in pipes, nodal pressures, and tank water levels. Thanks to its intuitive interface, open-source adaptability, and compatibility with numerous

The article was received on 27.01.2026, accepted on 27.05.2026 and published on 12.06.2026

extensions, it has become a widely used tool in academic studies as well as in real-world water system design and management.

In hydraulic simulations, two main methods are used to model demand: Demand-Driven Analysis (DDA) and Pressure-Driven Analysis (PDA). The DDA approach assumes that the required water demand at each node is completely satisfied, independent of the actual pressure conditions in the network. Although this method is computationally efficient and has long been the default in EPANET's engine, it fails to account for pressure shortfalls, which can result in overly optimistic predictions when the system is under st ress [2], [3]. In contrast, the PDA method modifies water distribution according to the pressure at each node, providing a more accurate depiction of how the system responds under unusual or emergency situations, including pipe failures, periods of high demand, or firefighting operations. [4].

Although the benefits of PDA are increasingly acknowledged, many legacy simulations and even newer studies still rely mainly on DDA models. This persistence is due in part to default configurations in software such as EPANET and in part to the limited number of comparative analyses conducted under consistent conditions. Consequently, pressure-deficient scenarios often crucial for assessing resilience and reliability remain underrepresented in system evaluations and planning. The omission of PDA in standard modeling can lead to misleading insights for operators and engineers, potentially affecting system reliability, emergency readiness, and long-term investment decisions [5].This study seeks to fill this gap by performing a controlled comparison between DDA and PDA simulations under the same network conditions.

Using EPANET along with suitable pressure-driven extensions, it examines how accurately and reliably each approach represents different demand and pressure situations. The findings will highlight how the selected modeling framework affects performance evaluation and will help practitioners adopt more informed simulation practices, particularly in relation to aging infrastructure and growing urban water challenges.

2. Calibration of the coefficients

2.1. Problematic

Studies in hydro informatics and water distribution network simulation show that pressure-based algorithms do not treat consumption flows at nodes as fixed values. Instead, the flow at demand nodes varies depending on the pressure available at those nodes. To represent this relationship, a mathematical function is needed to describe how flow changes with pressure, controlled by certain parameters.However, these parameters are not universal. They differ depending on factors such as consumer type and the regulatory standards in force, which vary across countries, regions, and applications. Because there is no standardized way to define these parameters, hydraulic simulations may be prone to inaccuracies, which can affect the planning, design, and management of water supply systems. For this reason, a reliable calibration procedure is required to connect regulatory pressure and flow requirements for different categories of consumers to the correct pressure–flow parameters. The

main aim of this paper is therefore to determine these parameters as precisely as possible based on relevant regulations. Once a suitable method for their determination is developed, numerical models will be constructed for several case studies, and their outcomes will be evaluated.

2.2. Determining Coefficients for Different Cases

Based on the emitter flow rate equation expressed as a function of pressure, and given the following formula:

$$q = C.P^{\gamma} \quad (1)$$

Where q: is the flow (ℓ/s), p: the pressure, C: the discharge coefficient, and γ: the pressure exponent, depending on the urban water distribution network.

The calculation of distribution networks under load has become increasingly complex, and traditional algorithms are no longer sufficient to address it. The challenge lies in the fact that pressure-based algorithms assume fixed consumption flows at nodes, whereas in reality these flows vary according to the pressure available at the most restrictive node. Therefore, it is essential to establish and accurately define the relationship between consumption flow and pressure, in line with applicable standards for the various categories of consumers. Concerning the determination of coefficients in accordance with the applicable standards in different countries, we will focus on two specific countries: Algeria and Romania.We will primarily rely on the data provided in (DTU 60.11 P1-1) for the Algerian case and on the information from the Official journal of Romania, (Monitorul Oficial al României, Part I, No. 1167 bis/6.XII.2022), for the Romanian case. Several cases were analyzed under the assumption that each floor accommodated the maximum possible number of dwellings. The buildings considered were characterized by their considerable height, typically comprising six to seven apartments per floor and extending over ten or more levels (R+ 10 floors). This building typology is exemplified by structures in the Tei-Colentina District of Bucharest, Romania, as depicted in (Fig.1).

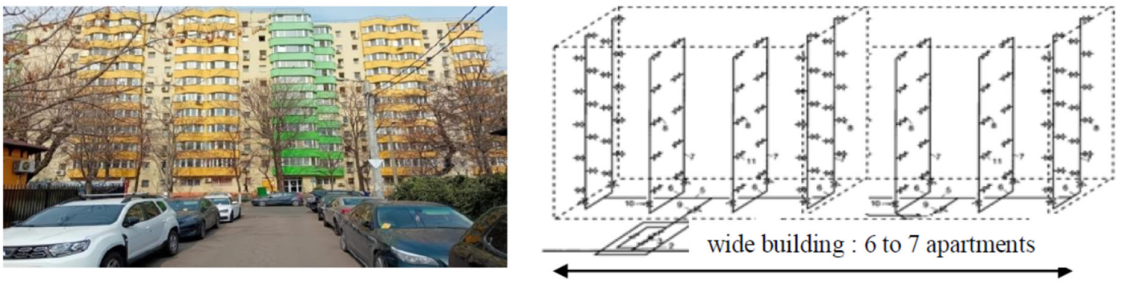

a) Apartment block in Romania Source: Photo: H - Lakhdari on: 22/02/2024

b) Isometric plan of the internal water (Tei-Colentina District in Bucuresti Supply system of buildings. [6]

Fig. 1. Residential building pattern in Romania (Tei-Colentina District - Romania).

As for Algeria, the building and the apartment block are composed of (2 to 4 apartments) on each floor with a height of (R + 4 floors). Like the city of N'gaous in the Wilaya of Batna in Algeria, as shown in (Figure 2).

a) Apartment block in N'gaous - Algeria. Source: Photo: H - Lakhdari on: 22/02/2024

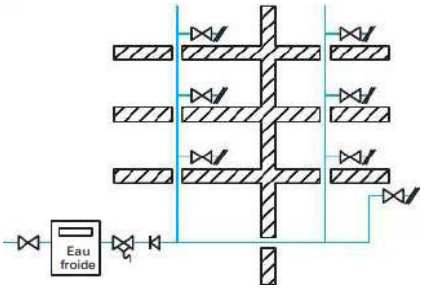

b) Plan of the internal water Supply system of buildings. [7]

Fig. 2. Residential building pattern in Algeria (city of N'gaous- Algeria).

Flow rates required to supply buildings ranging from 1 to 10 apartments per floor, and up to 10 floors in height, were estimated using standard calculation methods. For each configuration, the coefficients (C) and (γ) were determined and then used to produce graphs showing how flow rate varies with available pressure.

The choice of this method is mainly intended to enable direct comparison and highlight differences between national standards in each country. The 1-10 range ensures consistency when comparing the Algerian standard (DTU 60) with the Romanian standard (Monitorul Oficial 1167 bis/2022), and it also allows the development of coherent comparative curves for both.More generally, focusing on buildings with 1 to 10 apartments per floor offers a representative framework: it mirrors the most common urban layouts, facilitates the determination of C and γ for each case, and provides a uniform basis for cross-country and cross-standard analyses.

2.2.1. Proposed calculation methodology

The proposed methodology applies to collective residential buildings designed with between 1 and 10 apartments per floor, and up to a maximum of 10 floors. It defines the estimated flow rate requirements for each apartment, taking into account standard sanitary installations as prescribed by national regulations. In the case of Algeria, French standards [8] were referenced and adapted to local conditions, while Romania applies its own national standards [9].

Drawing on our knowledge of typical housing configurations in both countries, we observed that Romanian high-rise buildings often comprise 6 to 7 apartments per floor and generally extend up to 10 stories. In contrast, Algerian residential buildings tend to include 2 to 4 apartments per floor and are of moderate height, usually reaching around 4 stories depending on the location.

The methodology follows a series of calculation steps:

1. Specify the number of devices per building:

This section consists of determining the number of devices used per dwelling on one side and the estimated flow rate reserved for each type of device on one side using the data in (Table 01).

2. Calculating the total flow rate required for a home, called the base flow rate q_b:

In this section, we will calculate the base flow rate (q_b), which represents the sum of the base flow rates of each device present in a home using the calculation formula following the conditions of the DTU-60 standard (Table 02)

3. Calculation of the probable flow q_p:

The probable flow rate of a dwelling is defined by the formula:

$$q_p = \Sigma q \; x \; k$$

or $\sum q$: represents the basic flow rate in (ℓ/s), k: coefficient of simultaneity: $K = \frac{0,8}{\sqrt{x-1}}$ and x the number of devices per dwelling. For the case of several dwellings we have $q_p = N\Sigma q_b \; x \; k$ Where N is the number of dwellings.

4. Formatting a Data Table:

In this section, we will develop a table that includes all the calculation data, such as the flow rate of the devices, the pressure on each floor, and the simultaneity coefficient for each case, from 1 to 10 units / floor up to 10 floors.

5. Formatting the graphs of the variation of the flow rate as a function of the pressure q = *f* (p): In this step consists of mastering the format of the variation of the probable flow rate as a function of the pressure necessary at each level of a building which varies from 1 to 10 dwellings / floor up to 10 floors. First of all we worked with the directives of DTU60.

6. Formatting a Data Summary Table

This step involves formatting a data summary table, which primarily encompasses the form of the equation q = *f* (p) and the coefficients associated with this equation.

7. Processing and analysis of the data in the table from step 6:

In this step, we will analyze the processing and analysis aimed at defining coefficients

(a) and (b) that are unique for all cases, to the extent possible, and at least for the pressure exponent (b).

8. Data correction with the new value of the pressure exponent coefficient (b):

After processing and analyzing the data in the summary table, we were able to arrive at a single pressure exponent coefficient (b) for all cases processed, from 1 to 10 dwellings / floor up to 10 floors. We will apply this coefficient to all cases.

9. Correction of coefficient (a) unloading coefficient:

In this section, we will establish a relationship between the number of dwellings per floor and the variation of coefficient (a) to arrive at the final form of the equation: q = f (p).

For Romania case, we used the same methodology to structure the procedures. However, the determination of basic flow is carried out differently, since Romania applies its own standards and methods, distinct from those in NF DTU 60.11 P1-1. A major difference comes from the approach defined in the Romanian standard No. 1167 bis / 6.XII.2022.

● The coefficient of simultaneity for cold water is calculated with the following formula:

$$f_{AR} = \frac{0,83}{\sqrt{N-1}} \qquad (2)$$

According to the Roman Standard, two different formulas are used to calculate simultaneity coefficients one for cold water and another for hot water whereas the French standard relies on a single formula. Among the notable differences is that.

● The B-2 method was chosen, since the consumption unit Ui is applied when the reinforcement factor U ≥ 15 [9].

Consequently, the following flow rate calculation relations are used:

$$Q_{C,AR} = Q_{S,tot,AR} \; x \; f_{AR} \qquad (2)$$

With:
$Q_{c,\ AR}$: Design flow rates for cold water distribution (ℓ/s) ;
$Q_{s,tot,\ AR}$: Total specific cold water flow for a section (ℓ/s) ;
fAR: The coefficient of simultaneity for cold water.

3. Cases selected in the study

- Estimating of probable flows according to housing units and floors:
This study focuses s the estimation of probable flow rates based on the number of apartments per building and the total number of floors, in line with recognized national standards. In Algeria, the French DTU 60 standards were adjusted for local use, while in Romania the reference was the official standards (Monitorul Oficial al României, partea I, Nr. 1167 bis /6.XII.2022). The analysis covers buildings ranging from 1 to 10 apartments per floor, with a maximum of 10 floors. The methodology is illustrated in detail through two case studies: buildings with 4 apartments per floor in three Algerian cities, and buildings with 7 apartments per floor in the Tei– Colentina District of Romania. This same procedure is then extended to the other configurations.

3.1. Algerian Case

The procedure is illustrated using a reference building consisting of 10 floors, with 4 apartments per floor.

Tabelul 1

Estimated probable flow for a building with 10 floors and 4 apartments per floor.

Floor		Gf	F-1	F-2	F-3	F-4	F-5	F-6	F-7	F-8	F-9	F-10
designation		pressure demand per floor in (m)										
		5	8	11	14	17	20	23	26	29	32	35
Device Type in apartment	Flow (ℓ/s)	Basic Flow of devices according to the type and number of apartments in (ℓ/s)										
Sink	0,2	0,8	1,6	2,4	3,2	4	4,8	5,6	6,4	7,2	8	8,8
Wash basin	0,2	0,8	1,6	2,4	3,2	4	4,8	5,6	6,4	7,2	8	8,8
Shower	0,2	0,8	1,6	2,4	3,2	4	4,8	5,6	6,4	7,2	8	8,8
Bathtub	0,33	1,32	2,64	3,96	5,28	6,6	7,92	9,24	10,56	11,88	13,2	14,52
Basin hand wash	0,1	0,4	0,8	1,2	1,6	2	2,4	2,8	3,2	3,6	4	4,4
Washing machine	0,2	0,8	1,6	2,4	3,2	4	4,8	5,6	6,4	7,2	8	8,8
WC with flush tank	0,12	0,48	0,96	1,44	1,92	2,4	2,88	3,36	3,84	4,32	4,8	5,28
TOTAL	1,35	5,4	10,8	16,2	21,6	27	32,4	37,8	43,2	48,6	54	59,4
Number of apartments		4	8	12	16	20	24	28	32	36	40	44
Number of devices		28	56	84	112	140	168	196	224	252	280	308
Coefficient of simultaneity		0,154	0,108	0,088	0,076	0,068	0,062	0,057	0,054	0,050	0,048	0,046
Q probable in (ℓ/s)		0,831	1,165	1,423	1,640	1,832	2,006	2,166	2,314	2,454	2,586	2,712

- Graphical representation

The graphical representation in Fig.3 shows how the probable flow (qp) changes in relation to the requested pressure for the Algerian case (4 apartments per floor).

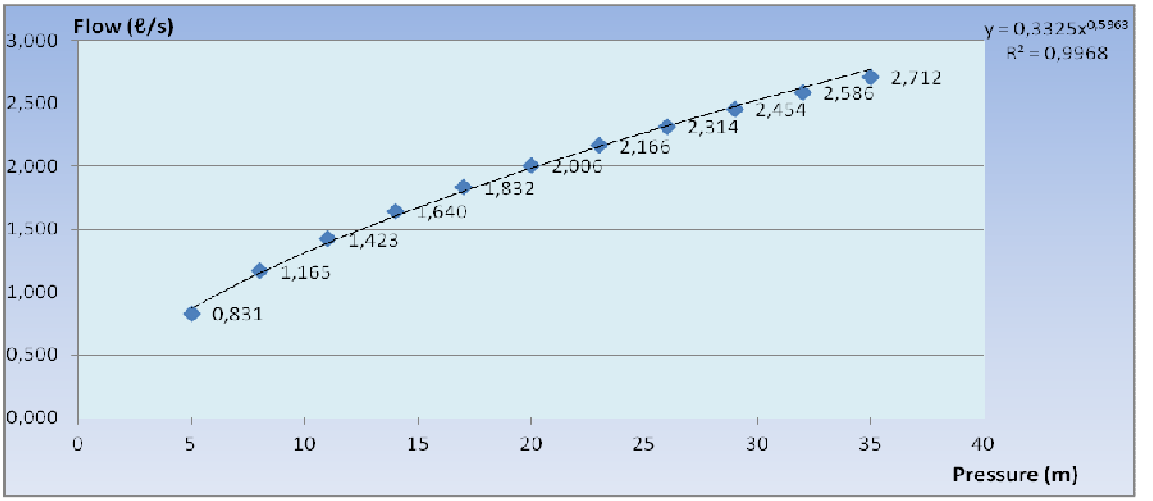

Fig. 3. Graph representing the variation in probable flow (qp) as a function of the requested pressure.

3.2. Romanian Case

This section describes the methodology applied to a building comprising 10 floors, each containing 7 apartments.

Tabelul 2

Estimated probable flow rates for this configuration of 7 apartments per floor across 10 floors

Floor			**Gf**	**F-1**	**F-2**	**F-3**	**F-4**	**F-5**	**F-6**	**F-7**	**F-8**	**F-9**	**F-10**
DESIGNATION			pressure demand per floor in (m)										
			5	**8**	**11**	**14**	**17**	**20**	**23**	**26**	**29**	**32**	**35**
Device Type/ apartment	**Flow (ℓ/s)**	**Unité (Ui)**	Basic flow rate of devices according to the type and number of dwellings ($Q_{s, tot}$) in (ℓ/s)										
Sink	0,2	2	1,4	2,8	4,2	5,6	7	8,4	9,8	11,2	12,6	14	15,4
Wash basin	0,15	1,5	1,05	2,1	3,15	4,2	5,25	6,3	7,35	8,4	9,45	10,5	11,55
Shower	0,2	2	1,4	2,8	4,2	5,6	7	8,4	9,8	11,2	12,6	14	15,4
Bathtub	0,25	3	1,75	3,5	5,25	7	8,75	10,5	12,25	14	15,75	17,5	19,25
Toilet sink	0,1	1	0,7	1,4	2,1	2,8	3,5	4,2	4,9	5,6	6,3	7	7,7
WC with wash tank	0,12	1	0,84	1,68	2,52	3,36	4,2	5,04	5,88	6,72	7,56	8,4	9,24

Floor			Gf	F-1	F-2	F-3	F-4	F-5	F-6	F-7	F-8	F-9	F-10
DESIGNATION			pressure demand per floor in (m)										
			5	8	11	14	17	20	23	26	29	32	35
Device Type/ apartment	Flow (ℓ/s)	Unité (Ui)	Basic flow rate of devices according to the type and number of dwellings (Qs, tot) in (ℓ/s)										
Washing machine	0, 2	2	1,4	2,8	4,2	5,6	7	8,4	9,8	11,2	12,6	14	15,4
Dishwasher machine	0,2	2	1,4	2,8	4,2	5,6	7	8,4	9,8	11,2	12,6	14	15,4
TOTAL	1,42	14,5	9,94	19,88	29,82	39,76	49,7	59,64	69,58	79,52	89,46	99,4	109,34
Number of apartments			7	14	21	28	35	42	49	56	63	70	77
Number of devices/ apartment			56	112	168	224	280	336	392	448	504	560	616
Coefficient of simultaneity			0,112	0,079	0,064	0,056	0,050	0,045	0,042	0,039	0,037	0,035	0,033
Q probable in (ℓ/s)			1,112	1,566	1,915	2,210	2,470	2,705	2,921	3,122	3,311	3,489	3,659

- Graphical representation

Figure 4 shows the relation between probable flow (q_p) and the required pressure. It also illustrates the variation of probable flow according to Romanian standards (7 apartments per floor), confirming the increasing demand on higher floors.

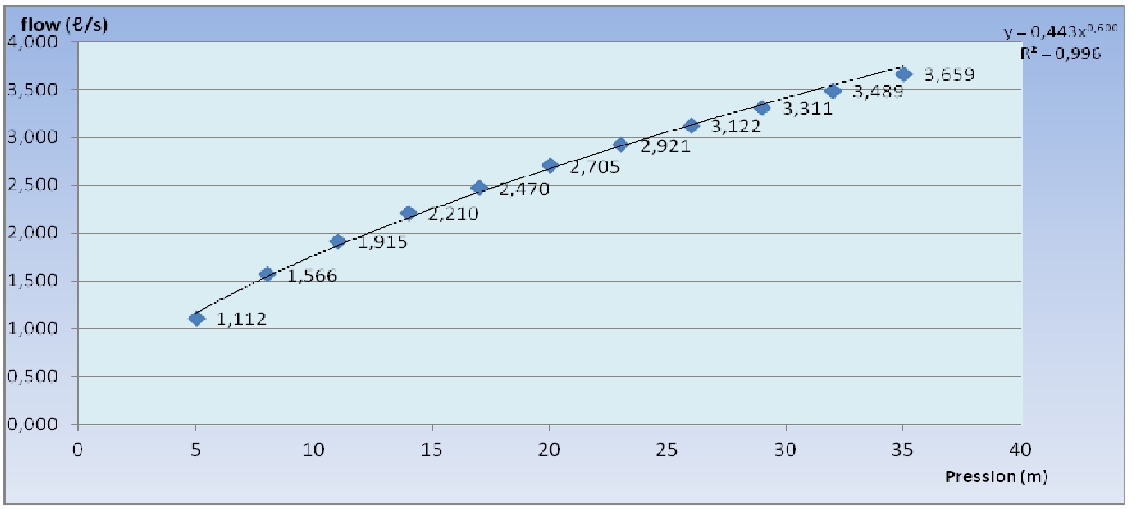

Fig. 4. Graphical representation of the probable flow variation (qp) as a function of the requested pressure.

4. Result and discussion

In the context of searching for the discharge coefficient (C) and the pressure coefficient (γ) related to the emitter formula (1)

After conducting a study on two cases, namely Algeria and Romania, the results obtained through the following two tables (3) and (4) were:

4.1 Case of Algeria

The coefficients determined for Algeria are presented in Table 3, showing the variation of discharge coefficient C with the number of apartments per floor.

Tabelul 3

The coefficients adopted (Case of Algeria)

Designation	Form of the equation	Coefficients	
	$q = c.\ p^{\gamma}$	c	γ
1 apartment / floor on 10 floors	$q = 0{,}176\ p^{0,6}$	0,176	0,6
2 apartment / floor on 10 floors	$q = 0{,}242\ p^{0,6}$	0,242	0,6
3 apartment / floor on 10 floors	$q = 0{,}292\ p^{0,6}$	0,292	0,6
4 apartment / floor on 10 floors	$q = 0{,}334\ p^{0,6}$	0,334	0,6
5 apartment / floor on 10 floors	$q = 0{,}370\ p^{0,6}$	0,370	0,6
6 apartment / floor on 10 floors	$q = 0{,}403\ p^{0,6}$	0,403	0,6
7 apartment / floor on 10 floors	$q = 0{,}432\ p^{0,6}$	0,432	0,6
8 apartment / floor on 10 floors	$q = 0{,}460\ p^{0,6}$	0,460	0,6
9 apartment / floor on 10 floors	$q = 0{,}486\ p^{0,6}$	0,486	0,6
10 apartment / floor on 10 floors	$q = 0{,}510\ p^{0,6}$	0,510	0,6

The relation between coefficient C and the number of apartments is depicted in Figure 5 (Case of Algeria).

- Graphical representation: C = *f* (N)

This curve represents the variation of the coefficient C as a function of the number of apartments per floor.

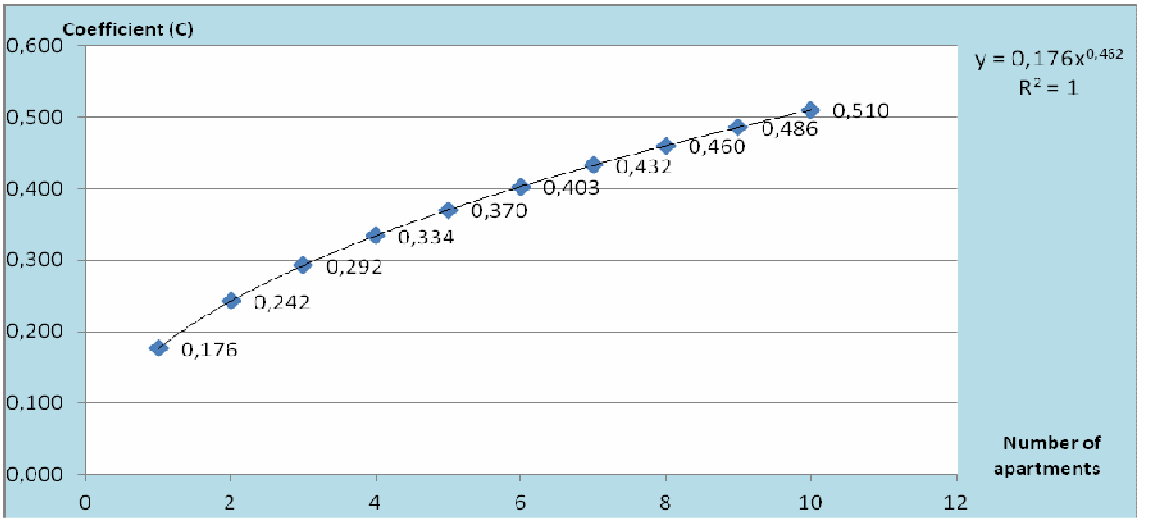

Fig. 5. Curve of the variation of the coefficient C as a function of the number of dwellings per floor
Curve of the equation: $y = 0.176\ x^{0.462}$.

4.2. Case of Romania

As shown in Table 4, Romania's adopted coefficients similarly indicate consistent pressure exponent values, with slight differences in C compared to Algeria.

Tabelul 4

The coefficients adopted (Case of Romania)

Designation	Form of the equation	Coefficients	
	$q = c.\ p^{\gamma}$	c	γ
1 apartment / floor on 10 floors	$q = 0{,}178\ p^{0,6}$	0,178	0,6
2 apartment / floor on 10 floors	$q = 0{,}246\ p^{0,6}$	0, 246	0,6
3 apartment / floor on 10 floors	$q = 0{,}297 p^{0,6}$	0,297	0,6
4 apartment / floor on 10 floors	$q = 0{,}340\ p^{0,6}$	0,340	0,6
5 apartment / floor on 10 floors	$q = 0{,}377\ p^{0,6}$	0,377	0,6
6 apartment / floor on 10 floors	$q = 0{,}411\ p^{0,6}$	0,411	0,6
7 apartment / floor on 10 floors	$q = 0{,}442\ p^{0,6}$	0,442	0,6
8 apartment / floor on 10 floors	$q = 0{,}470\ p^{0,6}$	0,470	0,6
9 apartment / floor on 10 floors	$q = 0{,}497\ p^{0,6}$	0,497	0,6
10 apartment / floor on 10 floors	$q = 0{,}522\ p^{0,6}$	0,522	0,6

The relationship between coefficient C and the number of apartments is depicted in Figure 7 (Case of Romania).

- Graphical representation C = *f* (N)

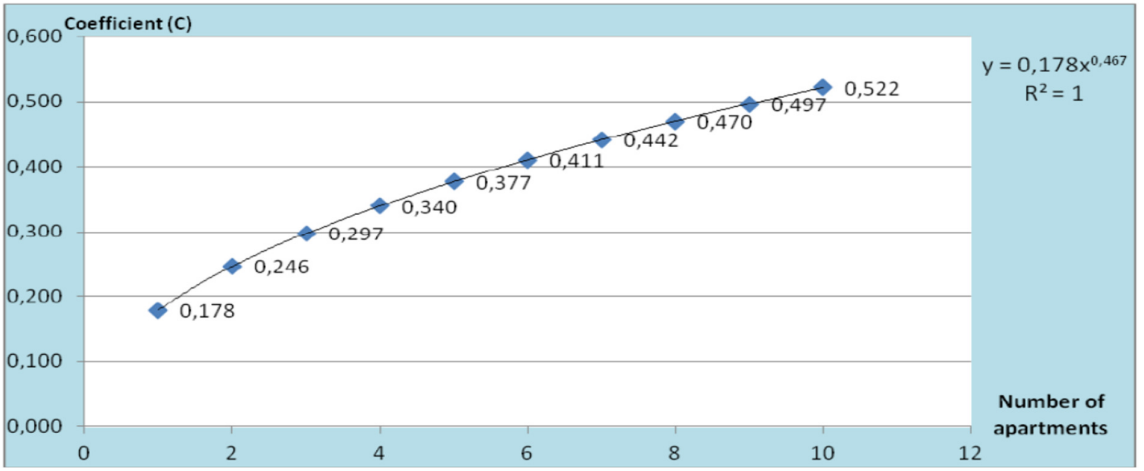

Fig. 6. Curve of the variation of the coefficient (C) as a function of the number of apartments per floor
Curve of the equation: $y = 0.178\ x^{0.467}$.

5. Comparison between flow and pressure-based analysis in water distribution systems serving a given population.

In this section, we will conduct a comparative case study of the two calculation algorithms currently used by EPANET 2.2. For the pressure-based analysis, the flow variation coefficients determined in the previous section will be used. The study will examine how results differ depending on the locality's geographical location across different countries.

5.1. Hydraulic simulation and analysis methods

There are two approaches that we normally use to run Hydraulic Modeling in EPANET, Demand Driven Analysis (DDA) and Pressure Driven Analysis (PDA).
The model-based distribution site identification methodology was tested in Two Algerian cities and one Romanian city under real-world distribution scenarios. The water distribution networks in these cities cover their entire urban areas, and the populations of the cities are listed in table 5 below.

Tabelul 5

Population number in each city

Cities	Total population
N'gaous	33619
Ras El Aioun	19850
Tei-Colentina	40 000

In these figures, the simulation process was carried out for two cases: Demand Driven Analysis (DDA) and Pressure Driven Analysis (PDA). The previously defined parameters were inserted into the numerical model for the PDA case at the nodes corresponding to the type of building they supply.

To our knowledge, the buildings in the studied Algerian cities each consist of five floors (ground floor + 4 upper floors) and contain four apartments per floor. In contrast, buildings in Tei-Colentina District, Romania, typically consist of eleven floors (ground floor + 10 upper floors) and contain seven apartments per floor, as previously explained.

Therefore, the parameters entered into the numerical models for each city are as follows:

- For the four cities in Algeria, the values were based on the equation obtained from Table 6.

Tabelul 6

The coefficients determined for the case of Algeria

Designation	Equation form	Coefficients	
4 apartment/ floor on 10 floors	$q=c.p^{\gamma}$	C	γ
	$q=0,334\ p^{0,6}$	0,334	0,6

For the city of Tei - Colentina District in Romania, the values were calculated based on the equation shown in Table 7.

Tabelul 7

The coefficients determined for the case of Romania

Designation	Equation form	Coefficients	
7 apartment/ floor on 10 floors	$q=c.p^{\gamma}$	C	γ
	$q=0,442\ p^{0,6}$	0,442	0,6

5.2. Simulation and analysis for cities

5.2.1. Analysis for the city of N'gaous

5.2.1.1. DDA (Demand-Driven Analysis)

As illustrated, the water distribution network of the city of N'gaous was simulated under demand driven analysis (DDA) conditions. Figure 7 shows the pressure distribution and the resulting flow, while Figure 8 shows the pressure and velocity results

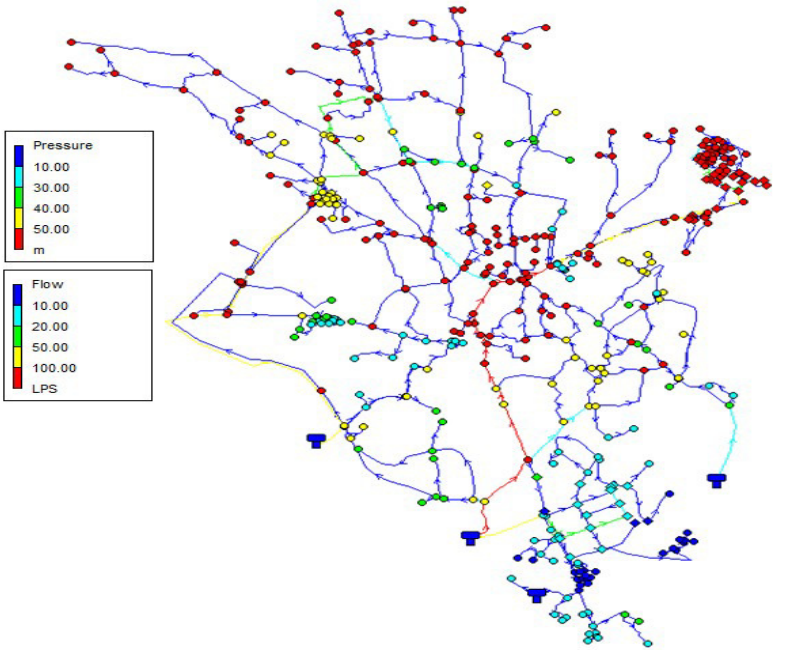

Fig.7. Water distribution network of the city N'gaous, simulation: Pressure – flow.

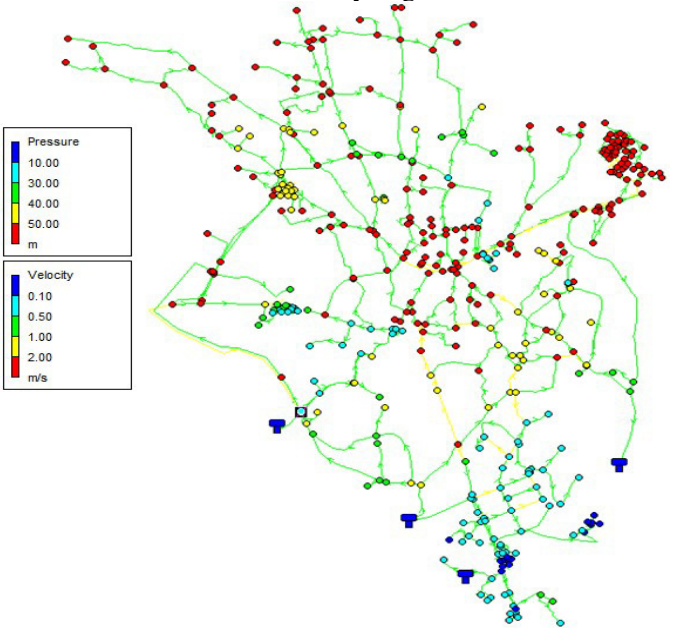

Fig.8. Water distribution network of the city N'gaous, simulation: Pressure – velocity.

5.2.1.2. PDA (Pressure Driven Analysis)

As illustrated, the water distribution network of the city of N'gaous was simulated under pressure driven analysis (PDA) conditions. Figure 9 shows the pressure distribution and the resulting flow, while figure 10 shows the pressure and velocity results.

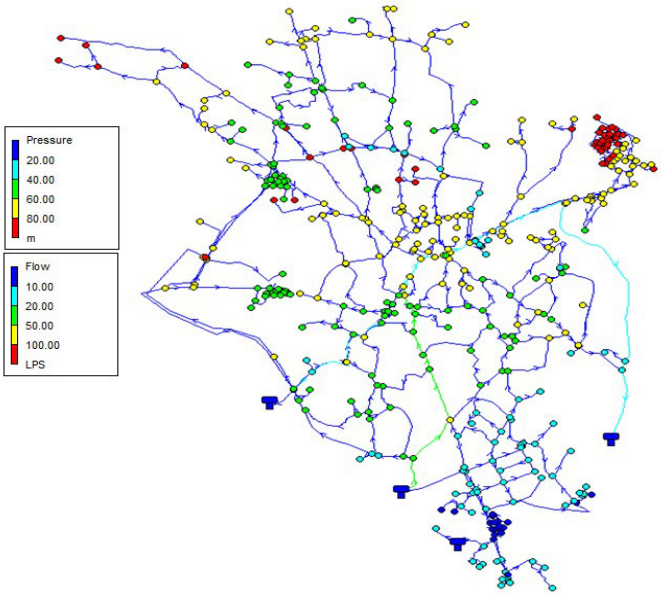

Fig. 9. Water distribution network of the city N'gaous, simulation: Pressure – flow.

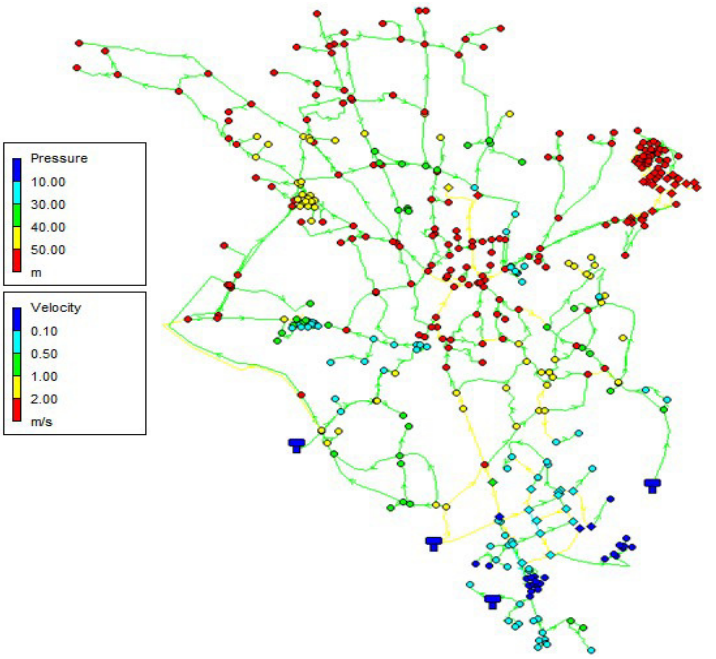

Fig. 10. Water distribution network of the city N'gaous, simulation: Pressure – velocity.

5.2.2. Analysis for the city of Ras El Aioun

5.2.2.1. DDA (Demand-Driven Analysis)

As illustrated, the water distribution network of the city of Ras ElAioun was simulated under demand driven analysis (DDA) conditions. Figure 11 shows the pressure

distribution and the resulting flow, while Figure 12 shows the pressure and velocity results.

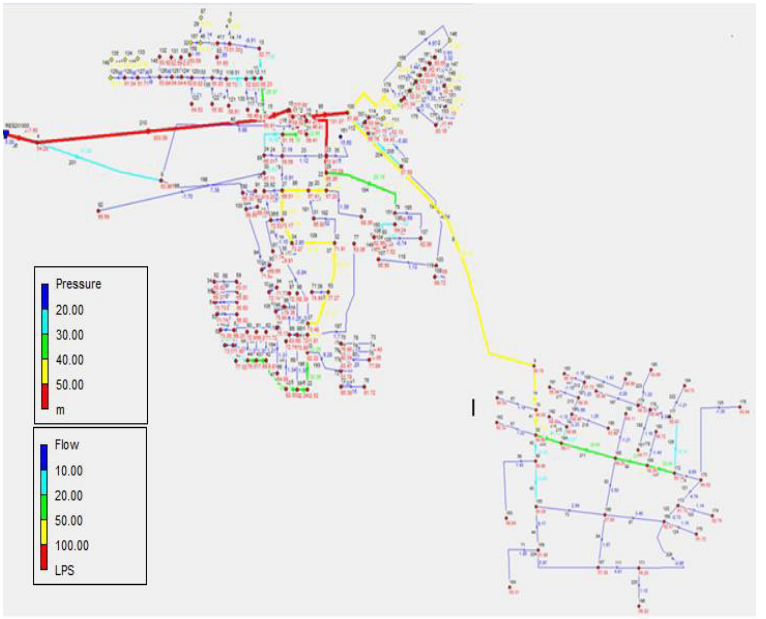

Fig. 11. Water distribution network of the city Ras El Aioun, simulation: Pressure – flow.

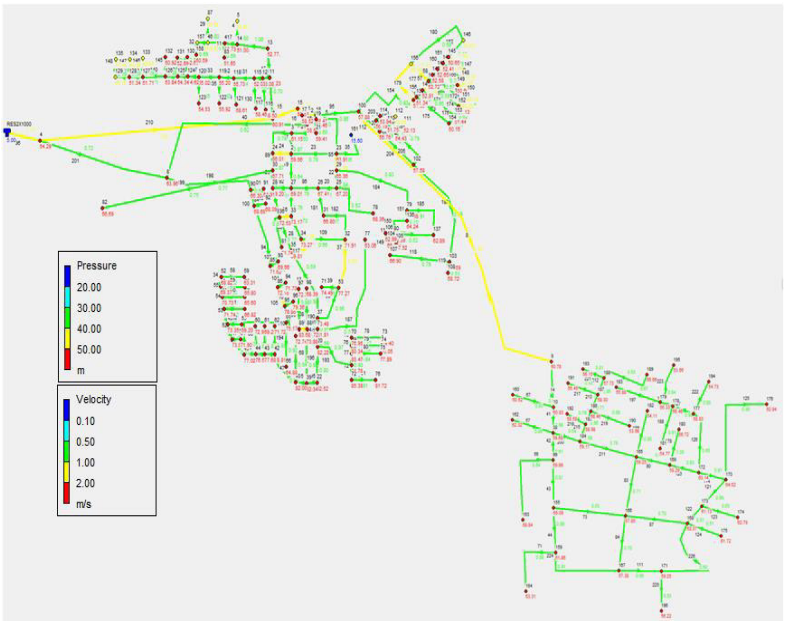

Fig. 12. Water distribution network of the city Ras El Aioun, simulation: Pressure – velocity.

5.2.2.2. PDA (Pressure Driven Analysis)

As illustrated, the water distribution network of the city of Ras El Aioun was simulated under pressure driven analysis (PDA) conditions. Figure 13 shows the

pressure distribution and the resulting flow, while figure 14 shows the pressure and velocity results.

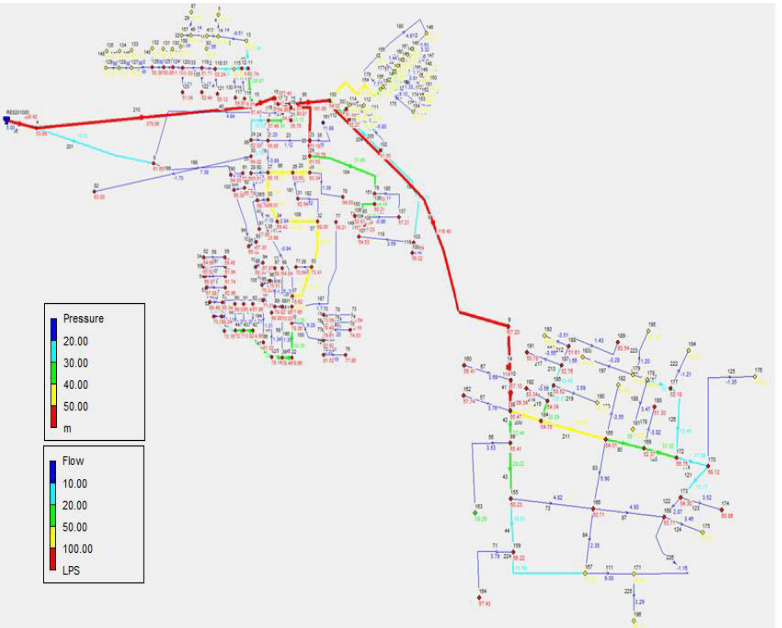

Fig.13. Water distribution network of the city Ras El Aioun, simulation: Pressure – flow.

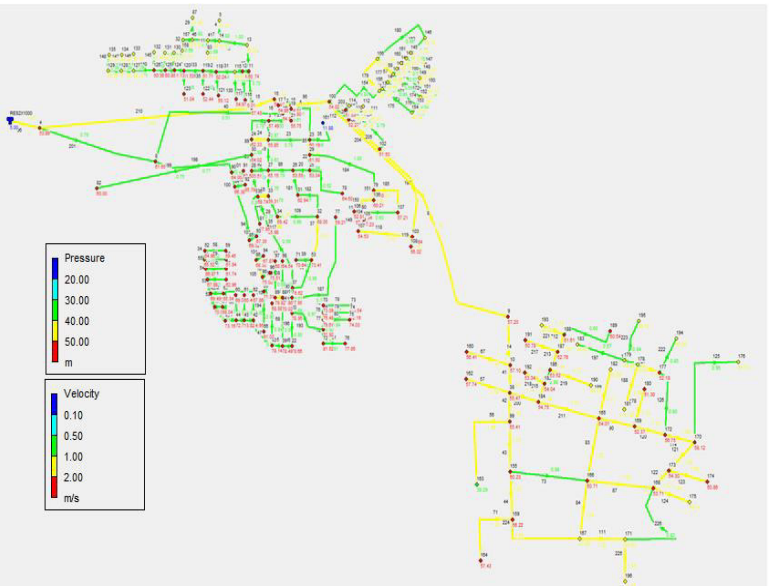

Fig.14. Water distribution network of the city Ras El Aioun, simulation: Pressure – velocity.

5.2.4. Analysis for the « Tei - Colentina District » (Bucarest)

5.2.4.1. DDA (Demand-Driven Analysis)

As illustrated, the water distribution network of the city of Tei - Colentina was simulated under demand driven analysis (DDA) conditions. Figure 15 shows the

pressure distribution and the resulting flow, while Figure 16 shows the pressure and velocity results.

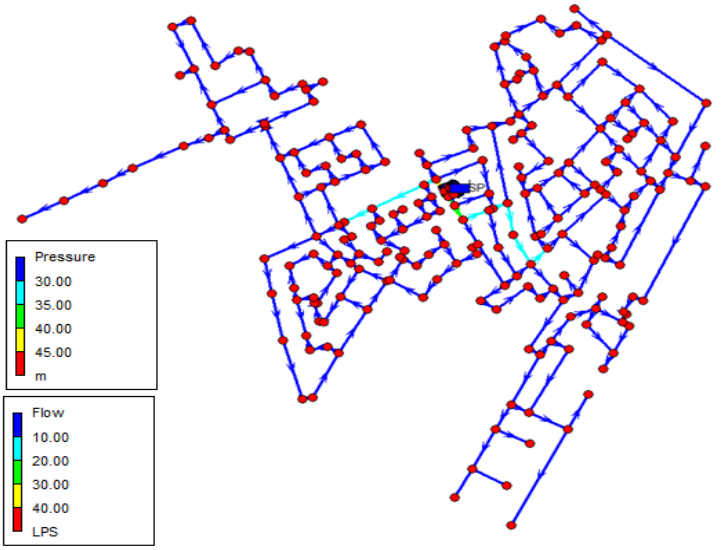

Fig. 15. Water distribution network of the city Tei-Colentina, simulation: Pressure – flow.

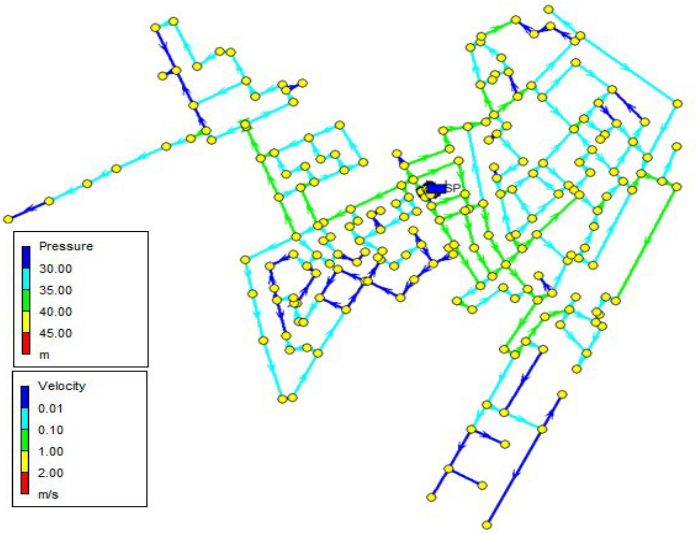

Fig.16. Water distribution network of the city Tei-Colentina, simulation: Pressure – velocity.

5.2.4.2. PDA (Pressure -Driven Analysis)

As illustrated, the water distribution network of the city of Tei - Colentina was simulated under pressure driven analysis (PDA) conditions. Figure 17 shows the pressure distribution and the resulting flow, while figure 18 shows the pressure and velocity results.

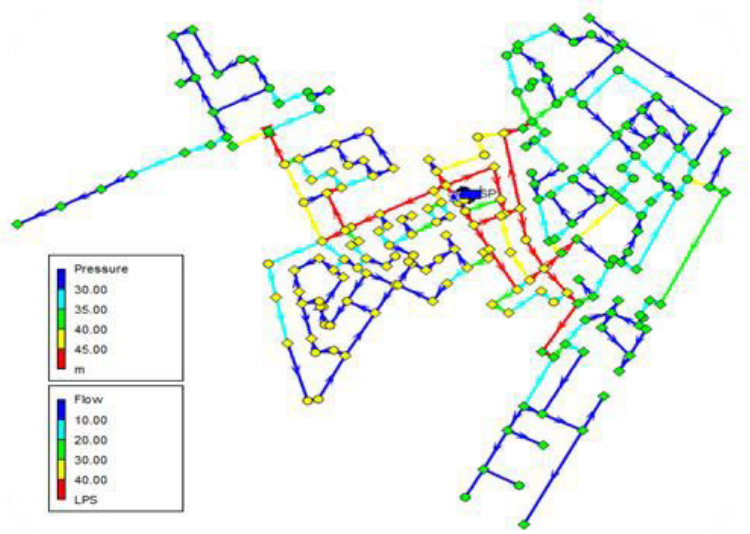

Fig. 17. Water distribution network of the city Tei-Colentina, simulation: Pressure – flow.

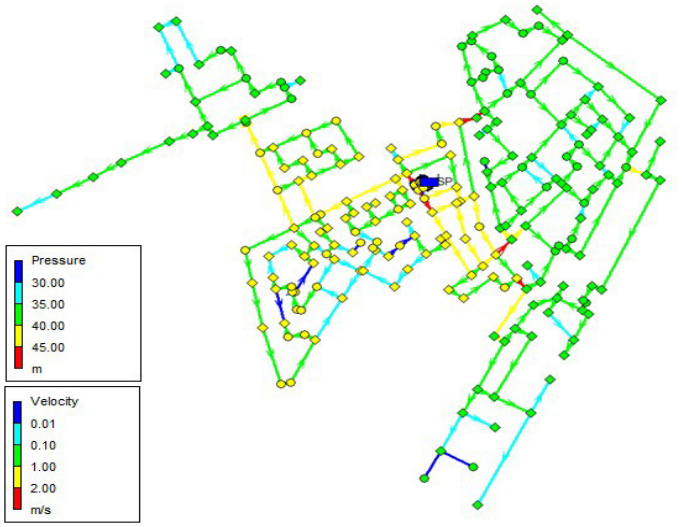

Fig. 18. Water distribution network of the city Tei - Colentina, simulation: Pressure – velocity.

6. Simulation results and discussion by city

6.1. City of N'gaous

•Analyse DDA (Demand Driven Analysis):
- Pressures are relatively high, ranging from 14 m to 66 m, with all demands fully met. as shown in Figures (7) and (8).
- This may seem ideal but does not reflect reality if the pressure were to drop or in the event of network overload.

•Analyse PDA (Pressure Driven Analysis):
- Results show more realistic pressure in high-altitude areas or at the end of the

network. as shown in Figures (9) and (10).
- In some nodes, demand is only partially met, and speeds vary more.
- We notice a progressive loss of pressure, revealing weak points in the network.

6.1.2. City of Ras El Aioun

• DDA (Demand Driven Analysis):
- Hypothesis: All demands are met regardless of pressure.
- Relatively high pressures, for example, from (54.29 m to 65.15 m) in the nodes. as shown in Figures (11) and (12).

• PDA (Pressure Driven Analysis):
- Slightly lower pressures than in DDA.
- Allows observation of areas where pressure is insufficient to meet demand. as shown in Figures (13) and (14).

6.1.3. Tei - Colentina

• DDA analysis:
- Provides optimistic results: demand is assumed to be fully supplied. As shown in the figure (15) and (16).

• PDA analysis:
- From Figure (17) and (18) highlights critical low pressure areas (e.g. pressures around 15 m).
The comparative analysis of the three urban networks shows that:
- Traditional methods (DDA) may overestimate the actual performance of the networks, especially under variable pressure conditions.
- The (PDA) approach allows for a better understanding of hydraulic behavior, taking into account the nonlinear relationship between flow and pressure. The data from the simulations clearly show that Algerian networks, although important, require technological updates and hydraulic optimization (better management of pressures, flows, water losses, etc.) to ensure efficient (good quality, waste-free, and cost-effective) and sustainable (long-term, even in the face of growing demand or limited resources) service.

In EPANET, when performing a Pressure Driven Analysis (PDA), the introduction of discharge coefficients and the emitter exponent has a direct impact on the modeling of flow rates at nodes based on the available pressure.
From what has been observed:
- Unlike Demand Driven Analysis (DDA), where demand at nodes is fixed, PDA adjusts flow rates at nodes based on available pressure.
- When the pressure drops below a certain threshold value, the delivered flow rate is reduced in accordance with the orifice emission equation (n°1): $q = C.P^{\gamma}$

Where: q: flow rate, c: discharge coefficient, It was determined with a variable value between: (0,176 - 0,510) in the case of Algeria. And between: (0,178 - 0,522) in the case of Romania. This coefficient varies according to the number of apartments on each floor of the building (see tables 3 and 4).
P : is the nodal pressure, γ: pressure exponent (generally between 0.5 and 0.6 for orifices), It was determined with a value of 0,6.
The formulas deduced for each of the two cities are:
• The 02 cities of Algeria: q = 0,334 . p 0,6
• Tei-Colentina: q = 0,442 . p 0,6
We observed that the difference between the two formulas is minimal, due to the type of equipment used by households either in Algeria or in Romania.
The same applies when we look at the basic flow rate tables, according to the French standard NF DTU 60.11P1-1. And the Roman standards (Monitorul Oficial al României, partea I, nr. 1167 bis/6.XII.2022) and standard (STAS 1478-90).
There is a slight difference in the estimated flow rates in buildings, for example, for (sinks French standards: 0.20 ℓ/s and Roman standards 0.15 ℓ/s while for bathtubs 0.33 ℓ/s vs 0.25 ℓ/s.(See Tables 1 and 2)
The same can be observed for the formula for calculating the simultaneity coefficient, given that in Romania, the formula is as follows: $f_{AR} = \frac{0,83}{\sqrt{N-1}}$; while those applied in Algeria are based on the French standards, which are: $K = \frac{0,8}{\sqrt{x-1}}$

This slight difference between the two constants (0, 8 in the French standards) and (0, 83 in the Roman standards) is:
• The difference between 0.83 and 0.8 comes from experimental data and analyses conducted in each country on how sanitary facilities are used.
- Romania adopted the coefficient of 0.83 based on local studies on the frequency of use and the distribution of water consumption.
- French standards adopted the coefficient of 0.8 following its own observations on the use of the facilities.
• Furthermore, the difference between these two constants is probably due to several factors:
- Building typology: In Romania and France, the use of sanitary facilities can vary depending on the building type (residential, hotel, industrial .....etc.).
- Consumption habits: Depending on lifestyle, the frequency and duration of use of water consumption points can differ between the two countries.
- Design safety: The slightly higher coefficient in Romania (0,83 versus 0,8) may indicate a more conservative approach, providing a greater safety margin for system design.
Ultimately, the difference between the two coefficients is relatively small (0.83 versus 0.8), but reflects national particularities in terms of water consumption and plumbing design philosophy. Romania adopts a slightly higher value, likely for safety reasons and to adapt to the specific requirements of local infrastructure.

•Regarding the analysis status :
- PDA allows for more accurate modeling of network pressure variability, which is essential for infrastructure design.
- PDA focuses on assessing network pressures, providing a more realistic representation of the service conditions offered to users.
- Regarding pressure and flow, in both analysis cases
•Flow-based analysis (DDA) and
•Pressure-based analysis (PDA), this must be done under two conditions:

- Flow rate: Q DDA $\neq$ Q PDA (Varies with pressure)
- Pressure: P (DDA) > P (PDA).

The flow-in state (DDA) is a theoretical state where all demands are met, but as soon as the pressure is insufficient, the analysis state moves to a pressure-based analysis state (PDA), where the flow is reduced based on the available pressure. This change allows for more realistic modeling of networks under hydraulic constraints.

7. Concluzii

This study presents a comprehensive methodology for simulating and calibrating water distribution networks using EPANET 2.2, with a particular focus on evaluating Demand Driven Analysis (DDA) and Pressure Driven Analysis (PDA) under realistic operating conditions. By deriving discharge coefficients (C) and pressure exponents (γ) based on national plumbing standards from Algeria and Romania, the research bridges theoretical hydraulic modeling with practical regulatory constraints and consumer behavior.
The calibration process yielded consistent values for the pressure exponent (γ =0.6), while the discharge coefficient (C) varied according to the number of apartments per floor ranging from 0.176 to 0.510 in Algeria and 0.178 to 0.522 in Romania. These parameters were essential in constructing pressure-dependent demand models that more accurately reflect flow conditions under variable pressure scenarios. Case studies from both gravity-fed and pumped systems (in Algeria and Romania, respectively) demonstrated that while DDA assumes ideal conditions with fully satisfied demands, PDA reveals actual network limitations, such as pressure deficiencies and unsatisfied demands during peak usage or infrastructure stress. PDA simulations enabled the identification of critical nodes, areas prone to underperformance, and design oversights that DDA tends to obscure.
This work contributes a novel framework by linking empirical regulatory data to hydraulic simulation parameters, thus improving the realism and transferability of network models across different urban contexts. It highlights the necessity of using PDA augmented by properly calibrated coefficients for informed decision-making in system design, infrastructure reinforcement, and operational management.
Ultimately, the study demonstrates that integrating country-specific standards into

pressure-based simulation models not only enhances their accuracy but also fosters a more resilient and responsive approach to managing water distribution systems in diverse geographic and technical environments.

References

[1] L. A. Rossman, „EPANET 2 Users Manual”, U.S. Environmental Protection Agency, 2000.
[2] T. M. Walski, D. V. Chase, D. A. Savic, W. M. Grayman, S. Beckwith, E. Koelle, „Advanced Water Distribution Modeling and Management”, Haestad Press, 2003.
[3] Z. Y. Wu, T. M. Walski, „Pressure-dependent demand extension to EPANET”, in Proceedings of the World Environmental and Water Resources Congress, 2006.
[4] C. Siew, T. T. Tanyimboh, „Pressure-dependent demand-driven modeling of water distribution systems”, Engineering Optimization, vol. 44, no. 6, 2012, pp. 627–647.
[5] P. Kalungi, T. T. Tanyimboh, „Redundancy model for water distribution systems”, Reliability Engineering & System Safety, vol. 82, no. 3, 2003, pp. 275–286.
[6] Asociația Inginerilor de Instalații din România, „Enciclopedia tehnică de instalații – Manualul de instalații”, Ediția a II-a, Editura Artecno, 2010.
[7] J. Delourme, „Tuyauteries de distribution et d’évacuation des eaux”, Éditions Techniques de l’Ingénieur, 2001.
[8] Normes Françaises, „NF DTU 60.11 – Travaux de bâtiment. Règles de calcul des installations de plomberie sanitaire et d'eaux pluviales. Partie 1-1: Réseaux d’alimentation d’eau froide et chaude sanitaire”, ISSN 0335-3931, 2013.
[9] Monitorul Oficial al României, Partea I, Nr. 1167 bis/6.XII.2022, „Normativ privind proiectar ea, execuţia şi exploatarea instalaţiilor sanitare aferente clădirilor, indicativ I9-2022”, Emitent: Ministerul Dezvoltării, Lucrărilor Publice şi Administraţiei, 2022.

Specific factors influencing the strength and durability characteristics of concrete structures of nuclear power plants.

Factori specifici care influenteaza rezistenta si durabilitatea structurilor din beton ale centralelor nucleare

Houssem Fatmi[1], Dan Georgescu[1]

[1]Technical University of Civil Engineering of Bucharest
121-126 Bvd Lacul Tei, Bucharest, Sector 2, Romania
E-mail: *fatmi.houssem@phd.utcb.ro*

DOI: 10.37789/rjce.2026.17.2.5

Abstract. *The purpose of this article is to provide an overview of the environmental effects that may influence the durability of concrete structures in nuclear power plants. Over time, the properties of concrete change as a result of the evolution of microstructural processes as well as under the action of environmental factors. These transformations are not necessarily severe enough to compromise the ability of concrete to meet its performance requirements. However, under certain conditions, concrete may experience undesirable deterioration due to inadequate specifications, noncompliance with those specifications, or unfavorable behavior of the cement paste or aggregate constituents as a result of physical or chemical actions.*

Key words: Nuclear structures, concrete, high temperatures, radiation, corrosion, durability, concrete shrinkage

Rezumat. *Scopul acestui articol este de a oferi o prezentare generală a efectelor de mediu care pot influența durabilitatea structurilor din beton ale centralelor nucleare. Odată cu trecerea timpului, proprietățile betonului se modifică ca urmare a evoluției proceselor microstructurale, dar și sub acțiunea factorilor de mediu. Aceste transformări nu sunt, în mod necesar, suficient de severe pentru a compromite capacitatea betonului de a îndeplini cerințele de performanță. Totuși, în anumite condiții, betonul poate suferi degradări nedorite din cauza unor specificații neadecvate, a nerespectării acestora sau a comportării nefavorabile a pastei de ciment hidratate ori a agregatelor, ca urmare a solicitărilor fizice sau chimice.*

Cuvinte cheie: structuri nucleare, beton, temperaturi ridicate, radiații, coroziune, durabilitate, contracția betonului

1. Introduction

Classic factors influencing concrete durability include mechanical actions, aggressive environmental conditions, and reinforcement corrosion.

The article was received on 21.02.2026, accepted on 27.05.2026 and published on 12.06.2026

In addition, nuclear structures may be exposed to high temperatures and ionizing radiation, which can accelerate concrete degradation and prestress loss.

These effects should be explicitly considered in long-term durability assessments.

2. The influence of high temperatures

Elevated temperature can significantly impact all heat treated and drawn wires. Such wires may not regain their initial strength when cooled because subsequent heating destroys crystal transformations achieved by the initial heat-treating process. Short term heating (e.g. 3–5 min) even to temperatures as high as 400°C, however, may not harm mechanical properties of prestressing wire [1]. A Belgian study [2] involving 30 types of prestressing steel indicated that thermal exposures up to ~200°C do not significantly reduce (<10%) tensile strength of prestressing wires or strands. References [3] and [4] support these results. The effect of elevated temperatures (from 21–649°C) on the stress-strain behavior of one type of prestressing steel (ASTM A 421) is provided in Ref. [5]. As temperature levels experienced by prestressing tendons in Nuclear Power Plant (NPP) containment are typically below 200°C, the risk of thermal damage under normal operating conditions is low.

The loss of prestressing force increases at elevated temperatures due to increases in the relaxation of steel and volumetric changes of concrete (i.e. creep and shrinkage). As shown in **Fig. 1**, the change in slope of prestress force versus time is associated with a reactor startup, when temperatures increase from about 20°C to 30–45°C [6].

Elevated temperature exposures impact the relaxation of prestressing tendons. As exposure temperature and initial stress levels increase, prestressing wire relaxation losses can increase significantly [7–8].

Results obtained from prestressing wires obtained from four British manufacturers indicate that as exposure temperature was increased from 18–120°C, stress relaxation was approximately proportional to the temperature increase [8].

Fig. 2 shows a 15.2 mm 7 wire strand stress loss from initial stress of 75% of specified minimum breaking strength [9]. Relaxation at 40°C is about twice as much as at 20°C. Based on testing performed by Briton Wires [7], the average relaxation after 40 years was estimated to be 2% at 20°C and 5% at 40°C.

Relaxation tests were performed at Forsmark NPP (Sweden) for 1000 hours, and to 70% of their ultimate strength at temperatures of 20°C and 50°C . Results were 1.4% at 20°C and 2.7 % at 50°C.

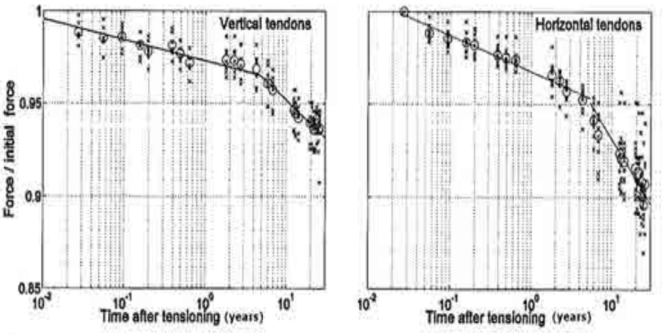

Fig. 1. Prestressing (initial) and residual force as a function of time as measured by fixed gauges at Forsmark 1(adapted from Ref. [6]).

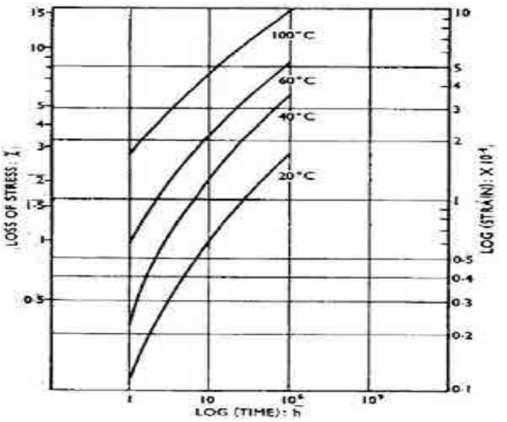

Fig 2 Relaxation of stabilized (low relaxation) 7 wire strands at 75% of f_{pk} at various temperatures [9].

Temperature has significant effect on creep [3, 5, 8, 9]. This is not typically addressed in generic creep prediction models, and temperature is only of concern for prestressed nuclear Containment Concrete Structures (CCS). Creep rate increases with temperatures up to about 70°C. The creep rate at 70°C was shown to be about 3.5 times higher than the rate at 20°C, at least for the first 15 months under load [10].

Based on results from a number of studies [3], creep at temperatures of between 40 and 50°C is about twice the creep at a temperature of 20°C. This is consistent with the results in **Fig. 3**, showing short term creep. Investigations in Ref. [11] show that the creep strain is 2–3 times greater at 52°C than at 27°C.

Elevated temperature effects on drying shrinkage are less pronounced than the effect of reduced relative humidity. A 15% increase in shrinkage can be expected when temperature is increased from 23°C to 60°C at a constant relative humidity [11].

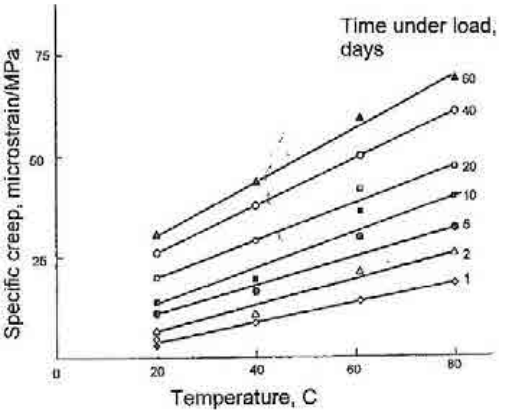

Fig. 3. Effects of temperature on creep [11]

2.1. Mechanical and structural changes

High temperatures affect the properties of concrete as follows:

Accelerated creep

Creep is the increased strain or deformation of a structural element under a constant load.

There are multiple levels of creep that a concrete structure can undergo:

- Primary creep is the immediate elastic strain or initial creep when the load is first applied to the concrete.
- Secondary creep is the slow progress of this creep over time resulting from a sustained load.
- Tertiary creep is the accelerated creep that eventually leads to a break or rupture of the structure.
- Drying creep is when basic creep and shrinkage are exceeded at drying.

Over time, hardened concrete can gradually change shape under constant pressure, causing a deformation.

Concrete creep has been accepted as an inevitable fact for decades. In fact, creep is still calculated in concrete projects to determine whether the structure will sustain the anticipated load.

- **Thermal shrinkage**

Thermal shrinkage in concrete is the reduction in volume and contraction of hardened concrete as it cools down from the high temperatures generated by the

chemical heat of hydration. It occurs when concrete, often in large pours, expands while setting and subsequently contracts upon cooling, leading to cracking if restrained.

2.2. Precompression losses.

Creep and thermal contraction lead to a decrease in stress in the prestressing cables, affecting the load-bearing capacity and tightness of the envelope.

2.3. Reinforcement corrosion amplification

High temperatures accelerate the diffusion of aggressive ions (**Carbonation**, ***Corrosion, Chloride penetration***), favoring reinforcement corrosion and decreasing durability.

2.3.1 Carbonation

Carbonation is a deleterious mechanism in concrete that can occur when atmospheric carbon dioxide (CO_2) reacts with hydration products, such as calcium hydroxide ($Ca(OH)_2$), to form calcium carbonates ($CaCO_3$).

Carbonation lowers the concrete pH, which may promote reinforcement corrosion and, eventually, lead to the formation of cracks, delamination, and spalling. The presence of sufficient moisture is essential for the carbonation process [12]. Also, the rate of carbonation depends on the quantity of Ca(OH)2 in the matrix and concentration of CO_2 [13].

To perform accelerated carbonation tests, special chambers are utilized with a high content of CO_2.

After performing the tests, by applying a phenolphthalein solution to a concrete surface, which appears pink, if the pH level is high, the carbonation depth can be determined. If a specimen shows no color change, it can be considered carbonated (see Figure 4).

Roux et al. [14] measured the resistance of RPC200 to carbonation. Using accelerated treatment at 100% CO_2, no carbonation was detected after 90 days of exposure. Sohail et al. [11] compared the carbonation rate of NSC and UHPC.

Both types of cylinders were placed in an environmental chamber with 50% CO_2 for six months. After six months, there were no signs of carbonation on UHPC, and a 12 mm carbonation depth was observed on Normal Strength Concrete (NSC). The studies of Pierard et al. [15] have also confirmed the superiority of Ultra-High Performance Concrete (UHPC) over NSC in terms of carbonation resistance: the researchers estimated the minimum concrete cover for a 100-year carbonation resistance of 65 mm for conventional concrete and 5 mm for UHPC (the specimens were exposed to a 1% CO_2 atmosphere for one year). Valcuende et al. [16] reported no statistically significant differences in carbonation of UHPC prepared using different curing temperatures (20 °C, 60 °C, or 90 °C) and fiber contents (0%, 1%, or 2%).

Excellent carbonation resistance was observed for UHPC prepared using different waste materials as a cement substitution. Sun and Lai [17] have performed the tests using UHPC prepared with silica fume, fly ash, and slag.

Fig 4. Examples of (a) pre-carbonized and (b) carbonized concrete specimens (reprinted from Ref. [18]).

2.3.2 Corrosion

Corrosion of steel in concrete is an electrochemical process. General corrosion refers to a relatively uniform reduction of thickness over the surface of a corroding material. It is relatively easy to measure and monitor. Pitting corrosion is a localized form of corrosion where the bulk of the surface remains unattached. Pitting is often found at locations where resistance against general corrosion provided by passive surface films or coatings has broken down.

Both water and oxygen must be present for corrosion to occur. There is no corrosion in dry concrete or in fully immersed concrete that does not contain entrained air. The electrochemical potentials that form corrosion cells may be generated in two ways:

(1) Composition cells formed when two dissimilar metals are embedded in concrete, such as rebar and aluminum conduit, or when significant variations exist in steel surface characteristics;

(2) Concentration cells formed due to differences in concentration of dissolved ions near steel, such as alkalis, chlorides and oxygen [19].

One of two metals (or different parts of the same metal) becomes anodic and the other cathodic to form a corrosion cell. Corrosion may also be induced by stray electrical currents or galvanic action with embedded steel of different composition. Figure 5 illustrates the electrochemical process of steel corrosion in moist and permeable concrete.

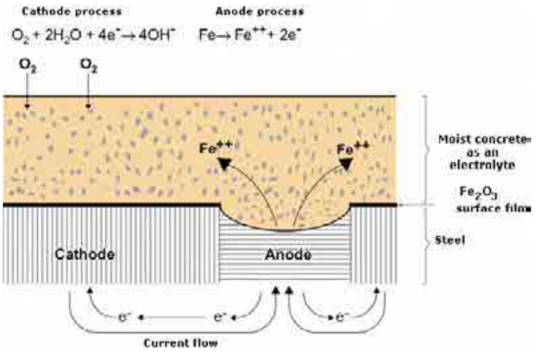

Fig 5. Electrochemical reaction illustrating corrosion of steel in concrete (adapted from Ref. [20]).

Figure 6 presents examples of rebar corrosion in general civil engineering structures.

In good quality, well compacted concrete, reinforcing steel with adequate cover should not be susceptible to corrosion, because the highly alkaline conditions (pH>12) cause a passive iron oxide film (gamma Fe_2O_3) to form on the concrete surface (i.e. metallic iron will not be available for anodic activity). The passive film may be relatively thick to inhibit corrosion by providing a diffusion barrier to reaction products of the reacting species (Fe and O_2) or, as is more common, the layer can be very thin.

The film does not actually stop corrosion, but reduces corrosion rates to insignificant levels [21].

Corrosion can occur if this passivating environment is altered by a reduction of concrete pH or by the introduction of chlorides that destabilize the passive layer.

Fig 6. Corrosion of reinforced concrete. (a) Seawater structure; (b) bridge structure on highway 401 in Ontario, Canada (adapted from Refs [22] and [23], respectively).

3.The influence of ionizing radiation

Irradiation in the form of either fast and thermal neutrons emitted by the reactor core or gamma rays produced as a result of capture of neutrons by members (particularly

steel) in contact with concrete can affect the concrete. Changes in the properties of concrete appear to depend primarily on the behavior of the concrete aggregate that can undergo a volume change when exposed to radiation. [24]

Behavior of the concrete aggregate that can undergo a volume change when exposed to radiation. [24] The fast neutrons are mainly responsible for the considerable growth, caused by atomic displacements, that has been measured in certain aggregate (e.g., flint). Quartz aggregates that contain crystals with covalent bonding should be more affected by radiation than calcareous aggregates that contain crystals with ionic bonding. [25] Furthermore, when nuclear radiation is attenuated or absorbed in the concrete almost all the absorbed radiation is converted into heat.

Nuclear heating occurs as a result of energy introduced into the concrete as the neutrons or gamma radiation interact with the molecules within the concrete material. The heat generated may have detrimental effects on the physical, mechanical, and nuclear properties of the concrete. Reference [26] indicates that nuclear heating is negligible for incident energy fluxes less than 1010 MeV/cm ^{2} per s. Determination of whether any deterioration that may occur in concrete properties is due to radiation damage or thermal effects can be difficult.

Prolonged exposure of concrete to irradiation can result in decreases in tensile and compressive strengths and modulus of elasticity. Figure 7 presents a summary of the effects of neutron radiation on the compressive strength and modulus of elasticity of several concretes.

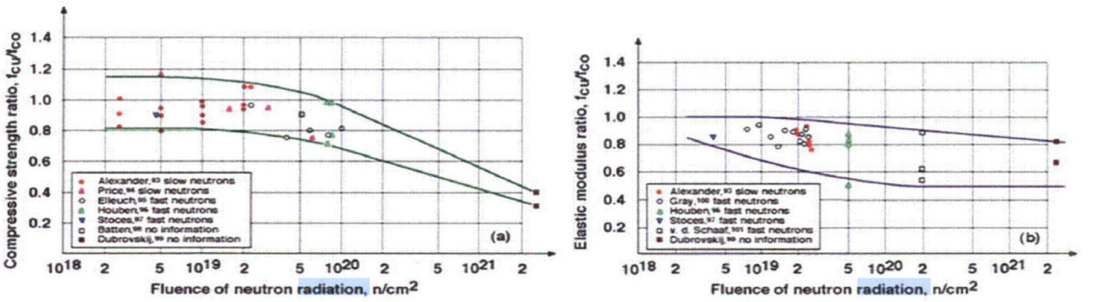

Fig.7 Effect of neutron radiation on concrete compressive strength and modulus of elasticity relative to unirradiated and unheated control specimen results

Results in the literature indicate that:

(1) for some concretes, neutron radiation above 1×10^{19} neutrons/cm² or doses of 10^{10} rad can cause significant reductions in compressive strength and modulus of elasticity, relative to unirradiated and unheated control specimens. Gamma radiation may cause a reduction in compressive strength;

(2) tensile strength of concrete is significantly reduced at neutron fluences exceeding 10^{19} n/cm^2 with the decrease of tensile strength caused by neutron radiation more pronounced than the decrease of compressive strength;

(3) resistance of concrete to neutron radiation apparently depends on the type of neutrons (slow or fast) involved, but the effect is not clarified;

(4) resistance of concrete to neutron radiation depends on mix proportions, type of cement, and type of aggregate;

(5) the effect of gamma radiation on concrete's mechanical properties requires clarification;

(6) the deterioration of concrete properties associated with a temperature rise resulting from irradiation is relatively minor;

(7) coefficients of thermal expansion and conductivity of irradiated concrete differ little from those of temperature-exposed concrete;

(8) when exposed to neutron irradiation, the modulus of elasticity of concrete decreases with increasing neutron fluence;

(9) creep of concrete is not affected by low-level radiation exposure, but for high levels of exposure creep probably would increase with exposure because of the effects of irradiation on the concrete's tensile and compressive strengths;

(10) for some concretes, neutron radiation with a fluence of more than 1 x 10^{19} neutrons/cm^2 can cause a marked increase in volume;

(11) generally, concrete's irradiation resistance increases as the irradiation resistance of the aggregate increases;

(12) irradiation has little effect on shielding properties of concrete beyond moisture loss caused by a temperature increase. Furthermore, there is an indication that nuclear radiation can significantly increase the reactivity of silica-rich aggregates to alkali (i.e., alkali-silica reaction). [27]

Results from an investigation of the effect of irradiation on the strength of a nuclear power plant concrete indicate that for a dose up to 6 x 10^5 Gy the compressive, splitting-tensile, and flexural strength of concrete decreased with dose, reaching a reduction of about 10%, 5%, and 5%, respectively, at the maximum dose. [28]

It was noted in the reference that interaction of concrete with irradiation generated a succession of chemical reactions starting with radiolysis of water and terminating in formation of calcite crystals that decrease both the size of pore space and the strength of the concrete.

Section III, Division 2 of the American Society of Mechanical Engineers (ASME) Pressure Vessel and Piping Code specifies an allowable radiation exposure level of 1×10^{21} n·vt [29].

The British Specification for Prestressed Concrete Pressure Vessels for Nuclear Reactors [30] states that the maximum permissible neutron dose is controlled by the effects of irradiation on concrete properties. These effects are considered insignificant for doses up to 5×10^{17} neutrons/cm^2.

Table 2.7 in Ref. [31] provides estimated radiation environments at the outside surface of light-water reactor pressure vessels for a 1000 MW(e) plant operating at an 80% capacity factor. The results indicate that radiation levels in a concrete primary shield wall may approach the above limits after 40 years of operation (equivalent to 32 full-power years). However, these values represent upper bounds and are likely higher than actual exposure levels, due to attenuation effects caused by air gaps, insulation, and other materials that may be positioned between the pressure vessel and surrounding concrete structures.

3.1. Microstructural changes

Gamma and neutron radiation causes:

- Radiolysis of interstitial water, generating free radicals that induce microcracks.
- Modification of cement hydration, reducing matrix cohesion with effects on decreasing compressive and tensile strengths.
- Increased porosity, favoring the penetration of aggressive agents, accelerating aggregate alkali reaction

3.2 Radiation–temperature interaction

High temperatures amplify the effects of radiation, accelerating chemical reactions and increasing prestressing losses. This interaction is critical for the durability of prestressed concrete.

4. Comparative analysis with common sustainability factors

Common factor	Normal effect	Temperature amplification	Radiation amplification	Notes for prestressed concrete
Material quality	Porosity, strength	Increased creep and shrinkage	Microcracking and matrix degradation	Strength and durability may be affected
Mechanical actions	Static and dynamic loads	Accelerated loss of prestress	Reduction of the cohesion of the concrete microstructure	Prestressing stresses decrease more rapidly
Aggressive environment	Diffusion of water and ions	Acceleration of diffusion	Increase in permeability	Corrosion of reinforcement is more likely
Reinforcement corrosion	CO_2, chlorides	Faster diffusion	Microcracking favors the penetration of aggressive agents	Combination of factors can affect homogeneity and tightness

5. Conclusion

High temperatures and ionizing radiation:

- Accelerate **Creep** and **Shrinkage**, increasing stress losses and reducing precompression.
- Promote microcracking and increased porosity, accelerating the diffusion of aggressive agents, reducing durability.
- Amplify the effects of classical degradation factors (**Carbonation**, ***Corrosion***, **Chloride penetration**, **Aggressive Environment**).
- Create synergistic effects, where combined degradation is much faster than under normal conditions.

The evaluation of the durability of prestressed concrete in nuclear power plants must integrate, in addition to classical influencing factors, combined temperature-radiation modeling.

Specific factors influencing the strength and durability characteristics of concrete structures of nuclear power plants

6. References

[1] PODOLNY, W.J., MELVILLE, T., Understanding the Relaxation in Prestressing, Prestressed Concr. Inst. J. 14 4 (1969).

[2] SCHNEIDER, U., DIERERICHS, C., EHM, C., Effect of temperature on steel and concrete for PCRV's, Nucl. Eng Des. 67 (1981) 245–258.

[3] MEHTA, P., Concrete-Structure, Properties, and Materials, Prentice-Hall Inc., Englewood Cliffs, NJ (1986).

[4] ELECTRIC POWER RESEARCH INSTITUTE, Nuclear Maintenance Applications Center: Guideline for Cooling Tower Inspection and Maintenance, Technical Report 1021060, EPRI, Palo Alto, CA (2011).

[5] ELECTRIC POWER RESEARCH INSTITUTE, Class I Structures License Renewal Industry Report, Revision 1, EPRI TR-103842, EPRI, Palo Alto, CA (1994).

[6] ANDERSON, P., Thirty Years of Measured Prestress at Swedish Nuclear Reactor Containments, Nucl. Eng. Des. 235 (2005).

[7] ANDERSON, P., Structural Integrity of Prestressed Nuclear Reactor Containments, PhD Thesis, Lund Univ. (2005).

[8] BATE, S., CORSON, R., "Effect of Temperature on Prestressing Wires", Group D, paper 21, paper presented at Conf. on Prestressed Concrete Pressure Vessels, London (1968).

[9] CAHILL, T., BRANCH, G.D., "Long-Term Relaxation Behavior of Stabilized Prestressing Wires and Strands", Group D, paper 19, paper presented at Conf. on Prestress. Concr. Press. Vessels (UDELL, M. Ed.), The Institute of Civil Engineers, London (1968) 219–228

[10] NEVILLE, A.M., Properties of Concrete, 4th edn, John Wiley and Sons, Inc., New York (1997).

[11] LUNDQVIST, P., Nuclear Reactor Containments: Evaluation of Prestress Losses and Prediction Models, 3rd FIB Int. Congress Inc. the PCI Annual Conv. and Bridge Conf., Precast Prestressed Concrete Institute, Washington, DC (2010).

[12] Rasheed, P.A.; Nayar, S.K.; Barsoum, I.; Alfantazi, A. Degradation of Concrete Structures in Nuclear Power Plants: A Review of the Major Causes and Possible Preventive Measures. Energies 2022, 15, 8011. [CrossRef]

[13] Sohail, M.G.; Kahraman, R.; Nuaimi, N.A.; Gencturk, B.; Alnahhal,W. Durability characteristics of high and ultra-high performance concretes. J. Build. Eng. **2021**, 33, 101669. [CrossRef]

[14] Roux, N.; Andrade, C.; Sanjuan, M.A. Experimental Study of Durability of Reactive Powder Concretes. J. Mater. Civ. Eng. 1996, 8, 1–6. [CrossRef] RPC200 Reactive Powder Concrete with ~200 MPa strength.

[15] Pierard, J.; Dooms, B.; Cauberg, N. Evaluation of Durability Parameters of UHPC Using Accelerated Lab Tests. In Proceedings of the RILEM-fib-AFGC International Symposium on Ultra-High Performance Fibre-Reinforced Concrete, Marseille, France, 1–3 October 2013.

[16] Valcuende, M.; Lliso-Ferrando, J.R.; Ramon-Zamora, J.E.; Soto, J. Corrosion resistance of ultra-high performance fibre-reinforced concrete. Constr. Build. Mater. **2021**, 306, 124914. [CrossRef]

[17] Sun, W.; Lai, J.Z. Dynamic Mechanical Behaviour and Durability of Ultra-high Performance Cementitious Composite. Key Eng. Mater. 2009, 400–402, 3–15. [CrossRef]

[18] Zhang, S.; Tan, G.; Qi, Z.; Tian, B.; Cao, J.; Chen, B. Relationship Between the Carbonation Depth and Microstructure of Concrete Under Freeze-Thaw Conditions. Materials **2024**, 17, 6191. [CrossRef]

[19] MEHTA, P., Concrete-Structure, Properties, and Materials, Prentice-Hall Inc., Englewood Cliffs, NJ (1986).

[20] ELECTRIC POWER RESEARCH INSTITUTE, Nuclear Maintenance Applications Center: Guideline for Cooling Tower Inspection and Maintenance, Technical Report 1021060, EPRI, Palo Alto, CA (2011).

[21] ELECTRIC POWER RESEARCH INSTITUTE, Class I Structures License Renewal Industry Report, Revision 1, EPRI TR-103842, EPRI, Palo Alto, CA (1994).

[22] AMERICAN WATER WORKS ASSOCIATION, Concrete Pressure Pipe (M9) manual, 3rd edn, AWWA, Denver, CO (2008).

[23] NUCLEAR REGULATORY COMMISSION, Inspection of Structures, Passive Components, and Civil Engineering Features.

[24] H. K. Hilsdorf et al., *The Effects of Nuclear Radiation on the Mechanical Properties of Concrete,* ACI SP-55, Douglas McHenry International Symposium on Concrete and Concrete Structures, American Concrete Institute, Detroit, Michigan, 1978.

[25] M. F. Kaplan, *Concrete Radiation Shielding - Nuclear Physics, Concrete Properties, Design, and Construction,* John Wiley & Sons, New York, New York, 1989.

[26] American Nuclear Society, *Guidelines on the Nuclear Analysis and Design of Concrete Radiation Shielding for Nuclear Power Plants,* American National Standard, ANSI/ANS-6.4-1985, La Grange Park, Illinois, 1985.

[27] T. Ichikawa and H. Koizumi, "Possibility of Radiation-Induced Degradation of Concrete by Alkali-Silica Reaction of Aggregates," *Journal on Nuclear Science and Technology* 39(8), pp. 880-884, Atomic Energy Society of Japan, Tokyo, August 2002.

[28] F. Voddk, K. Trtik, V. Sopko, **0.** Kapickovd, and P. Demo, "Effect of y-Irradiation on Strength of Concrete for Nuclear Safety-Related Structures," *Cement and Concrete Research* 35, pp. 1447-1551, Elsevier Ltd., 2005.

[29] American Society of Mechanical Engineers, "Code for Concrete Reactor Vessels and Containments," Section III, Division 2 of *ASME Boiler and Pressure Vessel Code,* ACI Standard 359, New York, New York, 2005.

[30] British Standards Institution, *Specification for Prestressed Concrete Pressure Vessels for Nuclear Reactors,* BS 4975, London, United Kingdom, 1973.

[31] Science Applications, Inc., *Study of Radiation Dosage to Structural Components in Nuclear Reactors,* EPRI NP-152, Electric Power Research Institute, Palo Alto, California, 1977.

Assessment of urban traffic flow characteristics using field observations and SUMO simulation: a case study of Oba Adesida Road Akure, Nigeria

Evaluarea caracteristicilor fluxului de trafic urban utilizând observații de teren și simularea SUMO: studiu de caz al drumului Oba Adesida din Akure, Nigeria

Tosin Samuel Ayeni[1, 2] Olumuyiwa Samson Aderinola[2]

[1]Directorate of Works and Services,
Federal University of Technology, Akure, Nigeria.
E-mail: Ayenits@futa.edu.ng

[2]Department of Civil and Environmental Engineering,
Federal University of Technology, Akure, Nigeria
Osaderinola@futa.edu.ng

DOI: 10.37789/rjce.2026.17.2.6

Abstract. The study assesses the characteristics of urban traffic flow along Oba Adesida Road, Akure, Nigeria, using a combination of field data and Simulation of Urban Mobility (SUMO). Physical measurements of the roadway were obtained, and a seven-day traffic count was conducted from 7:00 a.m. to 7:00 p.m. using videographic and manual methods. Vehicle volumes were converted into Passenger Car Units (PCU) using the British standard equivalence method. SUMO simulation was applied to replicate the observed conditions, enabling comparison between field and model outputs. Results indicate that the corridor is dominated by taxis, motorcycles, tricycles, and buses, with peak volumes ranging from 1080 to 2221 PCU/hr and daily totals between 13,908 and 25,788 PCU/day. The simulation closely matched field observations, with a mean deviation of about 10%. The findings highlight significant congestion patterns during morning and evening peaks, providing a basis for improving traffic management strategies in Akure.

Keywords: Urban Traffic Flow, SUMO Simulation, Passenger Car Unit, Traffic Congestion, Akure City

1.0 Introduction

Urban traffic flow analysis is a critical component of transportation engineering and sustainable city planning. As cities expand, understanding the dynamics of vehicular

The article was received on 05.12.2025, accepted on 27.05.2026 and published on 12.06.2026

movement becomes essential for managing congestion, optimizing road capacity, and improving travel efficiency. Efficient traffic management not only supports economic productivity but also reduces fuel consumption, air pollution, and travel delays that affect the overall quality of urban life [1, 2]. Consequently, the study of traffic flow characteristics provides valuable insights into road performance, driver behavior, and infrastructure needs in rapidly growing urban environments [3]. In developing cities, the challenges of traffic congestion have intensified due to unregulated urbanization, inadequate infrastructure, and the absence of integrated transport systems. Many African cities, including those in Nigeria, experience a rapid rise in motorization without corresponding improvements in road networks and traffic control systems [4, 2]. Traditional methods of traffic analysis relying solely on manual counts and limited observational data are increasingly insufficient for capturing the complexity of modern traffic conditions [5]. Moreover, there remains a significant gap in data-driven modelling approaches that can simulate and predict real-world traffic scenarios with high accuracy [6]. To address these limitations, advanced traffic simulation tools such as the Simulation of Urban Mobility (SUMO) have emerged as effective frameworks for modeling and evaluating urban traffic behavior. SUMO is an open-source, microscopic simulation platform developed by the German Aerospace Center (DLR) that allows researchers to replicate vehicle interactions, assess traffic control strategies, and estimate performance metrics such as flow, delay, and emissions under various conditions [6, 1]. When calibrated with accurate field data, SUMO can provide reliable insights into congestion patterns and system efficiency [5]. Therefore, this study aims to analyze urban traffic flow characteristics using field data and SUMO simulation for Oba Adesida Road, Akure**,** with the goal of understanding prevailing traffic dynamics, validating simulation performance, and proposing data-supported measures for improved mobility management in the city.

Figure 1: Oba Adesida Road, Akure during peak hours

Figure 1 shows Oba Adesida Road, featuring various traffic composition and commercial activities along both directions. The study corridor, extending from Sacred Heart Cathedral Junction to Oba Osupa/Police A-Division Junction, was assessed in

terms of drainage, median, carriageway, and length. Serving as a key feeder road to other major routes in Akure, it has experienced a marked increase in vehicular traffic due to growing socioeconomic activities. Analyzing its traffic characteristics is essential for understanding traffic volume, congestion patterns, and for evaluating the road's capacity and level of service.

2.0 Materials and Methods

Akure is a city in southwestern Nigeria and the capital of Ondo State. , it is located between latitudes 7^0 15^1 and 7^0 17^1 north of the Equator and between longitudes 5^0 14^1 and 5^0 15^1 east of the Greenwich Meridian. It is about 204 km east of Ibadan, capital of Oyo state; 168 km west of Benin City, capital of Edo state; 311 km north-east of Lagos; and 323 km south-west of Abuja, the Federal Capital Territory of Nigeria. Akure city spreads over an area of about 15,500 km^2 in about 370 m above the sea level. Akure is divided into two local government areas: Akure South and Akure North LGA. Notably, Oba Adesida Road falls within the jurisdiction of Akure South Local Government Area. Figure 2 depicts a map outlining the boundaries of the two local governments within Akure city.

Figure 2: Akure South and Akure North LGA Map

2.1 Methods of Data Collection

Data collection for this study was primarily conducted through direct field surveys, including traffic counts, road measurements, and observational assessments, following procedures recommended in recent traffic studies [11, 12]. The study was carried out over a seven-day period from Monday, 25th September to Sunday, 1st October 2023, under clear and dry weather conditions to minimize variability in traffic patterns. Road parameters, including carriageway width, median, and drainage, were measured using a measuring tape for each lane, consistent with standard field survey techniques [11]. Traffic characteristics were surveyed using a combination of manual counting and

video-graphic techniques, capturing traffic flow in both directions from 07:00 am to 7:00 pm daily. Data quality was ensured through error checking, cross-validation between manual and video counts, and handling of missing data via interpolation methods where necessary, as recommended in previous studies using mixed manual/video field surveys [12, 13]. The Passenger Car Unit (PCU) technique was applied to standardize vehicle flow, converting heterogeneous traffic into equivalent passenger car volumes. PCU factors were based on IRC: 106–1990 and the British Standard (UK Transport Research Laboratory) for each vehicle classification, in line with the approaches used in recent research [11, 12]. For simulation analysis, the study employed Simulation of Urban Mobility (SUMO) v1.18 (DLR, 2023). Field traffic data were used to generate road networks, define vehicle types, and configure simulation parameters including step size, car-following models, and route assignments, following methodologies described in SUMO simulation studies [13, 14].

Table 1

Vehicular Traffic Classifications with its equivalent PCU Factors

S/N	1	2	3	4	5	6	7
Vehicle Classifications	Motorcycle/ Tricycle	Car	Bus	2-Axle Truck	3-Axle Truck	4-Axle Truck	5-Axle Truck
PCU Factors	0.75	1.0	2.0	2.0	3.0	4.0	4.0

Source: [15]

Table 1 presents the classification of vehicular traffic along with the corresponding Passenger Car Unit (PCU) factors for each vehicle type. Tricycles and motorcycles have a PCU factor of 0.75, while a 5-axle truck is assigned a factor of 4.0. Cars and buses have PCU factors of 1.0 and 2.0, respectively. Trucks with two to four axles are assigned PCU factors ranging from 2.0 to 4.0**.**

3.0 Results and Discussion

The carriageway width of Oba Adesida Road, as well as its length includes measurements for both the shoulder and lateral clearance. The total width of 14.6 meters and length of 1800 meters, encompassing the right-of-way components, conforms to the provisions of the Code of Practice for Road Geometric Design [16]. Adequate lane width is critical for safe and efficient traffic operation. It was noted that lanes that are too narrow can increase collision risks and hinder vehicle maneuverability, while excessively wide lanes may encourage over speeding and reduce driver vigilance. Similarly, insufficient shoulder width limits space for emergency stops, heightening accident risk. The measured lane width on Oba Adesida Road strikes an appropriate balance, being neither overly narrow nor excessively wide. Furthermore, the median, walkway, and drainage dimensions of 1.2, 2.4 and 0.6 meters respectively are all within

the required standards, ensuring compliance with roadway safety and design specifications.

Table 2

Traffic Volume Capacity Per Hour With PCUE (First Day)

Time Interval		In-Coming Vehicles		Out-Going Vehicles		Average	
From	To	Field Values	PCUE Values	Field Values	PCUE Values	Field Values	PCU Values
7:00am	8:00am	2195	1958	1946	1774	2071	1866
8:00am	9:00am	2431	2165	2051	1884	2241	2025
9:00am	10:0am	2198	1970	1950	1775	2074	1873
10:0am	11:0am	2092	1855	1916	1730	2004	1793
11:0am	12:0pm	1818	1645	1849	1677	1834	1661
12:0pm	1:00pm	1819	1642	1789	1620	1804	1631
1:00pm	2:00pm	1866	1676	1811	1642	1839	1659
2:00pm	3:00pm	1986	1778	1884	1706	1935	1742
3:00pm	4:00pm	2036	1817	1889	1688	1963	1753
4:00pm	5:00pm	2195	1946	1994	1806	2095	1876
5:00pm	6:00pm	2273	2027	2043	1852	2158	1940
6:00pm	7:00pm	2173	1915	1931	1741	2044	1828
Total		**25082**	**22394**	**23053**	**20895**	**24068**	**21645**

Field Survey, 2023

It was observed from Table 2 that the highest traffic volumes on Monday, the first survey day were recorded between 8:00 a.m. and 9:00 a.m.**,** with average field and PCU values of 2,241 veh/hr and 2,025 PCU/hr, respectively, in both directions. The lowest traffic volumes occurred between 12:00 noon and 1:00 p.m.**,** registering 1,804 veh/hr (field count) and 1,631 PCU/hr**.** Overall, the total daily averages for Monday were 24,068 vehicles/day and 21,645 PCU/day for both directions combined.

Table 3

Differences between Field and PCU Using Simulation of Urban Mobility (SUMO) Technique

Category	Field Total	PCU Total	Difference	%Difference (PCU vs Field)
Incoming	25, 082	22, 394	- 2, 688	- 10.7%
Outgoing	23, 053	20, 895	- 2, 158	- 9.4%
Average	24, 068	21, 645	- 2, 423	- 10.1%

From table 3, the SUMO PCU results underestimate field traffic counts by roughly 9–11**%**, which is reasonable depending on simulation calibration, detector precision, or conversion factors.

Table 4

Difference Patterns (Hourly Deviation)

Time	% Difference (Avg)	Comment
7–8 am	–9.9%	Early buildup
8–9 am	–9.6%	Morning peak underestimated
9–10 am	–9.7%	Stable
10–11 am	–10.5%	Midday drop starts
11–12 pm	–9.4%	Consistent
12–1 pm	–9.6%	Lunch off-peak
1–2 pm	–9.8%	Lowest period
2–3 pm	–10.0%	Gradual recovery
3–4 pm	–10.7%	Afternoon buildup
4–5 pm	–10.5%	Evening rise begins
5–6 pm	–10.1%	Evening peak
6–7 pm	–10.6%	Post-peak decline

From Table 4 and Figure 3 the PCU simulation shows strong correlation in pattern (timing of peaks matches field data), but an underestimation in magnitude by about 10%. This may be due to default car-following parameters (e.g., gaps or speed distributions slightly conservative). It can also be as a result of simplified vehicle composition mix (car-heavy versus mixed fleet). However, A 10% difference is within acceptable limits for many urban simulation calibrations (typically ±15% is acceptable). Between 7: 00 am and 12: 00 noon are early build up traffic, stable and consistent. There was off peak hour before traffic began to rise to the peak between the hours of 1: 00 pm and 7:00 pm. Figure 3 shows this fall (off peak hour) and rise (Peak hour) of the traffic graphically. The traffic volume comparison between the field values and PCU (SUMO) can be seen clearly as presented in figure 3. Observations from figure 4 shows that GEH Statistics reveals that all hourly GEH values are below 5, indicating very good calibration (standard threshold: GEH < 5 for $\geq 85\%$ of intervals). This implies that the SUMO model is highly reliable, with strong temporal alignment and minor systematic bias. Coefficient of determination (R^2) is 0.995, indicating excellent correlation between field and SUMO PCU data. An average percentage difference of about –10%, shows consistent underestimation.

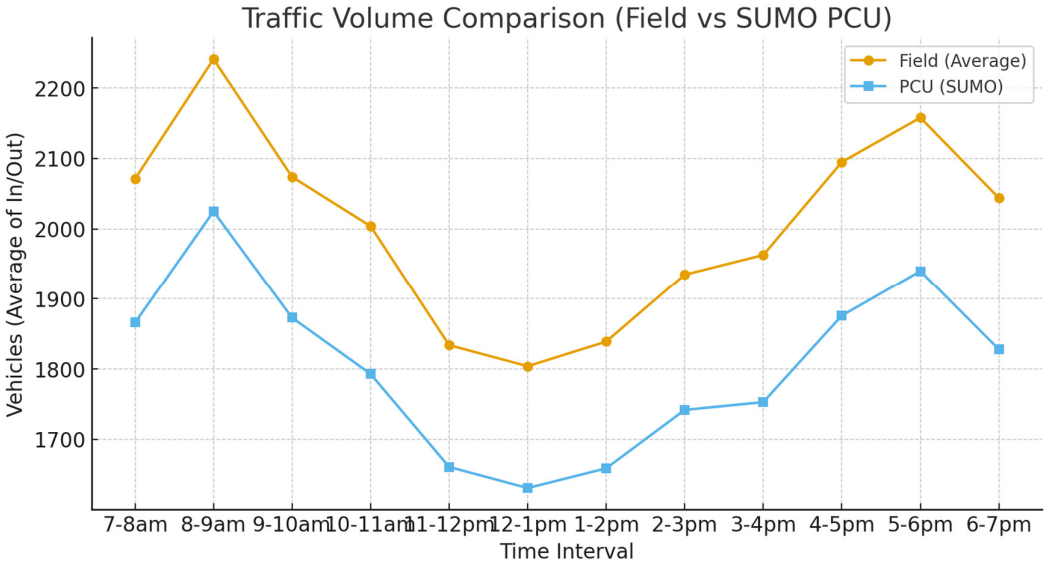

Figure 3: Showing Traffic Comparison between Field Values and SUMO PCU

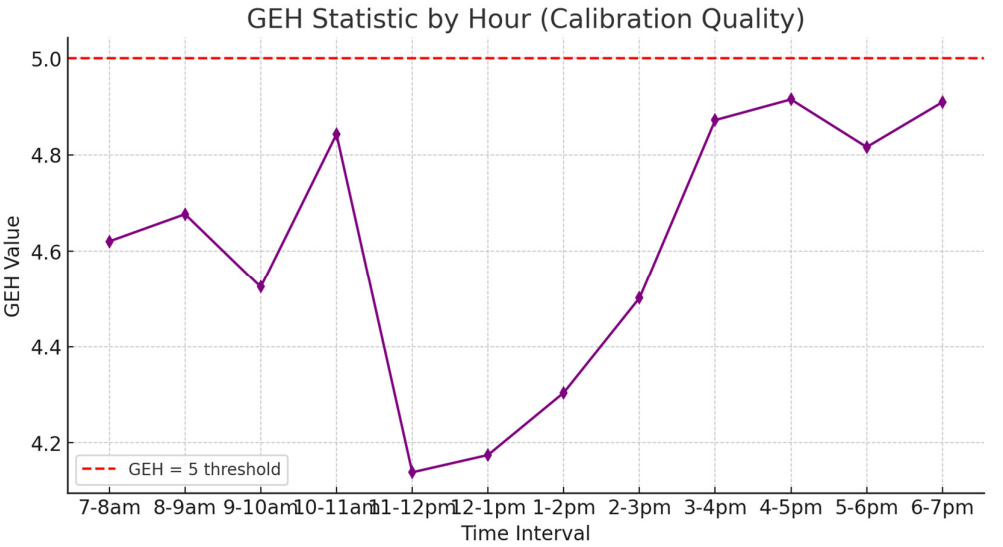

Figure 4: Showing Calibration Quality of SUMO by GEH Statistics per hour

Table 5

Traffic Volume Classifications per day with PCU Equivalent (First day)

Vehicles	In-Coming Vehicle Classifications PCU Factors	Field Values	PCUE Values	Out-going Vehicle Classifications Field Values	PCUE Values	Total Average Field Values	Total Average Average
Passenger car	1.00	12170	12170	12089	12089	12130	12130
Motorcycles/ Tricycles	0.75	12526	9395	10571	7928	11549	8662
Bus	2.00	329	658	313	626	321	610
2-Axle Truck	2.00	19	38	23	46	33	42
3-Axle Truck	3.00	20	60	23	69	22	65
4-Axle Truck	4.00	14	56	23	92	19	74
5-Axle Truck	4.00	04	16	11	44	08	30
TOTAL	**25082**	**22393**	**23053**	**20894**	**24068**	**21644**	

Field Survey, 2023

Table 5 shows that the traffic composition of Oba Adesida Road is characterized by a diverse mix of vehicles, including motorcycles, tricycles, taxis, buses, and trucks. The trucks are subcategorized based on the number of axles, namely 2-axle, 3axle, 4-axle, and 5-axle trucks. However, upon evaluation, the traffic composition of this road predominantly consists of taxis, motorcycles (Okadas), tricycles and buses. From tables 5 and 6, the passenger car categories for both directions was observed took the lead with average values of 12130pcu per day while 5-Axle truck settled for the least volume of 8 and 30 for field and PCU equivalent respectively.

Table 6

Traffic Composition Analysis with SUMO (Avg. of incoming and outgoing Vehicles)

Vehicle	Avg Field (veh)	Avg PCU (PCU)	Share of Field (%)	Share of PCU (%)
Passenger car	12,129.5	12,129.5	50.4%	56.0%
Motorcycle/Tricycle	11,548.5	8,661.5	48.0%	40.0%
Bus	321.0	642.0	1.33%	2.97%
2-Axle Truck	21.0	42.0	0.09%	0.19%
3-Axle Truck	21.5	64.5	0.09%	0.30%
4-Axle Truck	18.5	74.0	0.08%	0.34%
5-Axle Truck	7.5	30.0	0.03%	0.14%

In Table 6, the PCU of the passenger cars share rises from approximately 50% for field value to 56% because motorcycles are down-weighted by 0.75 PCU while heavy vehicles are up-weighted. Since PCU inflates the effective occupancy of lanes for heavy vehicles, junction performance indices (delay, queue, and throughput) will be sensitive to those vehicle classes.

Table 7

Traffic Volume Capacity for the whole week

Days	In-coming Vehicles		Out-coming Vehicles			
	Field Values	PCUE Values	Field Values	PCUE Values Field	Total Average Values	Total Average PCUE
Monday	25050	22393	23053	20894	24052	21644
Tuesday	25277	22633	23117	19945	24197	21290
Wednesday	24237	21894	23076	20899	23657	21397
Thursday	27090	25788	23539	22304	25315	24047
Friday	24031	22124	23387	21390	23709	21757
Saturday	17425	16065	16346	15289	16886	15677
Sunday	15090	13908	14970	13818	15030	13863

Field Survey, 2023

Table 8:

Day-by-Day Comparison (FIELD and SUMO values)

Day	Avg. Field	Avg. PCU	% Diff	Comment
Monday	24,052	21,644	–10.0%	Typical weekday calibration
Tuesday	24,197	21,290	–12.0%	Slightly higher deviation
Wednesday	23,657	21,397	–9.5%	Very good fit
Thursday	25,315	24,047	–5.0%	Excellent fit (well-calibrated)
Friday	23,709	21,757	–8.2%	Acceptable
Saturday	16,886	15,677	–7.2%	Weekend drop correctly captured
Sunday	15,030	13,863	–7.8%	Consistent pattern

Table 7 presents the week day data for both in-coming and out-going vehicles; while Table 8 depicts the comparison between day-by-day field data and SUMO PCU. It is evident that Thursday (Day 4) recorded the highest PCU values for inbound traffic at 25,788 PCU/day (Table 7) and well calibrated with SUMO, given excellent fit (Table 8). In comparison, the other weekdays showed relatively similar values: Monday at 22,393 PCU/day, Tuesday at 22,633 PCU/day, Wednesday at 21,894 PCU/day, and Friday at 22,124 PCU/day. However, Saturday and Sunday witnessed lower incoming vehicle numbers at 16,065 PCU/day and 13,908 PCU/day, respectively. Outbound traffic displayed a range between 13,818 PCU/day and 20,894 PCU/day (Table 7). In summary, SUMO successfully mirrors this pattern, indicating correct temporal behavior and demand assignment, though slightly conservative in magnitude (Table 8).

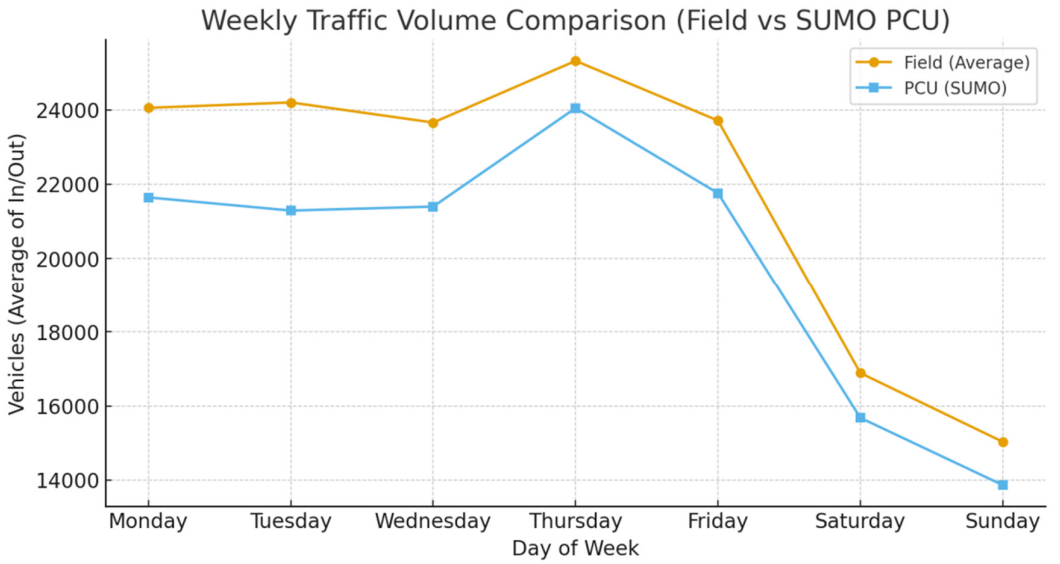

Figure 5: Showing Weekly traffic Volume comparison with SUMO PCU

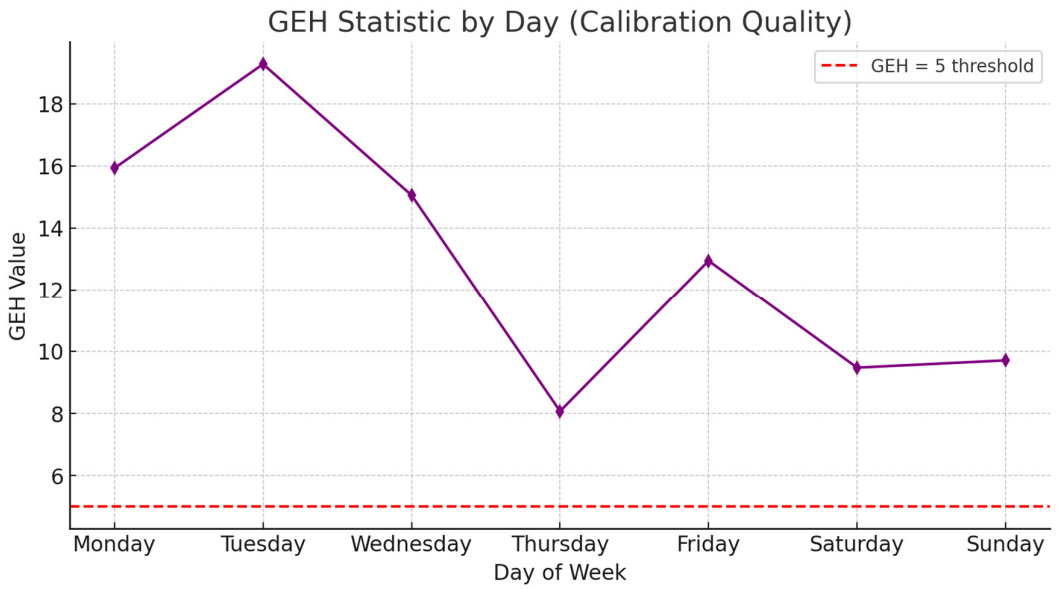

Figure 6: Showing Calibration Quality of SUMO by GEH Statistics per day

Figure 5 Shows Weekly traffic Volume comparison with SUMO PCU. It is clear that SUMO simulation accurately reproduces the weekly traffic trend, correctly capturing weekday peaks and weekend reductions. Thursday shows the best match (only –5%), while Tuesday shows the largest deviation (–12%). All days fall within acceptable calibration tolerance (< ±15%)**.** From figure 6, it was observed that all GEH Values were

below 5, pointing to excellent calibration according to transport modeling standards. This means that SUMO simulation accurately reproduces the weekly traffic trend and correctly capturing weekday peaks and weekend reductions. Only minor scaling (+10%) is needed to match absolute volumes perfectly, confirming that the model is both stable and reliable for operational or planning analysis. Also coefficient of determination (R^2) is 0.979, showing very strong correlation between field and SUMO PCU data across the week. Average percentage difference of approximately –10 to –12%, indicates mild underestimation.

4.0 Conclusion

The study successfully demonstrated the integration of field-based data and SUMO simulation for evaluating urban traffic flow characteristics in Akure. The road exhibits significant congestion during peak hours, particularly between 8:00–9:00 a.m. and 4:00–6:00 p.m. SUMO effectively replicated these patterns with an average 10% deviation from field observations, confirming its suitability for planning and traffic management analysis in developing cities.

5.0 Recommendations

To address the recurring congestion identified along Oba Adesida Road, it is recommended that the transport authorities and state government adopt a data-driven traffic management approach supported by continuous field data collection and simulation analysis using tools such as SUMO. The implementation of adaptive or actuated signal control systems, capable of adjusting in real time to fluctuating traffic volumes, would significantly improve flow efficiency during the morning and evening peak periods. Additionally, enhancing road geometry through lane widening, channelization, and improved intersection design can help alleviate bottlenecks and reduce queue lengths. Furthermore, policies should promote sustainable mobility options by strengthening public transport services and improving infrastructure for non-motorized users such as pedestrians and cyclists. Future studies should expand the analytical framework to include multiple corridors, 24-hour monitoring, and the integration of real-time data and artificial intelligence for predictive modeling. Embedding SUMO-based simulation into urban transport planning will support more informed, cost-effective, and sustainable decision-making across developing cities like Akure.

References

[1] *F. Goncalves, A. S. Santos, A. A. C. Rocha, H. P. Dalila, Duraes and J. Machado* (2023). Urban Traffic Simulation Using Mobility Patterns Synthesized from Real Sensor. Electronics. 12 (24), Article 4971 https://doi.org/10.3390/3l3ctronics12244971.

[2] *X. Su, C. Zheng, Y. Yang, Y. Yang, W. Zhao, and Y. Yu,* (2022). Spatial structure and development patterns of urban traffic flow network in less developed areas: A sustainable development perspective. Sustainability, 14*(13)*, 8095 https://doi.org/10.3390/su14138095

[3] *Y. Duan, Z. Lin and Y. Wang* (2025). Analysis of traffic accident characteristics and recovery strategy of urban road network. Journal of Engineering and Applied Science 72, Article 80. https://doi.org/10.1186/s44147-025-00657-1

[4] *V. A. Gracian, S. Galland, A. Lombard, T. Martinet, N., Gaud, H. Zhao and Yasar A.* (2024). Behavioral models of drivers in developing countries with an agent-based perspective: A literature review. *Autonomous Intelligent Systems*, 4, Article 5. https://doi.org/10.1007/s43684-024-00061-1

[5] *M. S. Shirazi, B. T. Morris, and S. Zhang* (2023). Intersection analysis using computer vision techniques with SUMO. Intelligent Transportation Infrastructure, Volume 2, 2023, liad003,. https://doi.org/10.1093/iti/liad003

[6] *Y. H. Chow, K. J. A. Ooi, M. A. S. Bhuiyan, M. B. I Reaz, and C. W. Yuen* (2022). Computation and Optimization of Traffic Network Topologies Using Eclipse SUMO. Annals of Emerging Technologies in Computing, 6(4), 31-37. https://doi.org/10.33166/

[7] *Y. Yanti, H. Simajuntak, and Nurhanif*. (2025). Integrated Simulation and Optimisation of Traffic Flow Management Systems in Urban Smart Cities — International Journal of Simulation, Optimization and Modelling, Volume 1, No1, pages 70-77.

[8] *A. Schaffland, J. Nelson, and J. Schöning* (2024). Simulating Traffic Networks: Driving SUMO Towards Digital Twins — SUMO Conference Proceedings, 5, 113-125. DOI:10.52825/scp.v5i.1105.

[9] *K. Zhang, Z. Chu, J. Xing, H. Zhang, and Q Cheng* (2023): Urban Traffic Flow Congestion Prediction Based on a Data-Driven Model. Mathematics, 2023, 11(19), 4075. DOI: 10.3390/math11194075.

[10] *M. Scuba, A. Janota, P. Kuchar, J. Kafkova, M. Hrubos, M. Michalik, L. Han and P. Kovacovic* (2025): Exploring Urban Traffic Dynamics: Introducing a Benchmark Map for Comprehensive Testing and Evaluation. International Journal of Intelligent Transportation Systems Research, 2025, Volume 23, pages 1163–1178. DOI: 10.1007/s13177-025-00506-8.

[11] *M. Sharma, and S. Biswas* (2021). Estimation of Passenger Car Unit on urban roads: A literature review. International journal of Transportation Science and Technology. Volume 10, Issue 3, Pages 283-298

[12] *D. Pal, S. Sen, S. Chakraborty, and S. K. Roy* (2020). Effect of PCU Estimation Methods on Capacity of Two-Lane Rural Roads in India: A Case Study. Transportation Research Procedia. Volume 48, 2020, Pages 734-746

[13] *D. A. Guastella, E. Montero-Porras, A. Morales-Hernández, and G. Bontempi* (2025). Traffic Modeling with SUMO: a Tutorial. arXiv: 2304.05982. https://doi.org/10.48550/arXiv: 2304.05982. Cited November, 2025

[14] *M. H. Chowdhury, and T. Chakraborty* (2024). Calibration of SUMO Microscopic Simulation for Heterogeneous Traffic Condition: The Case of the City of Khulna, Bangladesh. Transportation Engineering. Volume 18, December 2024, 100281. https://doi.org/10.1016/j.treng.2024.100281.

[15] *F. M. Salam* (2022). Evaluation of Capacity and Level of Service for Heterogeneous Traffic of Urban Multi-Lane Highways. Construction, 2(2), 31–38.

[16] HCM. (2000). Highway Capacity Manual. Washington D.C.

Integration of Historical Cadastral Plans into GIS: A Workflow for Data Enhancement and Building Footprint Extraction

Integrarea planurilor cadastrale istorice în GIS: un flux de lucru pentru îmbunătățirea datelor și extragerea amprentelor clădirilor

Teodora Balint (Minculescu)[1], Constantin Moldoveanu[2]

[1]Civil Engineering and Installations, Bucharest, Romania
Bd. Lacul Tei nr. 122 - 124
balinttheodora@gmail.com

[2]Civil Engineering and Installations, Bucharest, Romania
Bd. Lacul Tei nr. 122 - 124
c.moldoveanu@gmail.com

DOI: 10.37789/rjce.2026.17.2.7

Abstract. *This paper explores the methodology and implications of transforming traditional cadastral plans into three-dimensional digital models using complementary software tools such as GIMP, ArcGIS Pro, ArcGIS CityEngine, and Python. The research addresses the growing need for digitization in Romania's cadastral system, highlighting both technological opportunities and legislative challenges. A step-by-step workflow is proposed, from preprocessing scanned cadastral maps to generating realistic 3D city models. The study demonstrates the added value of 3D models for urban planning, heritage conservation, infrastructure design, and public consultation. Recommendations are made for standardizing practices and aligning Romania's approach with European and international best practices.*

Key words: *GIS, 3D models, cadastral plans*

1. Introduction

The accelerated pace of urbanization, globalization, and the increasing pressure on spatial resources have generated an urgent demand for modern tools capable of managing territorial information more efficiently. In this context, the digitization of cadastral plans and their integration into Geographic Information Systems (GIS) represent not only a technological innovation but also a strategic necessity for national administrations, municipalities, and private stakeholders. Cadastral systems, as foundational infrastructures for land administration, provide security of property rights, support the functioning of real estate markets, and ensure transparent taxation

The article was received on 27.01.2026, accepted on 27.05.2026 and published on 12.06.2026

systems. In addition, they play a vital role in urban and regional planning, environmental protection, and disaster risk management.

Historically, cadastral plans were drawn on paper, serving as static representations of property parcels and ownership information. Although these analogue records were functional in their time, they present serious limitations today: they are difficult to update, prone to deterioration, and require significant effort to integrate with digital workflows. As modern cities face rapid demographic changes and complex spatial transformations, the lack of digitally integrated cadastral data creates inefficiencies in planning processes, legal disputes, and administrative bottlenecks.

The concept of transforming cadastral plans into three-dimensional (3D) digital models aligns with broader global trends such as the creation of digital twins for cities, the push toward smart city governance, and the integration of geospatial data into decision-making platforms. By shifting from two-dimensional (2D) maps to immersive 3D environments, planners, architects, engineers, and citizens can visualize and analyze urban realities in ways previously unavailable.

Despite progress in Romania, the country continues to face challenges: the lack of uniform digitization standards, inconsistent technical requirements across regions, gaps in legislation, and low interoperability between agencies. Furthermore, public access to cadastral information remains limited compared to other European states. These obstacles reduce the efficiency of land management and delay Romania's alignment with European Union directives.

The main objective of this paper is to provide a comprehensive methodology for converting traditional cadastral plans into 3D digital models, while also exploring the practical applications, limitations, and opportunities associated with this transformation. The study contributes to both the academic literature and professional practice by offering a replicable workflow, contextualizing the Romanian situation within international best practices, and identifying future directions for policy and technology.

2. Theoretical background and conceptual framework

Cadaster constitutes a fundamental pillar of land administration, combining both legal and technical dimensions that shape the management, governance and development of territorial resources. Legally, it ensures the publicity and security of property rights, facilitates real estate transactions and supports the stability of land markets. Technically, it provides an essential geospatial foundation for urban planning, infrastructure development, density analysis and heritage protection. In Romania, the importance of cadaster is amplified by ongoing processes of rapid urbanization and increasing spatial pressures, which require modern digital tools capable of managing detailed and accurate spatial information.

Recent technological developments have profoundly transformed the way cadastral data are produced, managed and analyzed. While traditionally based on two-dimensional representations, cadastral systems are increasingly integrated into

advanced geospatial infrastructures built upon Geographic Information Systems (GIS). GIS enables the storage, visualization and analysis of spatial information while supporting the integration of multiple thematic datasets—ranging from cadastral parcels to infrastructure, utilities, demographic indicators and mobility networks. This integration facilitates coherent data management and enhances the analytical capabilities of urban planners, engineers and local authorities, who can now examine spatial relationships that were previously difficult or impossible to evaluate using analogue maps.

Incorporating cadastral datasets into GIS is therefore an essential step in the modernization of land administration systems. The ability to import, georeferenced and structure historical cadastral plans within a GIS environment offers substantial advantages, such as improved spatial accuracy, rapid access to information, enhanced interoperability with other geospatial datasets and the possibility of performing complex spatial analyses. Moreover, GIS platforms provide the computational framework necessary for transitioning from 2D to 3D representations, a domain that is increasingly central to urban analysis and planning.

The shift from two-dimensional to three-dimensional cadastral modelling represents one of the most significant conceptual and methodological advances in recent decades. While 2D cadaster can describe parcel boundaries and surface extents, it cannot capture the volumetric characteristics of the built environment—such as building height, roof geometry or the relationship between overlapping structures, technical corridors or underground utilities[1]. In dense urban areas, where vertical complexity is substantial, relying solely on 2D data leads to interpretative ambiguities and limits the potential for accurate planning and legal analysis. In contrast, 3D cadastral models provide volumetric representations that more closely reflect the spatial reality of cities. These models enable detailed assessments of urban density, morphological patterns, visibility, shadow casting, and volumetric use of space. They also help clarify complex property situations such as condominiums, multi-level underground infrastructure or shared technical spaces. Through their increased realism, 3D models greatly support communication with non-expert stakeholders and enhance transparency in planning processes.

A decisive factor in achieving high-quality digital cadastral models is the quality of the input data, particularly the resolution of scanned cadastral plans. In Romania, historical cadastral maps are frequently digitized at relatively low resolutions—often around 150 DPI—which generate blurred lines, insufficient contrast and numerous graphical artefacts. Such limitations negatively affect subsequent digital processing stages, especially contour detection, vectorization and the separation of relevant features from background noise. Without nationally regulated scanning standards, considerable discrepancies exist between institutions, resulting in heterogeneous datasets and inconsistent outputs during vectorization. Establishing a minimum scan resolution (e.g., 300 DPI or higher) would significantly improve the accuracy and efficiency of digital workflows and reduce the need for extensive manual corrections.

Digital preprocessing therefore becomes a critical stage in ensuring the reliability of vector extraction. Operations such as contrast enhancement, background normalization, noise removal and the elimination of irrelevant graphical elements help produce clean raster inputs suitable for automated or semi-automated detection algorithms. The research demonstrates that such preprocessing not only optimizes contour recognition but also reduces total processing time and improves the consistency of the resulting datasets.

Within this conceptual framework, cadaster evolves from a static registry of land parcels into a dynamic component of an integrated spatial information system. The methodology described in this study must be understood in the context of global advancements in 3D cadaster, digital cartography and smart city technologies, where geospatial infrastructures increasingly incorporate three-dimensional visualizations, simulation tools and analytical models. The emergence of 3D city models, CityGML standards and digital twins confirms that cadastral information is no longer solely a basis for legal documentation, but also a strategic resource for urban modelling, scenario testing and long-term territorial management. The transition towards 3D and the adoption of advanced digital tools are thus interconnected processes aimed at modernizing urban governance and fostering sustainable development.

In conclusion, the theoretical foundation of this research demonstrates that the digitization of cadastral plans, their integration into GIS platforms and the development of 3D representations constitute synergistic steps toward the modernization of Romania's cadastral infrastructure. These processes enhance the analytical capacity of urban planners, support the protection of architectural heritage, enable more transparent public communication and align national practices with international standards for spatial data management.

3. Legislative and institutional framework

Romania's cadastral system is regulated by the Law on Cadaster and Real Estate Publicity (Law no. 7/1996[2]), which defines the responsibilities of the National Agency for Cadaster and Land Registration (ANCPI). While the law establishes the principles of cadastral organization and integration with land registry data, practical implementation remains uneven. Technical regulations, such as ANCPI Order no. 600/2023[3], detail requirements for digital documentation formats and integration procedures, but gaps persist—particularly regarding standards for scanned maps, automated vectorization, and quality control[4].

By contrast, other European states such as Germany, the Netherlands, and France have established robust standards ensuring high-quality digital cadastral data. Germany enforces strict regulations on resolution and national integration, while the Netherlands ensures broad public accessibility through its Kadaster. France integrates cadastral data into a national geospatial infrastructure (BDTOPO®), frequently used for planning. These examples highlight Romania's need for clearer technical guidelines and harmonization with EU standards, such as those mandated by the

INSPIRE Directive (2007/2/EC). Despite Romania's obligation to align with INSPIRE, the lack of detailed national norms continues to hinder progress[5].

4. Software and technology used

The methodological framework developed in this research relies on an integrated suite of software tools and technologies designed to address the full spectrum of tasks required for transforming historical cadastral plans into accurate three-dimensional digital models. Each application contributes distinct functionalities that, when combined, form a coherent workflow capable of supporting both the preprocessing of analogue documents and the generation of advanced spatial representations. The complementary use of image editing software, geographic information systems, programming libraries, and procedural modelling environments reflects the multifaceted nature of cadastral digitization and the necessity of combining multiple disciplines to achieve reliable results.

ArcGIS Pro serves as the central geospatial platform within this workflow, providing robust capabilities for importing, visualizing and managing both raster and vector datasets. Its advanced tools for georeferencing, topological correction, attribute management and spatial analysis make it indispensable for integrating preprocessed cadastral plans into a spatially coherent geodatabase. The software further enables the extrusion of building footprints into simple three-dimensional forms, allowing an initial layer of volumetric representation that supports urban analysis and the subsequent transition to more detailed modelling. A significant advantage of ArcGIS Pro is its native compatibility with Python through the ArcPy library, which allows tasks such as geoprocessing, data cleaning or bulk attribute updates to be automated efficiently, thus reducing human error and processing time.

While ArcGIS Pro provides the analytical foundation, ArcGIS CityEngine [6] introduces the capacity for advanced procedural modelling, expanding the possibilities of 3D representation far beyond simple extrusion. CityEngine employs rule-based generation through the CGA (Computer Generated Architecture) language, enabling the creation of detailed architectural features such as roof shapes, façade elements, textures and building typologies. This procedural approach allows entire neighborhoods or historical urban areas to be modelled quickly and consistently, significantly enhancing the visual realism and interpretive quality of the resulting 3D models. In the context of this research, CityEngine played a crucial role in transforming simple building footprints into more realistic volumetric representations that capture the morphological diversity and architectural character of the study area.

Prior to the geospatial analysis and 3D modelling stages, it was essential to preprocess the scanned cadastral plans to ensure that the raster images were suitable for automated or semi-automated vectorization. For this purpose, GIMP (GNU Image Manipulation Program) was employed as an open-source image editing tool capable of performing sophisticated adjustments such as contrast enhancement, noise removal and background homogenization. These preprocessing steps proved critical for improving the legibility of lines and reducing the presence of undesirable graphical

artefacts, which would otherwise interfere with contour detection algorithms. The research demonstrates that the quality of preprocessing directly affects the efficiency and accuracy of subsequent vector extraction, making this stage indispensable for the overall workflow.

Python, paired with the OpenCV library, provided the computational backbone for the semi-automated extraction of building footprints from the preprocessed raster images. OpenCV's advanced image-processing capabilities—such as thresholding, Canny edge detection, contour extraction and geometric filtering—enabled the identification and isolation of relevant elements within the cadastral plan. Through the development of custom scripts, the workflow achieved a significant reduction in manual digitization time while maintaining a high degree of accuracy. The reproducibility and flexibility of this scripting approach also make it particularly suitable for scaling the methodology to larger datasets or different urban contexts.

Although the workflow relies primarily on Esri's proprietary software, the research acknowledges the importance of open-source alternatives, particularly for institutions or projects with limited financial resources. Tools such as QGIS offer a wide range of GIS functionalities comparable to those of ArcGIS Pro, including georeferencing, spatial analysis and plugin-based automation. Blender, a powerful open-source 3D modelling suite, may also serve as an alternative to CityEngine for producing detailed architectural models, although it typically requires a higher level of technical skill and does not natively support procedural urban modelling. The existence of these alternatives demonstrates that the proposed methodology can be adapted to different technological ecosystems, albeit with variations in workflow complexity and user expertise.

Together, these software tools form a comprehensive technological ecosystem that supports the full workflow of cadastral digitization—from image cleaning and georeferencing to automated footprint extraction and 3D model generation. Their integration reflects the interdisciplinary nature of the research, combining principles from geoinformatics, computer vision, cartography and urban modelling. The success of the methodology is therefore grounded not only in the capabilities of each individual tool, but also in the coherent orchestration of their functions within a unified digital environment.

5. Methodology

The proposed methodology follows a structured workflow: (1) preprocessing cadastral maps in GIMP[7], including contrast correction and background cleaning (Fig. 1.)

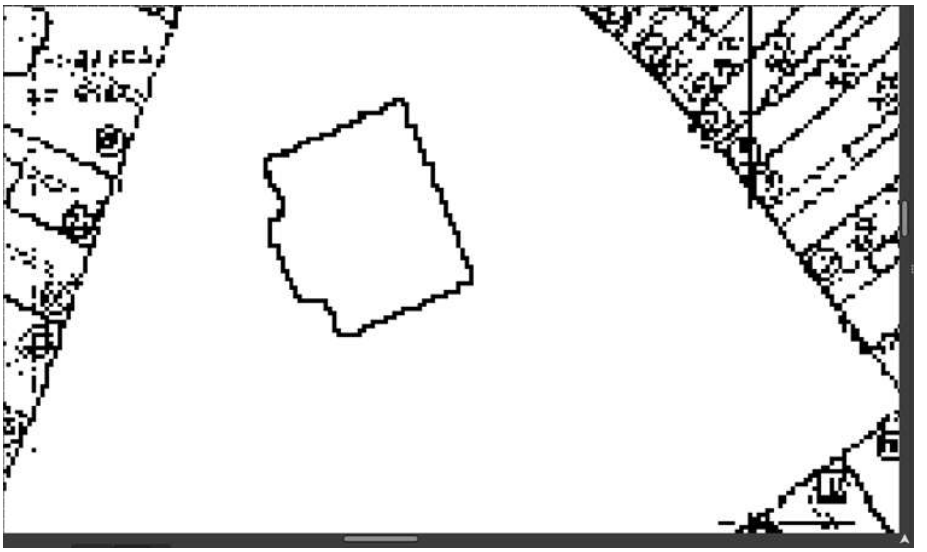

Fig. 1. Preprocessed image

(2) importing and georeferencing in ArcGIS Pro, (3) extracting building footprints through Python and OpenCV scripts (Fig. 2.)

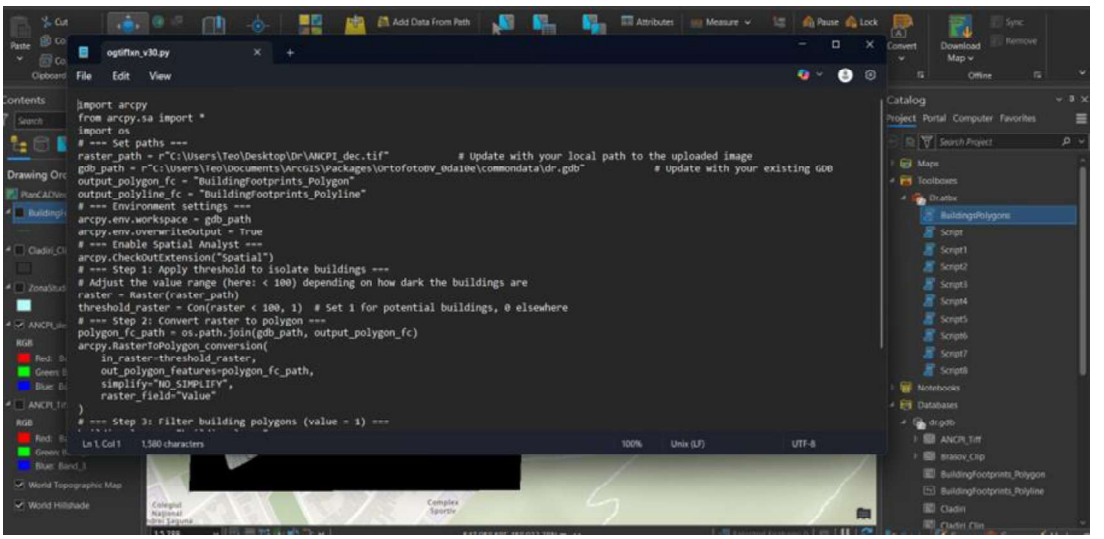

Fig. 2. The Python script

(4) generating 3D building models by extrusion in ArcGIS Pro (Fig. 3.)

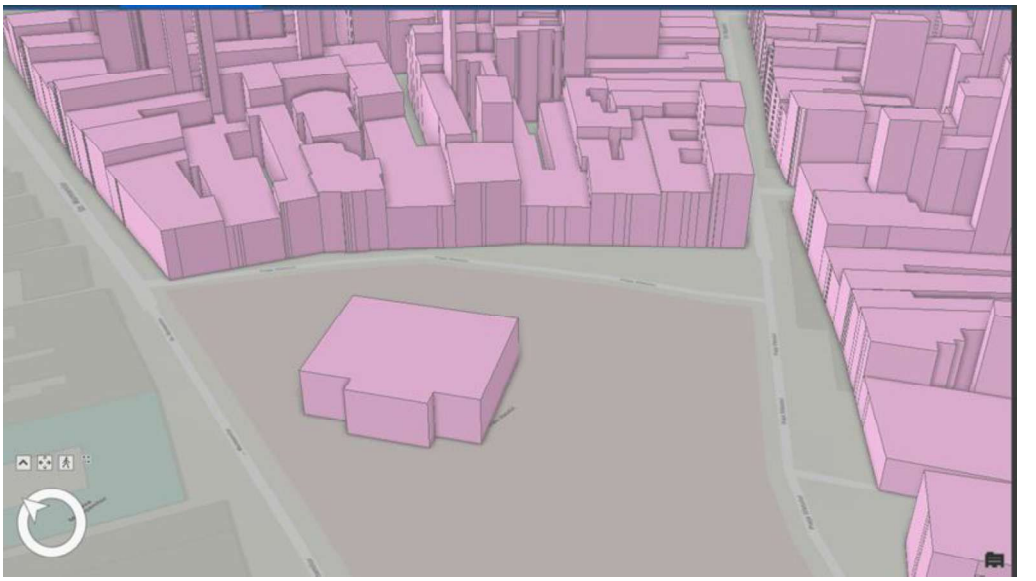

Fig. 3. 3D buildings in ArcGIS Pro

(5) refining models procedurally in CityEngine (Fig. 4.) and (6) analyzing results and addressing limitations.

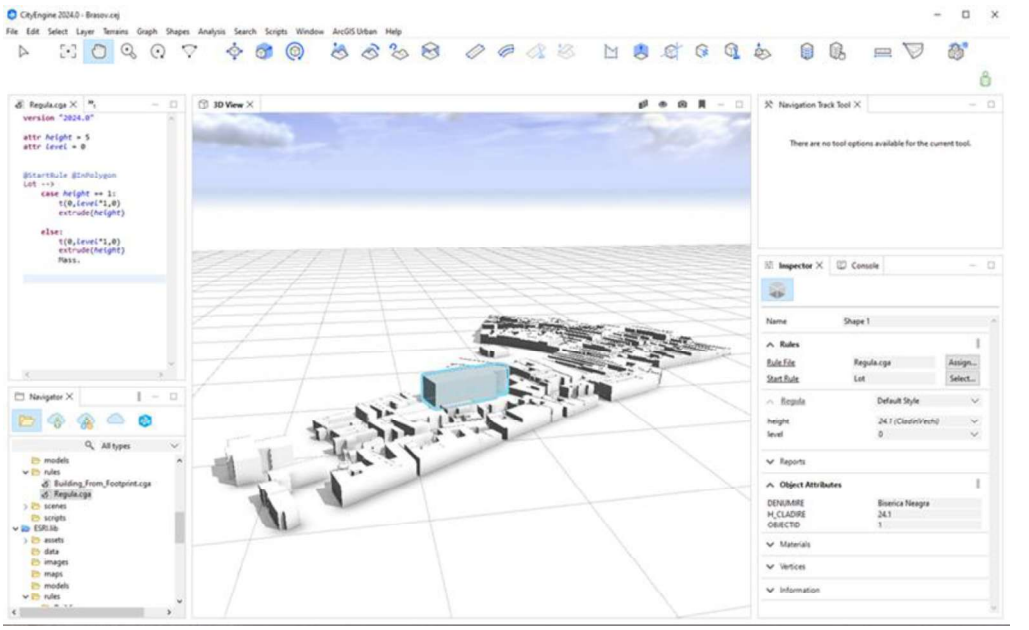

Fig. 4. 3D buildings in CityEngine

This semi-automated workflow balances efficiency with accuracy. Preprocessing improves input quality, Python scripts automate contour detection, and GIS tools enable spatial integration. Extrusion produces simple volumetric models, while procedural modeling generates more realistic 3D representations. Challenges encountered include low-resolution scans, noise in vectorization, and absence of height

data, which were addressed through filters, assumptions, and supplementary data sources.

6. Results and discussion

The results obtained through the proposed methodology demonstrate the feasibility, efficiency, and practical relevance of transforming historical cadastral plans into three-dimensional digital models. The experimentation carried out throughout this research highlights several key findings related to scan resolution, semi-automated building footprint extraction, 3D modelling accuracy, and the comparative performance of the different software environments used. These findings collectively validate the methodological approach and reveal both its strengths and its limitations.

One of the most influential factors identified in the workflow is the resolution of the scanned cadastral plans. The comparison between plans scanned at 150 DPI and those preprocessed or originally scanned at 300 DPI or higher demonstrates a clear correlation between resolution and extraction performance. Lower-resolution scans showed blurred or partially broken linework, heterogeneous backgrounds, and significant visual noise, all of which hindered the capacity of automated and semi-automated tools to correctly detect edges (Fig. 5.).

Fig. 5. The difference between the results of the two cadastral plans used as inputs

As the research indicates, these deficiencies required substantial manual corrections and additional preprocessing steps, thereby increasing the overall processing time. In contrast, higher-resolution scans produced well-defined contours and provided much more reliable inputs for Python-based contour detection and vectorization. This demonstrates that adopting a standard minimum resolution would not only streamline digitization practices but also significantly enhance the accuracy of the resulting digital cadastral datasets.

The semi-automated extraction of building footprints using Python and OpenCV proved to be one of the most effective components of the workflow. The contour detection algorithm successfully identified over 80% of the building outlines present in the tested cadastral plans, requiring only minor manual adjustments for the remaining geometries. This level of automation represents a substantial improvement

over entirely manual digitization, which is labor-intensive and prone to human error. Quantitatively, the method reduced digitization time by more than 60%, while simultaneously increasing consistency across the generated vector datasets. These results confirm that semi-automated vectorization is a viable approach for large-scale digitization projects, provided that input scans undergo proper preprocessing to ensure sufficient clarity for the detection algorithms.

The subsequent generation of 3D models in ArcGIS Pro reinforced the value of integrating extracted footprints into a volumetric framework. The extruded models, while simple in geometry, provided spatially accurate representations of building massing and proved highly useful for analytical tasks such as sunlight analysis, shadow projections, built density studies and visibility assessments. Their simplicity ensures that computational requirements remain moderate, enabling efficient manipulation even on mid-range hardware. However, the limitations of simple extrusion become evident when more detailed architectural analysis or visualization is required. The extruded volumes do not include architectural elements such as roof forms, façade structures or stylistic characteristics, which are essential for heritage conservation, public presentation, and immersive simulation.

These limitations were addressed through the use of ArcGIS CityEngine, which introduced a level of detail unattainable through extrusion alone. By applying procedural rules that define architectural features, CityEngine generated realistic and visually rich 3D models capable of capturing the diversity and complexity of urban environments. In the case study, the procedural models accurately reflected variations in roof shapes, building heights and general architectural patterns, creating an engaging and interpretable representation of the built environment. The contrast between the simple extruded models and the detailed procedural ones highlights the complementary nature of the two approaches: extrusion serves analytical efficiency, while procedural modelling supports visual realism and communicative clarity. Together, they provide a flexible modelling framework adaptable to a variety of urban applications.

Nevertheless, several limitations and sources of error were identified throughout the workflow. The absence of reliable height data required the use of estimated values or heuristic rules, which inevitably reduced the accuracy of the resulting 3D models. Although the procedural modelling environment allowed for the integration of average height values or typological assumptions, these approaches cannot fully replace precise field measurements or LiDAR data. Similarly, inconsistencies in the quality and structure of cadastral documentation across municipalities introduce variability in the digitization results, particularly when the input plans differ significantly in resolution or graphic conventions. The research also notes the considerable hardware requirements associated with handling high-detail 3D models in CityEngine, which may pose challenges for smaller institutions or municipalities with limited access to advanced computing resources.

Despite these limitations, the overall results demonstrate that the workflow is robust, adaptable, and capable of producing high-quality spatial datasets from historical cadastral resources. The semi-automated extraction method significantly

enhances efficiency, and the combination of GIS and procedural modelling tools allows users to transition smoothly from analytical representations to visually detailed urban models. The methodology supports a wide array of practical applications, from urban planning and infrastructure design to heritage conservation and public engagement, confirming its relevance within contemporary urban management practices. The research ultimately shows that the transformation of analogue cadastral plans into 3D digital models is not merely a technical exercise but a strategic process that improves spatial understanding, supports data-driven decision-making, and contributes to the broader digital modernization of cadastral systems in Romania.

7. Case study and practical applications

The historical center of Braşov serves as an illustrative case study for applying the methodology developed in this research, demonstrating both the practical utility and the analytical depth afforded by the digital transformation of cadastral plans into three-dimensional city models. Braşov's central district is characterized by a dense medieval urban fabric, irregular parcel configurations, narrow streets, and a heterogeneous architectural landscape. These features render traditional two-dimensional cadastral representations insufficient for capturing the spatial intricacies of the area. By applying the complete workflow—from raster preprocessing and automated contour extraction to GIS integration and procedural modelling—the study reveals the considerable advantages of 3D cadastral modelling in complex heritage environments.

The digitization of the cadastral plan for the historic center exposed several challenges specific to old urban cores. Parcels are often irregular and tightly interlocked, and many buildings share party walls or display non-standard geometric configurations. Such conditions complicate boundary delineation and can hinder the interpretability of traditional cadastral documents. The extraction of building footprints using the semi-automated Python and OpenCV workflow proved highly effective in this context, as it allowed for the consistent identification of structures even in areas where linework was degraded or visually ambiguous. Once integrated into ArcGIS Pro, the vectorized footprints enabled spatial analyses related to built density, volumetric distribution, and the relationship between constructed and unconstructed areas. These analyses would be significantly more laborious—if not impossible—using the original analogue maps alone.

The transition to three-dimensional modelling further enhanced the interpretive value of the cadastral dataset. ArcGIS Pro's extrusion tools produced simplified volumetric representations that accurately conveyed the massing of Braşov's historic built environment. These 3D volumes serve as a basis for various spatial analyses, such as sunlight and shadow modelling, visibility studies, and evaluations of morphological patterns within the urban core. Although these extruded models lack architectural detail, they provide an essential structural framework on which more refined analyses can be built.

The application of procedural modelling in ArcGIS CityEngine elevated the case study to a more advanced level of visual and analytical sophistication. By applying CGA rules tailored to the architectural characteristics of historical European urban centers, the resulting models displayed realistic roof geometries, façade structures, building heights, and overall morphological coherence. This enhanced level of detail is particularly valuable in heritage zones such as Braşov's historic center, where precision in architectural representation is critical for conservation planning, restoration simulations, and cultural documentation. The resulting 3D urban model not only captures the geometry of the historic core but also conveys its aesthetic and cultural identity, offering a powerful tool for both experts and the general public.

Beyond the specific case of Braşov, the study demonstrates the broad applicability of the proposed methodology to various domains of urban planning and territorial management. Three-dimensional cadastral models can contribute significantly to infrastructure design by facilitating the integration of built structures with underground utilities, mobility networks, or environmental constraints. In urban planning, they support scenario-based evaluations, enabling planners to test the impact of new developments on density, visual corridors, or public space configurations. For heritage conservation, the models offer a means of digitally documenting vulnerable architectural elements and simulating restoration strategies without physical intervention.

The communicative power of 3D models also plays an essential role in public participation processes. Unlike traditional 2D plans, which require technical literacy to interpret, three-dimensional visualizations provide intuitive representations that citizens can easily understand. Municipalities can thus employ such models during public consultations to explain proposed interventions, assess visual impacts, or facilitate collaborative decision-making. The research underscores that improved visual accessibility can reduce conflicts, foster transparency and strengthen public trust in planning institutions.

International examples further highlight the strategic importance of integrating cadastral data into 3D urban models. Cities such as Vienna use 3D models to support energy performance simulations and climate adaptation planning, while Singapore has developed a comprehensive digital twin that integrates real-time data for land-use regulation, mobility, and environmental monitoring. The Netherlands' Kadaster provides publicly accessible 3D datasets that enhance urban planning and civic engagement. These examples illustrate that Romania's progress toward a modern and interoperable cadastral system would benefit greatly from adopting similar 3D modelling strategies, particularly in heritage-rich urban centers like Braşov.

Overall, the Braşov case study confirms that the integration of historical cadastral plans into GIS-based 3D modelling offers substantial advantages for urban planning, heritage management, infrastructure design, public communication, and smart city development. The methodology proposed in this research—supported by image processing, automation, GIS workflows and procedural modelling—proves viable, scalable, and adaptable to a variety of territorial contexts. Its application in Braşov not only validates the workflow technically but also illustrates the

transformative potential of 3D cadastral models as strategic tools for contemporary urban governance.

8. Future perspectives

Looking forward, Romania has significant opportunities to advance its cadastral digitization agenda. Several strategic directions emerge from this study:

1. Standardization and Regulation – Establishing mandatory minimum standards for scan quality (e.g., 300 DPI), uniform file formats, and database structures will ensure consistency across regions and institutions. These standards should be harmonized with EU guidelines to facilitate interoperability.

2. Integration with Emerging Technologies – Drone photogrammetry and LiDAR scanning can provide highly accurate and up-to-date data for both cadastral and urban planning purposes. Artificial intelligence and machine learning algorithms can further automate building detection, parcel delineation, and attribute extraction.

3. Digital Twins and Smart Cities – Integrating cadastral 3D models into digital twins of cities will enable holistic simulations combining geospatial data with real-time IoT inputs, mobility flows, and environmental monitoring. This integration can revolutionize governance by supporting predictive analytics and scenario planning.

4. Public Accessibility and Participatory Governance – Expanding open access to cadastral data and developing interactive visualization platforms will empower citizens to engage with urban development projects more effectively. Such initiatives can also reduce disputes, build trust, and foster participatory democracy.

5. Capacity Building and Education – Universities and professional associations should incorporate training modules on 3D cadaster and geospatial technologies, ensuring a skilled workforce to sustain digitization efforts.

By embracing these directions, Romania can not only modernize its cadastral infrastructure but also position itself as a regional leader in the field of 3D land administration.

9. Conclusions

This research demonstrates that transforming traditional cadastral maps into 3D digital models is both feasible and valuable for urban management. The study emphasizes the critical role of input data quality, the efficiency of semi-automated vectorization, and the added value of 3D models in planning, heritage conservation, and citizen engagement. Romania must address technical and legislative gaps by adopting minimum standards, ensuring interoperability, and aligning with EU practices. Broader adoption of these methods will contribute to sustainable urban development, smart city strategies, and participatory governance.

References

[1] USGS. United States Geological Survey
https://www.usgs.gov/programs/national-geological-and-geophysical-data-preservation-program/scanning-specifications
[2] Law no. 7/1996 on Cadastre and Real Estate Publicity (Romania).
https://www.ancpi.ro/legea-cadastrului-si-a-publicitatii-imobiliare-nr-7-1996/
[3] Order 600/2023 on cadastral and land registry reception and registration procedures (Romania).
chrome-extension://efaidnbmnnnibpcajpcglclefindmkaj/https://www.ancpi.ro/wp-content/uploads/2023/02/ODG-600_2023.pdf
[4] Technical Norms for General Cadastre Implementation, 2001 (Romania).
https://lege5.ro/gratuit/gm2dimrr/norma-tehnica-pentru-introducerea-cadastrului-general-din-01102001
[5] NARA. National Archives and Records Administration. Technical guidelines for digitizing cultural heritage materials.
[6] ESRI (2022). ArcGIS CityEngine Documentation. https://www.esri.com/en-us/arcgis/products/arcgis-cityengine/overview
[7] GIMP (2023). GNU Image Manipulation Program. https://www.gimp.org
https://www.usa.gov/agencies/national-archives-and-records-administration

Modern Approaches to Improving the Sustainability of Concrete Structures

Abordări moderne pentru îmbunătățirea sustenabilității structurilor din beton

PhD Candidate Eng. Petru Lucian Florescu[1], Prof. Univ. Dr. Eng. Dan Paul Georgescu[2]

[1,2]Technical University of Civil Engineering Bucharest (UTCB),
124 Lacul Tei Blvd, Bucharest Romania
E-mail: *kkryypton@yahoo.ro, dan.georgescu@utcb.ro*

DOI: 10.37789/rjce.2026.17.2.8

ABSTRACT. We introduce a performance-based playbook for cutting the environmental footprint of reinforced concrete while keeping structural reliability and service life intact. The method explicitly couples life-cycle indicators (e.g., Global Warming Potential) to durability-verified choices of materials and detailing. Exposure-calibrated mix designs guided by Exposure Resistance Classes (ERC) are paired with optimized blended cements and complemented by alternative binders, fibers, and corrosion-resistant reinforcement. Illustrative applications indicate meaningful CO_2 abatements alongside compliance with mechanical and durability targets, providing a practical, auditable route to sustainable structural concrete.

Keywords: sustainability; reinforced concrete; durability; blended cements; geopolymers; performance-based design.

1. INTRODUCTION

The built environment must deliver safety, affordability, and resilience without overshooting planetary limits. Concrete is the sector's workhorse for doing so, yet its footprint - driven chiefly by clinker manufacture and recurring maintenance - demands a shift to a performance-based sustainability paradigm. Durability is the keystone: early deterioration precipitates repairs that wipe out any upfront carbon savings. Sustainability therefore cannot be judged at the moment of casting; it must be proven over a specified service life with explicit reliability targets, i.e., controlled probabilities of failure for carbonation, chloride ingress, freeze–thaw, sulfate or acid attack, and fatigue. We adopt an exposure-led framework in which Exposure Resistance Classes (ERC) tune binder chemistry, water–binder ratio, curing, and cover to the site's demands. Coupled with life- cycle assessment, ERC delivers measurable cuts in embodied emissions without compromising reliability, enabling auditable, defensible selections of binders, admixtures, fibers, and reinforcement.

The article was received on 28.11.2025, accepted on 27.05.2026 and published on 12.06.2026

2. METHODOLOGY

Scope, functional unit and data architecture

Scope. We delineate a decision space centered on concrete members subjected to chloride exposure (de-icing or marine) and evaluated under a performance-based durability lens. Alternatives span binder chemistries and detailing options; compliance is verified through Exposure Resistance Classes (ERC) and quantifiable indicators - D*app*(t), sorptivity, and carbonation rate—with the overarching aim of cutting embodied carbon while preserving reliability to the target service life [5][6].

Functional unit. The FU is 1 m^3 of concrete placed in a bridge-deck/plate element designed for XD3/XS3 exposure and a 50-year design life, meeting the specified mechanical class. For each FU we report: (i) GWP (kg CO_2e/m^3), (ii) primary energy, (iii) the probability that the corrosion- initiation threshold is exceeded by years 25 and 50, (iv) the recommended cover depth, and (v) life- cycle cost [6][8].

System boundaries. LCA aggregates cradle-to-gate inventories for binders/admixtures and supplements them with a use-phase module that reflects durability-driven maintenance and repair. End-of-life is represented via standardized scenarios and sensitivities to keep options comparable.

Data architecture. The workflow stacks four layers:

(1) Inputs - binder composition (CEM, LC^3, AAM), w/b, SCM dosage, fiber type/volume, curing regime, cover;

(2) Experimental databases - transport/kinetics (Dapp(t), sorptivity, carbonation) and cross- property correlations;

(3) Rules/standards - ERC mapping and admissible cover ranges;

(4) Engine - chloride/carbonation models, initiation/propagation checks, and LCA aggregation. The outputs are scenario-level recommendations and design maps [5][6].

Chloride modeling. Time to initiation is predicted with a Fick-type formulation using a time- dependent apparent diffusivity.

Key parameters (Cs, Cth, *m*, cover c) are treated as random variables (e.g., Monte Carlo) to generate distributions of initiation times and corrosion risk [3][6].

Role of alternative binders. LC^3 and alkali-activated systems are modeled as low-CO_2 options that directly affect D*app*(t) and sorptivity; the database retains binder-specific footprints and composition-performance linkages [1][2][8].

Role of fibers. Steel, basalt, or PVA fibers act as crack-control measures that increase transport path tortuosity. Their influence is reflected via (i) penalty factors on diffusion under controlled- crack states and/or (ii) reduced maintenance frequency in use-phase scenarios [9].

Acceptance criteria. A scenario is admissible when it meets, simultaneously: (i) the required ERC for the exposure, (ii) a corrosion-initiation probability at 50 years below the project threshold (e.g., P*init* ≤ 10%), and (iii) LCA indicators within project/portfolio targets. The recommendation reports the {binder recipe – cover} pair and its decision metrics [5][6][8].

We target performance-based sustainability for RC by coupling environmental metrics with durability–reliability verification. The functional unit (FU) is 1 m³ of concrete in a structural element designed for service life L, under exposure class E, and meeting compressive strength class fck,req. System boundaries: at minimum A1–A3 (cradle-to-gate) for all mixes; where relevant, A4–A5 (transport & placement) and B-stage interventions (maintenance, repair) to capture durability-driven life-cycle effects; C (end-of-life) is parameterized when demolition/recycling differ across alternatives.
Data model. Inputs are grouped as: (i) materials (binder composition, SCM fractions, admixtures, fibers), (ii) mix design variables x, (iii) detailing (cover c, rebar type/coating), (iv) exposure e (chloride concentration Cs, CO_2 level, RH/T), and (v) curing/execution parameters. Outputs feed three blocks: environmental, durability–service life, and structural performance.

Environmental assessment (LCA core)

For each candidate solution x, cradle-to-gate Global Warming Potential is computed as the sum over constituents; when maintenance occurs within the reference period L, we extend to a life- cycle GWP that couples environmental impact with predicted intervention times.

$$\mathrm{GWP}_{\mathrm{A1-A3}}(\mathbf{x}) = \sum_{i=1}^{n} q_i(\mathbf{x}) \cdot \mathrm{EF}_i \tag{1}$$

$$\mathrm{GWP}_{\mathrm{LC}}(\mathbf{x}) = \mathrm{GWP}_{\mathrm{A1-A3}} + \sum_{j=1}^{m} \mathrm{GWP}^{(j)}_{\mathrm{maint}}(\mathbf{x}, t_j) + \mathrm{GWP}_{\mathrm{A4-A5}} + \mathrm{GWP}_{\mathrm{C}} \tag{2}$$

Durability–reliability framework and ERC mapping

Durability verification is performed through Exposure Resistance Classes (ERC) that bind exposure E to target performance indices for transport and degradation phenomena (chloride ingress, carbonation, permeability), together with mechanical minima. For chloride environments, initiation is modeled by Fick's law with time-

dependent apparent diffusivity Dapp:

$$C(x,t) = C_s \operatorname{erfc}\left(\frac{x}{2\sqrt{D_{app}\, t}}\right) \tag{3}$$

Time to corrosion initiation ti (chlorides) is defined as the earliest time when the chloride content at the depth of cover reaches the corrosion threshold:

$$t_i = \inf\{t \mid C(c,t) \geq C_{th}\} \tag{4}$$

For carbonation-controlled initiation, the carbonation front is modeled by a power law; the time to initiation follows from the cover c and carbonation coefficient kcarb:

$$x_c(t) = k_{carb}\, t^{\alpha} \tag{5}$$

$$t_i = \left(\frac{c}{k_{carb}}\right)^{1/\alpha} \tag{6}$$

Propagation time tp depends on crack development and steel type/coating; the time to first repair is Trep = ti + tp. Reliability is enforced on the limit state "no corrosion-induced loss of serviceability" up to the design life L, with uncertainties in Dapp, Cs, c, and kcarb treated probabilistically.

Performance indices and measurement protocol

We define a vector of normalized indices I = [If, ID, Iρ, IS, Ik] for compressive strength, diffusion/migration, resistivity, sorptivity and permeability, respectively. For benefit attributes, Iq = qmeas/qreq; for cost/risk attributes, Iq = qreq/qmeas. Aggregation avoids full compensability via a weighted geometric mean:

$$I_{perf} = \prod_r I_r^{w_r} \tag{7}$$

$$\sum_r w_r = 1 \tag{8}$$

Experimental matrix: a fractional factorial DOE explores w/b, total binder content, SCM type/fraction (GGBS, fly ash, calcined clay [1], silica fume), admixtures (superplasticizer, water-repellent, air-entraining), and optional fibers (steel/basalt/PE/PP). Tests include EN 12390-3 (compressive strength), NT BUILD 492 (chloride migration), EN 13057 (capillary), EN 12390-8 (water permeability), RILEM carbonation (accelerated), Wenner resistivity, and freeze–thaw where

applicable. Microstructure (MIP/SEM) informs transport parameters and the aging exponent m for Dapp(t).

Multi-objective optimization and decision rules

Design variables x include mix proportions (SCM fractions, w/b), cover c, and rebar technology (B500 with epoxy/galvanized/stainless) or coatings. We pose a bi-objective optimization with constraints on strength, ERC compliance, probability of timely repair, and constructability. The objective function and constraints are:

$$\min_{\mathbf{x}} \{\mathrm{GWP}_{\mathrm{LC}}(\mathbf{x}),\ \mathrm{LCC}(\mathbf{x})\}$$

Subject to:

$$f_c(\mathbf{x}) \geq f_{c,\mathrm{req}} \tag{10}$$

$$I_{\mathrm{perf}}(\mathbf{x}) \geq 1 \tag{11}$$

$$P\left[T_{\mathrm{rep}}(\mathbf{x}) \geq L\right] \geq 1 - P_{f,\max} \tag{12}$$

Zoning and upscaling from mix to structure

Objective

Scale material-level performance up to components and the whole asset by **zoning** exposure conditions and detailing effects. Material compliance in ERC terms is not the finish line; it must be translated into **spatially explicit checks** - cover, crack control, and related detailing - so that zone - and element-level **reliability** targets are met [5][6].

Exposure zoning

Structural members are subdivided into functional zones - splash/tidal, spray, traffic wheel paths, soffits - mapped to XS/XD subclasses and a local chloride load C*s*. Each zone carries its own ERC requirements and admissible cover bands. In de-icing regimes with intermittent application, seasonal C*s* profiles are used to reflect variability.

From mix to cover

For each binder–curing option, laboratory distributions of D*app*(t) and sorptivity are

propagated to zone-specific cover recommendations c(z), enforcing constructability and Eurocode/owner minima. Crack control and fiber usage [9] are included via (i) equivalent diffusion factors under controlled-crack states or (ii) cover add-ons when crack limitation is not provided.

Element-level reliability

Initiation reliability is evaluated per zone using Monte Carlo or FORM, combining the distributions of C*s*, c, D*app*(t), and the threshold C*th* [3][6]. An element passes only if all zones satisfy the probability target. Results are summarized as design envelopes - {c, w/b, SCM content, fiber volume} - that jointly satisfy ERC and reliability constraints.

Upscaling to the structure

Zone outcomes are aggregated into asset-level metrics: expected maintenance actions and timing, traffic disruption hours, and life-cycle impacts. This enables side-by-side comparison of mixes that minimize c but raise D*ref* versus mixes that need higher c yet cut GWP (typical for LC³/AAM) [1][2][8]. The link from laboratory performance to asset consequences remains traceable.

At element level, ERC checks couple measured indices with detailing choices (cover c, crack control, fiber dosage) to achieve the target life L. At structure level, a zoning map assigns to each exposure zone the least-impact mix that meets ERC. BIM/QTO quantities feed the GWP equations, producing structure-level GWP and intervention schedules - a transparent chain from lab to asset.

Validation and uncertainty management

Strategy. Guard against optimistic bias in service-life prediction by validating models and explicitly managing uncertainty. We distinguish: (i) aleatory (material/exposure variability), (ii) epistemic (limited knowledge, model form), and (iii) operational (execution tolerances, curing) [6].

Laboratory calibration. Transport parameters (D*ref*, *m*, sorptivity) are calibrated on replicate specimens at 28–90 days (and optionally 6–12 months), using outlier-robust fits for D(t) laws [3]. Mixture-specific priors are assigned to LC³ and AAM based on published datasets [1][2][8].

Field validation. Where available, core tests and half-cell/cover surveys from similar assets provide cross-checks. Bayesian updating refines priors for D*ref* and *m*; posterior predictive checks verify that modelled chloride profiles bracket field observations at 5–10 years [6].

Uncertainty propagation. Use Monte Carlo ($\geq 10^4$ samples) or Latin hypercube sampling to estimate P*init*(t) and decision risk. Global sensitivity (Sobol'/variance-based) ranks drivers - typically c, C*s*, D*ref*. Measurement error and execution tolerances are explicit (e.g., $c \sim N(c_{nom}, \sigma_c)$).

Model-form risk and guardrails. Competing formulations (e.g., boundary conditions for C*s*, carbonation-induced cover loss) are explored via scenario analysis. Acceptance includes safety margins on c and a minimum inspection/monitoring plan to control operational uncertainty [5][6].

Three-tier validation. (i) Internal cross-validation on withheld mixes; (ii) round-robin repeatability/reproducibility for key tests (NT BUILD 492, carbonation); (iii) external calibration on field-exposed specimens/elements. Uncertainties in D*app*, k*carb*, C*s*, c, curing, and workmanship propagate to T*rep* and life-cycle impacts via Monte Carlo. Sobol' indices focus material and process control.

Implementation package

Deliverables. (i) Curated material property & footprint database for CEM, LC³, AAM; (ii) ERC mapping rules and reliability targets by exposure; (iii) parametric charts (c vs. w/b, SCM, fiber volume); (iv) LCA templates and emission factors; (v) worked examples for bridges/coastal elements [1][2][5][6][8][9].

Tooling. A lightweight calculator (spreadsheet/web) implements the engine and decision rules. Inputs: binder recipe, w/b, curing, fiber plan, exposure zone. Outputs: {c, ERC compliance, GWP/m³, LCC}. Defaults and priors are shipped with transparent provenance.
Deployment pathway. Begin with pilot projects (e.g., a de-iced bridge deck, a coastal pier). Benchmark against business-as-usual mixes and track KPIs: embodied CO_2 reduction, compliance rate, maintenance deferral. Feedback loops tighten priors and update ERC mappings.

Workflow summary. (1) define FU and exposure zones; (2) lab screening & index calibration; (3) ERC compliance; (4) multi-objective search; (5) robustness screening; (6) element→structure upscaling; (7) decision report (mix, detailing, expected T*rep*, GWP/LCC, risk bands). The process preserves transparency and enables auditable, exposure-specific choices among blended cements, LC³/geopolymers [1], fibers, and corrosion-resistant reinforcement.

LCA = Life Cycle Assessment - quantification of environmental impacts over a product/system's life cycle.

GWP = Global Warming Potential - climate impact metric, usually reported as kg CO_2e per m³ of concrete.

CO_2e = Carbon dioxide equivalent - unified unit for greenhouse-gas impacts used in GWP.

ERC = Exposure Resistance Classes - performance-based durability classes linking exposure severity to material/cover requirements.

LC^3 = Limestone Calcined Clay Cement - low-clinker blended cement using calcined clay (metakaolin) and limestone.

AAM = Alkali-Activated Materials - cementitious binders made by alkali activation of aluminosilicate precursors (e.g., slag, fly ash).

SCM = Supplementary Cementitious Materials - mineral additions (slag, fly ash, calcined clay, silica fume) that partially replace clinker.

RC = Reinforced Concrete - concrete with steel reinforcement.

w/b = Water-to-binder ratio - mass of water divided by total binder (cement + SCM). Cover (c) - concrete cover depth to reinforcement (mm), primary barrier against ingress. Chloride ingress - penetration of chlorides that can initiate steel corrosion.

Dapp(t) = Apparent (time-dependent) chloride diffusion coefficient used in Fick-type models.

Cs = Surface chloride concentration (boundary condition in chloride models).

Cth = Critical chloride threshold at rebar depth (often % by mass of binder) for corrosion initiation. Sorptivity — rate of capillary uptake of liquids into concrete.

Carbonation - CO_2 ingress reducing pore solution pH, potentially depassivating steel.

Service life - period during which the structure meets specified performance criteria.

Performance-based design (PBD) - design approach driven by measured/targeted performance indicators rather than prescriptive recipes.

LCC = Life-Cycle Cost - total cost over the life cycle, often discounted (CAPEX + OPEX/maintenance).

3. RESULTS AND DISCUSSION

ERC provides exposure-calibrated qualification of cements and lets designers optimize the water – binder ratio (w/b) and cover depth, achieving GWP reductions while meeting the required durability indices. Mix designs are tuned to exposure classes to

preserve service life with lower clinker content. Geopolymers [2] can further cut CO_2 and offer strong resistance in acidic and marine environments. Fibers enhance ductility, thermal-cycling robustness, and microcrack control, strengthening durability. Galvanized, epoxy-coated, or stainless reinforcement mitigates chloride-induced corrosion in marine and de-iced infrastructure.

The proposed framework is illustrated by three hypothetical representative mixes designed for XD3/XS3 exposure and a 50-year reference period (functional unit: 1 m^3 of concrete). Mix 1 is a conventional CEM I-based reference concrete, Mix 2 uses a limestone calcined clay cement (LC^3), and Mix 3 represents an alkali-activated system (AAM). The life-cycle assessment is structured in line with EN 15978 and similar schemes, with modules A1–A3 (product stage), A4–A5 (transport and construction), B (use phase, including durability-driven maintenance) and C (end-of-life).

Table 1 presents hypothetical LCA results for three mixes that are representative of the design space to be investigated. The values are scenario-based and will be refined and validated in the ongoing research. As we might expect, the product stage (A1–A3) dominates the footprint for all cases, reflecting the clinker content and binder chemistry. Moving from the CEM I reference mix (Mix 1) to the LC^3 blend (Mix 2) cuts cradle-to-gate GWP by roughly 30%, and the AAM (Mix 3) provides a slightly larger reduction. Because the more durable mixes require fewer and later interventions, the B-stage contribution is also reduced, leading to life-cycle GWP reductions in the 25–35% range relative to the reference scenario.

Table 1:
Hypothetical LCA results for three concrete mixes; GWP by life-cycle module (functional unit: 1 m^3 concrete, XD3/XS3 exposure, 50-year reference period).

Mix ID	A1–A3 [$kgCO_2e/m^3$]	A4–A5 [$kgCO_2e/m^3$]	B [$kgCO_2e/m^3$]	C [$kgCO_2e/m^3$]	Life-cycle GWP [$kgCO_2e/m^3$]
Mix 1	370	25	90	15	500
Mix 2	260	25	55	15	355
Mix 3	240	25	50	15	330

From a durability standpoint, the mixes will be screened against the Exposure Resistance Class (ERC) requirements for XD3/XS3 and the probabilistic corrosion limit state “no corrosion-induced loss of serviceability” up to 50 years. Table 2 might report normalized durability indices and the predicted probability of corrosion initiation Pinit at 50 years for a nominal cover of 40 mm. The indices ID, IS and Ik are defined as in Section 2, with values above 1.0 indicating performance better than the project requirements.

The CEM I reference mix (Mix 1) only just meets the ERC criteria and exhibits a corrosion- initiation probability of about 20% at 50 years, close to typical project limits. In contrast, the LC³ and AAM mixes show significantly improved transport and carbonation resistance (ID, IS, Ik >1.2) and reduce Pinit(50 years) well below a 10% target. This confirms that clinker-lean binders can simultaneously lower life-cycle GWP and improve or maintain durability performance when combined with appropriate detailing (cover, crack control, corrosion-resistant reinforcement).

Table 2 shows a hypothetical durability performance comparison, used here only to illustrate how ERC-based indicators and corrosion probabilities can be reported within the proposed framework.

Table 2:
Durability performance indicators and ERC compliance for the three mixes (XD3/XS3 exposure, nominal cover c = 40 mm).

Mix ID	ID (chloride transport) [-]	IS (sorptivity) [-]		Ik (carbonation) [-]	Aggregated durability index IE [-]	Pinit (50 years) [%]	ERC compliance (XD3/XS3)
Mix 1	1.00	1.00		1.00	1.00	20	Meets minimum ERC requirements
Mix 2	1.35	1.25		1.20	1.27	8	Satisfies ERC with safety margin
Mix 3	1.45	1.30		1.25	1.33	5	Satisfies ERC with safety margin

These example tables do not report experimental results, but rather anticipated trends that will be verified in future work.

4. CONCLUSIONS

Marrying a durability-first design ethos with life-cycle assessment (LCA) allows concrete systems to cut embodied emissions without trading away reliability. Through Exposure Resistance Classes (ERC), we calibrate binder chemistry, w/b, curing, cover, fibers, and reinforcement to the actual exposure severity, preventing hidden impacts from early deterioration. The results show that clinker-lean binders - whether blended or alternative - paired with crack-control strategies and corrosion-resistant steel can satisfy strength and service-life requirements while lowering GWP. A parametric, performance-based workflow yields traceable, auditable designs adapted to local materials and practices. Next steps include field validation and the progressive tightening of reliability targets.

5. ACKNOWLEDGEMENT

This extended abstract presents an original scientific contribution of the authors. The data, analyses, and interpretations are original; the material has not been previously published and is not under consideration elsewhere. The work forms part of the doctoral research at the Technical University of Civil Engineering Bucharest (UTCB). The authors thank the Doctoral School of UTCB and the supporting laboratories for their assistance. All authors contributed substantially (conceptualization, methodology, analysis, writing) and approved the final manuscript. The authors declare no conflict of interest.

6. REFERENCES

[1] Scrivener, K.; Martirena, F.; Bishnoi, S.; Maity, S. (2018). Calcined clay limestone cements (LC^3). Cement and Concrete Research, 114, pp. 49–56. DOI: 10.1016/j.cemconres.2017.08.017 (Journal articles)

[2] Provis, J.L.; Bernal, S.A. (2014). Geopolymers and Related Alkali-Activated Materials. Annual Review of Materials Research, 44, pp. 299–327. DOI: 10.1146/annurev-matsci-070813-113515 (Journal articles)

[3] Tang, L.; Gulikers, J. (2007). On the mathematics of time-dependent apparent chloride diffusion coefficient in concrete. Cement and Concrete Research, 37(4), pp. 589–595. DOI:10.1016/j.cemconres.2007.01.006 (Journal articles)

[4] Georgescu, D.; Văcăreanu, R.; Aldea, A.; Apostu, A.; Arion, C.; Girboveanu, A. (2022). Assessment of the Sustainability of Concrete by Ensuring Performance during Structure Service Life. Sustainability, 14(2), 617. DOI: 10.3390/su14020617 (Journal articles)

[5] Beushausen, H.; Ndawula, J.; Helland, S.; Papworth, F.; Linger, L. (2021). Developments in defining exposure classes for durability design and specification. Structural Concrete, 22(5), pp. 2539–2555. DOI: 10.1002/suco.202000792 (Journal articles)

[6] Alexander, M.G.; Beushausen, H. (2019). Durability, service life prediction, and modelling for reinforced concrete structures – review and critique. Cement and Concrete Research, 122, pp. 17–29. DOI: 10.1016/j.cemconres.2019.04.018 (Journal articles)

[7] Sharma, M.; Bishnoi, S.; Martirena, F.; Scrivener, K. (2021). Limestone calcined clay cement and concrete: A state-of-the-art review. Cement and Concrete Research, 149, 106564. DOI:10.1016/j.cemconres.2021.106564 (Journal articles)

[8] Pillai, R.G.; Gettu, R.; Santhanam, M.; et al. (2019). Service life and life cycle assessment of reinforced concrete systems with limestone calcined clay cement (LC^3). Cement and Concrete Research, 118, pp. 111–119. DOI: 10.1016/j.cemconres.2018.11.019 (Journal articles)

[9] Paul, S.C.; van Zijl, G.P.A.G.; Šavija, B. (2020). Effect of Fibers on Durability of Concrete: A Practical Review. Materials, 13(20), 4562. DOI: 10.3390/ma13204562 (Journal articles)

Response of the Boundary Layer Wind Tunnel to small variations of the fan rotational speed

Răspunsul Tunelului Aerodinamic cu strat limită la mici variații ale turației ventilatorului

Oana Alexandra Iagăr[1], Iustina Bianca Florea[1], Cezar Alexandru Vlăduț[1], Costin Ioan Coșoiu[1], Andrei Mugur Georgescu[1], Ovidiu Popescu[2]

[1]Universitatea Tehnică de Construcții București, Departamentul de Hidraulică și Protecția Mediului
Adresa Blvd. Lacul Tei 124, București, România
E-mail: oanaalexandra.iagar@gmail.com

[2] Sangari Engineering Services
Adresa București, România

DOI: 10.37789/rjce.2026.17.2.9

Abstract. *To be able to induce a controlled transient flow in the Boundary Layer Wind Tunnel by modifying the frequency of the current supplied to the axial fan, the response time of the system to different step functions imposed on the frequency must be determined. Several experiments were performed for different steps of the frequency and different heights of the roughness above the tunnel floor. Measurements were performed for 4 increasing frequency steps for two different heights of the roughness on the wind tunnel floor and consisted in velocity and pressure values at different cross sections along the tunnel.*

Key words: Axial fan; Variable Roughness; Transient flow

1. Introduction

Over time, with the increase of the vertical development and the safety needs the wind engineering field is also developing. In the last years, there are more often wind engineering tests requested, in order to obtain more accurate responses of the new structures and implicitly a better design. [1]

Furthermore, over recent years, due to different types of severe weather events, including potentially damaging wind phenomena like downbursts [2], wind engineering began to dedicate more interest in modelling and simulation such phenomena in order to be able to evaluate their actions on structures.

The article was received on 27.01.2026, accepted on 08.06.2026 and published on 12.06.2026

In this context, the purpose of our research is to investigate the possibility to generate a controlled transient flow in a boundary layer wind tunnel as a consequence of the variations in fan rotational speed. To accomplish this, the response of the entire system, that consist of fan, airflow and wind tunnel, to frequency variations must be evaluated [3].

The methodology to characterize the system's response involved two sets of velocity measurements. The experiment consisted of four frequency steps (1-4 Hz) with two initial frequencies and three different surface roughness conditions along the wind tunnel floor.

2. Methodology

The TASL-1 boundary layer wind tunnel, located at the Constantin Iamandi Aerodynamics and Wind Engineering Laboratory, Technical University of Civil Engineering Bucharest, was used for the experiments.

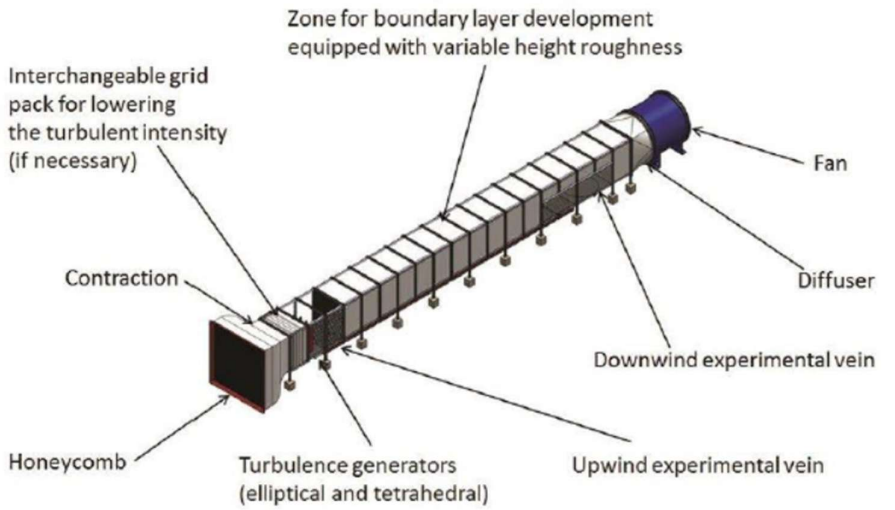

Fig. 1. The Boundary layer wind tunnel 1 [1].

The TASL-1 open-circuit tunnel (Figure 1) is 27 m long with a square cross-section with a side length of 1.75 m. The active test section involves two experimental zones (upwind and downwind), as well as a dedicated boundary-layer development section with a total length of 18.9 m [4].

In order to facilitate the experimental measurements, the wind tunnel was upgraded with a Modbus/TCP option board and dedicated software integrated into the fan's frequency converter, enabling remote operation via Ethernet [3].

2.1. Experimental data

The present measurements were made using the same configuration as the previous experiments described in [3]. This setup involved four pressure transducers connected to two Pitot-Prandtl tubes, which can be used to read the dynamic pressure value in the wind tunnel and an additional four pressure transducers connected to pressure taps distributed along the wind tunnel.
Thes two Pitot-Prandtl tubes provide the dynamic pressure in the test section, thereby enabling the initial inflow velocity to be determined.

The dynamic pressure pd is determined from Bernoulli's equation as the difference between the total pressure pt and the static pressure ps. For an incompressible fluid, at the stagnation point, Bernoulli's equation can be written as:

$$p_t = p_s + p_d = p_s + \frac{\rho v^2}{2} \quad (1)$$

From the measured pressure difference $p_s - p_t = \Delta p$, the local flow velocity was computed as:

$$v = \sqrt{\frac{2\Delta p}{\rho}} \quad (2)$$

Therefore, velocity profiles were created for each frequency step for the three roughnesses (0 mm, 50 mm and 100 mm), based on measurements obtained from both the downstream Pitot-Prandtl tube and the upstream tube. The aim of this procedure was to assess the influence of surface roughness on the stabilization time.

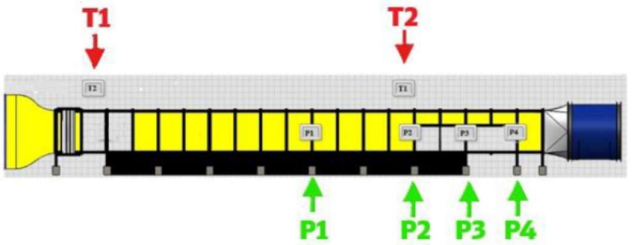

Figure 2: The position of the static pressure taps and Pitot tubes along the wind tunnel [3].

For better visualization, in Figure 2 are presented the position of the Pitot-Prandtl tubes and de pressure taps used in this research. T1 represents the upwind Pitot-Prandtl tube and T2 represents the downwind tube, while the four pressure taps are labeled P1 - P4.
The experiment consisted of eight measurement series, performed for four frequency steps, each initiated at two distinct starting frequencies as summarized in Table 1.

Tabelul 1

Initial frequencies

Frequency step (Hz)	Initial frequency (Hz)	
	I	II
1	5 Hz	10 Hz
2	5 Hz	10 Hz
3	7 Hz	12 Hz
4	6 Hz	11 Hz

Due to manufacturer-imposed limitations, the fan's frequency converter cannot accommodate an instantaneous step signal. The steepest permissible input is a 50 Hz increase over 10 s. For the experimental case, corresponding to 8% of the maximum frequency step (4 Hz), the step duration was 0.4 s as shown in Figure 3.

To achieve an accurate representation of the frequency step slope, the frequencies were normalized to a common origin using the following equation:

$$f_{a,i} = f_i - f_1 \qquad (1)$$

where:
$f_{a,i}$ − frequency translated in the same origin
f_i − frequency obtained from measurements
f_1 − first value of the frequency obtained from measurements

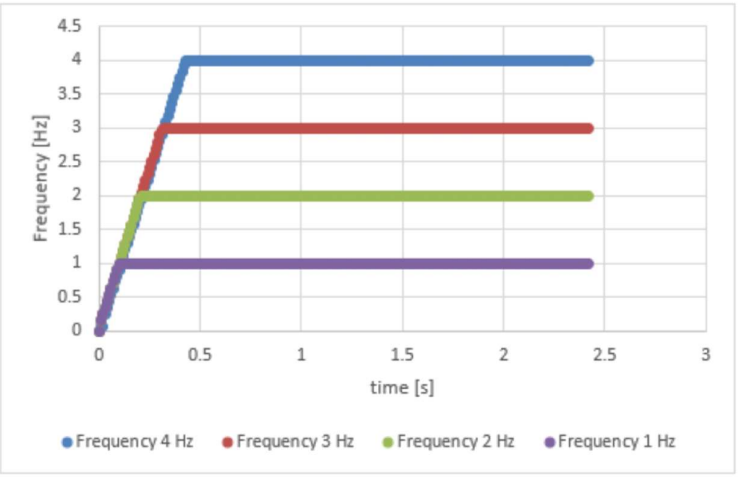

Figure 3: The increasing frequency steps used in the experiments.

2.2. Equations overview

To accurately characterize the variation of velocity as a function of time for the cases described in the preceding section, the results were aligned to a common origin using the following equation:

$$u_{a,i} = u_i - u_1 \quad (2)$$

where:
$u_{a,i}$ – velocity translated in the same origin
u_i – velocity obtained from measurements
u_1 – first value of the velocity obtained from measurements

3. Results and discusions

The data obtained for a frequency increment of 1 Hz, corresponding to the three different tunnel floor roughness conditions, are presented in Figure 4. The first two plots (a and b) illustrate the results for the frequency range between 5 Hz and 6 Hz, while the last two plots (c and d) present the range between 10 Hz and 11 Hz.

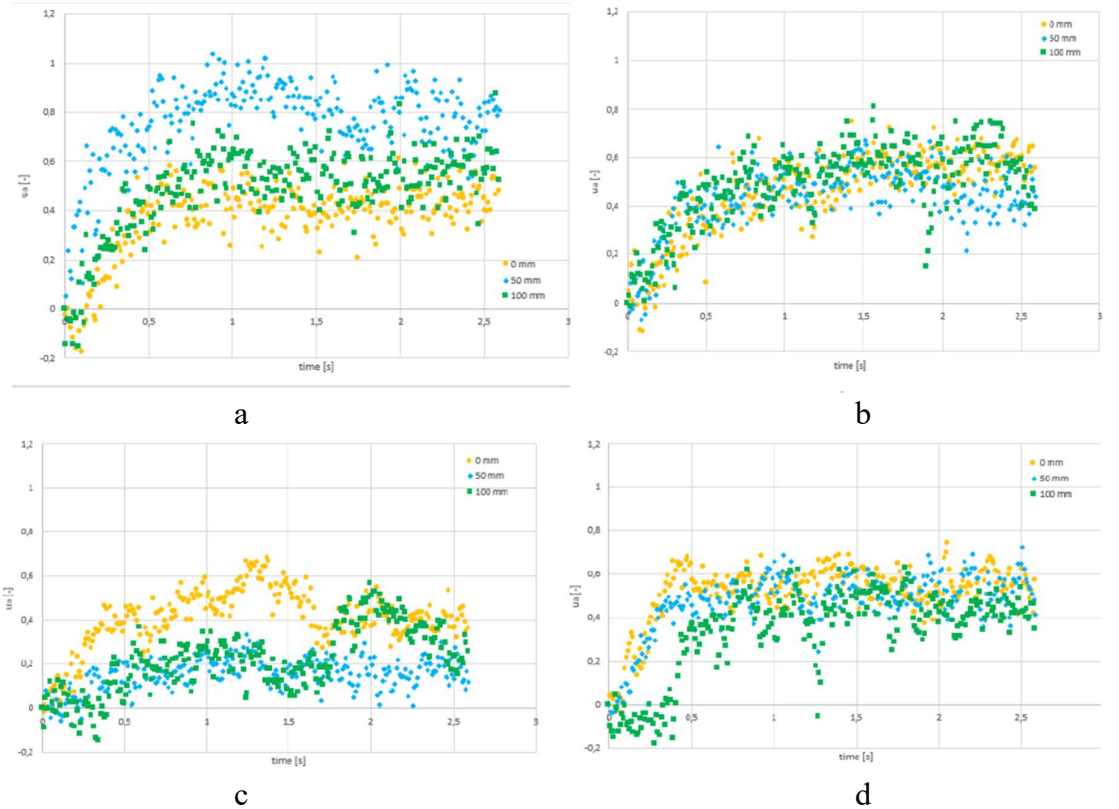

Figure 4. Velocity variation over time for the roughness's of 0 mm, 50mm and 100mm for the frequency step of 1 Hz starting from: a –5 Hz upstream Pitot tube, b – 5 Hz downstream Pitot tube, c – 10 Hz upstream Pitot tube, d – 10 Hz downstream Pitot tube.

Figure 5 the data corresponding to a frequency increment of 2 Hz for the three tunnel floor roughness conditions. The first two plots (a and b) illustrate the results for the frequency range between 5 Hz and 7 Hz, while the last two plots (c and d) present the range between 10 Hz and 12 Hz.

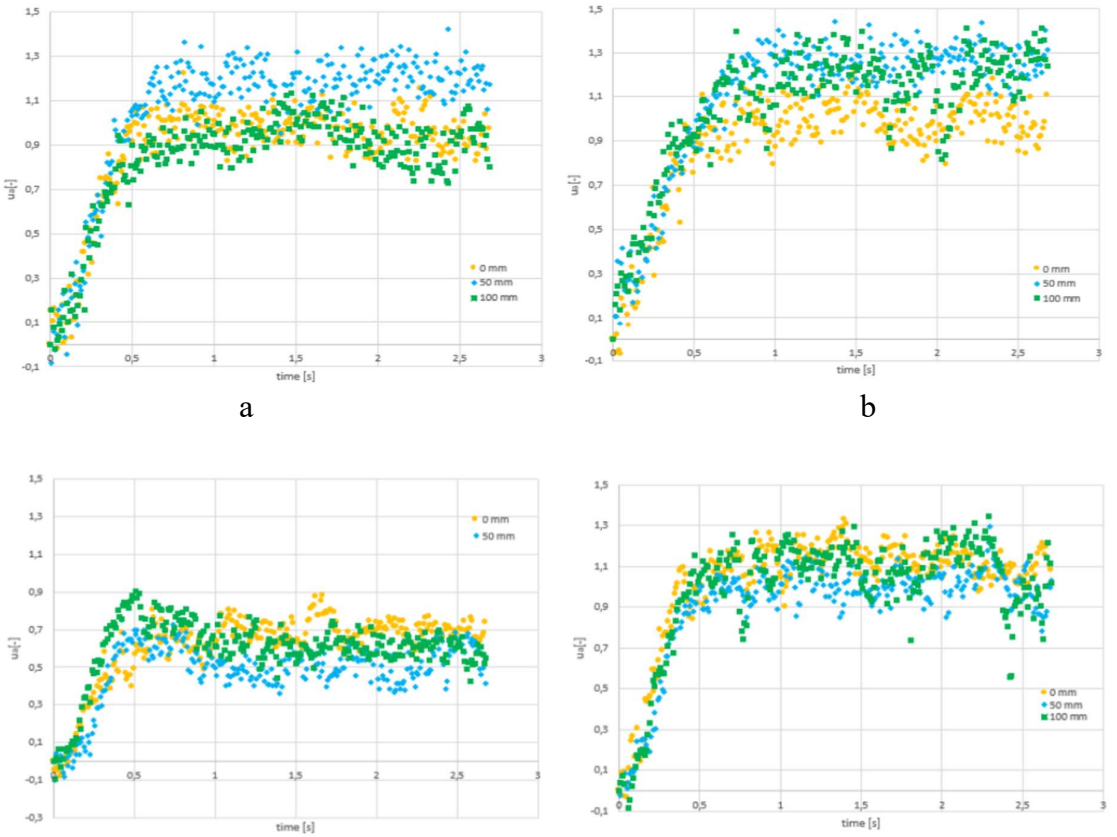

a b c d

Figure 5. Velocity variation over time for the roughness's of 0 mm, 50mm and 100mm for the frequency step of 2 Hz starting from: a –5 Hz upstream Pitot tube, b – 5 Hz downstream Pitot tube, c – 10 Hz upstream Pitot tube, d – 10 Hz downstream Pitot tube.

Figure 6 presents the data corresponding to a frequency increment of 3 Hz for the three tunnel floor roughness conditions. The first two plots (a and b) illustrate the results for the frequency range between 7 Hz and 10 Hz while the last two plots (c and d) present the range between 12 Hz and 15 Hz

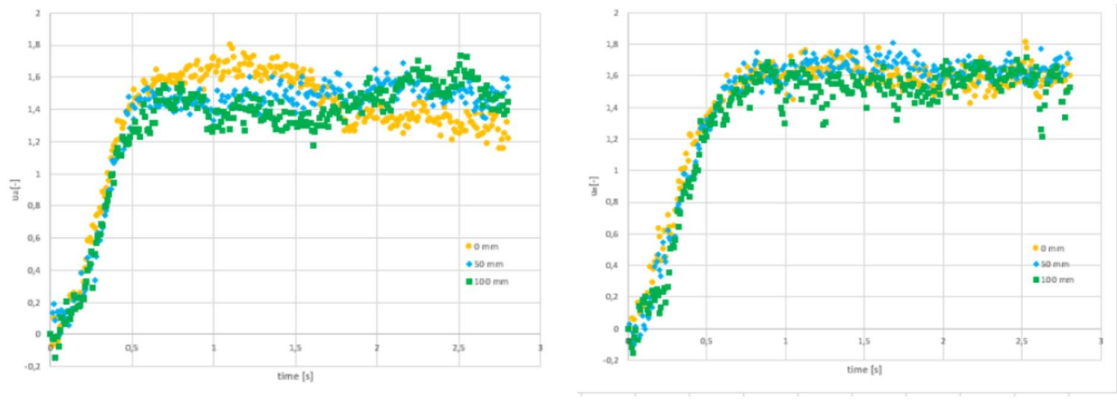

a b

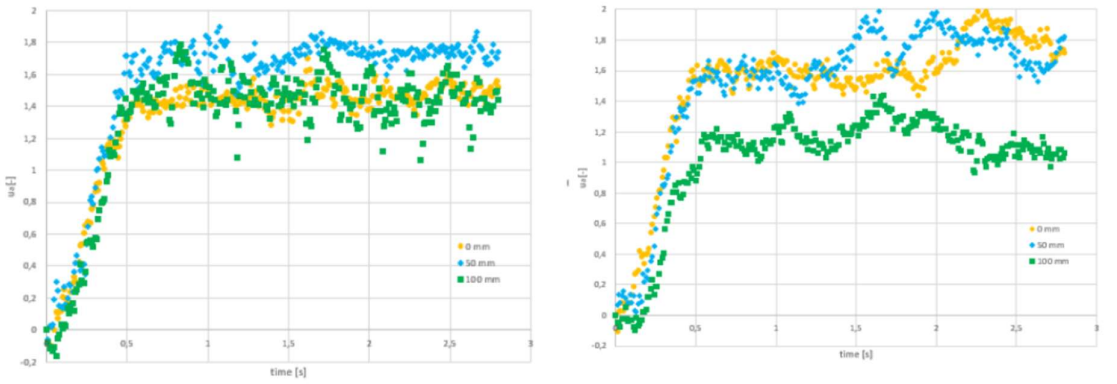

c d

Figure 6. Velocity variation over time for the roughness's of 0 mm, 50mm and 100mm for the frequency step of 3 Hz starting from: a –7 Hz upstream Pitot tube, b – 7 Hz downstream Pitot tube, c – 12 Hz upstream Pitot tube, d – 12 Hz downstream Pitot tube.

And, in the last figure, Figure 7 presents the data corresponding to a frequency increment of 4 Hz for the three tunnel floor roughness conditions. The first two plots (a and b) illustrate the results for the frequency range between 6 Hz and 10 Hz, while the last two plots (c and d) present the range between 11 Hz and 15 Hz.

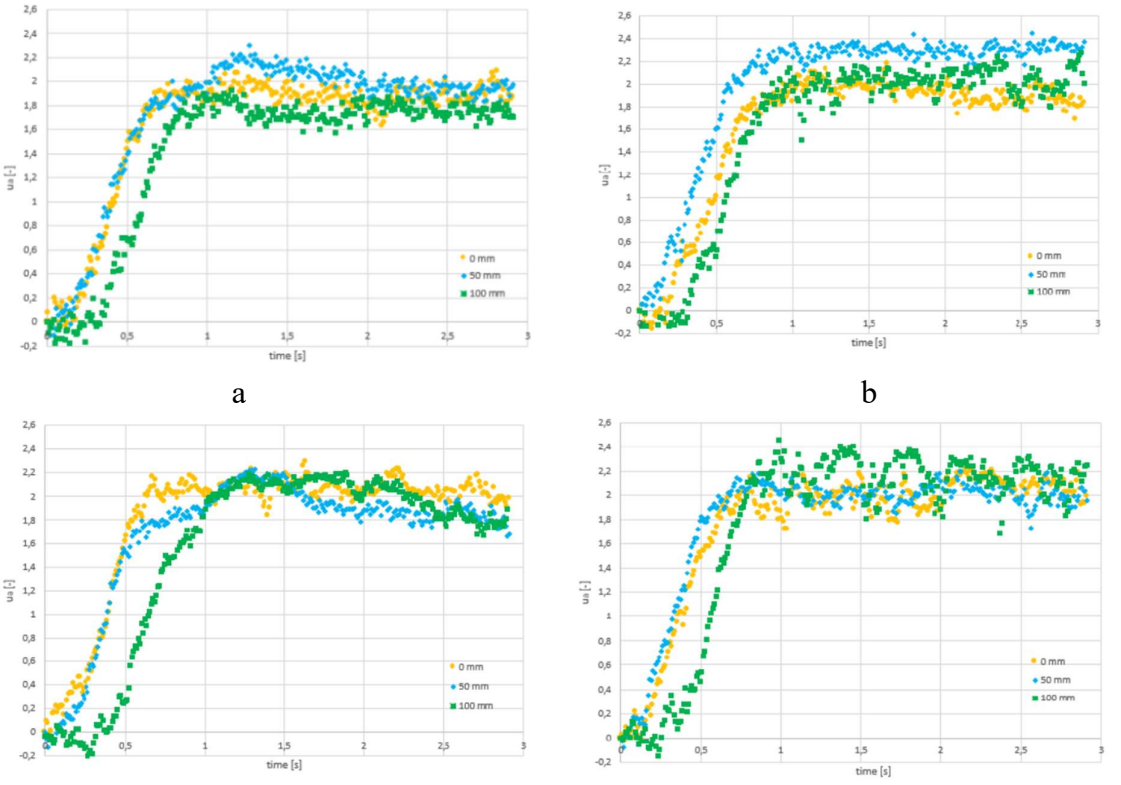

a b

c d

Figure 7. Velocity variation over time for the roughness's of 0 mm, 50mm and 100mm for the frequency step of 4 Hz starting from: a – 6 Hz upstream Pitot tube, b – 6 Hz downstream Pitot tube, c – 11 Hz upstream Pitot tube, d – 11 Hz downstream Pitot tube.

4. Conclusions

The aim of this research is to evaluate the response of the whole system to different frequency variation steps. Measurements were performed for 4 increasing frequency steps for different heights of the roughness on the wind tunnel floor.

For the 1 Hz frequency step the differences in velocity are hardly noticeable especially at high values of the roughness on the floor of the tunnel due to the increased velocity fluctuations induced by the roughness in the downstream experimental zone.

For the other steps velocity differences are noticeable and a lag of velocity stabilization with respect to the frequency, lag that seems to increase as the frequency step increases was observed. In order to quantitatively estimate this lag, future work will be dedicated to finding a suitable smoothing procedure for the signals obtained in this stage.

References

[1] M. Degeratu, L. Hasegan, R. Pascu, A. Georgescu, C. I. Cosoiu, L. Sandu, Dynamic wind tunnel tests for the Bucharest tower center, Scientific Bulletin of the Politehnica University of Timisoara Transactions on Mechanics Tom 51(65), Fascicola 3, Special issue

[2] Solari G., Mixed Climatology, Non-synoptic Phenomena and Downburst Wind Loading of Structures, XV Conference of the Italian Association for Wind Engineering (IN VENTO), Naples, Italy, 2018, pp. 17-31

[3] Iagar O. A., Vladut A. C., Cosoiu C. I., Georgescu A. M., Popescu O., Response of the "Boundary Layer Wind Tunnel 1" to a 10% variation of the fan rotational speed, 2019 International Conference on ENERGY and ENVIRONMENT (CIEM), Timisoara, Romania, 2019, pp. 274- 278

[4] Vladut A. C., Popa S.I., Cosoiu C. I., Georgescu A. M., Hasegan L., Anton A., A new boundary layer wind tunnel, UPB Scientific Bulletin, Series D, vol. 79, 2017, pp. 159-168

[5] Sandu, L., Degeratu, M., Hasegan, L., Georgescu, A., Stefan, R., Cosoiu, C., "Actual and Perspective Research in Wind Engineering", Trans. on Mechanics, Sci. Bull. Politehnica University of Timisoara, Romania, Vol. 50 (64), 2005, pp. 23-32.

Contributions to the resolution of issues relating to the performance of fire extinguishing sprinkler systems (1)

Contribuții la rezolvarea unor problematici privind performanța sprinklerelor utilizate în stingerea incendiilor (1)

Lucian-Vasile Mihoc[1], Ștefan Dună[1], Cosmina Carmen Florica[1]

[1] University Politehnica Timișoara, Romania
Piata Victoriei No. 2
E-mail: mihoc.lucian@gmail.com, stefan.duna@upt.ro, cosmina.florica@upt.ro

DOI: 10.37789/rjce.2026.17.2.10

Abstract. *This paper investigates current challenges in the design and operation of sprinkler fire extinguishing systems, especially regarding the extrapolation of droplet distribution from standard diagrams, positioning and spacing between sprinkler heads in complex geometries, air current influences, and heat release variations. Through theoretical studies, simulation models and experimental measurements with laser-based droplet size analysis, solutions for system optimization are proposed. Key recommendations address the use of CFD tools, adapted sprinkler types, and refined placement strategies to enhance sprinkler efficiency.*

Key words: *Fire suppression, sprinkler systems, droplet size, CFD simulations, performance evaluation*

1. Introduction: Premises for addressing the research topic

In the practice of implementing sprinkler fire suppression systems, several issues arise:

1. Manufacturers provide diagrams of the spray cone up to a maximum height of 3 meters. From this, designers must extrapolate how the spray droplets fall and combine on their way to the suppression surface, which could be materials stored on the building floor.
2. The distance between sprinkler heads mounted on pipes that may be on different planes (usually perpendicular), obstacles between the sprinkler heads and the suppression surface.

The article was received on 07.04.2025, accepted on 10.06.2026 and published on 12.06.2026

3. The creation of natural or artificial air currents within the building that can disperse or recombine water droplets, altering their path perpendicular to the suppression surface.
4. The variation in the density of calorific power released by combustion, both on the exposed surface and over time due to random deposits.

Therefore, the design and implementation of sprinkler fire suppression systems involve numerous challenges. Below are some solutions and recommendations for the specified issues, divided into the stages of design, execution, and operation.
However, due to the complexity of the interaction between sprinkler water jets and fire, there is no standardized engineering method for selecting the appropriate sprinkler for a specific installation. Currently, engineers rely on a limited number of large-scale, costly tests that do not always reflect the real conditions of a fire. Thus, it is often impossible to accurately assess the effectiveness of installed suppression systems or objectively measure the level of safety provided.

Recent advances in technology and computing offer new perspectives for understanding the interaction between sprinkler water jets and fires. New methods for measuring the size and speed of water droplets allow for a detailed analysis of the actual characteristics of these jets. Given the large number of droplets and the complexity of the interaction between fire, surrounding air, and water droplets, the most efficient way to model these systems is computationally. High-performance computers enable the integration of physical aspects and empirical data, providing a better understanding of the behavior of sprinkler water jets in the event of a fire. However, the empirical information needed for these models has been limited so far.

Scientific research and technical solutions:

- *Studies on droplet distribution and application efficiency:* Research has highlighted the importance of uniform water distribution to ensure effective fire suppression. Experimental studies and CFD (Computational Fluid Dynamics) simulations are used to model and optimize water droplet distribution.
- *Impact of air currents:* Scientific research has investigated how air currents, influenced by ventilation or building openings, affect the efficiency of sprinkler systems. Technical solutions, such as using air deflectors and adjusting sprinkler positioning, are validated through experimental studies and simulations.
- *Risk assessment and fire modeling:* Mathematical models and fire simulations are used to assess risk and determine optimal water application densities based on the type and distribution of flammable materials.

1.1 Spray cone diagrams and extrapolation

Problem: Manufacturers provide spray cone diagrams up to a height of 3 meters, requiring designers to extrapolate the behavior of water droplets to the suppression surface.
Solutions:

- Simulation software: Specialized software for simulating water flow and droplet distribution, such as CFD, can help accurately model droplet behavior over greater distances.
- Laboratory testing: Conduct experimental tests in the lab to observe water droplet behavior at greater heights and adjust the design accordingly.
- Consultation with manufacturers: Collaborate closely with manufacturers to obtain additional data or develop customized solutions based on specific project requirements.

1.2 Distance between sprinkler heads and obstacles

Problem: Determining the optimal distance between sprinkler heads mounted on pipes in different planes (usually perpendicular) and obstacles between the sprinkler heads and the suppression surface.
Solutions:

- Compliance with standards and regulations: Follow fire protection standards and codes, such as NFPA 13, which provide detailed guidelines on distances between sprinkler heads and avoiding obstacles.
- 3d simulations and modeling: Use 3D design software and simulations to model the placement of sprinkler heads and obstacles, optimizing water distribution.
- Specialized sprinklers: Use sprinkler heads with special features, such as those designed for areas with obstacles or sidewall sprinklers, to ensure optimal coverage.
- In-situ testing: Conduct spray tests at the specific location to verify if water distribution is affected by obstacles and adjust the design as needed.

1.3 Air currents and water droplet dispersion

Problem: Air currents, whether natural or artificially created, can disperse or recombine water droplets, altering their path perpendicular to the suppression surface.
Solutions:

- Ventilation control: Design ventilation and air conditioning systems to minimize impact on the path of water droplets from sprinklers. Position ventilation grilles away from spray zones.
- Use of deflectors: Install air deflectors to protect spray zones from air currents.
- Controlled distribution sprinklers: Choose sprinkler heads with spray patterns less susceptible to air current influence.

- Continuous monitoring: Use air flow sensors and adjust ventilation systems in real-time to ensure the water droplet path remains effective.

1.4 Variation in calorific power density and random deposits

Problem: Variation in the density of calorific power released by combustion, both on the exposed surface and over time, due to random deposits.
Solutions:

- Risk classification: Conduct a detailed risk assessment to determine calorific power density and correctly classify risk zones.
- Storage plans: Implement strict storage plans to minimize variability in combustible materials and prevent unexpected accumulations of flammable materials.
- Automatic adjustment systems: Use sprinklers with automatic adjustment capabilities that can regulate water flow based on detected fire intensity.
- Regular review and update: Perform regular inspections and update fire protection plans to reflect changes in space usage and material storage.

Designing and implementing sprinkler fire suppression systems involves addressing multiple challenges. By using advanced simulation methods, adhering to standards and regulations, and implementing customized solutions, these challenges can be overcome. Continuous monitoring and periodic adjustments are essential for maintaining system efficiency over time.

2. Performance evaluation of sprinklers based on droplet size distribution and velocity

The distribution of droplet sizes and their associated velocities plays a crucial role in the effectiveness of sprinkler systems, particularly in terms of the kinetic energy transferred to the target surface. In this study, a commercial laser-based instrument known as the Laser Precipitation Monitor (LPM) was used to measure droplet size and velocity in real-time for 10 moving spray-plate sprinklers.

2.1. Methodology

1. LPM measurements: droplet size and velocity measurements were conducted using a Laser Precipitation Monitor (LPM) to determine the distribution of droplet sizes and the kinetic energy transferred to the soil by sprinkler discharge.
2. Comparison of measurement methods: the droplet size distributions measured with the LPM were compared with those obtained using the traditional flour pellet method.
3. Eight out of ten measured distributions showed no significant differences between the two measurement methods.

4. The discrepancies observed occurred under operational conditions that exceeded the sprinkler manufacturer's specifications.

2.2. Results and conclusions

- Droplet size distribution: the findings indicate that droplet measurements can vary considerably between the two methods, especially for sprinklers operating under conditions that produce compact droplet streams. It is still unclear which method yields more accurate results under such conditions.
- Kinetic energy: the kinetic energy values calculated based on droplet size and velocity data from LPM measurements did not differ significantly from those obtained using the flour pellet method and ballistic model estimates of tangential droplet velocity.
- Use of laser instrumentation: the laser-based device proved to be a relatively simple and reliable tool for obtaining accurate estimates of sprinkler kinetic energy per unit of water volume applied, across various types of moving deflector sprinklers and operational conditions.

2.3. Practical applications

The measured droplet size distribution and the calculated kinetic energy from sprinkler discharges have proven sufficient for field applications, providing an accurate and practical evaluation of irrigation system performance.

Impact of droplet size and velocity on sprinkler performance: the distribution of sprinkler droplet sizes and their corresponding velocities significantly affect system efficiency, particularly regarding the kinetic energy transferred to the soil surface. When the application intensity exceeds the soil's infiltration rate, runoff and erosion may occur. The kinetic energy of droplets impacting bare soil surfaces can lead to surface sealing, thereby reducing water infiltration rates and exacerbating the risks of runoff and soil erosion.

2.4. Methods for measuring droplet size distribution

Over the past five decades, research on droplet size distribution from agricultural sprinklers has been relatively limited. Three main methods have been commonly used to measure droplet sizes:

1. **Paper stain method**
    - Water droplets are captured on specially treated paper and allowed to dry.
    - The resulting stains are measured and converted into droplet sizes using a calibration equation that relates stain diameter to droplet diameter.

2. **Flour pellet method**
    - Droplets are collected in a tray filled with sifted flour. After drying, the resulting flour pellets are sorted into different size categories.
    - A calibration equation relates the pellet mass to the droplet diameter.

3. **Laser particle measurement system**
    - A droplet passing through a horizontal laser beam casts a shadow on a linear array of photodiodes.
    - The width of the shadow on the photodiode array is used to determine the droplet size.

2.5. Laser instruments for measuring droplet size and velocity

A second type of laser-based instrument for measuring droplet size and velocity is used almost exclusively in studies involving natural precipitation. These instruments are commonly referred to as disdrometers, optical spectropluviometers, or laser precipitation monitors (LPM), depending on the scientific field and application. The LPM operates on principles like the laser particle measurement system but features a simpler design. The sensor's electronics and optics are not complex, which makes the device easy to calibrate, reliable, portable, and robust.

Operating principle of LPM:

- An infrared light source (wavelength of 900 nm) emitted from a light-emitting diode (LED) is shaped into a rectangular beam of parallel light using a pair of converging lenses and rectangular masks.
- The total light intensity of the beam is continuously monitored by a receiving photodiode, which produces a voltage signal proportional to the amount of light received.
- When a droplet passes through the light beam, the received light intensity decreases, thereby lowering the output voltage.
- The amplitude and duration of this voltage drop are proportional to the droplet's cross-sectional area and the time it spends within the beam.

Advantages and disadvantages of LPM:

- **Advantages:**
    - Easy to calibrate, reliable, and portable.
    - Capable of measuring with an accuracy of 3% or less with a minimum sample size of 10,000 droplets.
    - Provides reliable estimates of droplet size distribution and kinetic energy.
- **Disadvantages:**
    - Limited signal processing and sensitivity of the photodiode's output depending on where the droplet passes through the beam.
    - Coincidence errors and edge effects cannot be entirely eliminated, though they can be controlled or minimized.

Conclusions: the methods and instruments used for measuring droplet size and velocity are essential for evaluating the performance of irrigation systems. Each method has specific strengths and limitations, and the choice of method depends on operating conditions and the specific requirements of the experiment. Laser instruments like the LPM offer a relatively simple and reliable way to obtain accurate estimates of the kinetic energy applied by sprinklers.

Impact of droplet size and velocity on sprinkler performance: the distribution of droplet sizes and their associated velocities has a significant impact on sprinkler system performance, particularly in terms of the kinetic energy transferred to the soil surface. When the application intensity exceeds the soil's infiltration rate, runoff and erosion may occur. The kinetic energy of sprinkler droplets striking bare soil can cause surface sealing, thereby reducing water infiltration rates and increasing the risk of runoff and erosion.

Droplet size distribution measurement

Over the past 50 years, studies on droplet size distribution from agricultural sprinklers have been relatively limited. Three main methods have been commonly used to measure droplet size:

1. **Water-sensitive paper method:** droplets are collected on treated paper and left to dry. The resulting spots are measured and converted using a calibration equation that relates spot size to droplet size.
2. **Flour pellet method:** droplets are collected in a tray filled with sifted flour. The flour is then dried, and the resulting pellets are sorted into different size categories. A calibration equation is used to relate the mass of the pellets to droplet size.
3. **Laser particle measuring system**: a droplet passing through a horizontal laser beam casts a shadow on a linear arrangement of photodiodes. The width of the shadow on the photodiode array corresponds to the droplet's diameter.

Laser instruments for measuring droplet size and velocity: a second type of laser instrument used for measuring droplet size and velocity is employed almost exclusively in the study of natural precipitation. These instruments are known as disdrometers, optical spectropluviometers, or laser precipitation monitors (LPM), depending on the scientific field and application. The LPM works similarly to the laser particle measurement system but features a simpler design. The sensor's electronics and optics are not complex, making the instrument easy to calibrate, reliable, portable, and robust.

Operating Principle of the LPM

- An infrared light source (wavelength of 900 nm) from a light-emitting diode (LED) is shaped into a rectangular parallel light beam using a pair of converging lenses and rectangular masks.
- The total intensity of the light beam is continuously monitored by a receiving photodiode, which produces a voltage signal proportional to the amount of received light.
- When a droplet passes through the light beam, the intensity of the received light drops, which reduces the output voltage.

- The amplitude and duration of the voltage change are proportional to the droplet's cross-sectional area and its residence time within the beam.

Advantages and disadvantages of LPM

Advantages:

- Easy to calibrate, reliable, and portable.
- Can measure with an accuracy of 3% or less using a minimum sample size of 10,000 droplets.
- Provides reliable estimates of droplet size distribution and kinetic energy.

Disadvantages:

- Limited signal processing capabilities and sensitivity of the photodiode's output depending on where the droplet intersects the beam.
- Coincidence errors (when multiple droplets pass simultaneously) and edge effects (when only part of a droplet crosses the beam) cannot be fully eliminated but can be mitigated or controlled.

Validation and correction methods

1. Validation of Droplet Size Measurements: Droplets with measured velocities that deviate significantly from the terminal velocity corresponding to their measured size may be the result of coincidence errors or edge effects. These outliers can be excluded from the dataset to improve measurement accuracy.
2. Data Correction Techniques: Solomon et al. (1991) applied a criterion where droplet velocity measurements exceeding ±2 standard deviations from the average measured velocity were used to discard droplet size data from the dataset. This method helps reduce measurement errors, though it does not eliminate them entirely.

Relevant Studies and Findings

1. Study by Kincaid et al. (1996): Measured droplet size distributions for a wide variety of sprinkler types, nozzle sizes, and operating pressures using a laser particle measurement system. Measurements were taken at radial intervals of 1 meter within the sprinkler's wetted radius.
2. Study by DeBoer and Monnens (2001): Evaluated droplet size distributions for multiple types of rotating-plate sprinklers across various nozzle sizes and operating pressures. The droplet distributions were weighted according to the volume fraction of water applied in each radial measurement zone.

Ballistic Models and Kinetic Energy

Determining the kinetic energy transferred to the soil by sprinkler droplets requires knowledge of both droplet mass (or size) and velocity. Over the past 50 years, droplet trajectory models based on classical rigid-body motion laws have been developed to analyze and predict sprinkler operating characteristics. These are commonly known as ballistic models and involve simplifying assumptions to numerically simulate droplet trajectories.

Key simplifications used in ballistic models include:

1. Droplets form at the sprinkler nozzle.

2. Droplet volume remains constant during flight.
3. Droplets are spherical and do not deform.
4. Forces acting on droplets include gravity and drag.
5. Drag force acts opposite to the direction of motion.
6. The initial velocity and trajectory angle are known inputs.

Use of Laser Instruments in Irrigation Research

Laser-based instruments used for measuring droplet size are susceptible to two major types of measurement errors: coincidence and edge effects. Coincidence errors occur when two or more droplets simultaneously pass through the laser beam and cast overlapping shadows on the photodetector. Edge effects arise when only part of a droplet passes through the laser beam along one of its edges.

To control these errors, each droplet measurement can be validated by comparing its measured velocity with the terminal velocity expected for its measured size. In natural rainfall, droplet velocity is assumed to approach terminal velocity. Comparing measured velocity to theoretical terminal velocity helps validate the dataset.

3. Conclusions

The accurate assessment of sprinkler system performance is fundamentally dependent on the precise measurement of droplet size and velocity, which are key parameters in evaluating the kinetic energy delivered to the ground surface. This energy plays a crucial role in the effectiveness of fire suppression or irrigation, as it influences water distribution, soil infiltration, and the system's overall efficiency.

Among the measurement techniques explored, laser-based instruments—such as the Laser Precipitation Monitor (LPM)—have demonstrated notable advantages, including ease of calibration, portability, and reliable data acquisition across large sample sizes. Their application in controlled environments provides a solid foundation for evaluating sprinkler behavior under realistic operational scenarios.

This study was conducted using a dedicated experimental stand, specifically designed to support high-precision measurements. The stand dimensions (Height: 2000 mm, Width: 2000 mm, Length: 3000 mm) allowed for systematic data collection across different distances and sprinkler types. The configuration included alternating sprinkler heads of varying nozzle sizes, which ensured uniform coverage and a representative spray pattern for analysis.

The setup and measurement process are illustrated in the figure below, which provides a visual reference for the experimental conditions. This configuration enabled the controlled evaluation of droplet behavior and offers a replicable model for further investigations. Overall, the results confirm that LPM-based techniques represent a reliable and efficient approach for characterizing sprinkler performance and optimizing system design.

Fig. 1. Image of mobile experimental stand

References

[1] NFPA 13 - Standard for the Installation of Sprinkler Systems, National Fire Protection Association, current edition.

[2] Prahl, Joseph M., Wendt, Bruce, "Discharge Distribution Performance for an Axisymmetric Model of a Fire Sprinkler Head," Fire Safety Journal, Vol. 14, pp. 101-111, 1988.

[3] Huang, J.C.P., "Break-up of Axisymmetric Liquid Sheets," J. Fluid Mech., Vol. 43, Part 2, pp. 305-319, 1970.

[4] Wendt, Bruce, Prahl, Joseph M., "Discharge Distribution for an Axisymmetric Model of a Fire Sprinkler Head," NBS-GCR-86-517, National Bureau of Standards, Gaithersburg, MD, 1986.

[5] Chigier, N.A., "The Physics of Atomization," ICLASS-91 Proceedings, National Institute of Standards and Technology, Gaithersburg, MD, pp. 1-15, 1991.

[6] Krishnan, G., Gakkar, R.P., Prakash, S., "Water Droplet Evaporation in Fire Plumes," ICLASS-91 Proceedings, National Institute of Standards and Technology, Gaithersburg, MD, pp. 97-104, 1991.

[7] Yao, Cheng, "Overview of Sprinkler Technology Research," 5th Conference Proceedings of the International Association of Fire Safety Scientists.

[8] E.R. Galea, "Predicting the Performance of Fire Sprinkler Systems Using Computational Fluid Dynamics," Journal of Fire Sciences, Vol. 18, No. 4, pp. 237-263, 2000.
[9] B. Dlugogorski and D. Lucas, "The Influence of Water Drop Size on the Effectiveness of Sprinkler Systems," Fire Technology, Vol. 36, pp. 1-19, 2000.
[10] R.A. Bukowski and W.J. Parker, "Characterizing the Sprinkler Water Distribution Using Experimental Methods," NIST Technical Note 1423, National Institute of Standards and Technology, 1996.
[11] M. Puchovsky, "Sprinkler System Design: Approaches to Minimizing Water Damage," Fire Protection Engineering, Vol. 13, pp. 17-24, 2002.
[12] A. Grimwood, "Fire Control with Sprinklers in Large Enclosures," Fire Safety Engineering, Vol. 26, No. 2, pp. 75-83, 2003.
[13] Christiansen, J.E., "Irrigation by Sprinkling," *California Agricultural Experiment Station Bulletin*, No. 670, University of California, Berkeley, 1942. *(Aceasta este lucrarea originală în care a fost introdus coeficientul de uniformitate Christiansen pentru irigații, dar principiul poate fi aplicat și pentru evaluarea uniformității în sistemele de sprinklere pentru incendiu.)*
[14] Kincaid, D.C., Longley, A.E., "A Water Application Uniformity Coefficient for Center Pivot Sprinkler Irrigation Systems," *Transactions of the ASAE*, Vol. 22, No. 3, pp. 610-615, 1979. *(Deși se referă la irigații, metodologia de evaluare a uniformității poate fi aplicată pentru a evalua distribuția apei în sistemele de sprinklere.)*
[15] Lougheed, G.D., "Evaluation of Sprinkler Water Distribution Uniformity for Fire Protection Systems," *Fire Technology*, Vol. 25, No. 2, pp. 129-141, 1989.

Effects of elevated CO_2 concetrations in student dormitories: An experimental study

Efectele concentrațiilor ridicate de CO_2 în căminele studențești: un studiu experimental.

Andreea-Miruna Tokar [1]

[1] University of Oradea, Faculty of Medicine and Farmacy
December 1st no.10, Oradea, Romania
E-mail: tokar.andreeamiruna@student.uoradea.ro

DOI: 10.37789/rjce.2026.17.2.11

Abstract: *The impact of sleep quality on overall health is significant thus it is necessary to maintain the standards for air quality in civilian buildings. Student accommodations often lack these standards especially in thermal comfort, lighting and air quality. This study shows improper CO2 concertation in newly built student dormitories that have an effect on both mental and physical health The study shows that CO2 concentrations are above average (≈1278 CO2 ppm) especially during nighttime correlated with thermal discomfort caused by lack of proper ventilation in the sleeping and studding area.The collaboration between the medical and engineering field is important in order to maintain proper standards for air quality that will in turn also decrease several afflictions and risk of diseases.*

Key Words: air quality; CO_2 concertation; health effects.

1. Introduction

Sleep quality plays an important role in long time mental and phisical health and academic performance as shown in the speciality literature [1,2,3]. Sleep quality is defined as continuous sleep that from which one wakes up refreshed with few nighttime awakenings and fast initiation[4]. Students, especially, need to benefit from optimal sleep due their necesity to perform increased and continous intelectual activities.

Most students live in student housing for tree to six years and can suffers aflictions such as: diminised logical thinking, higher rate of awakening during the night [5], throat discomfort, dyspnea, dry and itchy skin, dificulty falling asleep and waking up, congested nose, bad air smell [6]. According to the standard I5-2022 [7], good air quality in civilian building has a CO2 concetration of less that 400 ppm. Bad air quality according to the same standard in cosidered to have a concetration of CO2 of more that 1000 ppm. It is worth mentioning that these symtoms can be acentuated by intrinsic

The article was received on 02.06.2026, accepted on 10.06.2026 and published on 12.06.2026

factors such as: stress, lack of proper nutrition, smoking, alcohool consumption, inadequent sleep hygene. Several other external factors are also be at play such as: suboptimal lighting as shown by other studies regarding the same student accomodation [8], thermal discomfort, noise pollution.

2. Considerations regarding the level of CO2 concentration during sleep on health

The scope of the paper is to determine if CO_2 concentrations in student living accommodations are up to standard while also correlating the findings with the health effects that subpar CO_2 concentrations have on occupants.

The study took 10 days (from the 18th of March to the 28th of March) and it focused on the CP1 student accommodations from the University of Oradea that opened in October 2024. The room that was used in the research as shown in Fig.1. is 58.85 m^3 and has no mecanical venitaltion sistems in the sleeping area. A small mecanical ventilator is used for the bathroom. The sleeping area has a window for natural ventilation that features a ventilation slot. The dormitory room studied is inhabited by two people.

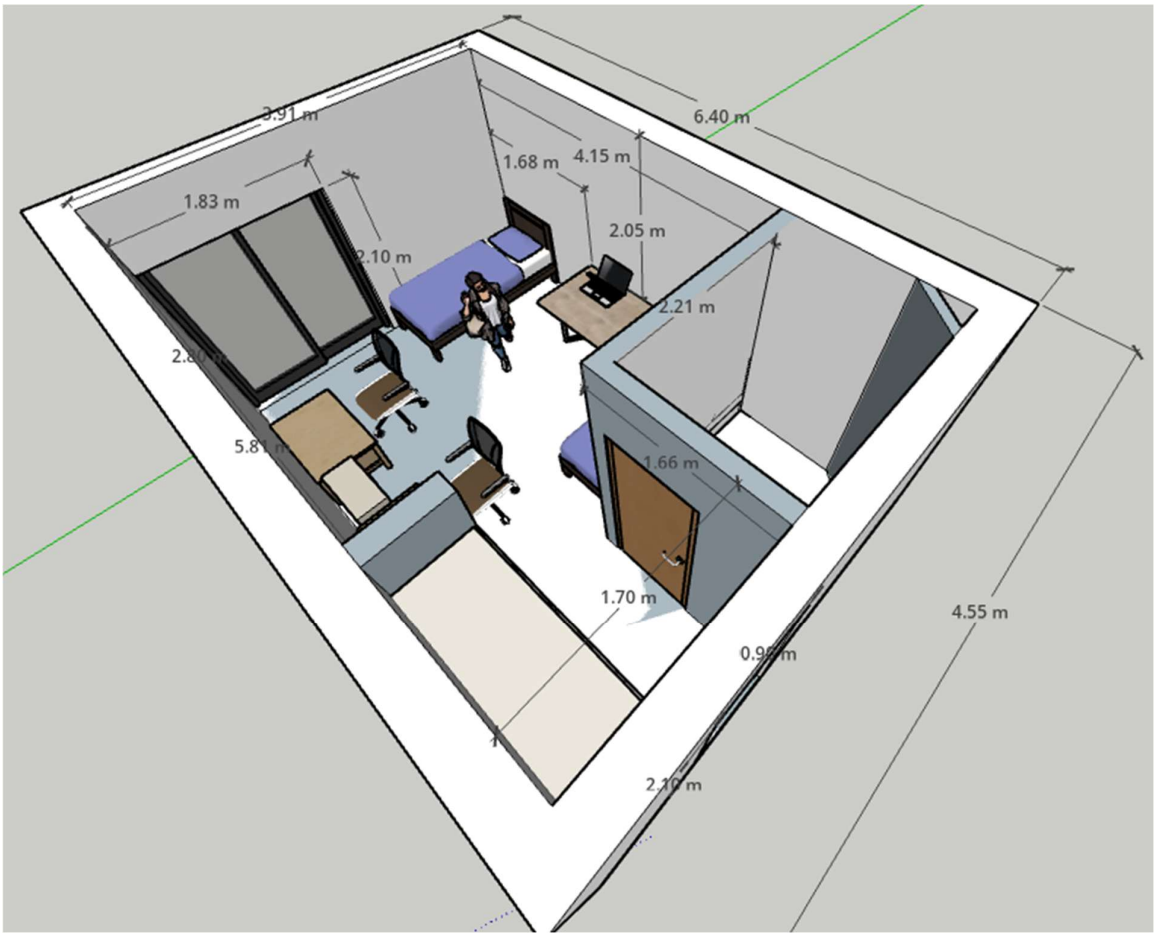

Fig.1. Floor plan

For the measurements a TESTO 480, SN 2309679, aparatus was used, that provides information about air pressure, humidity, temperature and CO_2 concetration. The paper was focused only on the latter two ones. The probe was set between the two beds at a distance from the window opening in order to prevent abrupt variontions from air currents caused by the window's opening (Fig. 2.).

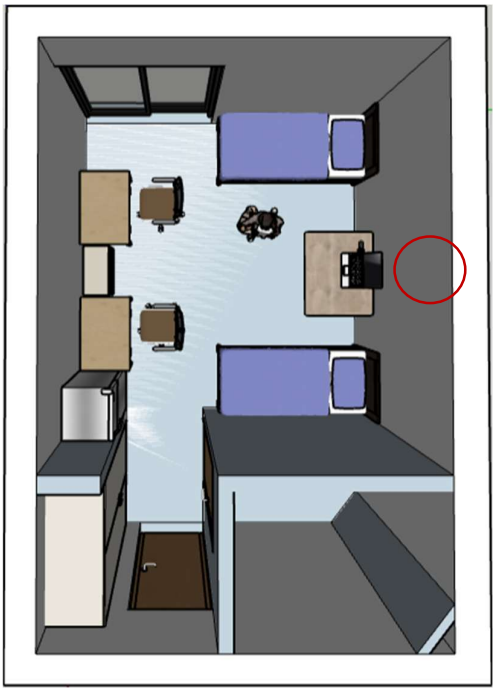

Fig.2. Probe placement

3. Results and Discutions

The data was analized for three diffrent perspectives in coreletion with temperature:

3.1. Overall assesment

Over the ten day period in which the study as conducted bowth CO_2 concetration and temprature were measured as shown in Fig.3.

Both inferior (less than 400 ppm) and superior (more than 1000 ppm) thresholds are showcased in the graph. As considered by the I5 normative a CO_2 concertation of over 1000 ppm is correlated with bad air quality.

As it can be seen in fig.3 the CO_2 concertation rarely goes below 400 ppm thus the registered air quality is between medium and low with an average of 1287 ppm which surpasses the superior threshold indicating lo air quality in the sleeping area during day time and especially during night time.

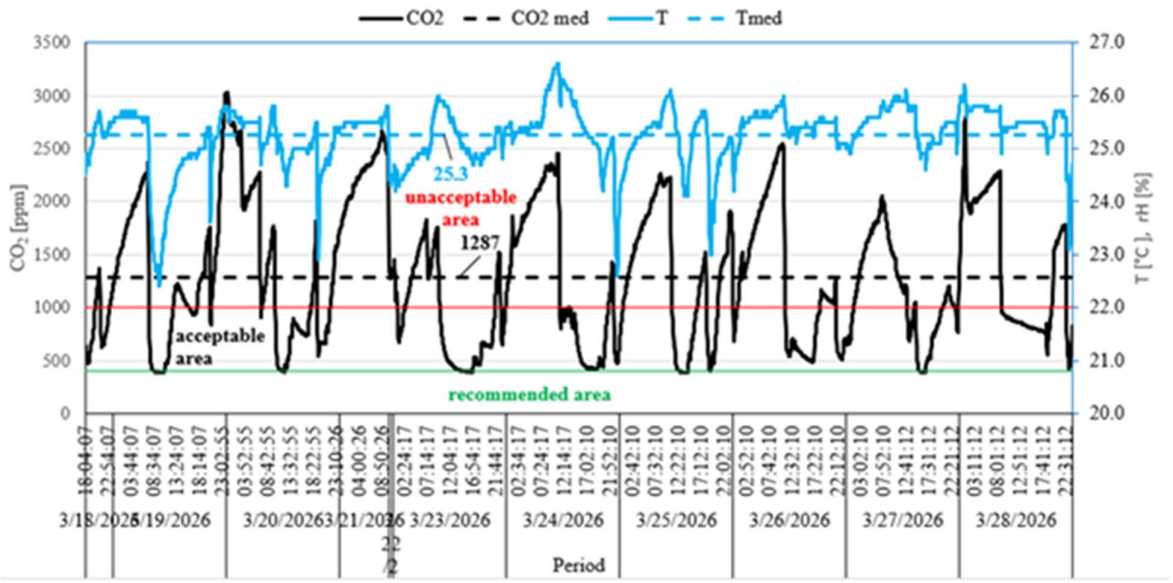

Fig.3. Measurements over a ten days period

Thermal comfort as also taken into consideration. It can be seen that CO_2 concertation is almost directly proportional with temperature that also reaches values correlated with thermal discomfort (≈25.3ºC median temp). Due to lack of mechanical ventilation thermal discomfort ill only worsen in the warmer season when temperatures can reach up to 28ºC during the day.

3.2. 24 h assesment

During a 24 hour period it can be seen that drastic CO_2 concetration increases happen both during the night and during the time students are not in the dormitories. This is caused by the lack of mechanical ventilation in the student accomodation. In addtion higher CO_2 concetrations may be registered in the cold season due to the fact that using natural ventilation, in this case, causes thermal discomfort. As shown in Fig. 4 there are drastic drops in CO_2 concentrations and temperature whenever the window is fully open for even less than 5 minutes (Segments AB and EF). While the ventilation sloth is used the CO_2 concetration curb decreases at a lower rate hile temperature still rises(Segment CD).

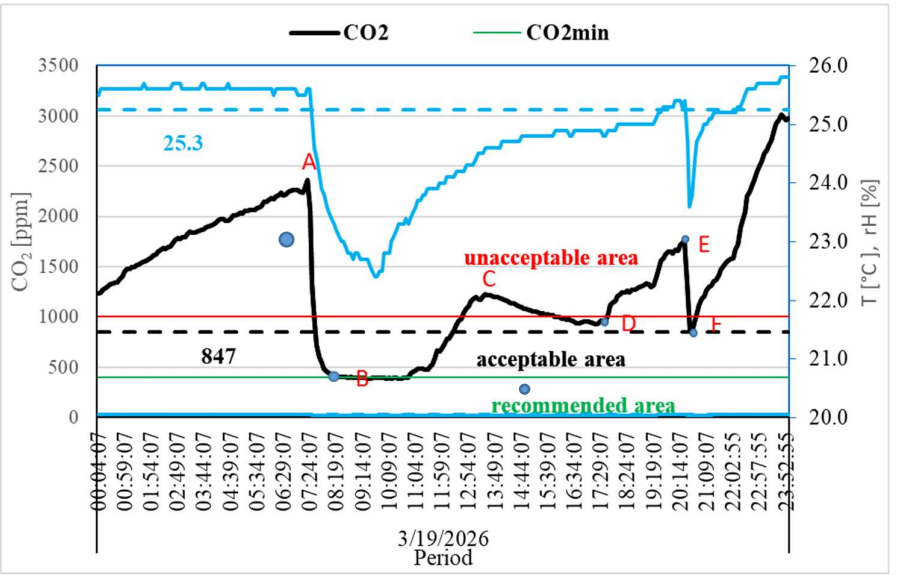

Fig.4. The 24 hours measurements

3.3. Nightime assesment (8 p.m.-8 a.m.)

Nighttime is the most affected perion during the day by the lack of mechanical ventilation as shown in Fig. 5.

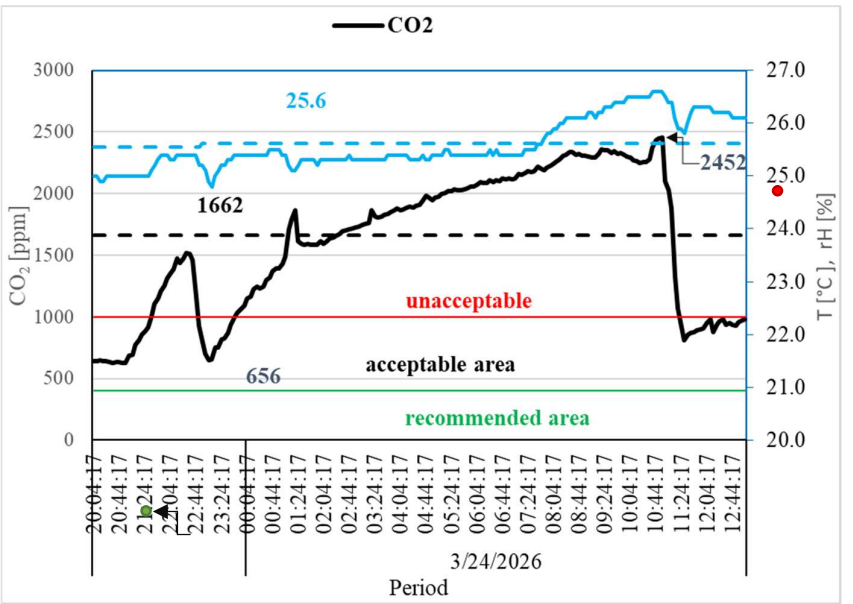

Fig.5. Night-time measurements

Both CO_2 concentration and temperature increase by morning, reaching above average values.

The theoretical CO_2 concentration is calculated using formula 1 [9]. Thus the CO_2 concertation accumulated from two people after a 12 hour sleep period in a room without mechanical or natural ventilation is 13.166 ppm.

$$C(t) = C_0 + (\frac{N \cdot \nu_b \cdot V_b \cdot C_b}{V}) \cdot t \quad (1)$$

Where:

V=58.85 m^3	room volume
N=2	number of people
ν_b=12 breaths/min [10]	breath frequency
t= 720 min	time
C_b=45000 ppm [11]	CO_2 concentration in exhaled breath
V_b=0.0005 m^3 [12]	volume per breath
C(t)=C_{teor}	theoretical room CO_2 concentration in accumulated in t minutes ppm
C_0=656 ppm	initial CO_2 concentration (at 11 p.m. as shown in Fig.5.)
C_{exp}= 2452 ppm	CO_2 concentration, determined experimentallyat 11 a.m. as shown in Fig.5.

Exchange rate ηe in %, is calculated with rel. 2.

$$\eta_e = \frac{C_{teor} - C_{exp}}{C_{teor}} \cdot 100 \quad (2)$$

Comparing the theoretical CO2 accumulation with the experimentaly measured CO2 concertation registered at 11 am after a 12 hours period without mechanical or natural ventilation the exchange rate is 0,81%.

4. Conclusions

In conclusion the authors propose stricter standards for student dormitories designs that take into consideration air quality and proper ventilation. This paper also shows the necessity of interdisciplinary collaboration between building services engineers and the medical field in order to account for the health impacts that deficient air quality has on buildings' occupants.

5. Refrences

[1] L. A. Musshafen, R. S. Tyrone, A. Abdelaziz, C. E. Sims-Gomillia, L. S. Pongetti, F. Teng, L. M. Fletcher, J. C. Reneker, „Associations between sleep and academic performance in US adolescents: a systematic review and meta-analysis", *Sleep Medicine*, vol. 83, 2021, pp. 71-82.

[2] S. Qu, M. Wang, Y. Peng, „Associations between residential environmental health and sleep quality: Potential mechanisms", *Sleep Medicine*, vol. 103, 2023, pp. 16-23.

[3] A. Agostini, S. Centofanti, „Normal Sleep in Children and Adolescence", *Child and Adolescent Psychiatric Clinics of North America*, vol. 30, no. 1, 2021, pp. 1-14.

[4] C. Kline, „Sleep Quality", în M. D. Gellman, J. R. Turner (eds.), *Encyclopedia of Behavioral Medicine*, Springer, New York, 2013.

[5] X. Zhang, T. Zhang, G. Luo, J. Sun, C. Zhao, J. Xie, J. Liu, N. Zhang, „Effects of exposure to carbon dioxide and human bioeffluents on sleep quality and physiological responses”, *Building and Environment*, vol. 238, 2023.
[6] R. Wang, W. Li, J. Gao, C. Zhao, J. Zhang, Q. Bie, M. Zhang, X. Chen, „The Influence of Bedroom CO_2 Concentration on Sleep Quality”, *Buildings*, vol. 13, 2023.
[7] MDLPA, I 5 – 2022, Normativ Normativ pentru proiectarea, executarea şi exploatarea instalaţiilor de ventilare şi climatizare, 2022.
[8] I.-D. Holecică, A.-M. Tokar, D. Tokar, „Considerations regarding the impact of artificial lighting on health”, *Revista Română de Inginerie Civilă*, 2026.
[9] Institute of Medicine (US), „Clearing the Air: Asthma and Indoor Air Exposures”, National Academies Press, Washington DC, 2000.
[10] S. Fritz, L. Chaitow, G. M. Hymel, „Review of Pertinent Anatomy and Physiology”, în *Clinical Massage in the Healthcare Setting*, Mosby, 2008, pp. 140-195.
[11] M. Li, G. Bekö, N. Zannoni, G. Pugliese, M. Carrito, N. Cera, C. Moura, P. Wargocki, P. Vasconcelos, P. Nobre, N. Wang, L. Ernle, J. Williams, „Human metabolic emissions of carbon dioxide and methane and their implications for carbon emissions”, *Science of The Total Environment*, vol. 833, 2022.
[12] J. L. Sparling, M. F. Vidal Melo, „Pulmonary Pathophysiology and Lung Mechanics in Anesthesiology”, în E. Cohen (ed.), *Cohen's Comprehensive Thoracic Anesthesia*, Elsevier, 2022, pp. 66-87.

Energy sources for district heating systems. Transition from 1st to 5th Generation

Surse de energie pentru sistemele centralizate de termoficare. Tranziția de la Generația 1, la Generația 5

Daniel Muntean[1], Adriana Tokar[1], Danut Tokar[1], Alexandru Dorca[1]

[1]Universitatea Politehnica Timișoara,
Victoriei Square, Nr.2,Timisoara, Romania
E-mail: *daniel-beniamin.muntean@upt.ro, adriana.tokar@upt.ro, danut.tokar@upt.ro*

DOI: 10.37789/rjce.2026.17.2.12

Abstract: *Given the critical global context that has been reached in terms of air pollution caused by carbon emissions and other pollutants resulting from the combustion of conventional fuels, we urgently need to reduce the impact on the environment and find solutions that slow down global warming. Energy in various forms is a need that we cannot do without, but we must resort to primary sources that are as less polluting as possible and that at the same time ensure energy demand. Renewable energy sources must be exploited to the greatest extent possible and installations/equipment optimized for the highest possible efficiency. This paper presents the main conventional and unconventional energy sources, the evolution of their use over time and proposals for optimizing thermal and electrical energy production systems.*

Key words: fossil fuels, natural gas, district heating systems, renewable energy sources, heat pumps

1. Introduction

At the global level, the International Energy Agency's (IEA) provides an energy outlook through three main scenarios designed to help policymakers, industry leaders and researchers understand the future of the entire energy system by analyzing trends in demand, supply, technology and emissions. [1].

These scenarios address energy perspectives from current policies to measures to achieve net-zero strategic plans involving the transition to renewable energy, namely:

- Current Policies Scenario (CPS) – indicates policies and regulations that are already in place;

The article was received on 08.04.2026, accepted on 08.06.2026 and published on 12.06.2026

- Stated Policies Scenario (STEPS) – indicates policies that have been officially proposed but have not yet been adopted, as well as other types of official strategic documents that indicate the direction of travel;

- Net Zero Emissions by 2050 (NZE) – indicates a path to reduce global CO_2 emissions by 2050. Romania's strategy for this scenario aims for massive decarbonization through the integration of renewable energy, increased energy efficiency, electrification and carbon capture [2].

A comparative picture of the evolution of the global average temperature for the three scenarios (CPS, STEPS and NZE) and the annual emission reductions in the NZE scenario, over a 5-year period, are presented in Fig. 1.

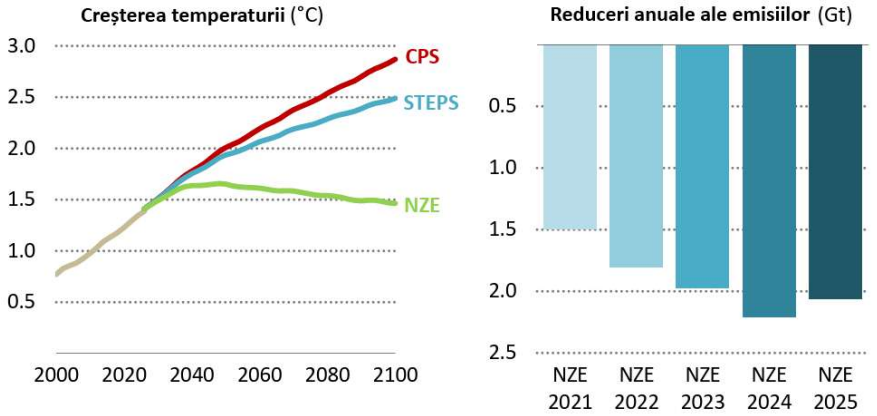

Fig. 1. Global average temperature increase and annual emission reductions from peak to 2035 in previous editions of the NZE scenario

An evolution of CO_2 emissions, by fuel type, is presented comparatively, in the world, in the EU and in Romania, in Fig. 2 [3].

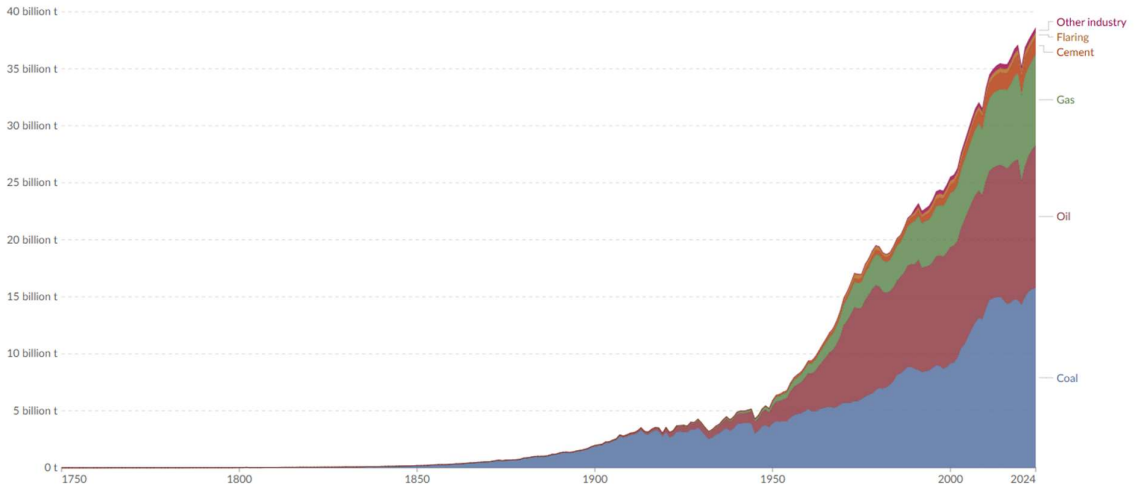

Fig. 2. CO_2 emissions by fuel or industry type, World

Generation I transported steam at temperatures above 200°C using concrete

pipes. As a result, it was not particularly efficient and was replaced due to the risk of pipe bursting. Generation II used concrete pipes to transport pressurized water at temperatures above 100°C and is known as high-temperature district heating. Generation III uses pre-insulated pipes buried directly in the ground and operates with water at supply temperatures between 65 and 95°C. Generation IV district heating systems are now being developed and referred to as low-temperature district heating systems (50–60°C). When end-user temperatures are increased with heat pumps, ultra-low supply temperatures (35–45°C) are also used [4]. Generation V district heating is an extension of generation IV, a new concept based on a decentralized network that allows direct energy flows between and within buildings. Its key features are: low exergy network using low-temperature heat sources; closed thermal energy loops that ensure the exchange of heat and cold between groups of buildings; integration and synergy between thermal and electrical networks; 100% renewable energy target [5]. The evolution of district heating generations over time is presented in Fig. 3 [6].

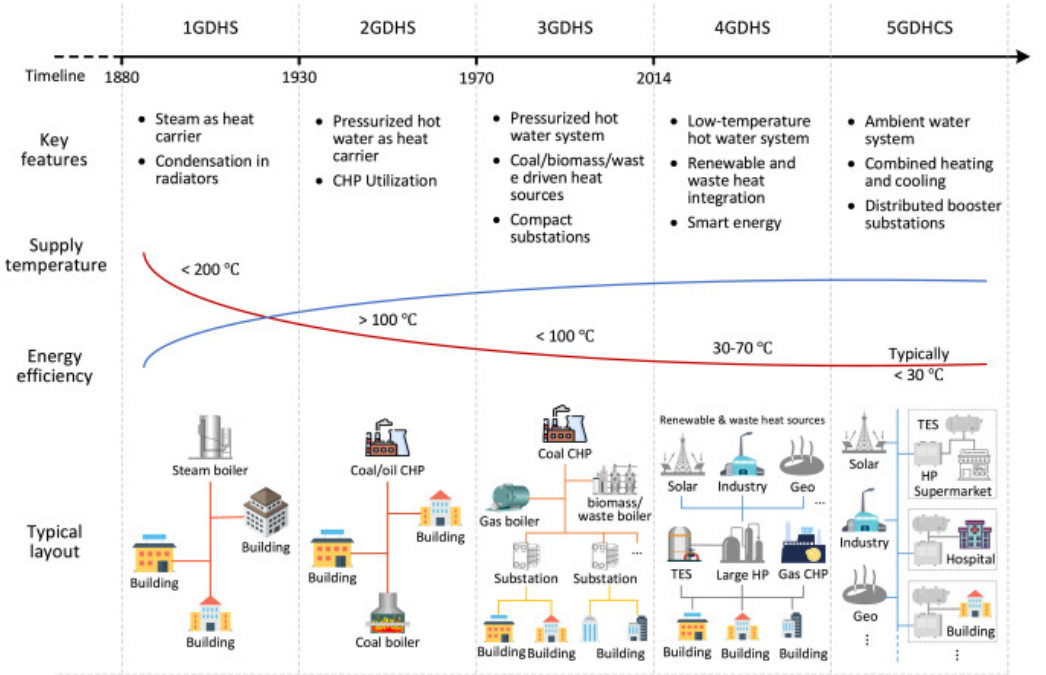

Fig. 3. The Evolution of District Heating Systems

2. Current status. Technologies and systems used

2.1. Fossil fuels

Until recently, coal was the main source of thermal energy, being responsible for high emissions of CO_2, but also other pollutants (SO_2, NOX, PM2.5 and PM10 particles, heavy metals, CO, etc.). Even though efforts are being made to optimize the efficient use of coal, the trend is towards total replacement.

For the period 2020-2030, Fig. 4 [7] shows coal consumption in the world. It can be seen that at the EU level there is a slight decrease starting from 2025, which is expected to continue until 2030. In the USA and Asian countries, a slight increase is recorded until 2030. However, the stabilization of energy consumption produced with coal stabilizes, by 2030, in a narrow band, except for China, Asia and India.

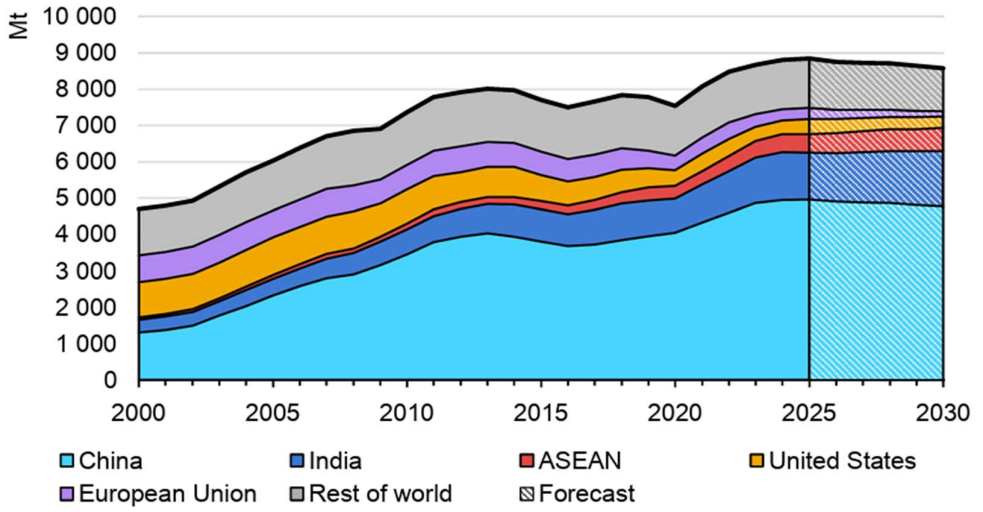

Fig. 4. Global coal consumption

At the Romanian level, although the country is engaged in a rather slow energy transition, coal has remained a safe source for high energy consumption. Romania's coal reserve is sufficient for the next decades, compared to current consumption [8].
With all the advantages that coal offers, its major disadvantage is that it is the least environmentally friendly conventional energy source. Through the emissions of CO_2, SO_2 and NO_2 as a result of coal combustion, it is estimated that this fuel has contributed massively to climate change and implicitly to global warming. In Romania, currently, considerable greenhouse gas emissions, in a percentage of about 70%, are recorded in the production of thermal and electrical energy, which can be seen in Fig. 5 [9].

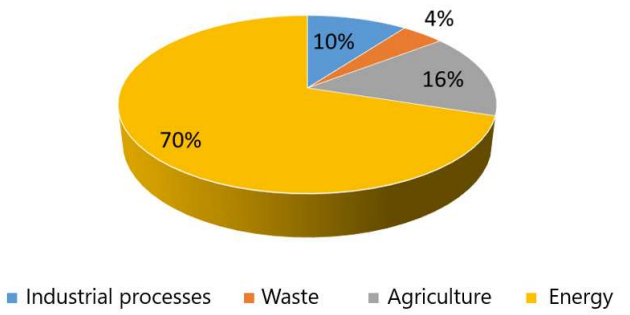

Fig. 5. Greenhouse gas emissions in different sectors

2.2. Natural gas

The use of natural gas mixed with coal (co-firing or alternative use) in district heating systems has emerged as an energy transition strategy imposed by the need to reduce polluting emissions, but also to maintain the security of thermal energy supply. Some district heating systems have resorted to partially replacing coal with natural gas in order to reduce pollution, and others use gas, either to support coal ignition or to take over peak load during winter. In either variant, coal is the basis, but the addition of gas offers greater flexibility in operation and a decrease in polluting emissions.

An evolution of CO2 emissions responsible for natural gas consumption, in the world, is presented in Fig. 6 [3].

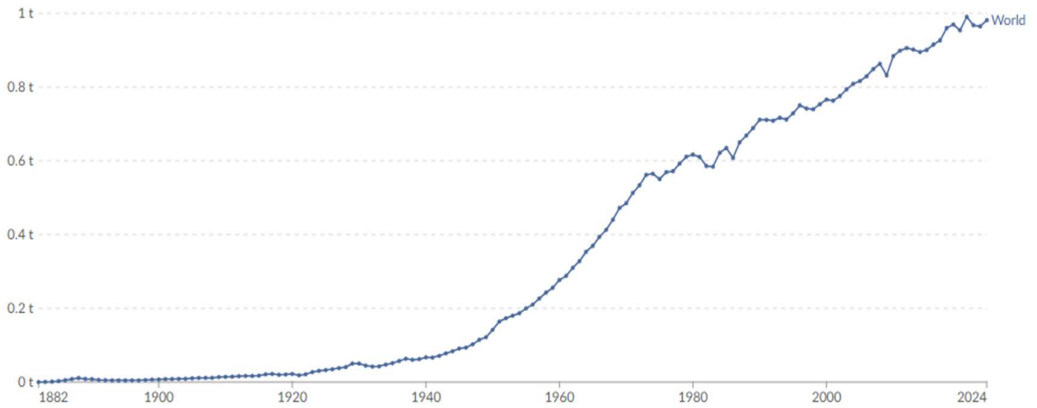

Fig. 6. Evolution of CO_2 emissions

În acest context al tranziției energetice prin startegia energetică pe termen lung, României a stabilit trei scenarii prin care a fixat ipoteze privind utilizarea cărbunelui și GN în ceea ce privește producerea de energie electrică și căldură [10].

Comparativ cu 1990, în 2030 se preconizează o reducere d 85% a emisiilor de gaze cu efect de seră pentru toate cele trei scenario Fig.7 [10].

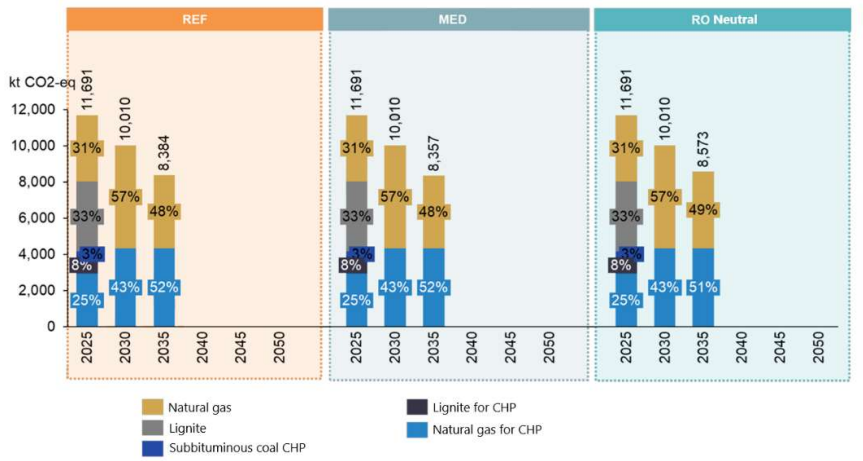

Fig. 7. Emissions evolution in the 3 scenarios: REF, Medium and RO Neutral

2.3. Renewable energy sources

The use of solar energy in district heating systems represents a sustainable investment and a necessity for the transition to RES, both at the EU level and at the Romanian level, considering the aspects presented above regarding the abandonment of coal and NG. Solar energy is the key factor in the transition of district heating systems from the 3rd generation to the 4th generation, a source that also plays a significant role in the transition to the 5th generation.

Figure 2 shows that direct solar energy is approximately 2850 times greater than the total energy we currently need on a global scale, therefore we only need 0.035% of solar energy to meet all the world's energy demand [11].

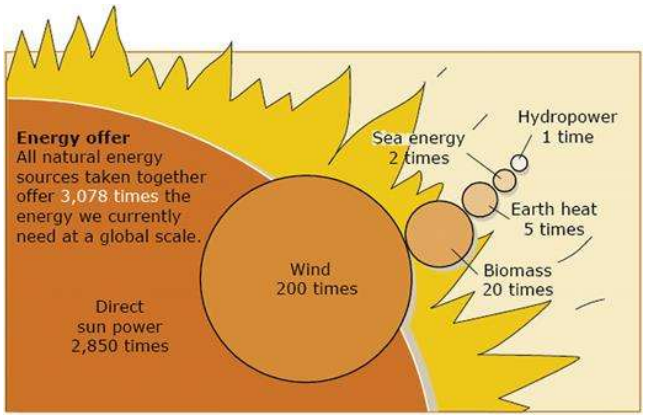

Fig. 8. Intensitatea diferitelor tehnologii de energie alternativă [12]

Fig. 9 shows the evolution of the installed capacity for producing energy from solar sources, in the world and more specifically in different regions.

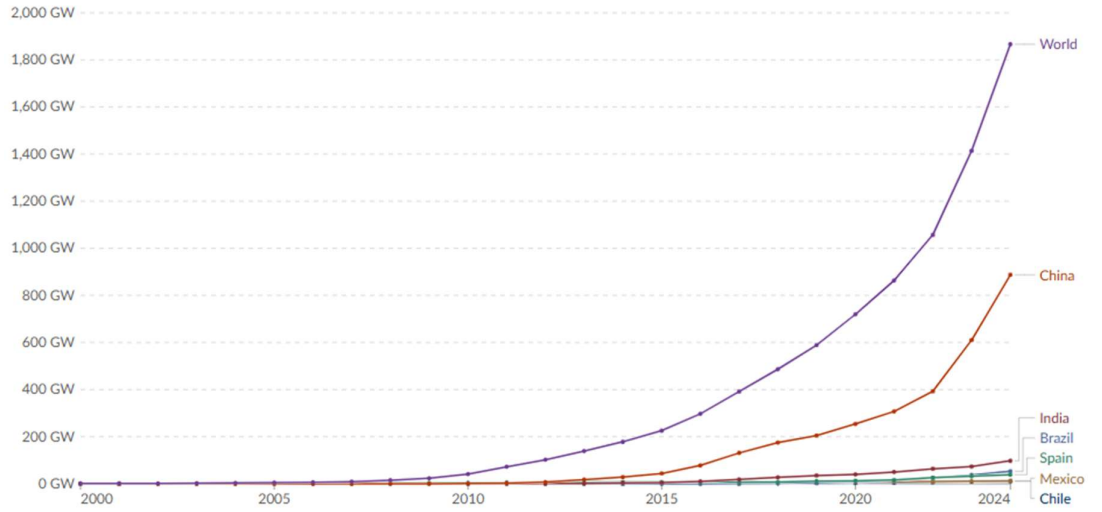

Fig. 9. Installed solar energy capacity [3]

Fig. 10. presents share of cumulative power capacity by technology, between 2010 – 2017 [12].

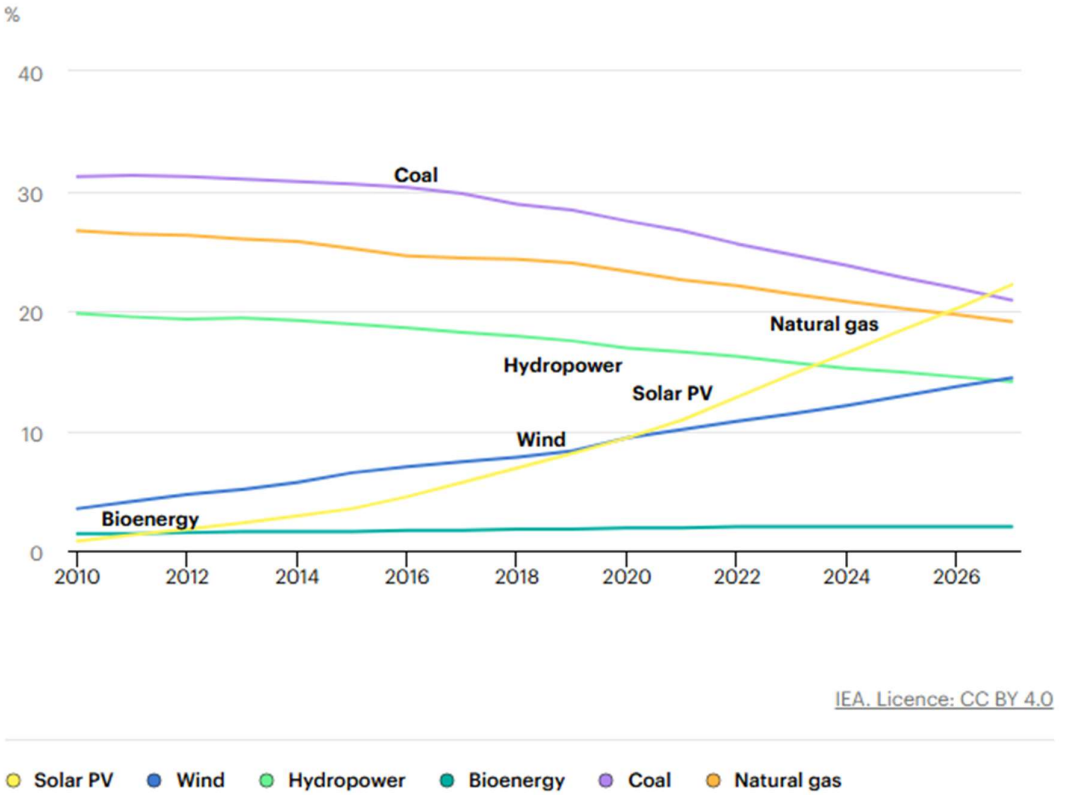

Fig. 10. Share of cumulative power capacity by technology, 2010-2027

Fig. 11 presents annual solar PV installed capacity 2000-2004 [13].

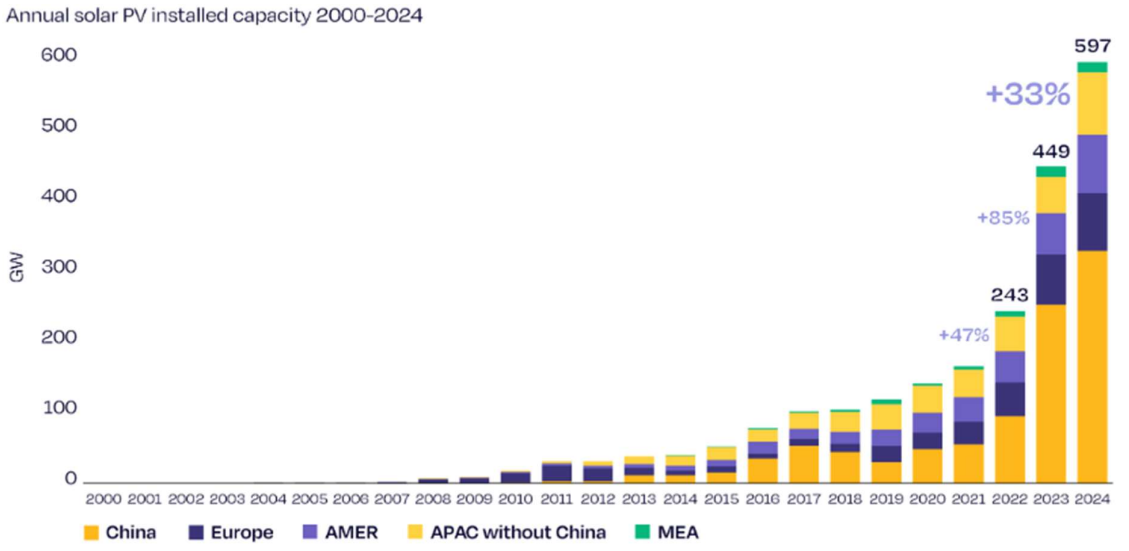

Fig. 11. Annual solar PV installed capacity 2000-2004

Although photovoltaic panels are usually used for direct electricity generation, they can be integrated into district heating systems through heat pumps.
Photovoltaic panel technology has evolved greatly in terms of materials used (from silicon – classic panels to perovskite – bifacial panels).

The main advantages and disadvantages of the main types of photovoltaic cells are presented in Table 1 [14].

Table 1

Advantages and disadvantages of the main types of photovoltaic cells [14]

Panel Type	Efficiency	Advantages	Disadvantages	Research Results
Polycrystalline	12–15%	Low price	Sensitive to high temperatures; short lifespan; low efficiency	Solar cell efficiency decreases significantly as temperature increases.
Monocrystalline	15–25%	High efficiency; suitable for commercial use; long lifespan	Expensive	Monocrystalline solar cells offer a very high output efficiency, while being among the most expensive solar cells compared to others.
Amorphous Silicon (Thin Film)	12–15%	Reduced costs; flexible; easy to manufacture	Short lifespan	Thin-film photovoltaic panels offer a short lifespan, but provide good constructability, being very flexible and lightweight.

The heat pump consists of four main components: a compressor, a condenser, an evaporator and an expansion device.

The refrigerant enters the compressor as a saturated vapor and is compressed to the condenser pressure, causing its temperature to rise above ambient. Then, the superheated refrigerant vapor enters the condenser and releases heat to the environment at constant pressure.
The liquid refrigerant is throttled by the expansion device, resulting in a temperature drop below the indoor air temperature.

The refrigerant enters the evaporator, absorbs heat from the conditioned space and evaporates completely. It then returns to the compressor as a saturated vapor, completing the cycle [15].

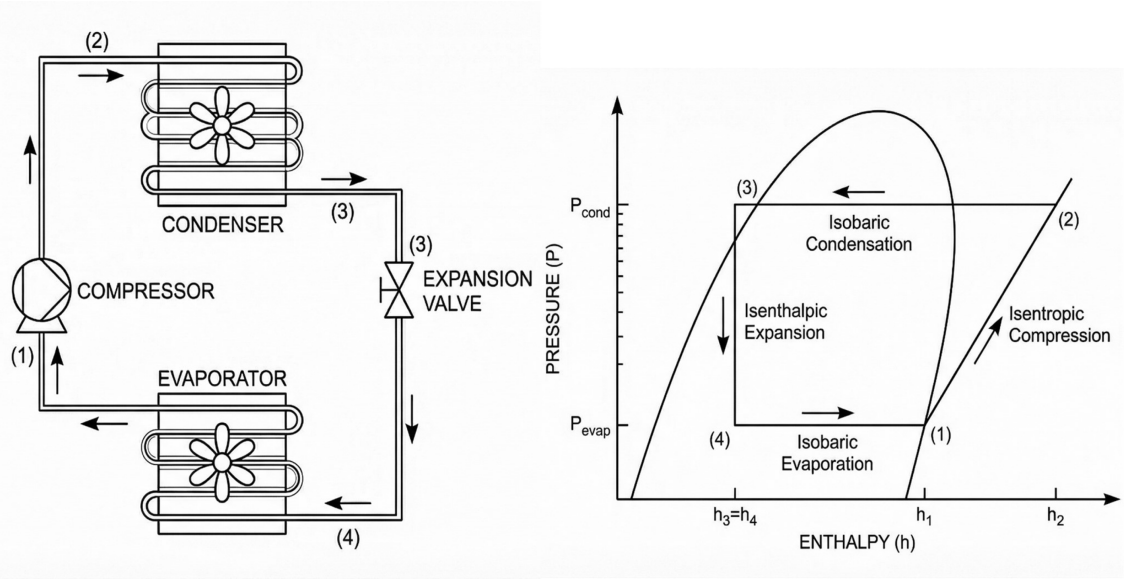

Fig. 12. The operating principle of the heat pump [15]

Table 2 summarises the progression of refrigerant generations. Refrigerant-based strategies are no longer viewed as isolated efficiency enhancements but as enabling constraints that define the feasible design space for optimized heat pump systems.

Table 2

Evolution of refrigerant generations

Generation	Type	Refrigerant	ODP	GWP	Safety	Amendment/Protocol
1st Generation (1830–1930)	Natural refrigerants	Ammonia (NH_3), CO_2, SO_2, Air	0	1	NH_3, B2L: higher toxicity & mildly flammable. CO_2, A1: low toxicity & non-flammable. SO_2, B1: higher toxicity & non-flammable	Pre-Montreal (before regulation)
2nd Generation (1930–1990)	CFCs	R-11, R-12	1.0	4750–10,900	A1: low toxicity & non-flammable	Montreal Protocol (1987)—phase-out of CFCs
3rd Generation (1990–2010)	HCFCs	R-22, R-123	0.01–0.1	1500–4800	A1: low toxicity & non-flammable	Montreal Protocol (1987)—phase-out (Copenhagen & Beijing Amendments)
4th Generation (2000–present)	HFCs	R-134a, R-410A, R-407C	0	1300–4000	A1 (most): low toxicity & non-flammable. A2L (some blends): low toxicity & mildly flammable	Kyoto Protocol (1997)—GWP reduction
5th Generation (2010–future)	HFOs & natural refrigerants	R-1234yf, R-1234ze, CO_2 (R-744), Propane (R290)	0	<1–10	A2L–A3: low-to-moderate toxicity & mildly to highly flammable	Kigali Amendment (2016)—HFC phase-down & HFO adoption

2.3.1 Optimizing the heat pump refrigeration cycle

Ejector-Assisted Vapour Compression Cycle – Fig. 13 [15].

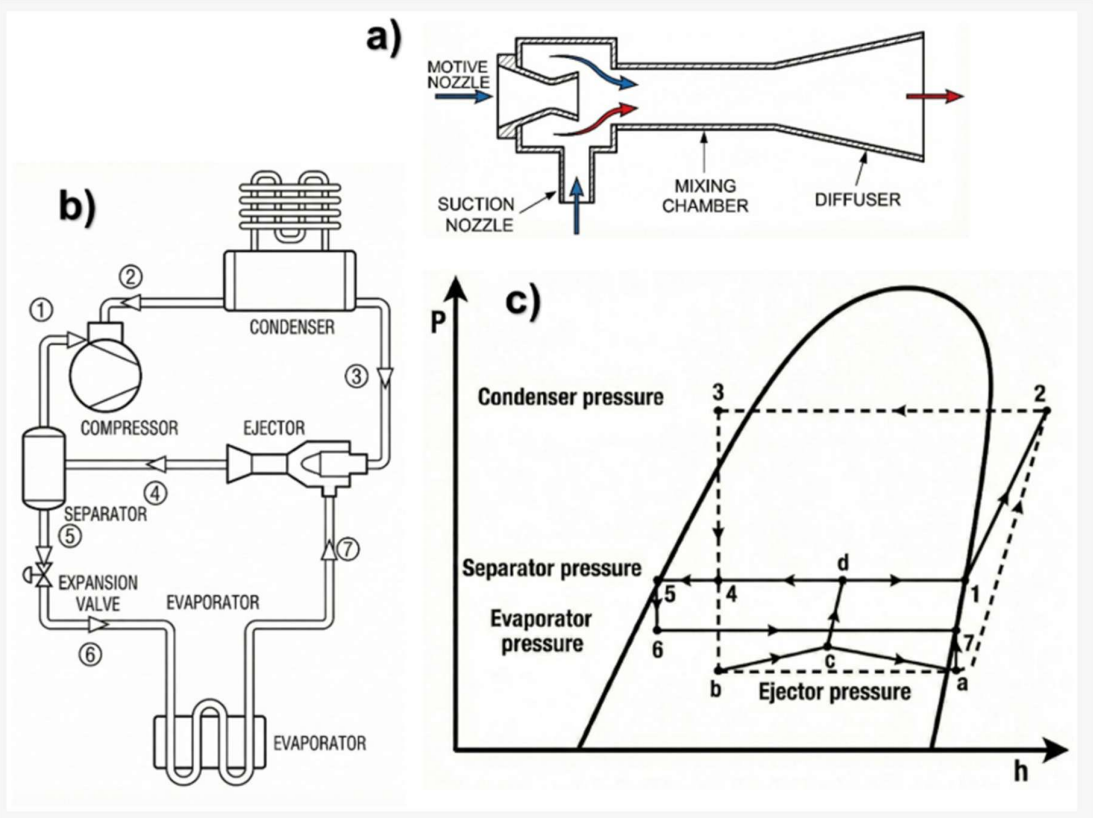

Fig. 13. Ejector-Assisted Vapour Compression Cycle [15]
(a) Schematic diagram of the basic ejector design, (b) VCC with ejector cycle, and (c) P-H diagram, where (3-b-a-2) is the basic VCC cycle

Internal Heat Exchanger Subcooling – Fig. 14 [15].

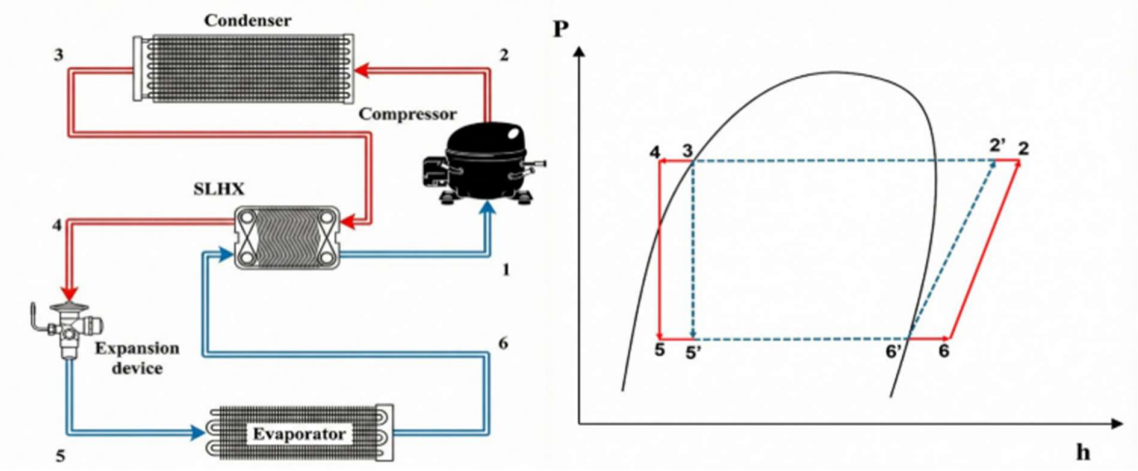

Fig. 14. Scheme of the modelled IHX & P-H diagram [15]

Thermoelectric Cooler (TEC) Integration – Fig. 15 [15].

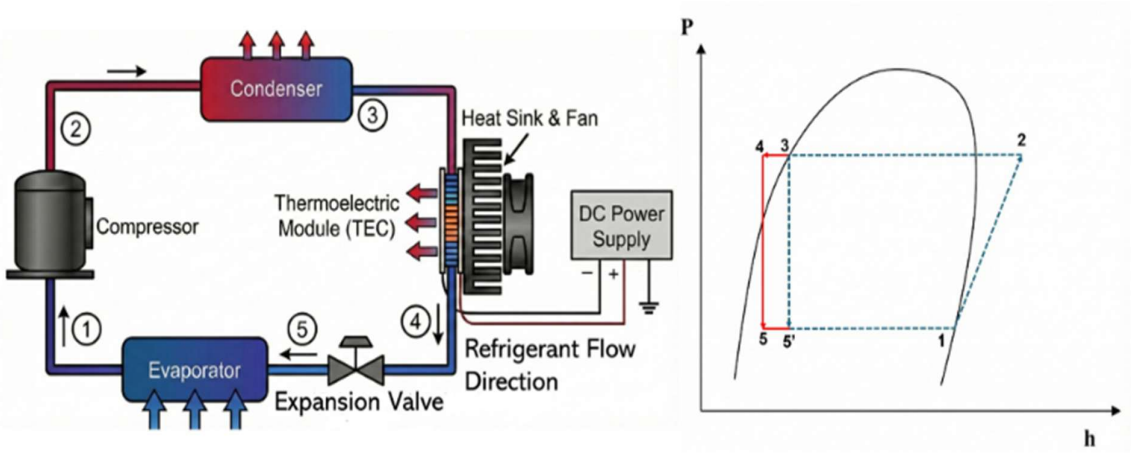

Fig. 15. Thermoelectric Cooler (TEC) Integration [15]

3. Conclusions

Considering the global energy needs, the solution is not necessarily to completely exclude certain fuels considered more polluting, but to use them together with renewable energy sources depending on need/weather conditions/efficiency. Renewable energy sources still have many limitations for which solutions must be found to optimize the installation systems so that energy can be provided constantly and at optimal parameters.

References

[1] Cozzi, L. Gould, T. Scenarios in the World Energy Outlook 2025. International Energy Agency: Paris, France, 2025.
[2] Gurza, V.G.; Cozmanciuc, R. Guide on the implementation of measures to increase energy performance applicable to new buildings, in the design, execution and acceptance stages, operation and monitoring of behavior over time to meet nZEB requirements, Indicative RTC 4 –2022. Ministry of Development and Public Works: Bucharest, Romania, 2022, pp.10-157.
[3] Our World in Data, https://ourworldindata.org/co2-and-greenhouse-gas-emissions, Met Office Hadley Centre - HadCRUT5 (2026), accessed 04.04.2026.
[4] Lund R, Mohammadi S. Choice of insulation standard for pipe networks in 4th generation district heating systems. Applied Thermal Engineering 2016;98:256–264.
[5] Zvingilaite E, Ommen T, Elmegaard B, Franck ML. Low temperature DH consumer unit with micro heat pump for DHW preparation. In Proceedings of the 13th International Symposium on District Heating and Cooling, Copenhagen, Denmark, 3-4 September, 2012.
[6] Shuai Yao, Jianzhong Wu, Meysam Qadrdan, A state-of-the-art analysis and perspectives on the 4th/5th generation district heating and cooling systems, Renewable and Sustainable Energy Reviews, Volume 202, September 2024, 114729.
[7] International energy agency, Coal 2025 Analysis and forecast to 2030, Typeset in France by IEA - December 2025.
[8] Ilie Pintea, 09 Februarie 2025, Studiu/ Valea Jiului: Suficient cărbune pentru minerit în următorii zeci de ani, https://www.romania-actualitati.ro/stiri/economie/studiu-valea-jiului-suficient- carbune-

pentru-minerit-in-urmatorii-zeci-de-ani-id205851.html, accessed 04.04.2026.
[9] Mihaela NEAGU, Ion ONUTU, Estimarea şi reducerea emisiilor de dioxid de carbon rezultate la arderea cărbunilor în termocentralele românești, Universitatea Petrol-Gaze din Ploieşti, EMERG 7–2018.
[10] Strategia pe termen lung a României pentru reducerea emisiilor de gaze cu efect de seră. Implementarea Planului Național Integrat pentru Energie și Schimbări Climatice și elaborarea Strategiei pe Termen Lung a României, REFORM/SC2021/043, 18 aprilie 2023.
[11] Muhyiddine Jradi , Saffa Riffat, Medium temperature concentrators for solar thermal applications, International Journal of Low-Carbon Technologies, Volume 9, Issue 3, September 2014.
[12] IEA (2022), Share of cumulative power capacity by technology, 2010-2027, IEA, Paris https://www.iea.org/data-and-statistics/charts/share-of-cumulative-power-capacity-by-technology-2010-2027, accessed 04.04.2026.
[13] New report: World installed 600 GW of solar in 2024, could be installing 1 TW per year by 2030, 6 May 2025, MUNICH, Germany https://www.solarpowereurope.org/press-releases/new-report-world-installed-600-gw-of-solar-in-2024-could-be-installing-1-tw-per-year-by-2030, accessed 04.04.2026.
[14] Lujean Ahmad, Navid Khordehgah, Jurgita Malinauskaite, Hussam Jouhara, Recent advances and applications of solar photovoltaics and thermal technologies, Energy Volume 207, 15 September 2020, 118254.
[15] Hussein A. Al Khiro and Rabah Boukhanouf, Recent Advancements in Design and Energy Performance of Vapour Compression Systems for Air Conditioning in Buildings: A Review, Energies 2026, 19(5), 1166.

Eco-friendly, effective, and inexpensive making technique of an alternative insulation building material based on wood foam

Tehnică ecologică, eficace și ieftină de producere a unui material de construcție izolator alternativ pe bază de spumă de lemn

Lucian Paunescu[1], Enikö Volceanov[2], Bogdan Valentin Paunescu[3]

[1]National University of Science and Technology "Politehnica", Faculty of Applied Chemistry and Material Science-Research Center for Environmental Protection and Eco-Friendly Technologies
1 Gh. Polizu street, sector 1, Bucharest 011061, Romania
E-mail: lucianpaunescu16@gmail.com

[2]National University of Science and Technology "Politehnica", Faculty of Engineering in Foreign Language
313 Independence Splai, sector 6, Bucharest 060541, Romania
E-mail: evolceanov@yahoo.com

[3]Consitrans SA
56 Polona street, sector 1, Bucharest 010504, Romania
E-mail: pnscbogdan@yahoo.com

DOI: 10.37789/rjce.2026.17.2.13

Abstract. *An alternative heat-insulating building material based on wood foam was tested. The adopted wood type was oak wood unused until now, according to data from the literature. The work objective was replacing plastics, commonly used in manufacturing insulating materials. The mixture included ground wood waste, an adequate surfactant (sodium dodecyl sulfate), and distilled water. The obtained wet suspension was expanded by stirring and dried at 80 °C. The physical-thermal properties were remarkably performant, while compressive strength reached only low values, but acceptable for the desired purpose. Results were similar to those reported in the literature regarding other wood foam types.*

Key words: *wood foam, oak wood, surfactant, low density, heat conductivity.*

Rezumat. *A fost testat un material de construcție alternativ termoizolant pe bază de spumă de lemn. Tipul de lemn adoptat a fost lemnul de stejar, neutilizat până în prezent, conform datelor din literatura de specialitate. Obiectivul lucrării a fost înlocuirea materialelor plastice, utilizate în mod obișnuit la fabricarea materialelor izolatoare. Amestecul a inclus deșeu de lemn măcinat, un surfactant adecvat (dodecilsulfat de sodiu) și apă distilată. Suspensia umedă obținută a fost expandată prin agitare și uscată la 80 °C. Proprietățile fizico-termice au fost remarcabil de performante, în timp ce rezistența la compresiune a atins doar valori scăzute, dar acceptabile pentru scopul dorit. Rezultatele*

The article was received on 17.06.2025, accepted on 27.05.2026 and published on 12.06.2026

au fost similare cu cele raportate în literatura de specialitate pentru alte tipuri de spumă de lemn.

Cuvinte cheie: spumă de lemn, lemn de stejar, surfactant, densitate mică, conductivitate termică.

1. Introduction

In the last decades of the previous century, the global oil crisis exhibited intensely [1], implying the need to develop and apply some plans for the conservation of energy sources at the level of the entire planet. By default, the effectiveness of thermal insulation materials of buildings has become an important objective of researchers and builders and this concern is still relevant at the beginning of the 21st century.

Currently, the main materials applied in the thermal insulation process of buildings are still plastic materials: polyurethane foam, expanded polystyrene, or glass wool. Although very effective practically, these material types can affect human health (through the possible inhalation of fine fibers) and, on the other hand, they are difficult to recycle at the end of the normal life cycle [2].

Substituting plastics with eco-friendly materials, without affecting the quality of polymer-based heat insulators by adding biomaterials or natural raw materials are interesting versions [2]. As an example, sintered polyurethane with biomaterials-based polyols [3] and polyurethane foams with polyols derived lignin [4] were produced with similar characteristics by comparing with traditional polyurethane.

The introduction of a gaseous phase in polymeric liquids or molten plastics during the synthesis process (similar to the production of polyurethane foam and, respectively, polystyrene or polyolefin) is known as the method of obtaining polymeric foams. The manufacture of cellulose fiber foams can be achieved by drying method of aqueous foam [5]. Blowing air into aqueous dispersion fibers in the presence of surfactant facilitates the formation of wet foams, that are then dried in the oven [6, 7].

In terms of quality, the production of a thermal insulator requires the adequate distribution of its structure to avoid heat circulation. Practically, insulating materials can be made from different types of cellulosic masses containing microfibrillated cellulose [8], cellulose nanocrystals [9], cellulose nanofibres [10], bacterial cellulose [11], and regenerated cellulose [12]. Cellulose-based materials made by lyophilization, supercritical drying or spray drying facilitate obtaining very low thermal conductivity values (0.013-0.075 $W \cdot m^{-1} \cdot K^{-1}$) similar to those of polyurethane foams and silica aerogels [13].

An interesting method of manufacturing wood foam using a residual pine wood (originally from North America) was applied by [2]. Polyvinyl alcohol was used as a binder. Also, sodium dodecyl sulfate, sodium bicarbonate as surfactants, and deionized water were introduced into the mixture. After drying in the oven at 70 °C, excellent values of density (0.12-0.14 $g \cdot cm^{-3}$) and heat conductivity (0.042 $W \cdot m^{-1} \cdot K^{-1}$) were obtained.

Some thermal insulation materials are made of wood fiber and are already applied in construction, but their main disadvantage is the low dimensional stability. Also, the insulation degree achieved with wood fiber is lower (heat conductivity within the limits of 0.038-0.043 $W \cdot m^{-1} \cdot K^{-1}$) by comparison with the level obtained by petrochemical products [14].

Specialists from the German Fraunhofer Institute are currently performing research to create wood foam with excellent heat-insulating properties. According to [15], finely ground beech wood was expanded with suitable surfactants, then the suspension was dried and hardened into an isolated room free from moisture. The foamed wooden product had density values between 0.04-0.28 $g \cdot cm^{-3}$ and can be processed in the form of boards or elastic foam.

Wood-furanic foam was made using a fine wood powder [16]. The preparing method of wood foam was chemical foaming, the expanding agent being diethyl ether. Low values of density and thermal conductivity due to the porous structure with closed cells and variable sizes were the main characteristics of this wood foam.

The authors' team of this work previously gained experience on wood foam production domain by removing the lignin from the wood (oak) composition [17]. The adopted method was taken over from the pulp and paper making technique by removing the lignin for other technological purposes. The wood chemical treatment with an aqueous solution including NaOH, $Ca(OH)_2$, and distilled water was adopted. Low values of density (0.024 $g \cdot cm^{-3}$) and heat conductivity (0,031 $W \cdot m^{-1} \cdot K^{-1}$) ensuring excellent thermal insulating properties, despite the relatively low value (900 kPa) of compressive strength, were features of wood foam.

The current paper presented below constitutes a contribution of the Romanian authors to the preparation of wood foam with excellent heat-insulating properties. The technique currently developed by the Fraunhofer Institute, superior in quality terms to the technique based on removing the lignin (previously experienced by the authors' team), was adopted by testing a type of wood unused until now through the new technique researched by the German institute (oak wood).

2. Methods and materials

The wood chosen for this experiment (oak wood) was recycled in the form of sawdust from a Romanian wood-working workshop. The wooden waste was ground under pre-wetting conditions in a little laboratory knife-grinding equipment. Over the ground wood (grain size in the range of 100-500 μm selected after sieving) a suitable surfactant was introduced in very low ratios in order to decrease the surface tension of the wet suspension and to facilitate forming the foam. Among the known surfactants, sodium dodecyl sulfate (known as SDS) with high purity of over 99 % was chosen.

The expansion of suspension was performed in an electric homogenization device by stirring at 750 rpm for no more than 10 min, until increasing the foam volume was no longer observed. After finishing the foaming process, the wet foam

was loaded into parallelepipedal stainless metal moulds and subjected to drying and hardening in an electric oven at 80 °C for 10 hours.

The materials used in this experiment were oak wood waste as the wooden material, sodium dodecyl sulfate as a surfactant, and distilled water for the wet suspension generation.

The most recent worldwide tests for the manufacture of high-performance wood foam did not include oak wood. As mentioned above, this wood type was tried by the paper's authors using the technique of removing lignin (usually applied in the pulp and paper industry) to obtain a wood foam with weaker thermal insulation properties. Now, oak wood waste was tested for the first time through the more effective method of chemical foaming currently being researched. The wood, recycled in the form of sawdust, was ground to sizes below 500 μm.

It has been found that an essential method for the generation of wood foam is reducing the solvent surface tension, that can be achieved by using surfactants. They facilitate the foam generation and enter into the composition of its membranes, giving them viscosity and surface elasticity properties [18]. The surfactant type adopted in this experiment was sodium dodecyl sulfate (SDS) with the purity over 99 % and having the following chemical formula $C_{12}H_{25}NaO_4S$. Available on the market in crystalline or powder state [19], the powder state was chosen by the authors.

The composition of the material mix for producing the wet suspension was adopted in four experimental versions, detailed in Table 1. According to the data in this table, the surfactant amount had variable values in the range of 16-28 mg, while the wet suspension was maintained at the constant value of 200 g.

Table 1

Wet suspension composition

Composition	Sample 1	Sample 2	Sample 3	Sample 4
Oak wood waste (g)	38	38	38	38
Surfactant SDS (mg)	16	20	24	28
Distilled water (g)	162	162	162	162
Wet suspension (g)	200	200	200	200

Methods for investigating the sample features are indicated below. Archimedes' principle was used to measure the apparent density of wood foam samples. Using ASTM C642-97 standard, the apparent porosity was determined by dividing the difference between wet and dry weight by the difference between wet weight and suspended weight of the sample. Heat conductivity was measured at room temperature using the HFM448 Lambda heat-flow-meter (SR EN 1946-3:2004). Measuring the compressive strength was performed using a universal testing machine. The samples were comprissed at 1.4 $mm \cdot min^{-1}$ (ASTM D695) and the compressive resistance was determined at 10 % compression (ASTM D1621-16). The microstructural appearance of foams could be investigated with the Biological Microscope MT5000 model, 1000 x magnification. Water uptake was determined by maintaining wood foam samples in humidity chamber at 85 % humidity for 30 days according to ASTM C272/C272M-18.

3. Results and discussion

After drying and hardening the wet suspensions at 80 ℃ for 10 hours, characteristics of wood foam samples, shown in Fig. 1, were investigated using the methods noted above. Results of these investigations regarding to physical, thermal, mechanical, water-absorbing features, and microstructural peculiarities are exposed further in Table 2.

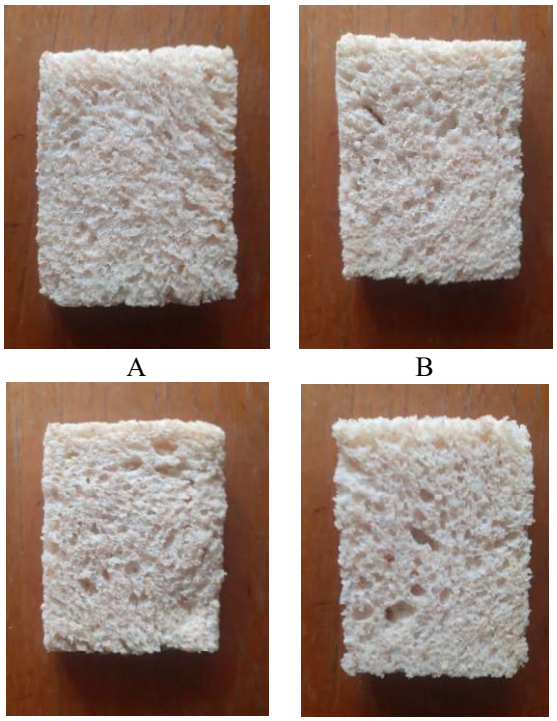

Fig. 1. Appearance of wood foam samples
A – sample 1; B – sample 2; C – sample 3; D – sample 4.

Table 2

Feature and peculiarities of wood foam samples

Feature	Sample 1	Sample 2	Sample 3	Sample 4
Apparent density ($g \cdot cm^{-3}$)	0.11	0.08	0.06	0.05
Apparent porosity (%)	88.9	89.6	90.7	91.3
Heat conductivity ($W \cdot m^{-1} \cdot K^{-1}$)	0.051	0.042	0.038	0.033
Compressive strength (kPa)	865	800	743	735
Water uptake (wt. %)	5.8	5.0	4.9	4.5
Pore size (mm)	0.6-1.1	0.6-1.5	1.0-1.7	1.3-2.0

The experimental results contained in Table 2 indicate remarkable thermal insulating properties of the expanded products, especially of those made using the highest amount of surfactant (version 4). Thus, apparent density decreased up to 0.05 $g \cdot cm^{-3}$ and heat conductivity decreased also up to 0.033 $W \cdot m^{-1} \cdot K^{-1}$. The compressive strength was normally influenced by the very porous structure of material, decreasing to 735 kPa, but this value is satisfactory for applications in the thermal insulation of the building. The level of water absorption measured by maintaining these products into a chamber with constant high humidity (85 %) for 30 days was within the normal limits for this type of material (4.5-5.8 wt. %).

The microstructural appearance of wood foam samples is shown in Fig. 2.

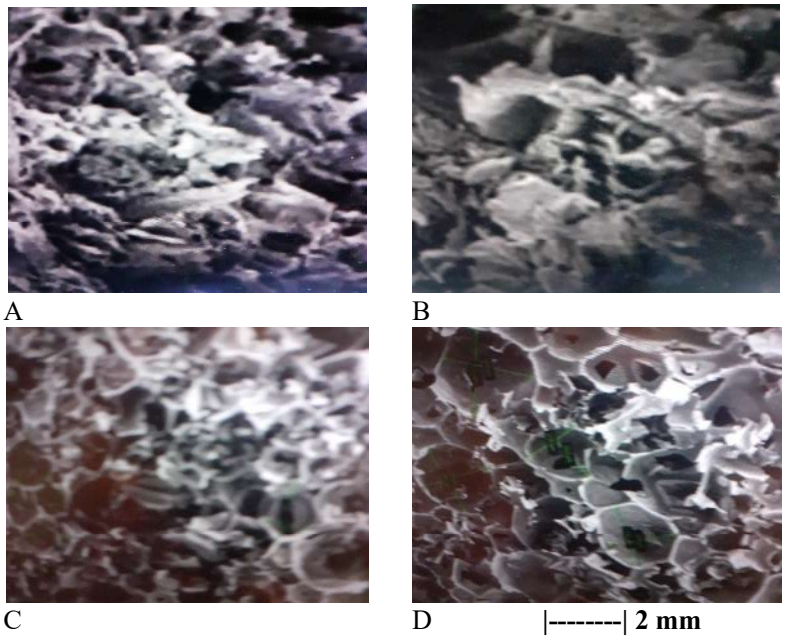

Fig. 2. Microstructural aspect of wood foam samples
A – sample 1; B – sample 2; C – sample 3; D – sample 4.

Examining the pictures in Fig. 2, the pore dimension could be determined. The largest pore sizes (1.3-2.0 mm) were identified in the case of the sample corresponding to experimental sample 4. In addition, the porous structure of the foam is partially characterized by the existence of open cells. Approximately similar structural characteristics were also noted in the case of the sample corresponding to experimental variant 3. The pore size range valid for this sample was 1.0-1.7 mm.

The remarkable results obtained by research teams from the Fraunhofer Institute for Wood Research (Germany) [15] on the apparent density (up to 0.04 $g \cdot cm^{-3}$) and heat conductivity (under 0.04 $W \cdot m^{-1} \cdot K^{-1}$) of beech wood foams, at a comparable value level to those of polystyrene and wood fibre thermal insulating panels, have were almost replicated in the experiment presented in this work using oak wood waste and a

surfactant (sodium dodecyl sulfate) recommended in the case of cellular concrete preparation [18], to form the required wet suspension in the presence of distilled water.

It should also be mentioned the performances reported by [2] on the preparation of a pine wood foam under the conditions of using a residual wood available in North America, sodium dodecyl sulfate, sodium bicarbonate, polyvinyl alcohol, and deionized water, the apparent density being lowed up to 0.12-0.14 $g \cdot cm^{-3}$ and heat conductivity to 0.042 $W \cdot m^{-1} \cdot K^{-1}$.

Different species of poplar wood were also used as feedstock in other experiments mentioned in the literature.

In principle, in the world, the research for manufacturing wood foam as a substitute for heat-insulating materials based on polymers is in full ongoing. Researchers from the Fraunhofer Institute investigate the possibility of also applying other lignocellulosic materials and consider that in a few years the wood foam manufacture could reach an industrial level.

6. Conclusions

The paper objective was making an alternative heat insulation material suitable for building construction based on the advanced technique of expanding wood waste. The new material type should have the capacity of replacing the current thermal insulating products based on plastics applied in construction. In present, researchers in construction field are testing different making techniques and more types of wood waste, the results being promising, but the optimal technical decision for manufacturing on an industrial-scale has not yet been reached. This paper aimed at experimentation an oak wood waste, un-used in previous tests reported in the literature in order to obtain wood foam with physical, mechanical, thermal, and morphological performance features adequate for use as an excellent insulating material in the building sector. The results showed remarkable values of apparent density (0.05-0.11 $g \cdot cm^{-3}$), heat conductivity (0.033-0.051 $W \cdot m^{-1} \cdot K^{-1}$), water-absorbing (4.5-5.8 wt. %) as well as a low but acceptable level of the compression resistance (735-865 kPa). The material obtained through the optimal testing version having a density of 0.05 $g \cdot cm^{-3}$, thermal conductivity of 0.033 $W \cdot m^{-1} \cdot K^{-1}$, water-absorbing of 4.5 wt. %, and the compressive strength of 735 kPa proved the reaching of value level of the material type produced so far in experiments presented in the literature. Taking into account the current trend of replacement the plastic-based materials, as in the case of thermal insulation materials usually applied in construction, as well as the continuation of the global research for this goal, the authors' team of the current paper have as future concern developing the own research on this investigation topic.

References

[1] D. Aperjis, „The Oil Market in the 1980s: OPEC Oil Policy and Economic Development", US Development of Energy Office of Scientific and Technological Information, Cambridge, Mass.,

Ballinger Publishing Co., Pensacola, Florida, the United States, vol. 24, 1982. https://www.osti.gov/biblio/6633202

[2] E.S. Ferreira, E. Dobrzanski, P. Tiwary, P. Agrawal, R. Chen, E.D. Cranston, „Insulative Wood Materials Templated by Wet Foams", in Materials Advances, Royal Society of Chemistry, London, UK, vol. 4, 2023, pp. 641-650. https://doi.org/10.1039/D2MA00852A

[3] P. Mukhopadhyaya, M.T. Ton-That, T.D. Ngo, N. Legros, J.F. Masson, S. Bundalo-Perc, D. van Reenen, „An Investigation on Bio-Based Polyurethane Foam Insulation for Building Construction", ASTM International, Special Technical Publication, vol. 1574, 2014, pp. 131-141. https://www.astm.org/stp157420130107.html

[4] J. Peyrton, L. Avérous, „Structure-Properties Relationships of Cellular Materials from Biobased Polyurethane Foams", in Materials Science and Engineering: R: Reports, Elsevier, vol. 145, 2021. https://doi.org/10.1016/j.mser.2021.100608

[5] M. Alimadadi, T. Uesaka, „3D-Oriented Fiber Networks Made by Foam Foaming", in Cellulose, Springer Netherlands Publishing, vol. 23, no. 1, 2016, pp. 661-671. https://doi.org/10.1007/s10570-015-0811-z

[6] E.S. Ferreira, C.A. Rezende, E.D. Cranston, „Fundamentals of Cellulose Lightweight Materials Bio-Based Assemblies with Tailored Properties", in Green Chemistry, Royal Society of Chemistry, UK, vol. 23, no. 10, 2021, pp. 3542-3568. https://doi.org/10.1039/D1GC00326G

[7] T. Hjelt, J.A. Ketoja, H. Kiiskinen, A.I. Koponen, E. Paakkonen, „Foam Forming of Fiber Products: A Review", in Journal of Dispersion Science and Technology, Taylor & Francis Online, vol. 43, no. 10, 2022, pp. 1462-1497. https://doi.org/10.1080/01932691.2020.1869035

[8] Chao Zheng, D. Li, M. Ek, „Improving Fire Retardancy of Cellulosic Thermal Insulating Materials by Coating with Bio-Based Fire Retardants". in Nordic Pulp & Paper Research Journal, De Gruyter Publishing, vol. 34, 2019, pp. 96-106. https://doi.org/10.1515/npprj-2018-0031

[9] B. Seantier, D. Bendahou, A. Bendahou, Y. Grohens, H. Kaddami, „Multi-Scale Cellulose Based New Bio-Aerogel Composites with Thermal Super-Insulating and Tunable Mechanical Properties", in Carbohydrate Polymers, Elsevier, vol. 138, 2016, pp. 335-348. https://doi.org/10.1016/j.carbpol.2016.09.068

[10] Clara Jimenez-Saelices, B. Seantier, B. Cathala, Y. Grohen, „Spray Freeze-Dried Nanofibrillated Cellulose Aerogel with Thermal Superinsulating Properties", in Carbohydrate Polymers, Elsevier, vol. 157, 2017, pp. 105-113. https://doi.org/10.1016/j.carbpol.2016.09.068

[11] B. Fleury, E. Abraham, J.A. de la Cruz, V.S. Chandrasekar, B. Senyuk, Q. Liu, V. Cherpak, S. Park, J.B. Bart ten Hove, I.I. Smalyukh, „Aerogel from Sustainability Grown Bacterial Cellulose Pellicles as a Thermally Insulative Film for Building Envelopes", in ACS Applied Materials & Interfaces, ACS Publications, American Chemical Society, vol. 12, no. 10, 2020, pp. 34115-34121. https://pubs.acs.org/doi/abs/10.1021/acsami.0c08879

[12] J. Feng, S.T. Nguyen, Z. Fan, H.M. Duong, „Advanced Fabrication and Oil Absorption Properties of Super-Hydrophobic Recycled Cellulose Aerogels", in Chemical Engineering Journal, Elsevier, vol. 270, 2015, pp. 168-175. https://doi.org/10.1016/j.cej.2015.02.034

[13] A.C. Pierre, G.M. Pajonk, „Chemistry of Aerogels and their Applications", in Chemical Reviews, ACS Publications, American Chemical Society, vol. 102, no. 11, 2002, pp. 4243-4266. https://doi.org/10.1021/cr0101306

[14] *** „Insulation materials and their thermal properties", GREENSPEC Ltd., Beverly, East Yorkshire, UK, 2000. https://www.greenspec.co.uk/building-design/insulation-materials-thermal-properties

[15] *** „Foam wood-From tree to foam", Fraunhofer Institute for Wood Research, Braunschweig, Germany, 2023. https://www.fraunhofer.de/en/institutes.htm

[16] V.K. Srivastava, A. Pizzi, „Characterization and preparation of wood-furanic foams", in Journal of Renewable Materials, Tech Science Press, the United States, vol. 2, no. 3, 2014, pp. 201-206. https://doi.org/10.7569/JRM.2014.634107

[17] L. Paunescu, Enikö Volceanov, B.V. Paunescu, „New Wood Foam-Heat Insulating Material Obtained through Oak Wood-Delignification Process", in Nonconventional Technologies

Review, Romanian Association for Nonconventional Technologies, Politehnica Publishing, Timisoara, vol. 27, no. 4, 2023, pp. 12-16.
[18] V. Moldovan, „Aditivi in betoane”, Editura Tehnica, Bucuresti, 1978.
[19] *** „Sodium Dodecyl Sulfate”, PubChem, National Library of Medicine, 2018. https://pubchem.ncbi.nlm.nih.gov/compound/Sodium-dodecyl-sulfate

State of the art of 3D printing of concrete in construction: Materials

Stadiul actual al imprimării 3D a betonului în construcții: materiale

Hicham Bensafi[1]

[1] Technical University Construction Bucharest.
Bulevardul Lacul Tei 124, București 020396, Roumanie
E-mail: bns.hicham41@gmail.com

DOI: 10.37789/rjce.2026.17.2.14

Abstract The paper provides an overview of current studies on 3D concrete printing, highlighting its transformative impact on traditional construction methods. It begins by reviewing advancements in materials specifically tailored for this technology, including fibers, binders, aggregates, additives, and admixtures essential for printed concrete. The article notes that 3D concrete printing requires special mortars that facilitate extrusion, set rapidly, and ensure strong mechanical performance while minimizing environmental impact. The focus is on the unique properties of these materials, differing from conventional concrete, such as rheology, durability, rapid setting, and a reduced carbon footprint, which are critical for additive manufacturing processes. Despite technological progress, challenges remain regarding the long-term mechanical behavior, material durability, and process consistency of 3D printed elements. The conclusion underscores the need for further research to overcome these obstacles and asserts that 3D concrete printing represents a promising pathway toward more automated, adaptable, and sustainable construction practices.

Keyword: 3D concrete printing, fiber reinforcing, the materials, technological advancements, material durability.

1. Introduction

The U.S. government, mainly NASA and the military, supports 3D printing for the development of rapidly deployable and sustainable space infrastructure. COBOD promotes 3D printing as a low-carbon alternative within the framework of the European Green Deal. China is leading in Asia in large-scale housing thanks to Winsun, while India is experimenting with it for affordable housing. 3D printing is expanding across Africa, as shown by Kenyan schools built by NGOs **[1].**

A thorough examination of Google Scholar, Web of Science, and Scopus was also required for the review. We used specific terms like 3D concrete printing, additive manufacturing in the construction sector, digitally created concrete, and rheology of

The article was received on 04.02.2026, accepted on 27.05.2026 and published on 12.06.2026

printable concrete. This careful research method covered a wide range of scholarly articles, conference presentations and journal papers published between 2010 and 2024, demonstrating the quick evolution and expanding academic interest in this topic **[2].**
In preliminary research for this review, 1,033 3D concrete printing papers were found. Subdivisions were established for sustainable materials (400 articles), structural topology optimization (472 articles), and tool path design (161 articles) **[3].**
This rise in publications, especially after 2020, shows the acceleration of 3D concrete printing (3DCP) research, showing its expanding importance and the concerted international effort to enhance its potential **[4].** The rise in research between 2016 and 2019, and again after 2020, shows that 3D printing has the ability to transform the building industry by solving major issues like material waste and energy usage **[5].**
ALAMI et al. **[6]** discuss how 3D concrete printing (3DCP) could transform the building industry, especially for UN Sustainable Development Goals (SDGs). They claim that 3DCP may lower costs by 78% and water use by 60% compared to conventional methods. It might cut global energy use by 5% by 2025, making it a sustainable powerhouse. Even though 3DCP has less climate impact, its sustainability needs improvement. The authors emphasize the importance of ongoing research and development to overcome current limits and maximize 3DCP's industry benefits **.**

2. TECHNOLOGIE

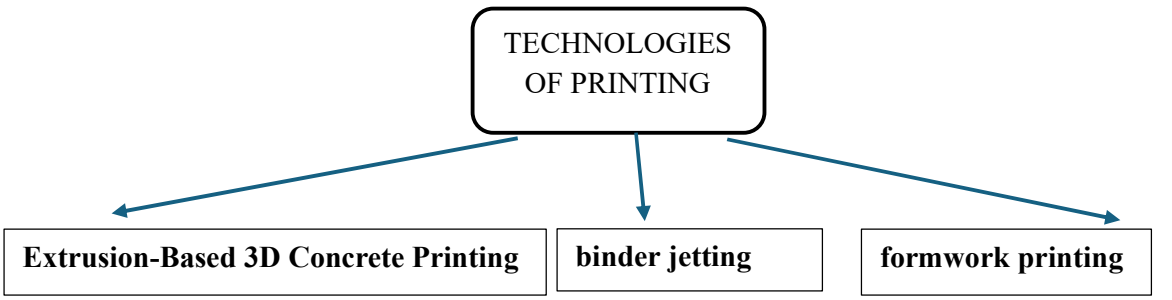

Fig.1. The most commonly used printing technologies

2.1 Extrusion-Based 3D Concrete Printing

Compared to traditional construction, extrusion-based 3D concrete printing (3DCP) increases efficiency, design flexibility, and environmental sustainability. It speeds construction, decreases labor costs, and allows complicated geometries that conventional approaches cannot.
3D printing with extrusion is a quickly developing technology in the building sector **[7].** Complex buildings and customized design solutions can be efficiently produced using extrusion-based 3D concrete printing due to its design flexibility, reduced manual labor, little material waste, and high automation via building information modeling (BIM) **[8].**
Construction applications for Extrusion-Based 3D Concrete Printing (3DCP) innovation are vast and significant. This technology boosts efficiency, sustainability, and design flexibility.

3.2 binder jetting

Binder jetting technology (BJT) in 3D printing concrete improves mechanical performance, adaptability, and sustainability. Sustainable construction approaches benefit from effective material use, including recycled aggregates. BJT can precisely produce complex geometries, making it perfect for architectural and construction applications.

ODAGLIA et al. note that Binder Jetting uses waste materials to create a circular economy and improve material characteristics, reducing CO2 emissions by 30%. BJT technology will improve manufacturing efficiency and increase output volume by 50%. Achieving a 0% safety incidence rate makes this project crucial to the building industry's sustainability. **[9].**

3D concrete printing with BJT benefits the construction industry. It boosts efficiency, sustainability, and design flexibility. BJT is appealing for modern building due to these qualities.

2.3 formwork printing

Traditional formwork construction technologies struggle to achieve complex geometries and optimal designs. 3D printing can do so. Material characteristics and reinforcement integration issues limit its industry adoption.

Formwork building with 3D printing improves load-bearing capacity, rigidity, material efficiency, and speed. However, stress concentrations over tensile limits require reinforcement in critical areas to prevent failure. **[10]**

3D printing can transform formwork building, but the industry must address its constraints. For wider adoption, innovation and established methods may need to be balanced.

3. Materials

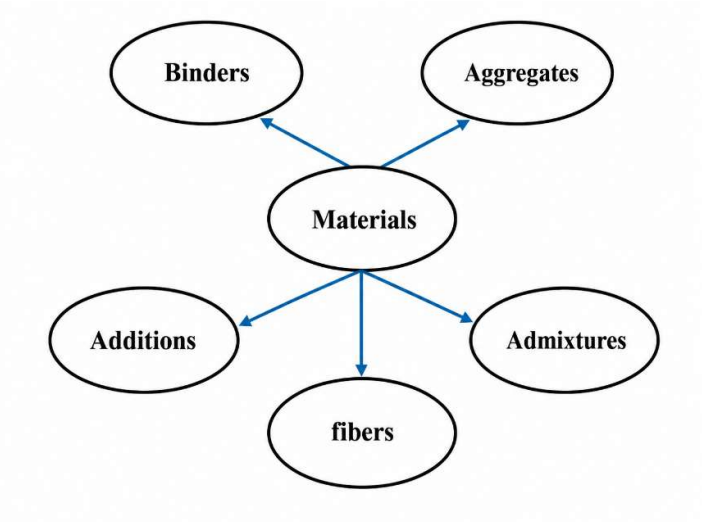

Fig. 2. The different types of materials used in 3D concrete printing

3.1. Binders
3.1.1 Traditional hydraulic binders

Research by BRAHIM A et al. explores the properties of 3D-printed Portland Pozzolana Cement (PPC) concrete, highlighting its sustainability and cost-effectiveness as an alternative to traditional Portland cement (OPC). PPC, incorporating 35% fly ash, is evaluated for its structural integrity and essential qualities such as extrudability, printability, and thixotropic open time, aiming to enhance eco-friendly construction methods **[11].**
MAROSZEK et al. note the increasing demand for cement-based concrete driven by urbanization, yet emphasize the environmental challenges posed by resource depletion and greenhouse gas emissions. They suggest that using industrial waste and recycled aggregates can substitute concrete while achieving controlled mechanical performance. Their analysis indicates that recycled 3D printing concretes can reduce CO2 emissions by 20-50% while maintaining structural performance **[12].**
LUO et al. examined how carbonation duration affects the mechanical characteristics and interfacial bonding of 3D printed cement-based material using 100% carbonated recycled sand. Carbonation time reduced mechanical anisotropy in printed specimens but did not remove it. As carbonation time extended, the interlayer shear strength and interstrip shear strength increased by 21.5% and 18.7%, respectively, improving interfacial bonding performance **[13].**

3.1.2 Binders based on complementary materials (partial cement substitutes)
3.1.2.1 fly ash (FA)

The study by COLYN et al. reveals that 3D printed concrete with fly ash (FA) as a supplementary material exhibits 28-day compressive strengths of 31 to 55 MPa and elastic moduli of 29 to 37 GPa. Their mixtures, containing 60% alternative binders including FA, not only showed suitable rheological properties for 3D printing but also produced smooth surfaces with no visible cracking, indicating improved performance and sustainability **[14].**
OVER et al. investigated eco-friendly 3D printed mixes using fly ash, granulated blast furnace slag, and marble dust. They also studied how VMA and silica fume affected their characteristics. In the study, SF increased fresh qualities and VMA mixes had greater static yield strength. The FA-SF blend was best for printability and sustainability, considering environmental impacts and engineering properties **[15].**
TSENG et al. studied 3D-printed concrete printing and hardening. They replaced cement in 3DPC with fly ash and crushed granulated blast furnace slag in various ratios. FA and GGBFS were tested for extrudability and buildability on 3DPC's printing and toughened characteristics. All mix designs satisfied 3DPC's printing standards, with larger GGBFS-content specimens being stronger and heavier. FA and GGBFS can replace 50% of 3DPC cement **[16].**

VICO LUJANO et al. optimized mortar rheology, hydration kinetics, and structural performance for extrusion-based 3D printing with a novel formulation. After extrusion, potassium-rich biomass fly ash (BFAK) and air-entraining plasticizer (APA) increase yield stress, thixotropy, and structural stability. BFAK alters hydration kinetics, extending setting time, which APA controls. BFAK improves cohesion without dispersion by reducing spread diameter in flowability testing **[17].** The maximum printed height is achieved by 1.5% APA and 2% BFAK, according to calibration cylinder tests, demonstrating its buildability and load-bearing capacity. This synergistic effect promotes sustainable cementitious materials by customizing fresh-state properties and structural dependability **[17].**

LI et al. tested FAM-nanosilica 3DP mortars. Optimization of water reducer dosage enhanced extrudability, buildability, and dimension stability. The w/cm ratio, FAM, and NS concentration defined 3DP mortar's mechanical qualities. FAM and NS boosted flexural, compressive, and bond strengths, suggesting they should improve 3DP mortar design together. **[18].**
Fly ash as a cementitious ingredient in 3D printed concrete increases mechanical characteristics and reduces CO2 emissions and energy use. Mixture composition and fly ash proportion affect these qualities.

3.1.2.2 Ground Granulated Blast Furnace (GGBS)

3D concrete printing (3DCP) and fresh and hardened performance were studied by ALI et al. Adding GGBS and SC to 3DCP mixes as partial substitutes for Portland cement and natural sand increased flowability, extrudability, and buildability. The best blend was 30% GGBS and 20% SC, with 28-day compressive and flexural strengths of 50.61 and 6.73 MPa, respectively. In 3DCP, GGBS and SC can improve environmental effect and structural performance without affecting printability, according to the study **[19].**
SI et al. examine how nano-silica (NS) and high GGBS replacement levels affect 3D printed concrete's mechanical characteristics and rheology. NS improved rheological behavior, compressive strength, plastic viscosity, and thixotropic characteristics. At 28 days, C3G7N1, the best mix, had 105 MPa compressive strength, exhibiting greater mechanical performance and decreasing carbon footprint for sustainable 3D concrete printing **[20].**

MISHRA et al. investigated using GGBS and fly ash in 3D printing mortar to minimize OPC consumption. Four mortar mixtures were tested for printability. The best blend, O70G30 (70% OPC, 30% GGBS), retained shape 18.3% and 54.3% better than the control and O70F30 mixes. Due to its finer particle size and larger specific surface area, GGBS had 22.2% less open time than the control. The printed specimens have anisotropic compressive strength 9.4–35.6% lower than mould-cast samples. GGBS improved hydration, microstructure, and 3D printed mortar performance **[21].**
The incorporation of fly ash in GGBS 3D printed concrete enhances its mechanical properties and promotes sustainability. Optimal material combinations lead to concrete

with superior compressive, flexural, and tensile strengths compared to conventional concrete, while also reducing carbon emissions from cement production.

3.1.2.3 Silica Fume

NASSRULLAH et al. adapted 3D printing systems with carbon nanotubes (CNTs) and silica fume to explore cementitious composites. According to tests, adding 0.2% CNTs and 20% silica fume improved the rheology, buildability, open time, and printing quality. While buildability and open-time increased by 201% and 263%, respectively, layer width and height error decreased from 140% and 6% to less than 1.5%. With CNTs and silica fume, cast and 3D-printed samples had better compressive and flexural strengths **[22].**

According to PANTIRU et al. Incorporating silica fume as a cement replacement in 3D printed concrete enhances strength, durability, and workability, optimizing fresh properties and promoting a more sustainable construction method while reducing concrete production's carbon footprint **[23].**

THAJEEL et al. examined how metakaolin (MK) and silica fume (SF) affect 3D printed concrete. Increased MK content enhanced early strength increase, shape retention, and buildability, the study revealed. However, large MK doses created cracking and extrudability issues. The optimal blend was MK10SF5, with 10% MK and 5% SF for shape retention, buildability, and compressive strengths. MK and SF synergistically increased particle packing, cohesion, and pozzolanic reactivity, suggesting they might optimize 3DPC for printability and mechanical performance **[24].**

In order to enhance the printability and mechanical performance of 3D printed magnesium phosphate cement (MPC), WANG et al. investigated the use of silica fume (SF). Through the formation of compact flocculation structures, SF was found to increase viscosity and yield stress. It also improved interlayer bonding, which decreased mechanical anisotropy. Additionally, the work demonstrated the failure mechanism of 3D printed MPC loaded in various loading directions and confirmed the impact of interlayer bonding on anisotropic behavior **[25]**
Silica fume usage improves 3D printed concrete's rheology and strength. Silica fume, a pozzolanic substance, has a denser microstructure, which is needed for 3D printing with high compressive and flexural strengths.

3.1.3 Geopolymer

Comparing additive building to traditional methods, AHMED et al. report accurate material deposition, reduced waste, more design freedom, and faster manufacturing. Concrete buildings pollute due to Portland cement manufacturing's energy and greenhouse gas emissions. To solve these issues, AHMED et al. study geopolymer concrete, a cement-free, eco-friendly option made from industrial wastes. Custom

geopolymer concrete mixtures, printability for 3D building designs, and hardened properties will be tested. Raising slag concentration boosts compressive strength, activator temperature improves printability, and idle time before printing improves uniformity **[26].**

YOUSSEF et al. found that because of its low Si/Al ratio, BFS amorphe, which contains 31% CaO and 42% SiO2, requires a significant amount of sodium silicate. MK and BFS have been used in combination to lessen the environmental impact. The addition of a superplastifier has decreased the mixture's weight loss and calcium carbonate content **[27].**

SILVESTRO et al. examined how low-carbon binders like CSA, LC3, and geopolymers affect concrete characteristics, mechanical performance, and durability. They found that CSA cement's composition and particle size greatly affect cementitious mixture viscosity and structural build-up. Metakaolin and limestone LC3 cements have good mechanical performance and sustainability, whereas geopolymeric binder has compressive strengths comparable to or greater than OPC **[28].**

GPC has compressive strength up to 50 MPa, compared to 40 MPa for OPC concrete. Tensile strength increases from 4.0 to 5.5 MPa and flexural strength from 6.0 to 8.0 MPa. GPC outperforms concrete in sulfate attack, chloride intrusion, thermal stress, and acidic conditions by 20% **[29].**

The use of waste concrete fine aggregates (WCA) in geopolymer mortar for 3D concrete printing is investigated by KRAVCHENKO et al. as a sustainable substitute for traditional building techniques. Their findings demonstrate that, in comparison to natural fine aggregates (NFA), WCA-based mixes have improved compressive strength and dimensional stability. The life cycle assessment (LCA) indicates a 3.4% decrease in both terrestrial acidification and global warming potential as compared to NFA. The study also highlights how crucial orientation is for 3D printing, as it demonstrates notable increases in compressive strength in every tested direction **[30].**

Sustainable 3D-printed geopolymer concrete (3DPG) has been evaluated by ELHAG et al. as a low-carbon, environmentally friendly substitute for conventional building materials. Fresh properties, mechanical performance, and microstructural development are examined in relation to printing circumstances and basic components. The function of activators, supplemental materials, and reinforcing techniques in performance optimization is also covered **[31].** Geopolymeric binder in 3D-printed geopolymer concrete has 20–70 MPa compressive strengths, depending on printing and curing **[32].**

MORTADA et al. examine how steel fiber affects 3D-printed Ca(OH) 2-activated geopolymer concrete. 1.2% steel fiber increased flexural, tensile, interlayer bond, and elastic modulus. Slower shrinkage but no change in self-induced stress were found in durability tests. Microstructural investigation demonstrated steel fiber crack-bridging **[33].**

Advances in geopolymer utilization improve the mechanical properties of 3D printed concrete, enhancing printability, strength, and durability through optimized mixtures and additives, thereby improving the performance of geopolymer concrete (GPC) in 3D printing applications.

3.1.4 Gypsum 3d printing

3D-printing materials need viscosity modifiers. Huang et al. tested HPMC to ATP, NB, and NS in gypsum-based products. ATP, NB, and HPMC decreased slurry fluidity, whereas NS enhanced it at lower doses. Increasing yield stress increased plastic viscosity minimally in all VMAs. Compared to HPMC, inorganic VMAs reduced 2-hour wet and compressive strength loss. NS and HPMC reduced hydration exotherm peaks, while NB and ATP cut maximum peaks at 1% but caused early, higher peaks at higher dosages. Microstructural analysis showed that 0.5% HPMC produced flaky structures while 5% NS produced short, thick gypsum crystals. In conclusion, inorganic VMAs improve mechanical properties, workability, and performance in high-performance 3D printing gypsum materials**[34]**.
Using 3D printing and gypsum based materials, XIANG et al. created advanced tunnel models and layered rock masses. Their research compared three innovative tunnel models to a traditional model and found that basic structures like inverted arch filling better simulate tunnel deformation and damage. Gypsum materials imitate tunnel failure under high in-situ stress, while 3D printing improves model precision. Under such load, tunnel vault and base collapse causes rock bending and shear-slip failures, according to study. To reduce damage, tunnel structures and rock at the bottom and vault must be reinforced**[35]**.
TARAHAN et al. investigate using industrial gypsum byproducts PG and BG as partial cement substitutes in 3D-printed concrete to improve sustainability and printability. Adding 7.5% PG to ground granulated blast-furnace slag cement mortars resulted in the maximum strength (~51 MPa), surpassing the control. The fly ash system maintained control strength at 2.5% PG, but BG decreased strength at 7.5% or higher, suggesting 5%. Although BG-Fly Ash mixtures improved open time, PG mixes remained steady. The study found that PG dosages of 5-7.5% improve mechanical performance without affecting workability, while BG is indicated only for extended open time.**[36]**.

3.1.5 Clay 3d printing

For building, urban furniture, maritime, and artistic purposes, large-format additive manufacturing (LFAM) uses cement and clay. Clay offers architectural freedom, while cement is structurally sound. Complex structural features require parametric design and high-performance clay materials. Architecture may be transformed by digital technologies to create complex forms that improve aesthetics and performance. Design flexibility, energy efficiency, and environmental impact can be improved by LFAM and parametric and generative design. Interdisciplinary collaboration, structural analysis, printing control, maintenance planning, and stakeholder approval are challenges. A parametric design study with Grasshopper shows façade panel geometry, verifying its application for facade component manufacturing **[37]**.
Rapid population increase has caused a global housing crisis. GONSALVES et al. note that additive manufacturing (AM) or 3D printing can address this issue because to its shorter building periods and design flexibility, although slow-setting concrete and

cement's environmental impact are drawbacks. They present a clay-based construction material that hardens quickly after printing and has concrete-like characteristics. This material's thermally triggered frontal polymerization sets immediately, allowing multilayer walls and complicated shapes. It reaches 3 MPa buildable strengths immediately after printing and exceeds the 17 MPa required for residential concrete in 3 days, compared to 28 days for standard concrete. The methods show promise for sustainable infrastructure construction **[38]**.

3.1.6 Hybrid and innovative binders

Due to reduced manual labor and resource efficiency, concrete 3D printing has grown worldwide over the past decade. Ternary gypsum–cement–pozzolanic (GCP) composites, developed by SAHMENKO et al., are water-resistant like Portland cement (PC) and harden quickly like gypsum. These composites exhibited compressive strength up to 37 MPa, comparable to typical PC mixes, and stability for printing up to 35 layers using recycled plasterboard gypsum and phosphogypsum. Life Cycle Analysis showed a 40% carbon footprint decrease over PC mortar, encouraging sustainable 3D printing**[39]**.

Incorporating 5% silica fume and 50% GGBS in 3D printed mortars resulted in a compressive strength of 109.10 MPa and improved flexural strength, showcasing better mechanical properties through optimized silica fume use **[40].**

Concrete 3D printing is a potential automation technology, but little is known about how strong and durable it is. In contrast to mold-cast (MC) specimens, KAUR et al.'s study examined the durability of 3D printed concrete (3DPC) made with fly ash (FA) and limestone calcined clay (LC). The results demonstrated that the FA-based mix had improved pore structure and decreased porosity, which led to a higher compressive strength and less water absorption. Porosity and drying shrinkage were strongly impacted by the casting/printing procedure **[41].**

Silica fume, fly ash, blast-furnace slag, meta-kaolin, paper sludge fly ash, limestone powder,reactive ultra-fine fly ash, oyster shell powder, and calcium sulfate whisker were examined by XUE et al. Hydraulic activity and microscopic particle size improved printability without strength loss, but FA and BF had minimal effect. Even with 30% cement replacement, these materials remained strong, indicating optimal print quality and environmental benefits at <30% **[42].**

High-performance concrete additives made of graphene are appealing, but cost and industrial scaling concerns limit their application. According to SUREHALI et al. ultra-low doses of fractal graphene (FG) and reactive graphene (RG) affect the rheology of 3D-printable concrete. Functional groups in RG-modified mixes increase dynamic and static yield stresses and viscoelastic characteristics more than in FG-modified mixtures. After mixing for 30, 60, and 90 minutes, we discovered that ultra-low graphene dosages doubled construct heights. Important rheological parameters required for material supply, expansion, and layer build-up in concrete3D printing are shown in this study using storage modulus and its development **[43].**

Advances in hybrid and innovative binders enhance the mechanical properties of 3D printed concrete by improving printability, reducing anisotropy, and optimizing interlayer bonding, addressing the limitations of traditional concrete in 3D printing applications.

3.2 Aggregates

PEPE et al. study 3D concrete printing (3DCP) focusing on sustainable raw material usage with recycled fine aggregates, achieving 100% recycled aggregate combinations without mechanical quality loss and promising compressive strength above 50 MPa **[44].**

Ma et al. explore the incorporation of recycled fine aggregate (RFA) and clay brick powder in 3DPC, noting reduced ambient compressive strength but improved high-temperature residual strength **[45].**

Jia et al. investigate recycled brick fine aggregates' impact on 3D printed concrete's plastic phase, finding that RBFA affects water evaporation and plastic shrinkage, suggesting specific additives for optimization **[46].**

Demirbaş et al. analyze 3D printable mixtures using Portland and white cement with (RCA), highlighting resulting high-strength mortars (70 MPa) and modest negative effects on water absorption compared to natural aggregates **[47].** MIM et al. explored the use of copper heap leach residue (CHLR) as a fine aggregate in 3D printed concrete (3DPC), finding that while greater CHLR content enhances buildability, it also diminishes flowability **[48].**

LIANG et al. studied the shear modulus in various sands, revealing that irregular particle morphologies notably enhance the maximum shear modulus, with local roundness impacting its sensitivity to stress **[49].** SHI et al. investigated marine coral sand-clay mixes with 3D-printed triaxial geogrid reinforcement, showing that higher confining pressure and more reinforcement layers significantly improve strength, providing insights for maritime engineering **[50].**

Using 3D-printed concrete waste, MENGISTU et al. evaluated (RAC). Researchers crushed 3DPC waste into fine and coarse aggregates with a jaw crusher. River sand and aggregates created C30/37 and C40/50 strength classes. The study tested compressive strength with destructive testing and rebound hammer. We observed that density gradually increases RAC compressive strength. Surface temperatures over 30°C reduced strength 11.5%. Except for C30-RA50, 50% and 67% recycled aggregate RAC combinations increased compressive strength **[51].**

LIU et al. examine pore structure and cold-weather 3D printed concrete durability. The researchers examined the impact of recycled coarse aggregate replacement ratios on 3D printed recycled aggregate concrete (3DPRAC) shape, mass loss, and dynamic elastic modulus under freeze-thaw cycling. 3DPRAC had lower F–T resistance to cast concrete, and its distinctive ellipsoidal pores and porous old mortar reduced its elasticity. The study also examined F–T resistance degradation methods based on pore structure, which could help cold regions use digital concrete manufacture **[52].**

MIM et al. examined the use of industrial by-products in 3D printed concrete (3DPC) for sustainable building, exploring materials such as mining wastes, seashells, and construction debris. The study assesses how these by-products influence the fresh, mechanical, and microstructural properties of 3DPC, suggesting a 20-40% substitution of fine aggregates to enhance strength and flowability while reducing waste and conserving resources **[53].**

Kumar et al. created earth-based 3D printed concrete (3DPC) instead of fine particles. They replaced 30–50% of natural sand with locally excavated 4% clay soil. Soil inclusion reduced printing flow and increased open time by 13-60% compared to the control mix. Increased extrudability and buildability allowed crack-free printing of over 30 layers. Crack onset was 30-50% slowed by soil addition **[54].**

WANG et al. investigated how paste-aggregate ratio and coarse aggregate content affect 3DPC properties to optimize mix composition and printing. Reduced paste-aggregate ratio increases static yield stress, dynamic yield stress, and plastic viscosity. Rheological characteristics and printing effect are best for concrete with a paste-aggregate ratio of 1.3. High coarse aggregate content degrades print quality. The best 3DPC performance is attained with 1.3 paste-aggregate ratio and 60% coarse aggregate. Cast concrete mechanical characteristics are less susceptible to specimen size than 3DPC **[55].**

China et al. developed a 3D concrete printing (3DCP) with high strength, low cost, and shrinkage. Their extrusion-based 3D printer printed 20mm-grain concrete. In the investigation, cement to aggregate volume ratio (C/A) affected printability and mechanical performance. The microstructure was analyzed using X-CT and SEM. Printable concrete's initial flowability should be 178-200mm, and its C/A should be 0.35-0.60. Non-uniform void distribution caused 3D printed specimens to have direction-dependent compressive and flexural strengths **[56].**

WANG et al. produced 3D printed concrete (3DPC) with coarse aggregates to improve performance. found that aggregate size diminishes extrudability, stabilizes, and reduces slump. Rheology and mechanical tests explain this. As aggregate particle size grows, 3DPC mechanical characteristics improve, and all groups show substantial anisotropy. Microscopic experiments showed 3DPC pores have directionality, explaining fracture mechanics anisotropy. Large coarse aggregates boost 3DPCAC compressive strength and elastic modulus but impair extrudability and increase anisotropy **[57].**

New construction approach using plastic trash by NAZIR et al. They improved self-compacting mortar (SCM) rheology utilizing 3D-printed plastic fine aggregates (3DPFA) and rheological testing equipment. Testing SCM mixes with different 3DPFA content showed considerable workability and flow benefits. With more 3DPFA, the mini-slump spread grew, T20 flow time decreased, and J-ring tests revealed better passing. Thermal conductivity dropped 22% and V-funnel flow time decreased. This shows a possible building plastic waste valorization path **[58].**

WANG et al.'s work investigates the application of (GGBFS) and ferronickel slag in 3D printing. The study discovered that while little aggregate size leads to insufficient yield stress, big aggregate size adversely impacts the smooth extrusion of concrete strips **[59].**

WANG et al. also discovered that the stability and quality of the printed concrete strips are impacted by the extrusion performance, which is strongly correlated with aggregate

size and nozzle diameter. 30% to 50% of the nozzle diameter is the maximum aggregate size suggested by the study for stable extrusion, 50% for smooth extrusion, and 30% for acceptable shape **[59].**

According to PARITALA et al. aggregate type, content, and paste rheology affect concrete mixture printability. They observed that higher yield stress paste mixes need additional paste to maintain fluidity, limiting aggregate content. Paste binder content depends on packing density and aggregate surface area. High-fine, low-sphericity mortar combinations need more paste despite increased packing density. Particles with irregular shapes and vast surface surfaces need more paste for flowability and coating. The investigation validated across aggregate types a unique linear relationship between paste yield stress and excess paste content. These proportioning instructions are for printed concrete compositions **[60].**

based on GIRSKAS et al. The most popular fine aggregate for the 3D printed concrete mixture is 0/2 mm fraction sand, which is the only fine aggregate utilized in its preparation. For 3D printed concrete, however, some studies show that 0/4 mm fraction sand and even coarse aggregates (crushed stone) of 4/8 mm fraction are feasible **[61].**

The mechanical properties of 3D printed concrete are significantly affected by the type and characteristics of aggregates, especially advanced aggregates. Important factors include aggregate size, type, and their interaction with printing parameters, which influence both printability and strength.

3.3. Additions

JIN et al. investigate how inorganic micro/nanomaterials can change the rheology and mechanics of cementitious composites in 3D concrete printing. Carbon-based, silicon-based, metallic oxide, and nano-calcium carbonate particles have been utilized in 3D printing concrete or may be employed in the future. The study also reveals the many uses that can result from combining 3D printing manufacturing methods with varied nanomaterial qualities **[62].**

According to BOS et al., additive manufacturing, particularly concrete (AMoC), has drawn more attention from the building sector. AMoC is still in its infancy even if a lot of scholars and private businesses are exploring this sector. 3D Concrete Printing (3DCP) at Eindhoven University of Technology is one of numerous AMoC versions being developed worldwide. 3DCP is compared to AMoC and 3D printing. They also study 3DCP product shape, structure, parameter relations, experimental research, and large-scale 3DCP application obstacles **[63].**

DAI et al. proved that 3D-printing may assist construction companies develop customized parts, remove formwork, and save materials. Pumpability, extrudability, and buildability of 3D-printed concrete are tricky. Fly ash (FA) accelerates portlandite-induced thermal stiffening and alkali-activation. CH-FA blends stiffen quickly at 75°C but build up less at low temperatures. The FA-CH mix ratio, ideally 20%, can develop cement-free 3D-printing compositions **[64].**

CAVALCANTE et al. investigated using recycled concrete powders (RCP) to minimize 3D printing cement. The study indicated that RCPs improve 3D printing rheology

depending on origin. RCP pastes of any origin showed elevated static and dynamic yield stresses and early hydration. RCP paste viscosity changed with packing density, and increased yield stress can impair extrudability and buildability. The LCI assessment suggested RCPs may reduce CO2 emissions by 62%. RCPs could be used to make environmentally friendly 3D printed combinations with rheological changes **[65].**
NASSRULLAH et al. modified 3D printing systems with carbon nanotubes (CNTs) and silica fume to research cementitious composites. Testing indicated that 0.2 % CNTs and 20% silica fume increased printing quality, buildability, open-time, and rheology. Layer width and height error dropped from 140 % and 6% to less than 1.5 %, while buildability and open-time rose by 210 % and 263%. Both cast and 3D-printed samples had stronger compressive and flexural strengths with CNTs and silica fume. It also found that silica fume filled cement matrix gaps and CNTs formed nanoscale connections **[66].**

3.4. Admixtures

based on GIRSKAS et al. The workability, adhesion, stiffness, short setting time, and high early strength of 3D printed concrete are all controlled by chemical admixtures such superplasticizers, viscosity-modifying agents, setting retarders, and accelerators **[67].**
CO2 mixing affects cement mortar with different concentrations of Polycarboxylate superplasticizer (PCE) and hydroxypropyl methylcellulose. Results reveal that CO2 mixing considerably alters HPMC and PCE effects on cement mortar characteristics. PCE practically disappears, however 0.2 %PCE improves workability and setting time. To explore coupling effects, heat evolution and microstructural features are analyzed. We propose employing CO2 mixing and PCE to improve 3DPC buildability (Fig 3) **[68].**

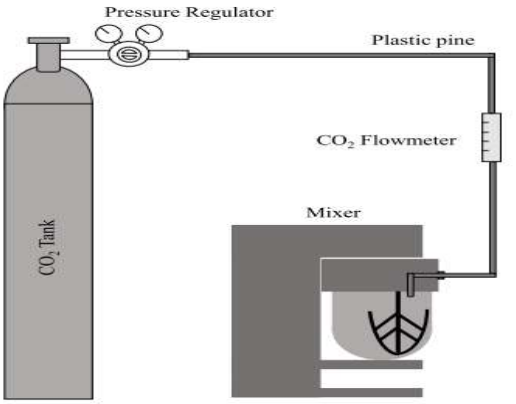

Fig.3. Schematic of the CO_2 mixing system [68].

GURUNANDAN et al. examined how water-to-binder ratio, admixtures, and increasing a/b ratio affect 3D-printable concrete mixture extrudability, buildability, and mechanical qualities. The study indicated that w/b ratio increased extrudability but decreased buildability. Adding fly ash improved extrudability, but increasing a/b ratio increased

surface imperfections and decreased it. Extrudable and buildable combinations had lower compressive strength than mold cast specimens and 2.1-2.6 kPa static yield stress. The printed specimens were not anisotropic in compression, and sequential layers had no weak joints. The findings could help create 3D-printable combination design recommendations **[69].**

Polysaccharides were added to alkali activated materials (AAMs) to improve their 3D printing properties in a comprehensive rheological investigation by SHILTON et al. AAMs are popular in construction, however printability and buildability issues prevent their use. Shirley et al. examined how Xanthan Gum (XG) concentration affected rheology, printability, and mechanical characteristics. The results are useful for developing a rheology-modifying admixture for AAMs, which will improve 3D printing without affecting setting times or compressive strength **[70].**

3D-printed concrete (3DPC) reduces labor costs, material waste, and building time, although its durability is still questioned. The layer-by-layer manufacturing technique affects material characteristics and durability. Interfacial porosity and anisotropic microstructures can weaken structures and make them more susceptible to environmental degradation. Increased layer interface porosity and shrinkage-induced cracking impair durability. Proper mix formulations and air-entraining agents can make 3DPC as durable as cast concrete. Additional cementitious components have improved chemical resistance **[71].**

ANOP et al. study investigates the use of conventional 70 mm cubes as a trustworthy indicator of in situ compressive strength in additive manufacturing. Compressive strengths were assessed after seven, fourteen, and twenty-eight days after five Portland cement mixtures were extruded into wall blocks using a 3D printer. Although the ratios between the core and cube strengths stayed constant, the core strengths were constantly inferior. For the non-destructive strength evaluation of 3D-printed concrete, the findings offer a straightforward, empirically supported procedure that opens the door for future standardization of quality-control procedures in additive construction **[72].**

3.4.1 Superplasticizer

The study by FELIPE et al. studied the impact of water/cement ratio and superplasticizer % on the use of LC^3-25 mortars in 3D printing. Results indicated that 75% metakaolin and limestone filer mixes were lighter than 100% Portland cement. Over time, superplasticizer (SP) increased air incorporation and distributed loss. In ternary mixes, SP level between 1% and 1.50% did not alter mechanical strength. The study recommends researching eco-friendly 3D printing materials **[73].**

By altering the dosage of superplasticizer and the water/binder, JANANI et al. created a 3D-printable concrete mix. They also replaced cement with 10% leftover marble powder. The process include modifying methods, material fineness, and mix proportions. The mix was improved through experimental studies with a 3D printer; the best combination with a dose of 0.35% SP, a ratio of 0.35 w/b, and a substitution of 10% marble powder produced excellent printing quality **[74].**

MAHMOOD et al. identified four research themes regarding recycled waste materials in 3DPC. They highlighted the importance of assessing physical and chemical properties, buildability, and the impact of additives like HPMC and superplasticizers on performance. Their findings indicate that higher cement content in 3D printed concrete can be economically and environmentally harmful, emphasizing the need for standardized testing and improved integration of designed architectural shapes **[75].**
DONG et al. used aeolian sand and ferrochrome slag to improve 3D printed concrete (3DPFAC). They used one-way testing to examine how critical materials affect 3D printed concrete (3DPC) operating and mechanical qualities. Silica fume, superplasticizer, polyvinyl alcohol powder, and polypropylene fiber were tested orthogonally. Silica fume 7%, superplasticizer 0.6 %, polyvinyl alcohol powder 1.2 %, and polypropylene fibers 0.2 % were the best combinations **[76].** Experimental validation indicated the improved material had good printability, uniform extrusion, smooth surface, and low height variation. 3DPFAC was more easily destroyed by external force due to its higher interfacial microcracks between layers, lower hydration degree, and evident fiber-matrix fissures **[76].**
Superplasticizers enhance the workability and rheology of 3D printed concrete (3DPC) by modifying flow characteristics and reducing viscosity, thereby facilitating essential extrusion and layering processes for successful 3D printing.

3.4.2 Viscosity agents

The construction industry is adopting automatic construction technology, especially 3D printing. This process is fast, eco-friendly, and architecturally flexible, however 3D-Printed Concrete (3DPC) has extrusion difficulties. PRATHIPATI et al. investigated how Viscosity Modifying Agents (VMAs) can improve 3DPC printability and structural integrity by altering its rheological properties. Results show that controlling VMA concentrations improves 3DPC mixture workability and buildability, which has major implications for concrete additive manufacturing technology **[77].**
SHOAEI et al. compare suspension and paste microfibrillated cellulose (MFC) with hydroxypropyl methylcellulose powders as viscosity-modifying agents (VMAs) for 3D-printable Portland cement mortars. MFC mortars had higher workability, mechanical strength, denser microstructure, viscosity, and yield stress than HPMC. While HPMC mortars were marginally more extrudable, MFC was more shape stable. Both types of 3D-printed samples demonstrated 40% lower compressive strength than mold-cast samples but equivalent flexural strength. MFC paste was the best VMA for shape stability and printability **[78].**
To assess their suitability for use in 3D printing gypsum building materials, Huang et al. contrasted three inorganic viscosity modifier admixtures (VMAs) with hydroxypropyl methylcellulose ether (HPMC): attapulgite (ATP), sodium bentonite (NB), and nano-silica (NS). According to the results, NS increased slurry fluidity at low dosages, but ATP, NB, and HPMC decreased it. While all VMAs raised yield stress, inorganic VMAs barely affected plastic viscosity. Superior workability, mechanical characteristics, and

printing performance were displayed by ATP, while NS was excellent at improving mechanical properties and NB enhanced workability and performance **[79].**
The buildability of cement-based mortars made with nanoclays (NC) and viscosity-modifying admixtures (VMA) was investigated by MARQUEZ et al. They discovered that RMA has a major impact on CBM's buildability and hydration processes. NC improved buildability and dimensional stability by exhibiting a stiffening effect. Although more superplasticizer was required, NC dominated the shear stiffening effect when coupled. Setting and initial hardening after 90 minutes were linked to the change from fresh plastic behavior to a stiff state **[80].**
Viscosity agents affect 3D-printed concrete's workability, strength, and printability. VMAs increase concrete rheology, which is necessary for 3D printing.

3.4.3 Accelerator

Accelerators affected the rheology of 3D printed concrete (3DPC) with cellulose microfibers, according to CHO et al. CMFs reduce shrinkage and damage but delay setting, limiting 3DPC structuration and buildability. The study investigated 16 cement composites with different CMF and accelerator concentrations. CMF presence increased dynamic yield stress by 18% and plastic viscosity by 12%, while static yield stress was unaffected. The accelerator enhanced static yield stress by 290% and structuration rate by 400%. To improve 3DPC buildability and combat CMF deterioration, accelerators are recommended **[81].**
Active management of limestone calcined clay cement (LC3) paste fluidity and adjustable structural build-up improve subterranean shotcrete and 3D-printed concrete applications. JI et al. study LC3 paste fluidity and structural build-up using a non-alkaline accelerator and polycarboxylate ether (PCE) superplasticizers and retarders. The study found that high PCE dosages or lower PCE with a retarder can sustain fluidity for 6 hours. In high-PCE mixes, early accelerator addition accelerates ettringite production and structural acceleration, affecting penetration force and modulus. In situ XRD, heat release analysis, differential thermal gravimetry (DTG), and scanning electron microscopy were used to evaluate rheological behavior and microstructural development **[82].**
The use of advancement accelerators in 3D printing concrete enhances efficiency, sustainability, and design flexibility in construction projects, improving overall processes and outcomes.

3.4.4 Retarder

SENF et al. creates concrete mixes utilizing calcium sulfoaluminate (CSA) cement and blast furnace cement (CEM III/B) for 3D printing in response to environmental issues caused by regular Portland cement. In comparison to combinations without retardation, retarders specifically, a 0.60 weight percent mixture of tartaric acid and phosphate optimize the setting time for a 90-minute 3D printing window, resulting in early compressive strengths of about 96% and 28-day strengths of around 55%. According to

analyses, the slower hydration of Portland clinker and CSA is the cause of the 28-day strength decrease. When stresses were applied perpendicularly to printed layers, the application of 30 weight percent CSA and 70 weight percent CEM III/B demonstrated enhanced compressive strengths. Because of regulated setting, early strength, and steady long-term strength development, these findings encourage the efficient manufacture of precast concrete parts **[83].**

The use of retarders in 3D printing concrete improves material performance by extending the setting time, enhancing workability, and reducing temperature stress, which is vital for large-scale printing. This overview will examine the types of retarders, their advantages, and their effects on the mechanical properties of 3D printed concrete.

3.5. fibers

3.5.1 steel fibers

In order to increase the flexural strength, toughness, and stiffness of mortar beams, LI et al. have created a two-scale technique utilizing 3D concrete printing (3DCP). Three patterns—rectangle, triangle, and Hilbert curve are used to generate steel fiber reinforced 3DCP infills. According to four-point bending tests, a rectangular arrangement of steel fibers enhanced flexural strength and toughness by more than 100%, while a triangular configuration resembling a truss boosted flexural stiffness by 59%. Additionally, the technique showed that it was possible to create structures with planned interior designs that were material-efficient **[84].**

A method for in-situ magnetization of steel fibers in 3D printed concrete is proposed by HUANG et al. with the goal of enhancing crack-bridging capacity. They look at the connection between fiber magnetic orientation and crucial process parameters (Fig 4). According to the results, 25mm bow steel fibers (BF25) significantly improve mechanical characteristics by more than 50% and have the greatest impact on bridging cracks. This demonstrates how fiber magnetic orientation can be used in 3D printed engineering concrete (Fig 5) **[85].**

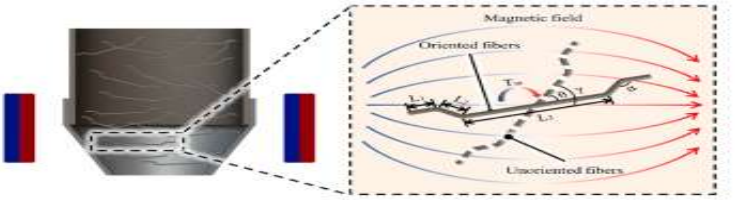

Fig 4. Schematic diagram of steel fiber orientation in magnetic field [85].

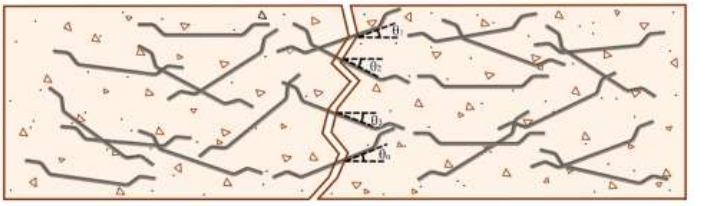

Fig 5. Schematic illustration of fiber alignment evaluation in concrete [85].

3D printing ultra-high performance concrete (UHPC) reduces structural steel reinforcement, according to CHEN et al. Their study examined how water-to-binder ratios, recycled steel fibre (RSF) volume, and thickener concentration affected RSF-reinforced UHPC rheology and extrudability. Lower water-to-binder ratios, higher RSF content, and thickening application enhanced static and dynamic yield stress, extrudability, and buildability. At 0.16 water-to-binder ratio, 3% RSF volume, and 0.1% thickener concentration, the best combination was found.**[86].**

In order to improve mechanical qualities, interlayer bonding, and durability without sacrificing printability, MORTADA et al. have effectively reinforced 3D-printed Ca(OH)2-activated geopolymer concrete (GPC) with recycled steel fibersFlexural strength increased 69% and tensile strength tripled to 3.75 MPa after 28 days with 1.2% SF. A crucial issue with 3D-printed concrete, the study also discovered that SF enhanced early-age toughness and minimized fracture propagation between printed layers. The study shows how recycled steel fibers may enhance the qualities of 3D-printed concrete and provides a sustainable reinforcing method for 3D printing in construction **[87].**

Using steel fibers as responsive elements, GUO et al. studied cement paste magneto-rheology. A camera-equipped mini-slump device recorded cement paste flow under magnetic fields at varying water-to-cement ratios and steel fiber concentrations. After a short-term vertical magnetic field, cement pastes with steel fibers reduced by 0.7%-8.2%, and after a horizontal magnetic field, the flow velocity and parallel flow diameter decreased. Steel fibers migrate under a magnetic field and retain their places, causing an uneven distribution, the study found. These findings suggest active regulation of steel fiber-reinforced cement-based composites' rheology **[88].**

Advanced steel fibers enhance the mechanical properties of 3D printed concrete, improving tensile strength, compressive strength, and durability. Their specific shapes and volumes allow for better alignment during printing, optimizing concrete performance.

3.5.2 polypropylène fibers

Polypropylene fibers improve the mechanical properties of 3D printed concrete, increasing compressive strength, flexural strength, and dimensional stability, particularly with an optimal fiber length of 6 mm and a utilization ratio of 0.4%. **[89]**

HOPKINS et al. analyze the impact of polypropylene (PP) fibers in three-dimensional printed concrete (3DPC). While PP fibers enhance form retention, rheological properties, and interlayer bonding, they can increase yield stress and viscosity, affecting extrudability. An optimal dosage of fibers improves compressive and flexural strength, but excessive amounts may lead to clustering and decreased performance. Aligned fibers can reduce shrinkage-induced cracking and affect mechanical anisotropy. The study highlights gaps in the understanding of hybrid systems and fiber orientation, advocating for standardized testing. Optimal print quality is associated with 6 mm fibers, nozzle sizes of 4 to 6 mm, and speeds of 40 to 60 mm/s **[90].**

Polypropylene fibres enhance the compressive strength of materials by 5–30%, flexural strength by 10–50%, and ductility and toughness by 30% to 160%. They significantly

improve crack resistance and fire resistance, retaining up to 80% of residual strength at 600°C. Additionally, polypropylene fibres increase freeze-thaw resistance by 15–40% and sulfate and chloride resistance by 20–55% **[91].**

XIA et al. studied how polypropylene (PP), basalt, and steel fibers (Fig 5) affect 3D printed concrete's workability, printability, rheology, and mechanical qualities. owing to greater cement paste consumption, PP fibers reduced flow spread, basalt fibers reduced it owing to water absorption, and steel fibers reduced it the most due to density and interlocking. Steel fibers had the most influence, with ideal mechanical characteristics at 0.5% PP, 0.3% basalt, and 0.7% steel. Steel fibers' stiffness and matrix interlocking increased strength best. The study also discovered that print strips had primarily vertical PP fibers **[92].**

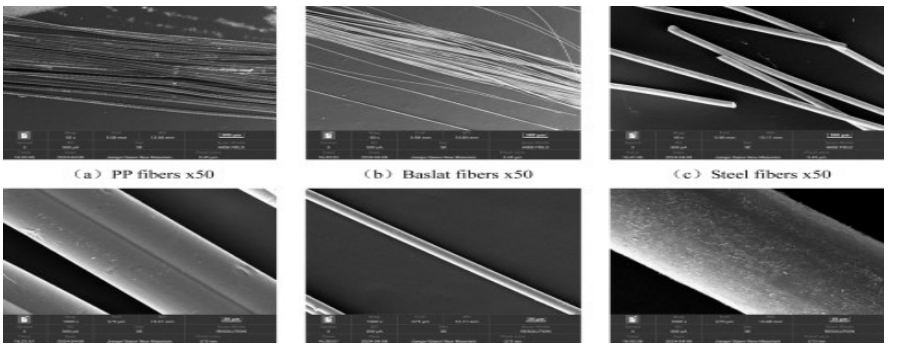

Fig 6 Micro morphology of PP fibers, basalt fibers, and steel fibers [92].

Polypropylene fibers enhance the mechanical properties of 3D printed concrete, im proving strength, ductility, and durability, which makes the mix more suitable for various structural applications.

3.5.3 polyethylene fibers PE

All three types of embedded filament fibers—Basalt, Glass, and Polyethylene—enhanced the mechanical properties of 3D printed mortar, with Polyethylene fiber providing the most significant improvements: a 36.4% increase in flexural strength, a 29.9% increase in compressive strength, and a 36.1% improvement in interlayer bond strength. LI et al. concluded that these fibers bonded effectively with the cement mortar **[93].**

As formwork, LIU et al. suggested hollow 3D printed mortar (3DPM) columns reinforced with continuous PE or carbon fibers. The hollow formwork was filled with concrete to build columns to study continuous fiber reinforcement's impact on compressive strength and confinement. Compressive strength and nonlinear behavior were studied using theoretical and finite element approaches. 23.36% increased strength for 12 K carbon fibers, while 996% increased ductility for 3 K. Due to the 8.72% and 811% strength increases of three-strand and single-strand PE fibers, ductile failure occurred. These results show that continuous fiber-reinforced 3D printed concrete can increase ductility by following the production process (Fig 7) **[94].**

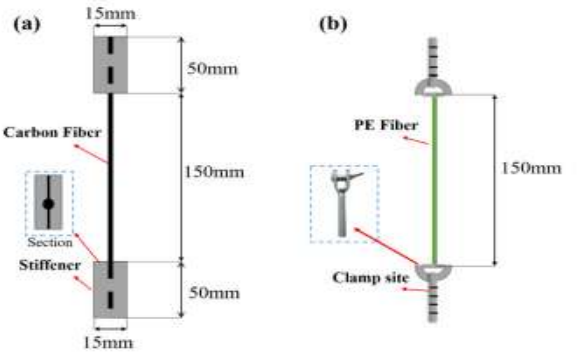

Fig 7 Fiber tensile strength test (a) carbon fiber (b) PE fiber [94].

LIU et al. demonstrated that enhancements in polyethylene (PE) fiber parameters—length, aspect ratio, and elastic modulus—significantly enhance the tensile properties of high-strength high-ductility concrete (HSHDC). Improvements in tensile strength, strain, and energy dissipation range from approximately 10.1% to 34.8%, 10.6% to 120%, and 14.1% to 186%, respectively. The optimal fiber parameters for HSHDC were determined to be a fiber length of 12 mm and a diameter of 24 μm for compressive performance, while a length of 15 mm and diameter of 27 μm were found optimal for tensile performance. Additionally, a mechanical constitutive model was developed that correlates well with experimental outcomes **[95].**

According to PHAM et al., molded specimens demonstrated superior strength compared to 3D-printed ones, with Z orientation strengths surpassing those in Y orientation. The optimal fiber content for polyethylene (PE) and high-modulus polyethylene (HPE) reinforcement in printed concrete was found to be 0.5%. The study evaluated the flexural and compressive strengths of thirty-six printed and twenty-one molded specimens, analyzing cracking patterns that highlighted differences in mechanical behavior between the two types **[96].**

Using 3D printing cementitious composites 3DP-ECC eliminates steel reinforcement to increase crack resistance. As a cheaper, greener quartz sand substitute, 3DP-ECC uses hybrid polyethylene and polyvinyl alcohol fibers with Yellow River Sand. RAZA et al. explore its mechanical and microstructural properties. Above 3% tensile stress, Cast and 3DP-ECC strain-harden. With 4.60% and 3.90% stresses, cast ECC has 6.58 MPa tensile strength and 3DP-ECC 4.60 MPa. Exemplars bent less in X and Y than Z. R50 castings collapse at 49.7 MPa, 3DP specimens 45.9. YRS concentration lowered 3DP-ECC porosity and interlayer gaps, although fiber-matrix bonding and hydration gels were found. The study suggests optimizing fiber alignment and interlayer bonding to strengthen 3DP-ECC **[97].**

Polyethylene fibers improve the mechanical properties of 3D printed concrete by enhancing compressive and flexural strengths, along with interlayer bond strength. Their incorporation compensates for the limitations of traditional 3D printing, which often excludes steel bars, resulting in a more robust and durable material for structural applications.

4. Conclusion

Innovation in materials for 3D concrete printing is revolutionizing the construction sector by improving productivity, offering greater architectural freedom, and enhancing durability. However, for this technology to become a reliable and widely adopted standard, it is essential to continue research on several critical aspects such as interlayer strength, durability, material reinforcement, mixture stabilization, and process standardization. Addressing these technical and scientific challenges is crucial to enable 3D concrete printing to evolve from an emerging technology to a fully mastered and sustainable solution for the future of buildings. This transition could transform not only construction methods but also the standards that underpin the modern construction industry.

Reference

[1] GULATI, Hemant; LU, Tianxiang. Customized 3-D printable concrete: a systematic review of challenges, methodologies, and adoption strategies. *Innovative Infrastructure Solutions*, 2025, 10.4: 154.
[2] HASSAN, Amer, et al. 3D printed concrete for sustainable construction: A review of mechanical properties and environmental impact. *Archives of Computational Methods in Engineering*, 2025, 1-31.
[3] ZHUANG, Zicheng, et al. A comprehensive review of sustainable materials and toolpath optimization in 3D concrete printing. *npj Materials Sustainability*, 2024, 2.1: 12.
[4] WIJETHUNGE, Anjalee, et al. A Systematic Review on Sustainable 3D Concrete Printing: Opportunities and Challenges. In: *CIB Conferences*. 2025. p. 204.
[5] BANIHASHEMI, Saeed, et al. 3D printing in construction: sustainable technology for building industry. *Progress in Additive Manufacturing*, 2025, 1-34.
[6] ALAMI, Abdul Hai, et al. 3D concrete printing: recent progress, applications, challenges, and role in achieving sustainable development goals. *Buildings*, 2023, 13.4: 924.
[7] HIREMATH, Shivashankarayya, et al. Performance evaluation of cementitious composites by designing an extrusion system for construction 3D printing. *Scientific Reports*, 2025, 15.1: 17669.
[8] GIRSKAS, Giedrius; KLIGYS, Modestas. 3D Concrete Printing Review: Equipment, Materials, Mix Design, and Properties. *Buildings*, 2025, 15.12: 2049.
[9] ODAGLIA, Pietro. *3D PRINTING ARCHITECTURE-Open Framework for Binder Jetting in Construction*. 2024. PhD Thesis. ETH Zurich.
[10] REZNIK, Petro, et al. Numerical Analysis of 3D-Printed Permanent Formwork in Multi-story Building Construction. In: *International Conference on Smart Technologies in Urban Engineering*. Cham: Springer Nature Switzerland, 2024. p. 254-265.
[11] IBRAHIM A, Mohamed; KUMAR N, Senthil. 3D printed concrete using Portland pozzolana cement-fly ash based. In: *E3S Web of Conferences*. EDP Sciences, 2024. p. 01019.
[12] MAROSZEK, Marcin; RUDZIEWICZ, Magdalena; HEBDA, Marek. Recycled Components in 3D Concrete Printing Mixes: A Review. *Materials*, 2025, 18.19: 4517
[13] LUO, Surong, et al. Effects of carbonated recycled sand on the interfacial bonding performance of 3D printed cement-based material. *Journal of Building Engineering*, 2025, 99: 111551.
[14] COLYN, Markus; VAN ZIJL, Gideon; BABAFEMI, Adewumi John. Fresh and strength properties of 3D printable concrete mixtures utilising a high volume of sustainable alternative binders. *Construction and Building Materials*, 2024, 419: 135474.
[15] OVER, Derya, et al. An investigation of rheological properties and sustainability of various 3D printing concrete mixtures with alternative binders and rheological modifiers. *Journal of Sustainable Cement-Based Materials*, 2025, 14.3: 521-533.

[16] TSENG, Kuo-Chang, et al. Influence of Slag/Fly Ash as Partial Cement Replacement on Printability and Mechanical Properties of 3D-Printed Concrete. *Applied Sciences*, 2025, 15.7: 3933.
[17] VICO LUJANO, Raúl, et al. Optimized Mortar Formulations for 3D Printing: A Rheological Study of Cementitious Pastes Incorporating Potassium-Rich Biomass Fly Ash Wastes. *Materials*, 2025, 18.15: 3564.
[18] LI, Leo Gu, et al. Improving mechanical properties of 3D printed mortar through synergistic effects of fly ash microspheres and nanosilica. *Magazine of Concrete Research*, 2025, 77.5-6: 255-269.
[19] ALI, Noorwirdawati. 3D Concrete Printing with Industrial Waste: Effects of GGBS and Spent Catalyst on Fresh and Hardened Properties. *International Journal of Integrated Engineering*, 2025, 17.3: 68-76.
[20] SI, Wen; KHAN, Mehran; MCNALLY, Ciaran. Effect of nano silica with high replacement of GGBS on enhancing mechanical properties and rheology of 3D printed concrete. *Results in Engineering*, 2025, 106680.
[21] MISHRA, Sanjeet Kumar; UPADHYAY, Bikash; DAS, Bibhuti Bhusan. 3D printing aspects of fly ash and GGBS admixed binary and ternary blended cementitious mortar. *European Journal of Environmental and Civil Engineering*, 2025, 1-31.
[22] NASSRULLAH, Ghaith, et al. Optimizing cement-based material formulation for 3D printing: integrating carbon nanotubes and silica fume. *Case Studies in Construction Materials*, 2025, 22: e04579.
[23] PANTIRU, Alexandru; LUCA, Bogdan Ionel; BARBUTA, Marinela. Experimental study of mixture proportions and fresh properties of concrete with fly ash and silica fume as a replacement for cement for 3D printing. *Environmental Engineering and Management Journal*, 2023, 22.9: 1647-1653.
[24] THAJEEL, Marwah M.; KOPECSKÓ, Katalin; BALÁZS, György L. Enhancing printability of 3D printed concrete by using metakaolin and silica fume. *Structural Concrete*, 2025.
[25] WANG, Chaofan; LI, Bin; CHEN, Bing. Enhancing printability and mechanical performance of 3D printed magnesium phosphate cement through silica fume modification: Rheological, microstructural, and numerical insights. *Construction and Building Materials*, 2025, 477: 141302.
[26] AHMED, Aly Muhammed Aly; MANTAWY, Islam M. Additive Construction of Low Embodied Carbon Concrete: Geopolymer Concrete. *Journal of Building Engineering*, 2025, 112984.
[27] YOUSSEF, Passant, et al. Characterization of geopolymer composites for 3D printing: a microstructure approach. *Innovative Infrastructure Solutions*, 2024, 9.5: 157.
[28] SILVESTRO, Laura; SCOCZYNSKI, Rodrigo; NAVARRETE, Iván. Advancements in low carbon emission cements for 3D printing: a state-of-the-art review. *Revista Ingeniería de Construcción*, 2024, 39.Special Issue: 1-10.
[29] OUMAR, Ali Idriss. Review of Geopolymer Concrete: Reaction Mechanisms, Mechanical Behavior, and Environmental Benefits.
[30] KRAVCHENKO, Ekaterina, et al. Transforming Construction Waste into Resources for 3D Printed Concrete. In: *ISARC. Proceedings of the International Symposium on Automation and Robotics in Construction*. IAARC Publications, 2025. p. 792-796.
[31] ELHAG, Ahmed Babeker, et al. Advances in Sustainable 3D-Printed Geopolymer Concrete: Materials, Performance, and Environmental Impact in Next Generation Green Construction. *JOM*, 2025, 1-39.
[32] SILVESTRO, Laura; SCOCZYNSKI, Rodrigo; NAVARRETE, Iván. Advancements in low carbon emission cements for 3D printing: a state-of-the-art review. *Revista Ingeniería de Construcción*, 2024, 39.Special Issue: 1-10.
[33] MORTADA, Youssef, et al. 3D Printable Ca (OH) 2-based geopolymer concrete with steel fiber reinforcement. *Materials and Structures*, 2025, 58.2: 73.
[34] HUANG, Jianxiang, et al. Feasibility of applying attapulgite, sodium bentonite and nano-silica as a viscosity modifier admixture for 3D printing of gypsum-based materials. *Journal of Building Engineering*, 2025, 112745.
[35] XIANG, Maolong, et al. Advanced physical modeling of tunnel behavior in stratified strata: insights from 3D printing and gypsum-based materials. *Case Studies in Construction Materials*, 2025, e04772.

[36] TARHAN, Yeşim; ATALAY, Berrin. Phosphogypsum and borogypsum as additives for sustainable and high-performance 3D-Printable concrete. *Polymers*, 2025, 17.18: 2530.
[37] TEIXEIRA, João, et al. Large Format Additive Manufacturing with Cement and Clay Applications. *Large Format Additive Manufacturing: Polymers, Metals, and Ceramics*, 2026, 245-268.
[38] GONSALVES, Nicolas A., et al. 3D printing of sustainable infrastructure using rapid-set clay concrete with biobased additives. *Advanced Composites and Hybrid Materials*, 2025, 8.5: 359.
[39] SAHMENKO, Genadijs, et al. Gypsum–cement–Pozzolan composites for 3D printing: properties and life cycle assessment. *Journal of Composites Science*, 2024, 8.6: 212.
[40] SI, Wen, et al. Towards Sustainable Mortar: Optimising Sika-Fibre Dosage in Ground Granulated Blast Furnace Slag (GGBS) and Silica Fume Blends for 3D Concrete Printing. *Buildings*, 2025, 15.19: 3436.
[41] KAUR, Zinnia, et al. Pore structure analysis and durability performance of sustainable 3D printed concrete incorporating fly ash and limestone calcined clay based binders. *Construction and Building Materials*, 2025, 490: 142577.
[42] XUE, Jia-Chen, et al. Development of Sustainable 3D Printing Concrete Materials: Impact of Natural Minerals and Wastes at High Replacement Ratios. *Journal of Building Engineering*, 2025, 114020.
[43] SUREHALI, Sahil, et al. Ultra-low dosages of novel graphene types enhance the rheological properties and buildability of 3D printed binders. *Next Materials*, 2025, 8: 100811.
[44] PEPE, Marco, et al. Experimental Evidence on the Possible Use of Fine Concrete and Brick Recycled Aggregates for 3D Printed Cement-Based Mixtures. *Materials*, 2025, 18.3: 583.
[45] Ma, Jinyi, et al. "Effect of clay brick powder and recycled fine aggregates on properties of 3D printed concrete after high temperature exposure." *Construction and Building Materials* 491 (2025): 142676.
[46] Jia, Lutao, et al. "Initial plastic shrinkage of 3D-printed concrete incorporating recycled brick fine aggregates: Insights from water transport and structural evolution." *Journal of Building Engineering* 106 (2025): 112665.
[47] Demirbaş, Ali Osman, et al. "A comprehensive study on the valorization of recycled concrete aggregates in 3D-printable cementitious systems." *Structures*. Vol. 77. Elsevier, 2025.
[48] MIM, Nusrat Jahan, et al. Rheological and early age mechanical properties of 3D printed concrete containing copper heap leach residue as fine aggregate. *Results in Engineering*, 2025, 106280.
[49] LIANG, Hui, et al. Effect of multiscale particle morphology on small-strain shear modulus of irregularly shaped sand under isotropic consolidation: triaxial bender element tests on 3D-printed sand. *Journal of Engineering Mechanics*, 2024, 150.4: 06024001.
[50] SHI, Danda, et al. Experimental study on mechanical properties of triaxial geogrid reinforced marine coral sand-clay mixture based on 3D printing technology. *Frontiers in Marine Science*, 2025, 12: 1660611.
[51] MENGISTU, Girum Mindaye; NEMES, Rita. Evaluating the performance of recycled aggregate concrete incorporating 3D-Printed concrete waste as aggregate using the rebound hammer test. *Heliyon*, 2025, 11.4.
[52] LIU, Chao, et al. Effect of X-ray CT characterized pore structure on the freeze–thaw resistance of 3D printed concrete with recycled coarse aggregate. *Construction and Building Materials*, 2025, 469: 140492.
[53] MIM, Nusrat Jahan; SHAIKH, Faiz Uddin Ahmed; SARKER, Prabir Kumar. Sustainable 3D printed concrete incorporating alternative fine aggregates: A review. *Case Studies in Construction Materials*, 2025, e04570.
[54] Kumar, Sandeep, et al. "Low-clay soil as fine aggregate in 3D printed concrete: insights into fresh and hardened properties." *Journal of Sustainable Cement-Based Materials* (2025): 1-17.
[55] WANG, Xianggang, et al. Optimization of 3D printing concrete with coarse aggregate via proper mix design and printing process. *Journal of Building Engineering*, 2022, 56: 104745.
[56] CHEN, Yidong, et al. Extrusion-based 3D printing concrete with coarse aggregate: Printability and direction-dependent mechanical performance. *Construction and Building Materials*, 2021, 296: 123624

[57] WANG, Hailong, et al. Influences of particle size on the performance of 3D printed coarse aggregate concrete: Experiment, microstructure, and mechanism analysis. Construction and Building Materials, 2025, 463: 140059.
[58] NAZIR, Usman; LIAO, Min-Chih; VO, Duy-Hai. Sustainable use of 3D-printed plastic waste as aggregate in self-compacting mortar: A study on rheological, mechanical and thermal performance. *Environmental Science and Pollution Research*, 2025, 1-13.
[59] WANG, Suguo, et al. Effects of Aggregate Size and Nozzle Diameter on Printability and Mechanical Properties of 3D Printed Ferronickel Slag–GGBFS Concrete. *Materials*, 2025, 18.15: 3681.
[60] PARITALA, Spandana, et al. Designing 3D printable concrete by integrating the influence of aggregate characteristics. *Materials and Structures*, 2025, 58.8: 1-21.
[61] GIRSKAS, Giedrius; KLIGYS, Modestas. 3D Concrete Printing Review: Equipment, Materials, Mix Design, and Properties. *Buildings*, 2025, 15.12: 2049.
[62] JIN, Peng, et al. Micro/nano additives in 3D printing concrete. *Cement and Concrete Composites*, 2025, 155: 105799.
[63] BOS, Freek, et al. Additive manufacturing of concrete in construction: potentials and challenges of 3D concrete printing. *Virtual and physical prototyping*, 2016, 11.3: 209-225.
[64] DAI, Xiaodi, et al. Thermally stimulated stiffening and fly ash's alkaline activation by Ca (OH) 2 addition facilitates 3D-printing. *Cement and Concrete Composites*, 2025, 156: 105870.
[65] CAVALCANTE, Tiago Canavarro; FILHO, Romildo Dias Toledo; REALES, Oscar Aurelio Mendoza. Rheological and Environmental Implications of Recycled Concrete Powder as Filler in Concrete 3D Printing. *Buildings*, 2025, 15.8: 1280.
[66] NASSRULLAH, Ghaith, et al. Optimizing cement-based material formulation for 3D printing: integrating carbon nanotubes and silica fume. *Case Studies in Construction Materials*, 2025, 22: e04579.
[67] GIRSKAS, Giedrius; KLIGYS, Modestas. 3D Concrete Printing Review: Equipment, Materials, Mix Design, and Properties. *Buildings*, 2025, 15.12: 2049.
[68] LI, Long, et al. Strategy for improving buildability of 3D printing concrete using CO2 mixing and chemical admixtures. *Construction and Building Materials*, 2025, 489: 142122.
[69] GURUNANDAN, M.; MALLA, Hiranya Jeet; NANTHAGOPALAN, Prakash. Effect of water to binder, aggregate to binder ratio and admixtures on printability and mechanical properties of 3D printable mortar mixtures. *Journal of Building Engineering*, 2025, 99: 111649.
[70] SHILTON, Robert; WANG, Shen; BANTHIA, Nemkumar. Use of polysaccharides as a rheology modifying admixture for alkali activated materials for 3D printing. *Construction and Building Materials*, 2025, 458: 139661.
[71] BRADSHAW, James, et al. Emerging Insights into the Durability of 3D-Printed Concrete: Recent Advances in Mix Design Parameters and Testing. *Designs*, 2025, 9.4: 85.
[72] ANOP, Darya, et al. Additive manufacturing as an alternative to core sampling in concrete strength assessment. *Applied Sciences*, 2025, 15.14: 7737.
[73] FELIPE, Maria Luíza Cardoso, et al. Effects of water/cement ratios and superplasticizer on LC³-25 to 3DCP mortars. *Caderno Pedagógico*, 2025, 22.5: e14892-e14892.
[74] JANANI, Parthiban; SANTHI, A. S. A study on the optimization of superplasticizer and water-to-binder ratio for enhancing 3D printable concrete with marble powder waste. *Advances in Science and Technology. Research Journal*, 2025, 19.6.
[75] MAHMOOD, Ali Ahmed Mahmood, et al. Recycled waste materials utilised in 3D concrete printing for construction applications: a scientometric review. *Buildings*, 2025, 15.19: 3572.
[76] DONG, Wei, et al. Optimal design of mix proportions for 3D printed concrete with ferrochrome slag and aeolian sand. *Journal of Building Engineering*, 2025, 113385.
[77] PRATHIPATI, SRR Teja, et al. An experimental study on the effect of a Viscosity Modifying Agent on the rheological and strength behaviour of 3D Printed Concrete. In: *Journal of Physics: Conference Series*. IOP Publishing, 2024. p. 012087.
[78] SHOAEI, Parham, et al. Comparative analysis of 3D printing of Portland cement mortars with hydroxypropyl methylcellulose and microfibrillated cellulose as viscosity modifying agents. *Materials & Design*, 2024, 244: 113124.

[79] HUANG, Jianxiang, et al. Feasibility of applying attapulgite, sodium bentonite and nano-silica as a viscosity modifier admixture for 3D printing of gypsum-based materials. *Journal of Building Engineering*, 2025, 112745.
[80] MARQUEZ, Alvaro; VARELA, Hugo; BARLUENGA, Gonzalo. Influence of rheology modifying admixtures on the buildability of 3D printing cement-based mortars. *Journal of Sustainable Cement-Based Materials*, 2025, 1-13.
[81] CHO, Eunsan, et al. Impact of accelerator on rheological properties of cement composites with cellulose microfibers: 3D printing perspective. *Journal of Building Engineering*, 2025, 106: 112538.
[82] JI, Yanliang, et al. Structural build-up in sustainably plasticized limestone calcined clay cement (LC3) pastes with accelerator addition. *Construction and Building Materials*, 2025, 487: 142074.
[83] SENF, Ferdinand, et al. Enhanced environmental sustainability of 3D-printed concrete mixtures based on calcium sulfoaluminate (CSA) and blast furnace cement (CEM III/B). In: *MATEC Web of Conferences*. EDP Sciences, 2025. p. 06004.
[84] LI, Shuai, et al. Two-scale 3D printed steel fiber reinforcements strategy for concrete structures. *Construction and Building Materials*, 2025, 458: 139626.
[85] HUANG, Junxiang, et al. Mechanism analysis of the magnetic field assisted 3D printed steel fiber reinforced concrete. Construction and Building Materials, 2025, 458: 139737.
[86] CHEN, Meng, et al. 3D printability of recycled steel fibre-reinforced ultra-high performance concrete. *Construction and Building Materials*, 2025, 462: 139877.
[87] MORTADA, Youssef, et al. 3D Printable Ca (OH) 2-based geopolymer concrete with steel fiber reinforcement. *Materials and Structures*, 2025, 58.2: 73.
[88] GUO, Xintong; HU, Shengming; JIAO, Dengwu. Flowability responses of cement paste containing steel fiber to external magnetic field. *Journal of Building Engineering*, 2025, 103: 112220.
[89] ŞAHIN, Hatice Gizem; AKGÜMÜŞ, Fatih Eren; MARDANI, Ali. Mechanical and rheological properties of fiber-reinforced 3D printable concrete; in terms of fiber content and aspect ratio. *Structural Concrete*, 2025, 26.2: 1597-1612.
[90] HOPKINS, Ben, et al. Recent Advancements in Polypropylene Fibre-Reinforced 3D-Printed Concrete: Insights into Mix Ratios, Testing Procedures, and Material Behaviour. *Journal of Composites Science*, 2025, 9.6: 292.
[91] KUDOLI, Anand B.; PATIL, Rahul S.; YEOLE, Mayura M. Recent Advances in Polypropylene Fibre-Reinforced Concrete: A Systematic Review on Mechanical Characteristics and Durability Performance. *Journal of Mines, Metals & Fuels*, 2025, 73.9.
[92] XIA, Zhenjiang, et al. Comparative analysis of polypropylene, basalt, and steel fibers in 3D printed concrete: Effects on flowability, printabiliy, rheology, and mechanical performance. *Construction and Building Materials*, 2025, 465: 140098.
[93] LI, Weihong, et al. Effect of Embedded Filament Fibers on Mechanical Properties of 3D Printing Cement-Based Materials. In: *International Conference on Green Building, Civil Engineering and Smart City*. Singapore: Springer Nature Singapore, 2023. p. 439-446.
[94] LIU, Qiong, et al. Compressive performance and damage evolution of concrete short columns with shell-filling structure confined by continuous fiber reinforced 3D printed mortar. *Construction and Building Materials*, 2025, 475: 141212.
[95] LIU, Jintao, et al. Influence of polyethylene fiber parameters on the mechanical properties of high-strength high-ductility concrete: An experimental study and constitutive model. *Journal of Building Engineering*, 2024, 88: 109128.
[96] PHAM, Loan Thi; NGUYEN, Thi Hoai Thu; HUANG, Jie Yi. Experimental study on anisotropic mechanical properties of 3D reinforced concrete with discrete polyethylene fibers. 2025.
[97] RAZA, Ali, et al. Evaluation of Mechanical and Microstructural Properties of Sustainable 3D-Printed Engineered Cementitious Composites Incorporating Hybrid PE/PVA Fibers and Yellow River Sand. *Case Studies in Construction Materials*, 2025, e05578.

Reducing the risk associated with dams through dedicated tracking systems. Selection of options for additional behaviour monitoring for existing dams

Reducerea riscurilor asociate barajelor prin sisteme dedicate de monitorizare. Selectarea opțiunilor pentru monitorizarea suplimentară a comportării barajelor existente

George Boian[1], Dan Stematiu[1], Catalin Popescu[2], Alexandru Ilie[1]

[1]Universitatea Tehnică de Construcții București
124 Lacul Tei Blvd., Bucharest, Romania
e-mail: *stematiu@utcb.ro*

[2]Universitatea Tehnică de Construcții București
124 Lacul Tei Blvd., Bucharest, Romania
e-mail: *catalin.popescu@utcb.ro*

DOI: 10.37789/rjce.2026.17.2.15

Abstract: Ensuring the safety of large dams is a legal and ethical obligation that requires continuous assessment of structural behaviour and associated risks. This study proposes a decision-based framework for risk reduction through dedicated behaviour monitoring systems (BBM), emphasizing their role in detecting atypical responses and preventing potential failures. A quantitative method is developed to evaluate the effectiveness (r) of supplementary monitoring interventions by correlating reductions in failure probabilities across distinct failure mechanisms. The framework is applied to the Vidraru Dam (Romania), a concrete arch dam undergoing refurbishment, including a full filling–emptying operational cycle. Historical behaviour data and previous emptying events are reviewed to identify specific vulnerabilities related to thermal, hydraulic, and structural stress variations. Multiple supplementary monitoring options—mathematical modelling, telemeter reactivation, 3D laser scanning, InSAR tracking, hydrogeological boreholes, and inclinometer casing are evaluated based on risk reduction efficiency, implementation cost, and net benefit. Results show that a combined strategy integrating finite element modelling, telemetric upgrades, 3D scanning, and hydrogeological instrumentation yields the optimal balance between safety and cost- effectiveness, achieving the greatest reduction in annual risk rate. The proposed methodology provides a systematic approach for decision-making in dam safety management under atypical operating conditions.

Key-words: dams, safety, BBM

The article was received on 27.01.2026, accepted on 27.05.2026 and published on 12.06.2026

1. Decision criterion

Reducing the risk associated with dams to a rational minimum is a legal and moral obligation of dam owners as well as authorities. An effective means of reducing risk is to ensure an adequate system for monitoring dam behaviour, capable of detecting atypical behaviour and adverse events that may dangerously evolve towards dam failure. If such a tendency is identified, structural and/or non-structural measures can prevent failure. The behaviour monitoring system, together with the other structural safety measures, ensures risk reduction by decreasing the probability of failure [2]. Most specialists consider that an adequate monitoring system reduces the probability of failure by an order of magnitude [3], going as far as to state that a well monitored dam will not fail (Lafitte, 1996).
The behaviour monitoring system must be well targeted to the relevant safety parameters and must be sufficiently detailed to monitor the whole dam-foundation-lake ensemble. In the case of atypical behaviour or particular operating conditions, the dam behaviour monitoring system shall be supplemented.
The effectiveness of risk reduction through additional behavioural surveillance (or maintenance and restrictions in operational plans) is quantified by the rate of reduction of the annual rate of risk. If P_r is the probability of failure of the existing dam and $P_r^{'}$ is the new probability of failure, reduced as a result of the planned measures, the relationship is used:

$$P_r^{'} = P_r(1-r) \quad (1.1)$$

where *r* is a measure of the effectiveness of the interventions.

The dam may fail by different failure mechanisms depending on the primary events that trigger them. The measures envisaged or the way of supplementing the behaviour monitoring system have different effects on the different failure mechanisms, also reducing the associated failure probabilities differently. For example, pendulum supplementation does not provide relevant information for the prevention of spill rupture and thus has minimal effects on the corresponding rupture probability of this mechanism. Likewise, an additional system of automatic condition checking and control of the hydromechanical equipment reduces the probability of overtopping failure over crest (while maintaining the maximum flow discharge capacity), but has no effect on the probability of internal erosion failure.
If we denote by *j (j* = 1,...., *n)* the potential failure mechanisms and by $P_{r,\,j}$ their associated failure probabilities, then the total probability of failure is given by the relation:

$$P_r = \sum_{1}^{n} \cdot P_{r,j} \quad (1.2)$$

A particular measure expected to increase safety (e.g. increasing the number of piezometers) has different effects in reducing the probabilities of breakage associated

with different mechanisms:

$$P'_{r,j} = P_{r,j}(1 - r_j) \quad (1.3)$$

where r_j is the effectiveness of the intervention for mechanism j.

From relations (6.1) and (6.3)

$$P'_r = P_r(1 - r) = \sum_1^n P_{r,j}(1 - r_j) \quad (1.4)$$

whence the overall effectiveness of the envisaged measures:

$$r = \sum_1^n j(P_{r,j} / P_r) \cdot r_j \qquad (1.5)$$

The expression (6.5) is a weighted sum of the efficiencies by failure mechanism, the weights being the relative probabilities associated with them.
The annual hazard rate associated with the existing dam has the known expression:

$$R, = P_r \cdot C \qquad (1.6)$$

here P_r is the probability of failure, and C is the quantitative measure of the consequences, this time including damage to the owner.

In the case of dams under the control of the authorities, as in the case of SPEEH Hidroelectrica S.A., the loss of human lives caused by dam failure is minimised to the minimum possible by warning-alarm- evacuation plans. Assuming that, in terms of consequences in terms of loss of human life, all measures are taken to minimise the risk to the limit of tolerable risk, the quantitative measure of consequences C has only a monetary expression. C is the operating cost (actual or potential), as we have seen.
The benefit created by reducing the risk rate by supplementing the behaviour tracking system, BBM, is [1]:

$$b = P_r \cdot C - P'_r \cdot C = P_r \cdot C \cdot r_s \quad (1.7)$$

where r has the expression (6.5), and the subscript s denotes a particular BBM supplementation system or supplementation strategy.
Each strategy has a corresponding annual realisation cost ΔC_s and consequently the net benefit will be:

$$b_n = b - \Delta C_s = P_r \cdot C \cdot r_s - \Delta C_s \qquad (1.8)$$

The selection of the additional BBM strategy is naturally made on the criterion of maximum net benefit (b_n = max.). A suggestive representation is contained in Figure 6.1.8.

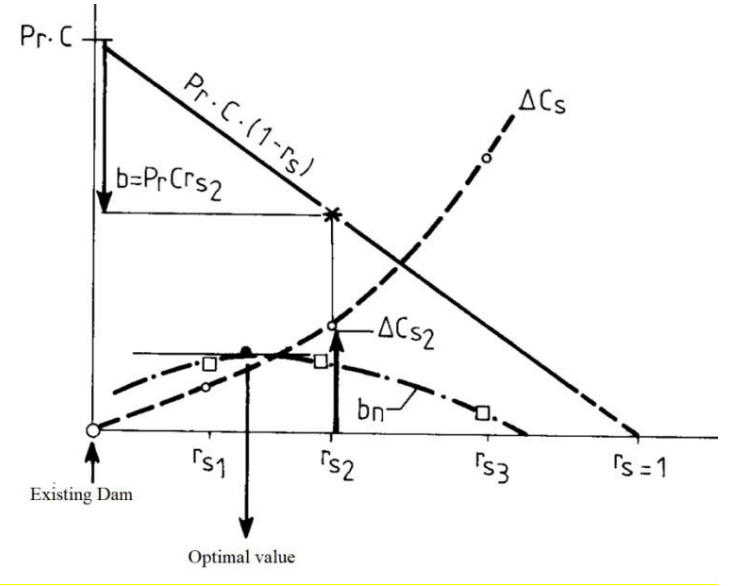

Figure 1. *Optimal variant selection based on net benefit maximisation.*

2. VIDRARU dam case study for the filling - emptying cycle

SPEEH Hidroelectrica S.A. awarded in 2024, the "Vidraru dam refurbishment" project. During the period of the Vidraru CHE refurbishment, the Vidraru reservoir operation mode will include a filling - emptying cycle. As a result, an efficient approach [4] to the monitoring of the Vidraru dam during the period of the revitalisation works is required.

2.1. Presentation of the dam and the existing BBM system

The Vidraru dam is of the "concrete arch" type, with a height of 166.60 m, an arch length at the crest of 314 m and a volume of 470,000 m^3 of concrete. The thickness at the base is 25.0 m and at the crest is 6.0 m; the road on the crest is 10 m wide (with pavements); the crest elevation 834.00 mdM.
The dam consists of 22 plots separated by helical jointed joints so that, for any given elevation of the dam, the lateral faces of each joint are radially oriented and converge in the mean centre of the respective arc. The width of the plots is variable, ranging from 10 to 14 metres each.

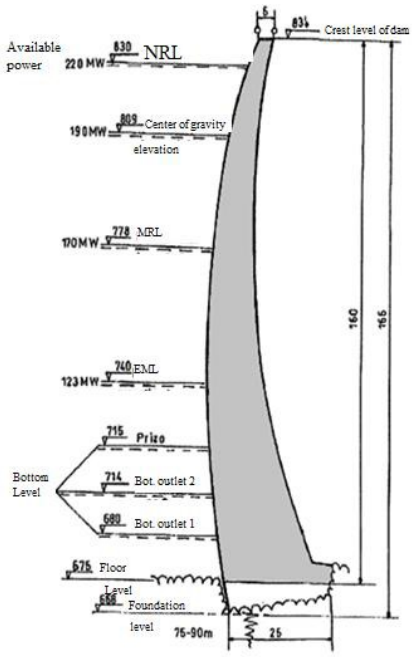

The dam has the following construction characteristics:

- canopy height 834.00 mdM
- maximum height 166.60 m
- length at crest 317.00 m
- rope length at canopy 245.00 m
- key thickness at canopy 6.00 m
- thickness at base 25.00 m
- chord to height ratio (L/H) 1.48
- base thickness to height ratio (B/H) 0.15
- volume of concrete 470 thousand cubic metres

Figure 2. *Main dam section*

The spillways equipping the Vidraru dam have the following capacities (according to the operating regulation):

– Three-field free-flowing surface spillway (832.85 mdMN) = 260 m^3/s.
– Bottom drains: (2 x 80m^3/s = 160 m^3/s)
– Hydroelectric power plant: 90 m^3/s.

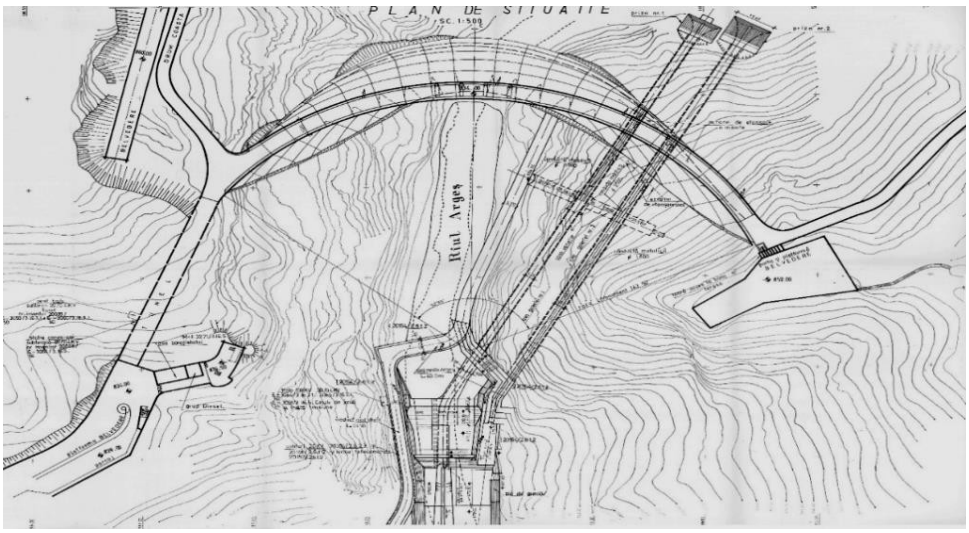

Figure 3. *Situation plan*

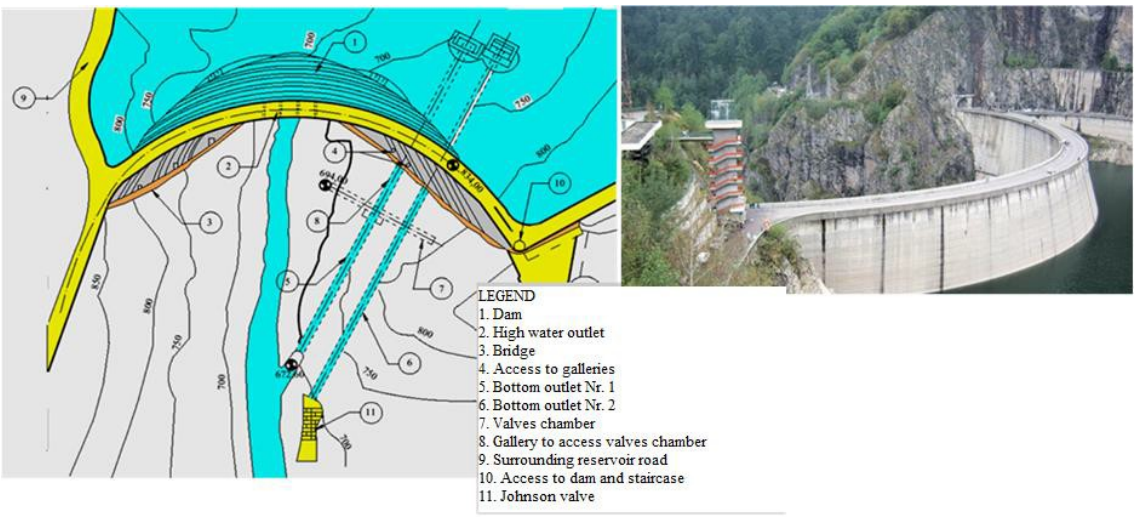

Figure 4. *Components*

The location of Vidraru dam is situated on the gnais ocular of Cozia downstream the tectonic contact.

The main faults in the area of the dam's crest have oblique or normal directions in relation to the bedding, forming angles of 20^0- 80^0. At their intersection and on the main faults there are crushing zones, i.e. breccias 0.5 - 3.0 m thick. These breccias are well cemented, silicified or calcareous. The fissuring, represented by cracks and fissures proper, is characteristic of the surface zone (8 - 10 m deep) and in the depth is more developed on the slopes. They form a complex system both by their orientation in the spaces and by the discontinuity effect they cause in the rock massifs. In areas with faults and cracks, there is a reduction in the physical-mechanical characteristics of the rock, the presence of seepage water circulation and the possibility of detachment of rock blocks on the crack planes with the inclination parallel to the slope of the slopes, which are facilitated by freeze-thaw processes.
The measuring and control equipment at the date of commissioning comprised the following apparatus:

- Reverse pendulum and direct pendulum;
- clinometric bolts;
- deforming bolts;
- discedometers;
- interstitial pressure cells;
- telerocmeters;
- telemeters;
- Triangular displacement gauges;
- levelling protractors;
- micro-triangulation protractors;
- fundamental levelling levelling marks;
- micro-triangulation pilasters;
- drainage boreholes;
- piezometric boreholes.

The present situation of the measuring and control apparatus is:

Table no. 2.1

Nr. crt	Device type	Parameter monitored	AMC No	Location
1	Direct pendulum	Horizontal displacements	5	in plots 2, 7, 12 (2 pcs.), 17
2	Reverse pendulum	Horizontal displacements	4	in plots 2, 7, 12, 17
3	Deformation bolt	Displacements in rost	96	in joints between plots, in galleries
4	Discedimeter	In-row displacements	24	in the joints between studs, in galleries
5	Clinometric bolt	Inclinations	5	in plot 12, in galleries
6	Telerocometer	Foundation rock deformations	4	at contact between dam and slopes
7	Telepiezometer	Water level in slopes	10	at contact between dam and slopes
8	Micro-triangulation marker	Horizontal and vertical displacements	14	on the downstream face of the dam

The monitoring system at the dam is undergoing an extensive modernisation process consisting of the installation of new monitoring devices and equipment (direct and reverse telependulum, telepiezometric boreholes, telemeters, etc.), automatic reading systems on the measuring and data transmission devices. Within the project "Vidraru Dam. Additional AMC installation including BBM data acquisition and processing system " the following devices were installed:

– telependulums, 14 pcs;
– telemeters, 4 pcs;
– telepiezometers, 14 pcs;
– telemeters, 20 pcs;
– discedometers, 20 pcs;
– teledebitmeters, 1 pc, mounted in the gallery at Vana Johnson;
– telemetre and telepluviometer 1 pc. , mounted at the dam house;
– complex seismic monitoring system.

2.2. Lake discharge data

UHE Vidraru is about to enter an extensive programme of refurbishment. This programme also includes rehabilitation works on the hydromechanical equipment related to the bottom drains (flat valves and Johnson valve), which suffered some

failures caused by the accident that occurred on the slope in 1974. During the period of operation, the seals of the sluice gates have suffered damage which has increased over time, as signalled by the increase in the flow of water lost downstream of these sluice gates due to the deterioration of the sealing elements of this equipment. The cumulative value of these lost flows downstream of the dam was estimated at around 150 l/s, with small fluctuations, depending on the water level in the reservoir. As part of the upgrading works, an important point for the safety of the bottom drains is the replacement of the by-pass installations for balancing the pressures at the safety valves. These by-pass installations no longer fulfil the functional role for which they were designed, as they are blocked/corroded and no longer safe in operation.

In order to be able to repair/rehabilitate the hydromechanical equipment at the bottom outlet No 1, which has a minimum level of 689.25 mdMN, it is necessary to empty the Vidraru reservoir up to this level. The emptying of the Vidraru reservoir is to be carried out in accordance with the emptying instructions drawn up by the specialised designer. The conditions and stages of emptying (times, discharged volumes, emptying mode - by machining and/or bottom emptying, etc.) between different characteristic heights of the reservoir, as well as the corresponding time periods have been established. Figure 6.5. plots the lake curve over the emptying period.

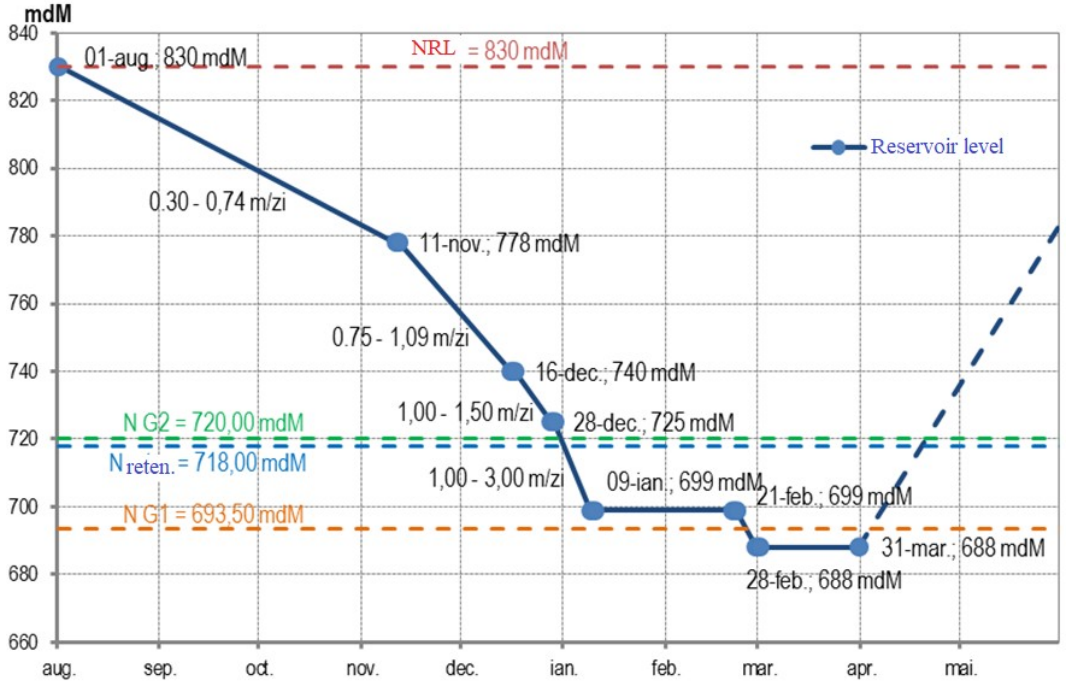

Figure 5. *Proposed emptying programme*

In order to ensure the safety status of the hydro-technical objectives related to the Vidraru PHE during the emptying of the reservoir, the special monitoring programme for the Vidraru dam and reservoir, as well as special instructions for monitoring these objectives by means of measurements and visual observations, prepared by ISPH PD SA, will be followed, even when the dam and reservoir no longer exist.

2.3. Behaviour of the dam at previous embankments

The Vidraru reservoir was completely emptied in the period 1974-1975, after the accident on 05 July 1974. The lake was emptied from the following day from the level of 823.00 mdMN up to the minimum level of 690.25 mdMN, reached in March 1975. This emptying is similar to the expected one, being carried out at the same time of the year (August-March).

Figure 6.6. shows the time evolution of the measured displacements of the direct pendulum in centre plot 12. The values plotted are the displacements of the point at elevation 748 mdM relative to the gallery 712 mdM for centre plot 2.

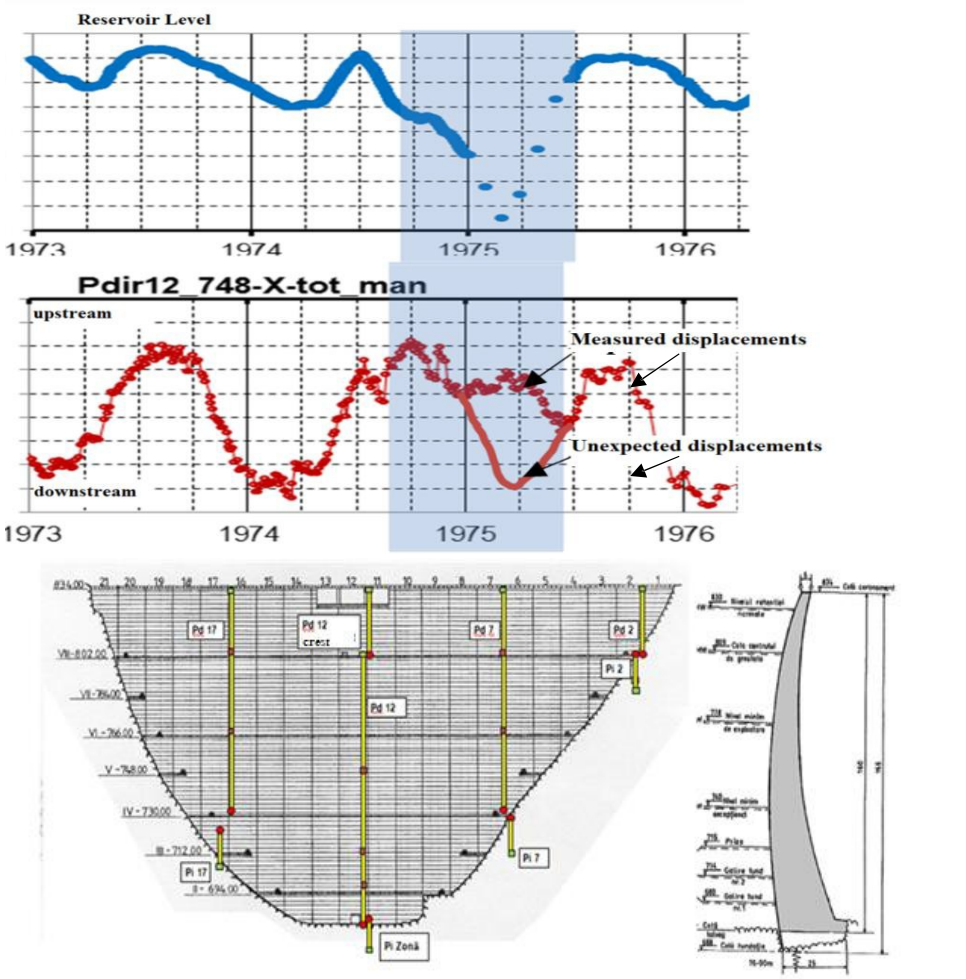

Figure 6. *Dam displacements at 1974 emptying*

Prior to the emptying of the lake, there is a normal upstream displacement due to the air temperature acting on the dam concrete, which is increasing, expanding the horizontal arcs. The emptying of the lake occurs during the autumn and winter when the air temperature is decreasing, which in normal operation mode should have a

downstream displacement by shrinking the concrete, but the emptying of the lake decreases the hydrostatic pressure on the upstream face, which induces an upstream displacement. As the two factors acting on the dam (water level in the lake through hydrostatic pressure and air temperature) are in opposite directions, in the end the two causes cancel each other out to some extent, the displacement having a much smaller variation and the downstream displacement no longer occurs.
From the above considerations, it follows that the emptying of the lake during August-February is favourable for the dam safety, the two factors directly influencing the dam behaviour cancel each other out, the dam displacement is predicted to be within the previous limits.

2.4. Specificity of the problem

In the case of the Vidraru dam the approach is similar to the one exposed in subchapter 6.1 but the risk is not associated with the breach defined as uncontrolled loss of water from the reservoir and the formation of a breach wave. We will keep the name breakage improperly to use the mathematical relations related to the adopted decision criterion, but by breakage we mean the loss of the functionality of the reservoir through the long-term forced emptying of the lake for the rehabilitation works imposed by the dam damage subjected to an atypical operating regime.
The breakage cost (**C**) in the given case is defined as the cost of the dam rehabilitation works, plus the cost of the energy not produced during the repairs.

2.5. Damage mechanisms and specific additional tracking systems

In order to select dam failure mechanisms due to atypical stress, potential structural effects upon emptying and refilling of the lake are reviewed.

– Ambient temperature exposure of the upstream face as the level is lowered and as a result the thermal field in the concrete changes, with transient regime and altered boundary conditions.

– Direct exposure of the upstream face to air temperature fluctuations causing in the cold season the joints to open, with the effect of reduced spatial co-operation and increased seepage.

– Alteration of the infiltration regime and interstitial pressures from rock discontinuities in the rock mass of the slopes of the reservoir and implicitly in the slopes of the dam.

– The change in the thermal regime in the slopes resulting in the expansion of the rock, which is felt by the tendency of the valley to close. The details that are necessary are:

– During the long period of exploitation of the lake, with levels of more than 800 mdM since 1996, a saturation of the rock mass occurred, with interstitial pressures corresponding to the water level in the lake. When the lake is emptied, the water stored in the rock flows towards the face of the slopes and at the same time the interstitial pressures are released. The flow spectrum induces gradient-

type infiltration forces, opposite to the direction of flow, which lead to displacements of the lake contour inwards towards the slope. At the same time, the decrease in interstitial pressures leads to an increase in the effective stresses, which are mainly self-weight. These changes in the state of effort also have consequences on the displacements of the slopes, tending to open the valley.

– At the same time, the emptying of the lake also produces a change in the thermal regime of the slopes. In high dams, such as the Vidraru dam, the temperature of bedrock below the mean operating level has a low quasi constant temperature, and below 60 m from the NNR even a constant equal to $4.5^{(0)\ C}$. If the duration of emptying is long and exposes the slopes to warm-season air temperature there is an increase in the temperature of the rock mass over a limited depth. The increase in temperature has the effect of dilation of the rock, which is felt by the tendency of the valley to close.

– Deformation of the slopes upstream of the dam during the filling and emptying phases can affect the structural behaviour and long-term safety. In the first filling phase, the valley tends to converge, and in the emptying phase it tends to open up, especially at the upper reaches of the dammed valley. The dam is subjected to additional loading by the displacement of springs towards or away from the centre section.

– For the filling phase, the effect of "dam ageing" also occurs. If over time there has been a flexibilisation of the structure through joint openings and possibly structural degradation it is possible that the displacements recorded with increasing hydrostatic loading are larger than for previous lake fills (loading and refilling after the 1974 event). Such a situation must be examined from the point of view of the induced stresses in the structure.

Based on the behavioural data presented, the "failure" mechanisms, i.e. the mechanisms leading to the dam being taken out of service, have been established:

– Excessive cracking as a result of a drop in the temperature of the structure due to exposure of the upstream face to the ambient;

– Displacement of the dam's shoulder settlement due to convergence displacement of the slopes;

– Structural wear due to displacements imposed on the foundation contour by slope displacements;

– Landslide of the slopes with blockage of the dam's related outlets;

– Structural degradation and flexibilisation of the structure, accompanied by seepage through the interplot joints as a result of the joints opening in the cold season with the dam empty.

In order to follow the stresses to which the dam is exposed under the conditions of the emptying - filling cycle and respectively the response of the structure to these stresses, the following additions are proposed to the existing BBM system:

– Creation of a finite element mathematical model of the dam structure that takes as input imposed displacements, temperature fields and structural discontinuities

– Reactivation of telemeters, if possible;

– 3D laser scanning of the downstream face of the dam - bedrock system
– InSar tracking of lake basin displacements
– Tracking of interstitial pressures in the slope rock mass by hydrogeological boreholes
– Monitoring the stability of the slopes upstream and downstream of the dam by a network of inclinometer casing.

Clarifications.
In order to monitor the displacements, deformations and stability of the slopes immediately upstream of the dam embedment, it is proposed to carry out geodetic topographic measurements on the slopes using 3D laser scanning technology.
The general view of 3D scanning technology is that it represents a more advanced method of surveying - a more accurate, more detailed and faster method of data acquisition. Whilst all of these properties of 3D laser scanning are true, this technology also brings countless opportunities. 3D scanning provides decision-makers with a tool to assess the progress of construction works, to carry out structural assessments.
A recommended alternative is the use of InSAR technology. Interferometric synthetic aperture radar, abbreviated InSAR is a method of interest here. It uses two or more synthetic aperture radar (SAR) images to generate surface deformation maps. With InSAR technology, millimetre spatial measurement accuracy can be obtained, because the radar signal acquisition mode can simulate a sufficiently large antenna, and most importantly, the measurements are coherent (the phase of the electromagnetic wave is maintained).

2.6. Risk analysis

The decision on the provision of an adequate CCU supplement, based on the maximum benefit criterion, requires knowledge of the risk posed by the dam. It is therefore necessary to assess the likelihood of a failure leading to the storage being taken out of service and also to assess the consequences of the situation created.
In the reports and papers presented at ICOLD congresses and symposia there are no useful reports on the damage caused by emptying-filling cycles in concrete dams. Still less a database that allows statistical processing as exists for breakout cases.
In such situations, the probabilities of an adverse event occurring are assigned on the basis of engineering judgement, which in fact quantifies subjective opinions. Usually the *chance* of occurrence of a particular event is described verbally and numerical equivalences of these judgements are used. Considering the robustness of the Vidraru dam and the behaviour in operation so far, the damage in the case of the emptying-filling cycle can be categorised as "very unlikely". For this categorisation the probability of occurrence of a damage with the effect of emptying the storage is given $P_r = 10^{-1}$.
For the five failure mechanisms inventoried the relative probabilities of occurrence were recognised as:

– ① Excessive cracking as a result of a decrease in the temperature of the structure by exposure of the upstream bulkhead to the ambient ($P_{r,1}/P_r = 0,12$);
– ② Displacement of the dam shoulder rebound as a result of slope convergence displacement (); $P_{r,2}/P_r = 0,10$;
– ③ Structural cracking as a result of displacements imposed on the foundation contour by slope displacements (); $P_{r,3}/P_r = 0,28$;
– ④ Slope failure with blockage of the dam's related manoeuvres (); $P_{r,4}/P_r = 0,32$;
– ⑤ Structural degradation and flexing of the structure, accompanied by seepage through the interplot joints as a result of the joints opening in the cold season with the dam empty (); $P_{r,5}/P_r = 0,18$;

The financial losses as a result of the decommissioning of the storage are the cost of the dam rehabilitation works and the cost of electricity not produced during the rehabilitation works. The rehabilitation works have different costs depending on the failure mechanism.
For mechanisms 1,3 and 5 the works are localised to the structure and consist of injections to restore structural continuity and re-injection of joints. The estimated cost is C_{135}= 12 mil EURO.
Mechanism 2 requires partial restoration of the slope plots and possibly a culee. The construction solutions are demanding and very expensive. The estimated cost of the concreting works is approx. 14 million euros, plus the rehabilitation of the remaining structure, approx. EUR 10 million, which comes to C2 = EUR 24 million
In the case of mechanism 4, the works are intended to stabilise the slope, which has had rock detachments and displacements towards the base. The estimated cost is EUR 14 million.
It should be noted that the cost estimates are rough approximations in the absence of specific rehabilitation solutions. These approximations do not affect the purpose of the case study, the procedure remains valid, of course with the variant selection adjusted in accordance with the correctly evaluated prices.
In order to assess the monetary loss during the period when the hydropower plant is not in operation, it is necessary to estimate the duration of the rehabilitation and restoration works. Assuming a duration of procurement and project preparation of 15 months, a duration of actual works of 20 months and a duration of controlled refilling of the lake of 12 months, a total duration of 47 months, i.e. round 4 years, is given. The annual energy production of AHE Vidraru is 400 GWh/year. SPEEH Hidroelectrica S.A. has put up for sale 5 MW per hour electricity packages, with delivery throughout the year 2025, at a price of 625 lei/MWh. As a result, the cost of the energy not delivered during the period of repair of the damage at the Vidraru reservoir is 50 mil EURO.
The total cost of a damage due to the phenomena associated with the emptying and filling of the reservoir is C = 74 million EURO.

2.7. Effectiveness of dedicated behaviour monitoring variants on the emptying - filling cycle

The analysis of the efficiency of the systems envisaged to reduce the risks for the damage mechanisms inventoried is centralised in Table 6.2. The justification of the values is detailed with reference to Table 6.2.

Damage due to excessive cracking, as a result of the temperature drop of the structure due to exposure of the upstream face to the ambient, can be detected by the existing AMC system to a small extent (0.4), the response quantities being displacements (relative and absolute). By linking to the mathematical model, the measured quantities are translated into efforts which are a measure of the risk of cracking (effectiveness rate increases to 0.80). Reactivation of the telemeters increases the system effectiveness to some extent (0.85). The other measures to improve the BBM system (laser scanner, hydrogeological boreholes and inclinometer casing) do not bring increased efficiency in detecting excessive cracking. Damage due to displacement of the dam shoulder due to convergence displacement of the slopes is poorly detected by the existing BBM system (0.05). The associated mathematical modelling provides an efficiency gain (0.2). The reactivation of the telemeters does not provide relevant information for this damage mechanism. The efficiency in detecting this mechanism is provided by laser scanner measurements and information from hydrogeological boreholes and inclinometer casings (0.44, 0.55, 0.75)

Damage by structural cracking due to displacements imposed on the foundation contour by slope displacements can be highlighted to some extent by the existing BBM system (0.15) and with increased efficiency if the mathematical modelling is added (0.34). The other expected measures have efficiency in detecting the phenomenon by emphasising slope displacements (0.64).

Table 2.2.

Effectiveness of the BBM system

Damage mechanism (j)			$j = 1$ Excessive cracking	$j = 2$ Dislocation of the dam shoulder	$j = 3$ Structural cracking	$j = 4$ Landslide	$j = 5$ Structural degradation	
Relative probability $P_{r,j}/P_r$			0,12	0,10	0,28	0,32	0,18	
Effectiveness risk reduction ( ) R_j			r_1	r_2	r_3	r_4	r_5	Effectiveness Overall $\Sigma(P_{r,j}/P_r)\cdot r_j$
S	Existing BBM system		0,40	0,05	0,15	0,10	0,3	0.226
1	Existing BBM +Mathematical modelling		0,80	0.2	0.34	0.10	0,53	0,3386
2	**Math**	Telemetre reactivation	0,85	0,2	0,40	0.10	0,65	0.383
3		Laser scanner Or	0,85	0,44	0,64	0,65	0,65	0.6502

Damage mechanism (j)			$j = 1$ Excessive cracking	$j = 2$ Dislocation of the dam shoulder	$j = 3$ Structural cracking	$j = 4$ Landslide	$j = 5$ Structural degradation	
		InSar						
4		Hydrogeological boreholes	0,85	0,55	0,64	0,85	0,65	0.7252
5		Inclinometer tubing	0,85	0,75	0,64	0,95	0,65	0,7772

Damage by landslide with blockage of the dam's related nozzles cannot be warned by measurements from the existing BBM system, even if the mathematical modelling is associated. The efficiencies have slope scanning (0.65) plus data on interstitial pressures (hydrogeological boreholes 0.85) and inclinometry monitoring (casing 0.95).
Damage by structural degradation and flexibilisation of the structure, accompanied by seepage through the interplot joints as a result of opening the joints in the cold season with the dam empty, can be evidenced to some extent by the existing BBM system (0.3) with a plus in efficiency, if the mathematical modelling is added and with a plus in the activation of telemeters (0.65).
The overall effectiveness is however rather modest (0.7772) despite a consistent supplementation of the existing system due to the complex phenomena involved.

2.8. Choice of the optimal variant

The optimal variant was selected using the maximum net benefit criterion. The calculations are presented in Table 6.3.
For each variant (strategy) of supplementing the existing BBM system the annual costs were first evaluated C.Δ

Table 2.3.

Calculation of benefits per variant

Strategy of BBM system		Cost per cycle ΔC (EURO)	Effectiveness of additionality $r_s=r-r_{existent}$	Benefit $b=P_r \cdot C \cdot r_s$ (EURO)	Net benefit $b-C\Delta$ (EURO)
Mathematical	(1) Mathematical model	40000	0.1126	157600	117600
	(2) Telemetre reactivation	30000	0,157	219800	189800
	(3) Laser scanner Or InSar	315000	0.4242	593800	278800
	(4) Hydrogeological drilling	124000	0,4992	698800	574800
	(5) Inclinometer pipes	235600	0,5512	771600	536000

A cost of $\Delta_{C(1)}$ = 40000 EURO has been estimated for the realisation of a dedicated mathematical model, in line with UTCB's prices. The reactivation of telemeters has

been estimated at $\Delta_{C(2)}$ = 30000 EURO, based on the experience of reactivating some telemeters at Paltinu dam. Laser scanner monitoring during the emptying - refilling cycle requires 7 campaigns, 4 during the emptying period and 3 during the refilling period. A campaign with a suitable number of points is valued at 45000 Euro, totalling over the period of interest $\Delta_{C(3)}$ =315000 Euro. Hydrogeological drilling is carried out on a network of 4 profiles on each slope with 3 boreholes per profile. The average depth is 65 metres. With a valuation of 80 EURO / ml of borehole, this gives a cost of $\Delta_{C(4)}$ = 124000 EURO. The inclinometer casing is arranged on a similar network. Given the additional equipment compared to a hydrogeological borehole, taking also into account the higher cost of measurements and processing, a 90% increase in costs compared to the network of hydrogeological boreholes has been estimated, giving a total cost of $\Delta_{C(5)}$ = 148800 EURO.

The maximum financial loss is Max Remediation cost + cost of unproduced energy + 24 + 50 mil Euro = 14 mil Euro. In sub-chapter 6.26 it was estimated that the probability of a failure with the effect of emptying the storage is $P_r=10^{-1}$.

The effectiveness of the additional variant was calculated by simply subtracting from the overall effectiveness of the additional variant (last column in Table 6.1) the overall effectiveness of the existing BBM system. The benefit and then the net benefit resulted from relations (6.7) and (6.8).

It is noted that the optimal variant (b_n = max) corresponds to a substantial additional BBM endowment, including the creation of a mathematical model, the reactivation of telemeters, the 3D laser scanning of the downstream dam face - foundation ground system and the tracking of interstitial pressures in the rock mass of the slopes by hydrogeolog ical boreholes. The inclinometer casing network is expensive and does not provide an acceptable benefit- cost ratio.

Bibliography

[1] S t e m a t i u , D . , A b d u l a m i t , C . , 1998 - *Decision analysis in dam safety monitoring* - Proceedings of International Symposium on "Rehabilitation of Dams", .New Delhi

[2] S t e m a t i u , D . , I o n e s c u , Ș t . , 1999 - *Siguranță și risc în construcții hidrotehnice* - Editura Didactică și Pedagogică, București.

[3] ICOLD, 2009. Surveillance: basic elements in a dam safety process

[4] Stematiu, D., Drobot, R., 2007 - *A procedure for rating the dam safety improvement works* - Proceedings of Int. Symposium on "Dam Safety Management", Sankt Petersburg.

[5] Iacob, I., Pecingine, M., Mateescu, O., Popovici, A., Stematiu, D. 2015Upgrading of the monitoring system from Vidraru - Argeș dam, Romania*. Proc. Of TWENTY THIRTY THIRD CONGRESS OF LARGE DAMS *Stavanger, June, 2015*

[6] Sarghiuta, R., 2019. Expertiza starii de siguranta a barajului Zigioneni, Raport pentru ANAR, Bucuresti

[7] Toubar, K., Nour El-Din, M. 2003 - *Use of indicators to simplify the risk management process for planning rehabilitation works for dams*. Proc. of International Symposium on Major Chalanges in Tailings Dams,Montreal .

[8] Asman(,) I, Diacon(,) P. Role of The Dam Monitoring System Within Romanian Water Authority in the Rehabilitation of Some of its Major Dams

[9] Li, B., Yang, D Hu - Structural Control and Health Monitoring, 2020 - Wiley Online Library